
Electronic Thesis and Dissertation Repository

4-14-2014 12:00 AM

The Aricheng Basement-Hosted Albitite-Type Uranium Deposit, Roraima Basin, Co-Operative Republic Of Guyana, South America.

Jim A. Renaud, *The University of Western Ontario*

Supervisor: Dr. Norman Duke, *The University of Western Ontario*

A thesis submitted in partial fulfillment of the requirements for the Doctor of Philosophy degree
in Geology

© Jim A. Renaud 2014

Follow this and additional works at: <https://ir.lib.uwo.ca/etd>



Part of the [Geology Commons](#)

Recommended Citation

Renaud, Jim A., "The Aricheng Basement-Hosted Albitite-Type Uranium Deposit, Roraima Basin, Co-Operative Republic Of Guyana, South America." (2014). *Electronic Thesis and Dissertation Repository*. 1960.

<https://ir.lib.uwo.ca/etd/1960>

This Dissertation/Thesis is brought to you for free and open access by Scholarship@Western. It has been accepted for inclusion in Electronic Thesis and Dissertation Repository by an authorized administrator of Scholarship@Western. For more information, please contact wlsadmin@uwo.ca.

THE ARICHENG BASEMENT-HOSTED ALBITITE-TYPE URANIUM DEPOSIT,
RORAIMA BASIN, CO-OPERATIVE REPUBLIC OF GUYANA, SOUTH AMERICA.

(Thesis format: Monograph)

by

Jim Antonio Renaud

Graduate Program in Geology

A thesis submitted in partial fulfillment
of the requirements for the degree of
Doctor of Philosophy

The School of Graduate and Postdoctoral Studies
The University of Western Ontario
London, Ontario, Canada

© Jim Antonio Renaud 2014

Abstract

The Kurupung batholith is situated in a west dipping mylonite zone within the Transamazonian-aged Mazaruni granite greenstone terrane. Mylonitic shearing is a result of regional sinistral strike-slip faulting during the post-collisional stage of the Transamazonian orogenic cycle. Deformation was active between 2103 +/- 3 Ma, the age of the batholith, and 1995 +/- 15 Ma, the age of hydrothermal uranium and zircon mineralization. Mineral chemical and geochemical characterization of the batholith identifies a uranium-enriched low-Ti sanukitoid generated by partial melting of slab metasomatized mantle which retained unresorbed Cr-bearing mantle inclusions. Rapid unroofing to greenschist facies conditions at approximately 2094 +/- 5 Ma, juxtaposed the Kurupung batholith against Transamazonian volcanoclastics. Textural evidence supports a continuum from Cr-bearing clinopyroxene and hornblende to actinolite-biotite-magnetite-chlorite(1) and minor sausseritization of Ca-plagioclase to albite(1)-muscovite-epidote. Decompression resulted in Ba-Kfeldspar pegmatite dikes at 2085 +/- 9 Ma and voluminous Ba-Kfeldspar metasomatism at 2071 +/- 13 Ma. Pervasive replacement of early primary Ca-plagioclase by secondary Ba-Kfeldspar partitioned Na into the fluid phase resulting in pervasive albite(3) replacement. Lamprophyre dike injection at 2011 +/- 11 Ma marks the transition from ductile to brittle deformation within the mylonitic shear zone which allowed devolatilization of mantle-derived fluorine and CO₂-rich fluids.

Meteoric ingress resulted in development of zones of mixing where chlorite(2) cemented albitite(3) breccia. Devolatilization along deeply penetrating shears resulted in a long-lived shear zone with Na metasomatism, diagnostic of an albitite-type uranium system. Fluorine and CO₂-rich fluid interacted with zircon granules in the batholith and sequestered uranium and zircon from their marginal domains. The result was an F-rich fluid carrying uranium and zircon in solution re-precipitating uranium in hydrothermal zircon veins. The basement-hosted uranium mineralization of the Kurupung batholith pre-dates the Roraima sedimentation and hence, the mineralization is not unconformity related.

Keywords: *Transamazonian, Roraima Basin, Kurupung batholith, Sanukitoid, Basement-Hosted, Alkali metasomatism, Albitite uranium-zircon*

Acknowledgements

This PhD work is a testimony to my interest in rocks cultivated from childhood. In many ways it reflects the support of the countless people who influenced me and this work. Foremost, I would like to thank Dr. Keith Barron and Dr. Richard Spencer of U3O8 Corp. for giving me the opportunity to undertake such an interesting project in an incredible part of the world. Their enthusiasm in the field, guidance and constructive comments generated throughout the thesis is greatly appreciated. I would also like to thank U3O8 Corporation who supported this thesis by contributing to an industry supported NSERC scholarship. A special thanks also to U3O8 personnel including: Sandra for wonderful morning pancakes, Oscar and Luis for discussions on core logging, Leslie for negotiating the core library, Hayden for keeping the 4-wheelers running, Tom for the Sunday morning malaria smears, Warren, Mike and Benidict for clearing paths through the vine entangled jungle, to Chuckie for his riverboat skills and especially Marcel for his wisdom of local flora, fauna, and the inhabitants of nearby villages.

A special thanks to my thesis supervisor Dr. Norm Duke who spent several weeks with me in the snake-ridden jungle of Guyana. Thank you for helping make sense of critical textures, complicated structures, regional processes, and helpful direction in editing this thesis. Appreciation is extended to the “President” of R.L. Barnett Geoanalytical Ltd. for his patience and constructive discussions pertaining to minerals chemistry, mantle metasomatism, and thoughtful conversations on life in general. A thank you is also extended to Dr. John Armstrong for his discussions on the mantle and sanukitoid genesis, and his help in bringing a new dimension to the thesis by introducing me to mantle geothermobarometry. I am also grateful for personal communications with Oscar Laurent for his interest and expertise regarding sanukitoid chemistry and genesis.

To my family, thank you for your invaluable moral support through the duration of this thesis. I would like to thank my wife Natalie for her help with editing, constructive geological conversations late at night, and most importantly helping keep me together and on track. And finally, to my daughter Katrina, thank you for adding humour to my

day, making me take time out to dance and most importantly putting a smile on my face.
You have all made this extremely rewarding.

Table of Contents

Abstract	ii
Acknowledgements	iii
List of Tables	ix
List of Figures	x
List of Plates	xiv
List of Appendices	xx
<u>Chapter 1: Introduction</u>	1
1.1 Opening Statement	1
1.2 Geography of Guyana	2
1.3 Location, Property Description and Access	5
1.4 Previous Work	10
1.5 Objectives and Methods of Study	12
<u>Chapter 2: Regional and District Geology</u>	15
2.0 Introduction	15
2.1 Geology of the South American Craton	15
2.2 Geology of the Transamazonian Orogen	18
2.3 Local Geology of the Aricheng District	20
<u>Chapter 3: Petrography</u>	30
3.0 Introduction	30

3.1 The Unmetasomatized Kurupung Batholith	30
3.1.1 <i>Cr-bearing Clinopyroxene</i>	32
3.1.2 <i>Amphibole</i>	37
3.1.3 <i>Plagioclase</i>	41
3.1.4 <i>Microcline(1)</i>	41
3.1.5 <i>Titanite</i>	44
3.1.6 <i>Accessory Phases</i>	44
3.2 Chloritic Shear Zones	48
3.3 Ba-Kfeldspar Metasomatism	48
3.4 Main Ore Stage	56
3.4.1 <i>Main Ore Stage: Calcite, Zircon Veining and Uranium</i>	61
3.4.2 <i>Main Ore Stage - Uranium Minerals</i>	66
3.5 IOCG-style Mineralization at Aricheng	70
3.6 Avanavero Dikes	79
<u>Chapter 4: Geochronology</u>	82
4.0 Introduction	82
4.1 Radiometric Dates	83
4.2 U/Pb Geochronology of Titanite	84
4.3 U/Pb in Pegmatite Dikes and Ar/Ar in Metasomatic Ba-Kfeldspar	84
4.4 Ar/Ar Geochronology of Foliated Lamprophyre Dikes	91

<u>Chapter 5: Geochemistry</u>	99
5.0 Introduction	99
5.1 Classification of the Kurupung Batholith	101
5.2 Geochemistry of the Intensely Altered and Mineralized Kurupung Batholith	110
<i>5.2.1 Factor Analysis and Mass Balance (Isocon) Evaluation of IOCG-style Alteration</i>	111
<i>5.2.2 Pearson Factor Analysis: Accori and Aricheng Prospects</i>	111
5.3 Mass-balance Calculations: Drill hole scale analysis	118
<u>Chapter 6: Discussion</u>	123
6.0 Introduction	123
6.1 Tectonic Setting	123
6.2 Implications Regarding Mantle Source of the Kurupung Batholith	124
6.3 The Kurupung Batholith: A Post-Collisional Sanukitoid	134
6.4 Growth of Secondary Ba-Kfeldspar Megacrysts	137
6.5 Discussion of Factor Analysis and Mass Balance Results	141
6.6 The Kurupung Mineralizing System	142
6.7 Origin of Uraniferous Hydrothermal Zircon Veins	147
6.8 IOCG Processes Pre-Dating the Roraima Formation	147

<u>Chapter 7: Conclusions</u>	151
7.0 The Metallogenic Evolution of the Kurupung Batholith	151
7.1 Summary	152
References	155
Appendix	166
Curriculum Vitae	318

List of Tables

3.0 The paragenetic sequence defining a mineralogical continuum from host sanukitoid to post ore alteration.	31
4.0 Summary table of geochronological data specifically related to the Kurupung batholith, age of mineralization, and overlying stratigraphy.	83
4.1 (a) A summary data table for U/Pb age dates on titanites; (b) A summary data table for U/Pb age dates on zircon.	86
4.2 Lamprophyre dike Ar/Ar age data on biotite phenocrysts.	98
5.0 Whole rock and trace element geochemistry of a representative sample suite of unaltered Kurupung batholith. See Appendix C for data tables from ActLabs.	100
5.1 A comparative table of characteristic whole rock and trace element data for TTG, adakite, sanukitoid, closepet granitoids, and the Kurupung batholith.	105
5.2 The drill log for hole ARN-031 with columns denoting meterage, lithology, magnetic susceptibility, alteration, mineralization, and scintillometer readings in counts per second (CPS). See Appendix C for drill core images of ARN-031.	119
5.3 A table of geochemical analyses pertaining to drill hole ARN-031. The geochemical data represented here only pertains to the first 34m of drill core. Note that the 2000-series sample numbers are samples originally selected by U3O8 Corp. for geochemical analysis of the prospective areas of the drill core with high CPS. These sample numbers are located on the drill log in Table 5.2. The 5000-series sample numbers were selected for mass-balance calculations and were collected from the various intervals detailed in this table. Density measurements were carried out by U3O8 Corp. See Appendix C for complete analytical package of drill hole ARN-031.	120

List of Figures

1.0 Graph illustrates the evolution of uranium price from 1948-2008. Note that from 1990 onwards, there is a gap between uranium demand (red line) and world production (background grey).	3
1.1 Graph illustrates the volatility of uranium market price relating to global current events from February 2011 to February 2012. The black line represents the Ux Consulting Company (UxC) broker average price of uranium. It is an average of the best bids and offers reported by the brokers. The orange line represents the uranium stock market trend.	4
1.2 Map illustrating the exploration property. The property encompasses six granted Prospecting Licenses and four Prospecting License applications totaling approximately 47,923 ha (118,420 acres) (modified after Workman, A., and Breede, K., 2012).	6
1.3 Map outlining the mining districts within Guyana. Note the Kurupung batholith is within the Mazaruni mining district (modified after a map created by Geographic and Environmental Management Solutions Guyana Inc.).	7
1.4 Aerial view illustrating the Aricheng airstrip, and U3O8 Corp's Aricheng base camp, including an office, core shed, accommodations, kitchen, and storage.	8
1.5: (a) Black and yellow butterfly (b) Howler monkey range in size from 22 to 36 inches (c) Smooth-sided toad (<i>Bufo guttatus</i> ~5 inches in length) (d) Dynastinae or Rhinoceros Beetle climbing a handrail (~6 inches in length) (e) Anaconda crossing the road (~30 feet long) (f) Coral snake (~5 feet long).	11
2.0 Crustal provinces of South America: AM – Amazonian craton; SF – Sao Francisco craton; RP – Rio de la Plata craton; SL- Sao Luis, and LA-Luiz Alves. Figure is from Cordani and Sato, 1999.	16
2.1 Tectonic provinces of the Amazon craton illustrating a progressive younging of accreted terranes to the west. The figure is after Santos et al., 2003.	17
2.2 A sketch map of Guyana illustrating the locations, extent, and names of the granite-greenstone belts. The Kurupung batholith (red star) is located with the Mazaruni greenstone belt at the edge of the Pakaraima Mountains. Figure is modified after Gibbs, 1979.	19
2.3 Geotectonic evolution of the Guyana shield from the collisional Rhyacian to post-collisional Neorhyacian-Orosirian periods. Note the importance of sinistral strike-slip and transpressional tectonics between 2.11-2.08 Ga.	22

2.4 Regional map illustrating the location of the Kurupung batholith in Tramazonian volcanics (Modified after Baker, 2008)	23
2.5 Simplified geological map of the Aricheng district (Modified after Baker, 2008)	24
2.6 Airborne magnetic surveys delineating sigmoidal shears and illustrating uranium prospects within the Kurupung batholith. Modified after image from U3O8 Corp. website (www.u3o8corp.com)	25
2.7 Magnified view of the Aricheng South sigmoid illustrating contours of uranium enrichment. Note that the contours of uranium concentration occur in less magnetic domains of the sigmoids.	26
2.8 The figure illustrates the drill hole locations for the Aricheng South area.	27
2.9 Non-magnetic mineralized shears within background magnetic Kurupung.	28
2.10 Drill section illustrating six holes at Aricheng South.	29
3.0 Clinopyroxene ternary illustrating the compositional variation between Cr-diopside cores and Cr-augite margins within mantle aggregates.	36
3.1 Graph illustrating ratios of Al ^{vi} to Al ^{iv} for clinopyroxenes. Data points falling within the “granulites and inclusions in basalts” field support the interpretation that Cr-diopsides represent the primitive mantle composition derived at elevated P-T conditions and that the Cr-augite overgrowths plotting in the “igneous rocks” field formed at lower P-T conditions during ascent of the partial melt.	37
3.2a,b (a) Leake classification diagram for amphiboles illustrating the progression from most primitive Cr-edenite through Cr-magnesiohornblende to low temperature retrogressive actinolite; (b) a plot of total alkalis versus Al ^{iv} illustrating the more elevated alkali and tetrahedral Al content of most primitive amphibole compared to the more depleted alkali and tetrahedral aluminum content of the retrogressive actinolites.	40
3.3 Chlorite classification diagram illustrating chlorite(1) compositions plotting in the pycnochlorite field and chlorite(2) compositions plotting as clinocllore. Diagram modified after Zane et al., 1998.	51
4.0 Concordia diagram for titanite with axes of the ratios of the radiogenic daughter Pb isotope divided by their respective parent U isotope. A concordia age of 2094 +/- 4.9 Ma has been calculated for the titanites.	87

4.1 Concordia diagram for zircon in pegmatite dike with axes of the ratios of the radiogenic daughter Pb isotope divided by their respective parent U isotope. A Concordia age of 2085 +/- 9.2Ma has been calculated for the age of the pegmatite dikes.	90
4.2 Cumulative ³⁹ Ar step-heating results. Reheating events yield a staircase-like profile; the 0% value is the age of the reheating event, and the 100% value is the minimum age of initial crystallization of the sample.	91
4.3 Cumulative ³⁹ Ar step-heating results. Reheating events yield a staircase-like profile; the 0% value is the age of the reheating event, and the 100% value is the minimum age of initial crystallization of the sample.	98
5.0a,b (a) A/CNK versus SiO ₂ wt% illustrating the metaluminous character of the unaltered Kurupung batholith; (b) Binary diagram illustrating the Kurupung dataset within the magnesian post-collisional A-type granite field (after Frost et al., 2001).	103
5.1 Total alkalis vs SiO ₂ diagram for the Kurupung batholith. The rock classification is after Middlemost (1994). The line separating the alkaline and subalkaline fields is after Miyashiro (1978). The samples plot as alkaline monzonite to quartz-monzonite.	105
5.2a,b (a) Ternary diagram illustrating the red and green sanukitoid and closepet granite fields, respectively. The data points of the unaltered Kurupung batholith fall within the sanukitoid field (after Moyen et al., 2003); (b) Harker diagram showing data points falling within the high-K calc-alkaline to shoshonite series.	106
5.3a,b Chondrite normalized REE patterns for the unaltered Kurupung. The pattern illustrates high LREE contents and low HREE contents resulting in strongly fractionated patterns; (b) Typical chondrite normalized REE patterns of TTG, sanukitoid, and closepet granitoids (Martin and Moyen, 2005).	107
5.4a,b (a) Primitive mantle normalized multi-element diagram for the Kurupung; (b) Primitive mantle normalized multi-element diagram for TTG, sanukitoid, and closepet granitoids.	108
5.5 A radiometric map with illustrating prospective uranium targets.	113
5.6a,b (a) Factor analysis diagrams for the Accori South and (b) Accori North B areas.	114
5.7: Factor analysis diagrams for the Accori North A area.	115
5.8a,b (a) Factor analysis diagrams for the Aricheng South (ARS) and (b) Aricheng West (ARW) areas.	116

5.9a,b (a) Factor analysis diagrams for the Aricheng North (ARN) area; (b) Scatter plot of U concentration versus Na concentration for the entire Kurupung batholith. High U concentrations are associated with low Na concentrations (red loop). Note that above 7 wt% Na, U concentrations diminish.	117
5.10 Graphical representation of mass balance results illustrating overall volume change and overall mass change with respect to sample number. The yellow squares represent the alteration and mineralized zones; red arrows point in the direction of overall volume loss; green dots represent the areas of most elevated uranium concentration down the drill hole.	122
6.0 Ternary diagram illustrating the substitution of Al, Na, and Cr into the clinopyroxene structure as high pressure jadeite-kosmochlore and lower pressure CATS-kosmochlore.	126
6.1 A plot of ureyite versus calcium number. The plot illustrates an elevated ureyite component corresponding with a low calcium number at high pressure and a stronger Tschermack substitution at lower pressures.	127
6.2 The geothermobarometer of Nimis and Taylor (2000) which allows precise determination of P-T conditions of Cr-clinopyroxene with >0.5 wt% Cr ₂ O ₃ . Due to the lack of clinopyroxene mineral chemistry of other sanukitoids, the Kurupung batholith dataset is plotted here with Cr-clinopyroxene compositions of xenoliths from various kimberlites worldwide as a comparison.	129
6.3 Binary plot of Cr+Al versus Na with fields defining “spinel peridotite (SP)” and “garnet peridotite (GP)”. The graph illustrates the Kurupung batholith’s Cr-clinopyroxene trend from most primitive Cr-diopside compositions in the “spinel peridotite” field to more evolved Cr-augite compositions. The diagram is modified after Sobolev et al., 1992.	135
6.4 Synthetic cross-sections of subduction zones (after Martin & Moyen 2002).	136

List of Plates

- 3.1 Piece of core representing background Kurupung with mafic clots of Cr-Clinopyroxene-Cr-amphibole in a more felsic matrix. 32
- 3.2a,b: (a) Plane light image of Cr-clinopyroxene at the centers of the mafic clots forming large simple twins and compositional zoning with primary magmatic high Mg,Al,Cr-clinopyroxene cores zoned outward to high-Fe, low-Al,Cr-clinopyroxene margins; (b) crossed polarized image of (a) with bright orange Cr-clinopyroxene core mantled by actinolite+magnetite. 34
- 3.3a,b: (a) Crossed polarized light image of lozenge shaped Al,Cr-amphibole replacement lamellae and growth of fine-grained Cr-Ti-magnetite forming herringbone texture along lattice planes within the clinopyroxene; (b) higher magnification of (a) illustrating the delicate exsolution texture which is crystallographically controlled by the clinopyroxene crystal structure. 35
- 3.4a,b: (a) Plane light photomicrograph illustrating a mafic aggregate with Cr-clinopyroxene cores mantled by Cr-amphibole (dark green) and retrogressive actinolite (light green) in a matrix dominated by quartz and microcline; (b) Crossed polarized image of (a) illustrating the birefringent orange-red Cr-amphibole and magnetite growth within domains of actinolite. 39
- 3.5a,b (a) Plane light photomicrograph illustrating relict Cr-clinopyroxene core with pervasive honey-yellow epidote growth after actinolite; (b) Crossed polarized light image of (a) illustrating the pervasive birefringent yellow epidote growth on feathery to fibrous actinolite. 42
- 3.6a,b (a) Plane light image depicting ragged and intensely replaced coarse-grained primary magmatic plagioclase with remnant oscillatory growth zones hosted within a matrix dominated by microcline, quartz and mafic enclaves now actinolite, chlorite(1) and epidote. The inset ternary plot illustrates that the relict plagioclase grains fall along the base of the ternary between An₁₀-An₂₁ (within the oval). 43
- 3.7a-c (a)-(b) Relict plagioclase phenocrysts show a rhythmic concentric zoning Formed during Ba-Kfeldspar metasomatism, now albite(3); (c) Backscatter electron image illustrating the alternating rhythmic growth zones and the relict Ca-plagioclase domain preserved after both K- and Na-metasomatism. Numbers represent analysis locations relating to analyses 44-48 in Appendix A Table 5. The 100 micron scale bar for the backscatter image is located along the left margin of the image. 45
- 3.8a,b (a) Plane light image illustrating coarse-grained brown titanite growing on margins of late retrogressive amphibole and magnetite; (b) Crossed polarized image illustrating strongly birefringent titanite on actinolite margins. 46

- 3.9a,b (a) Plane light image of remnant Cr-clinopyroxene core with retrogressive growth of actinolite and magnetite replaced by medium-grained laths of biotite; (b) Crossed polarized image illustrating the highly birefringent biotite laths on actinolite. 47
- 3.10a,b (a) Backscatter electron image illustrating a zircon grain with quite well-defined crystal outline with adjacent titanite and domainal apatite. The 100 micron scale bar is located on the left margin of the image; (b) SEM image of a magmatic zircon used for age determination of the Kurupung batholith (Davis, 2006). 49
- 3.11a,b (a) Plane light image illustrating the mylonitic shear fabric defined predominantly by chlorite(1) and domains of quartz and carbonate; (b) Crossed polarized image illustrating the low birefringence of chlorite(1), multigranular quartz and microcrystalline calcite. 50
- 3.12a,b (a) A section of drill core illustrating megacrystic Ba-Kfeldspar overgrowing the dominant fabric defined by chlorite(1) indicating secondary growth; (b) Hand specimen illustrating the infiltrating pink Ba-Kfeldspar fluids along site specific zones of fluid ingress. 53
- 3.13a,b (a) Plane light photomicrograph illustrating the early onset of the Ba-K-metasomatic event beginning with degradation of the primary plagioclase; (b) Crossed polarized image of first order grey Ba-Kfeldspar within plagioclase noted as patchy replacement domains. The inset of the feldspar ternary diagram illustrates the location of the early Ba-Kfeldspar mineral chemical compositions. The data points are within the circle (bottom left area of the ternary). 54
- 3.14a-e (a) Plane light image showing a veinlet of Ba-K-rich fluids infiltrating a primary plagioclase and converting it to Ba-Kfeldspar; (b) Crossed polarized image illustrating the relict plagioclase twin with white mica and albite development at the center of the grain and Ba-Kfeldspar growth; (c) Backscatter image of plagioclase grain cut by Ba-Kfeldspar vein and development of Ba-Kfeldspar interior to the plagioclase (see feldspar analyses 113-115); (d) Ba-Kfeldspar domain interior to plagioclase illustrating dark and bright Ba-zones of up to 7.27% BaO (see feldspar analyses 124-128); (e) Dark domains of Ba-poor and bright domains of Ba-rich feldspar. Bright white linear zone of REE development parallel to the bright Ba-rich zone. See feldspar analyses 116-123, mica analysis 6 (low Ti-mica). 57

- 3.15a-c (a) Plane light image illustrating inclusions attaching to the growth faces of the evolving Ba-Kfeldspar. The biotite and chlorite(1) inclusions have been incorporated from the matrix material; (b) Crossed polarized image illustrating the highly birefringent biotite laths and darker chlorite(1) laths included within developing Ba-Kfeldspar growth zones; (c) Crossed polarized light image illustrating biotite and chlorite(1) inclusions incorporated from the groundmass whereas the albite(2) inclusions have grown in situ. The feldspar ternary inset illustrates the composition of the albite(2) inclusions within the growing Ba-Kfeldspar megacrysts. Albite(2) data points are within the circle at the albite (Ab) apex of the ternary. 58
- 3.16a,b (a) Merged backscatter images illustrating the concentric zoning of the Ba-Kfeldspars (see feldspar analyses 93-112); (b) Oscillatory zoned feldspar with albite+epidote in core, grey bands of Ba-Kfeldspar, and darker bands of albite (see Appendix A Table 5 analyses 55-64). The 100 micron scale bar is located along the left margin of all images. The inset ternary diagram shows a green circle near representing the Ba-Kfeldspar core compositions. The red circle nearest the “Or” apex represents Ba-Kfeldspar marginal compositions where all Na has been partitioned out of the megacryst. The blue circle nearest the “Ab” apex represents the alternating albite growth zones. 59
- 3.17a,b (a) Plane light image of oscillatory zoning of Ba-Kfeldspar obliterated by late hydrothermal microcline evidenced by cross-hatched twinning. Note relict nucleating kernel of primary plagioclase at the center of the grain now albite+epidote; (b) Crossed polarized image defining outlines of relict growth zones and the pervasive microcline(2) twinning. 60
- 3.18a,b (a) A section of drill core illustrating the white albite rinds on pink Ba-Kfeldspar, an effect of Na-metasomatism following Ba-K-metasomatism; (b) Crossed polarized photomicrograph of albite rind on secondary Ba-Kfeldspar. 62
- 3.19a,b (a) Plane light image illustrating pervasive albitization of a Ba-Kfeldspar megacryst with albite inclusions, however, initial texture still preserved; (b) Crossed polarized image illustrating the pervasive first-order grey albitization of the Ba-Kfeldspar megacryst. 63
- 3.20 Reticulate texture cataclasite where hematite-stained “red” albite is sealed by birefringent blue chlorite(2). 64
- 3.21a,b (a) Plane light image depicting replacement of green chlorite(1) by birefringent blue chlorite(2) interstitial to and sealing albite cataclasite; (b) Crossed polarized image illustrating birefringent blue chlorite(2) interstitial to first-order grey albitite fragments. 65

- 3.22a,b (a) A section of drill core representing blocky red cataclasite sealed by orange-brown zircon; (b) A section of drill core illustrating zircon microbreccia where brecciated fragments of cataclasite material is sealed by zircon. 67
- 3.23a,b (a) Backscatter image of a zircon vein demonstrating the compositional variation of the zircon with darker (low U) domains and brighter (high U) domains. The veins are host to a variety of U-bearing minerals including uraninite, coffinite and brannerite; (b) Backscatter image illustrating the ramifying zircon veining (Chl = chlorite(2); Qtz = quartz; Alb = albite(3); Ap = apatite; Zr = zircon). Scale bars are located along the left margin of each image. 68
- 3.24a,b (a) Backscatter electron image illustrating a zircon grain with quite well-defined crystal outline. The porous outer margin contains less uranium than the core and reflects resorption associated with hydrothermal fluids; (b) A less bright image of (a) illustrating the complex internal zoning of the zircon. The 10 micron scale bar is located on the left margin of both images. 69
- 3.25a,b (a) Plane light image illustrating zircon veins forming a zircon microbreccia and yellow-brown uranium phases intergrown with zircon veins; (b) Backscatter image of altered uraninite filling a fracture in albite. The 100 micron scale bar is located along the left margin. 71
- 3.26a,b (a) Backscatter image of a Th-rich grain, potentially thorite/ekranite with 55.31 wt% ThO₂ associated with the hydrothermal zircon veins. See Appendix A Table 5 analyses 6 and 7; (b) Backscatter image of U-bearing minerals included within the albite(3) groundmass, intergrown with zoned apatite, and intergrown with hematite. The 100 micron scale bar is located along the left margin of each image. 72
- 3.27 Backscatter images showing a zircon with compositional variation evident by dark Zr-Si+/-U+/-Ca and brighter domains of U-Zr-Si-Ca-Ti. These grains tend to be discrete domains outside the zircon veins within zones of intense albite(3). The 10 micron scale bar is located along the left margin of each image. 73
- 3.28a,b (a) Plane light image illustrating the blue-green chlorite(2) and albite(3) intergrown with sulphides; (b) Crossed polarized image showing birefringent blue chlorite(2) intergrown with highly birefringent epidote and associated opaque areas of sulphides. 74

3.29a,b (a) Backscatter image illustrating a genetic relationship between Ba-Kfeldspar and chalcopyrite-magnetite; (b) Backscatter image of the same field of view as (a) with the brightness intensity reduced to illustrate the sulphide population. This texture is quite interesting as it displays mineralogical characteristics associated with IOCG-type deposits including the deep/early K-metasomatism associated with Cu-mineralization and magnetite. The 100 micron scale bar is located on the left margin of each image.	75
3.30a,b: (a) Backscatter image illustrating the deep/early chalcopyrite-magnetite association and the late/shallow hematite-bornite association. The 100 micron scale bar is located along the left margin of the image; (b) Reflected light photomicrograph illustrating the oxidation of magnetite to hematite and the development of coarse domains of bornite with inclusions of chalcopyrite.	76
3.31a,b (a) Backscatter image illustrating an included grain of galena intergrown with Ag-telluride hosted in bornite; (b) Backscatter image of (a) with brightness intensity reduced to illustrate the two sulphide domains. The scale bars are located along the left margin of each image.	77
3.32a,b (a) Backscatter image illustrating the albite(3), chlorite(2), and bornite association. Note the bornite development along cleavage planes in chlorite(2). (b) Backscatter image showing the intergrowth of bornite with Se-bearing galena. The 100 micron scale bar is located along the left margin of each image.	78
3.33a,b (a) Plane light image of the coarse-grained interior of late Avanavero diabase dikes; (b) Crossed polarized light image of coarse-grained highly birefringent clinopyroxene intergrown with amphibole, chlorite, plagioclase, quartz, and minor magnetite.	80
3.34a,b (a) Backscatter image of coarse clinopyroxene grains with development of retrogressive chlorite, amphibole, and apatite. Relict primary andesine laths penetrate clinopyroxene suggesting primary equilibrium mineral growth; (b) Backscatter image of relict coarse Fe-Ti oxide with crystal faces still evident. Retrogression has caused exsolution of ilmenite needles out of bright coarse-grained Ti-Mt. The 100 micron scale is located along the left margin of each image. (Ilm = ilmenite; Ti-Mt = Ti-magnetite; Amp = amphibole; Cpy = chalcopyrite; Cpx = clinopyroxene).	81
4.0 Plane light photomicrograph illustrating the coarse-grained population of red-brown titanite growth on amphibole margins.	85
4.1 Crossed polarized photomicrograph of the pegmatite dike with Ba-Kfeldspar intergrown with quartz and carbonate. Note the growth zones in the Ba-Kfeldspar defined by alignment of inclusions parallel to the growing crystal face.	89

4.2 The image illustrates a box of drill core containing the pegmatite dike selected for radiometric dating. The pegmatite dike is enclosed within the red box.	89
4.3 Backscatter images of the zircon grains extracted from Ba-Kfeldspar. These zircons were selected for radiometric age dating.	90
4.4 Sample of drill core illustrating the growth of secondary Ba-Kfeldspar megacrysts (white arrow).	91
4.5a,b (a) Plane light photomicrograph illustrating the faint alignment of biotite phenocrysts; (b) Crossed polarized light image of the dark vein hosting birefringent blue chlorite(2), U-Pb-silicates (Kasolite), and Ti-magnetite-hematite.	93
4.6a,b (a) Backscatter image showing intergrowth of phengite-biotite-albite. Micas have internal zones of Ti-magnetite developed along cleavage planes; (b) Backscatter image illustrating a biotite phenocryst with Ti-magnetite development along cleavage planes and grain margin. The majority of oxides exterior to the micas are simple magnetite.	94
4.7 Retrogressive chlorite–apatite intergrowths with fine-grained U-Pb-Si (kasolite) disseminated throughout the apatite. All fine-grained bright domains within the apatite are U-Pb-Si minerals. A higher magnification image is also presented here to establish grain size of these U-minerals.	96
4.8a,b (a) Plane light photomicrograph illustrating the association of chlorite(2) and carbonate veinlets hosting U-Pb-silicates (Kasolite), the same chlorite(2) noted in the mineralized shears of the Kurupung. Note the cataclastic texture of the groundmass material sealed by chlorite(2); (b) Crossed polarized image showing the birefringent blue chlorite(2) and associated calcite.	97
6.0a,b (a) Plane light photomicrograph illustrating the most primitive relict Cr-clinopyroxene core region in the study accentuated by fine-scale Cr-Ti-magnetite exsolution lamellae; (b) Crossed polarized image illustrating the birefringent Cr-clinopyroxene core mantled by a highly birefringent corona of Cr-magnesiornblende.	130
6.1 Backscatter image illustrating the relict Cr-clinopyroxene core representing the most primitive compositions obtained in the study. Numbers 4 and 6 pertain to analytical locations represented in Appendix A Table 1 (analyses 104 and 107).	132

List of Appendices

Appendix A (Electron Microprobe Analyses)	167
Table 1: Clinopyroxene Analyses	169
Table 2: Amphibole Analyses	184
Table 3: Muscovite and Biotite Analyses	194
Table 4: Chlorite Analyses	197
Table 5: Plagioclase and Feldspar Analyses	201
Table 6: Oxide Analyses	219
Table 7: Epidote Analyses	222
Table 8: Analyses of Zircon and Uranium-bearing Phases	224
Appendix B (Geochronology)	227
Geochronology of Sphene	228
Geochronology of Pegmatite Dikes & Ba-Kfeldspar	232
Geochronology of the Lamprophyre Dike	241
Appendix C (Geochemistry)	248
Table 1: Whole Rock and Trace Element Data	249
Factor Analysis and Mass Balance Methods	257
Drill Logs and Photographed Drill Core for Sample ARN-031	261
Table 2: Rock Density Calculations and Trace element Analysis of Drill Hole ARN-031(for mass balance calculations)	273
Appendix D (Sample Locations)	290
Drill Core and Outcrop Sample Lists with Location Maps	291
Appendix E	301
Report by Donald W. Davis: Geochronology of magmatic and hydrothermal zircon from an altered granite in Guyana	302

Chapter 1: Introduction

1.1 Opening Statement

In recent times, there has been a global effort to reduce greenhouse gases by producing affordable and clean nuclear energy. Unfortunately, there is a current threat of shortages in uranium supply due to rising global energy consumption (Figure 1.0). Future uranium supplies are dependent on new uranium discoveries in politically stable areas. The present thesis investigation is an outgrowth of these global concerns. It involves the study of a basement-hosted uranium prospect that occurs just outboard of the Roraima basin in the Co-Operative Republic of Guyana, South America. Guyana is a poor but politically stable nation that may be rich in untapped uranium resources. If Guyana could develop a uranium resource similar to the Athabasca Basin in Canada or Olympic Dam in Australia, it would be a tremendous economic boost to the country and provide substantial uranium reserves into the future.

Uranium prices had stabilized well above \$100US/lb before the February 2011 Fukushima nuclear disaster in Japan. Uranium market prices fell from US\$110/lb to US\$60/lb uranium oxide (U₃O₈). Market prices continued to slide as the uranium market was inundated with negative news and confusion. In the latter part of 2011 to early 2013, prices had become more stable. Markets forecast that spot prices would strengthen through 2012 to values between US\$65 and US\$75/lb. The current cost of production is US\$40/lb. U₃O₈, while the current market price for uranium oxide is US\$35/lb. U₃O₈.

The “1993 Megatons to Megawatts” agreement came to an end on August 21 2013 when the last of the “highly enriched uranium” (HEU) was shipped to the U.S. for nuclear disarmament from military stockpiles in Russia. Analysts believe the end of the 20-year program will serve as a positive catalyst for the industry (Saywell, 2013). The end of the program signaled the end of the annual supply of 24 million lb. U₃O₈ to the market and while global inventory levels remain high, the primary mine supply does not currently meet global requirements. Forecasters predict a supply deficit in 2014 and a large,

unavoidable deficit by 2019. It has been stated that in 2014 the U.S. would need 49.1 million lb. U₃O₈ to supply the country's nuclear power reactors, while domestic production is expected at 5 million lb. U₃O₈. Global production in 2014 is likely to be 172 million lb. U₃O₈ compared with demand of 184 million lb. U₃O₈ (Saywell, 2013). One would predict that with supplies diminishing, uranium prices will soon rise and surpass production costs.

China remains a key driver for uranium prices. They are still moving forward with building nuclear facilities and continue to acquire uranium projects globally. Since Fukushima, global prices are not solely based on demand, they are also based on stock performance and mine growth. Current stock prices have been dictated by the post 2008 economic crisis, foreign debt and skittish investors (Figure 1.1). All stocks are still struggling to gain traction, and junior exploration companies are finding it particularly difficult to raise funds.

1.2 Geography of Guyana

The study area is located northeast of the Pakarima Mountains in the western part of the Co-Operative Republic of Guyana (Figure 1.2). Guyana, sandwiched between the Latin American giants Venezuela and Brazil, is home to fewer than a million people. Eighty percent of its land is covered by an intact rainforest larger than England. Prior to its independence in 1966, the country was the colony British Guiana. The stewardship of the colony changed from Dutch to French to English and then to Spanish, which is reflected in the names of localities within the interior. Aside from the small mining and forestry-based villages, the majority of the colonial population settled along coastal areas suited to sugar plantations (Smock, 2008). Subsequently, agriculture has diversified and bauxite mining has brought some of the population into the Berbice basin. However, the majority of people still live along the Atlantic coast. Guyana is located just above the equator (06°50'N 58°12'W). Temperature shows very little seasonal variation, averaging about 26°C (80°F). Rainfall amounts to several meters per year, May-June and December-January are wet seasons.

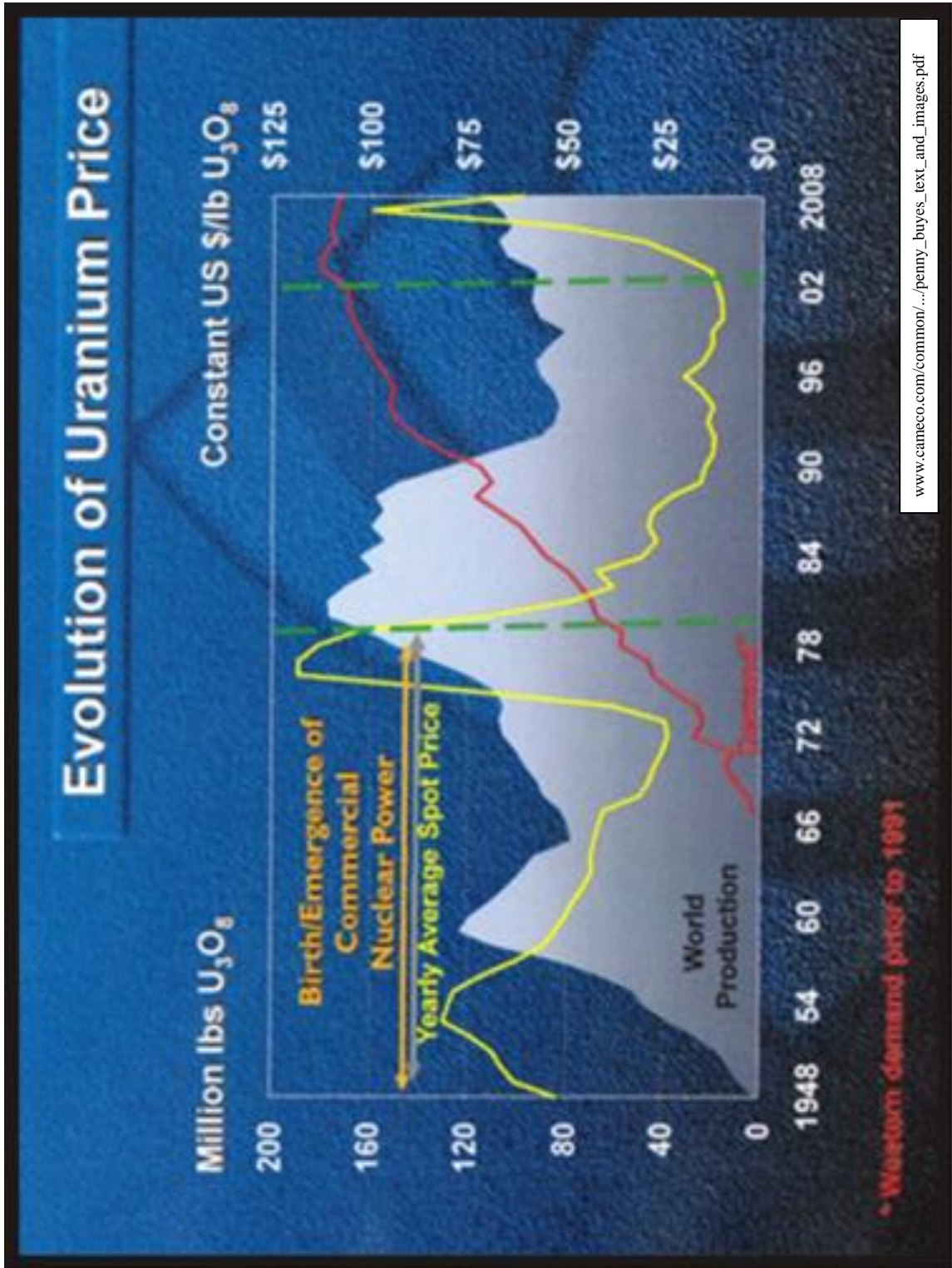
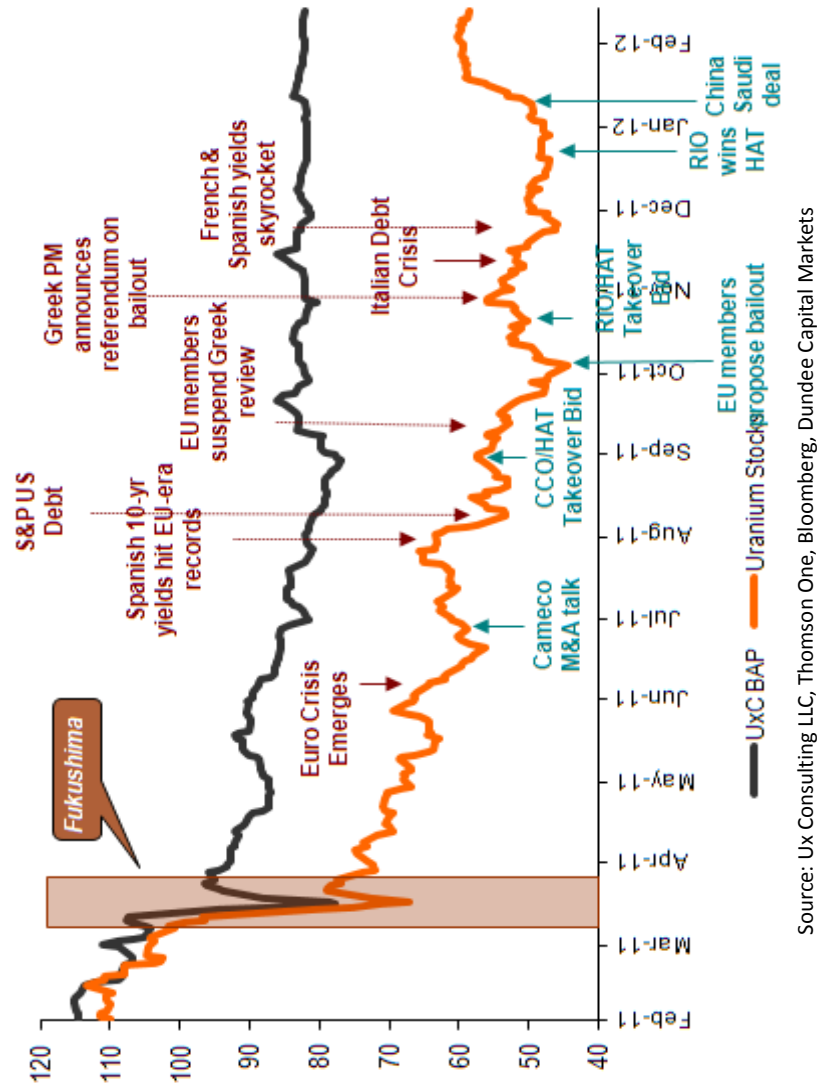


Figure 1.0: Graph illustrates the evolution of uranium price from 1948-2008. Note that from 1990 onwards, there is a gap between uranium demand (red line) and world production (background grey).

The geographical interior of Guyana is the homeland of various Amerindian tribes, many live in coastal lowlands, the Pakaraima Mountains, and the southern savanna areas of Guyana.



Source: Ux Consulting LLC, Thomson One, Bloomberg, Dundee Capital Markets

Source: Ux Consulting LLC, Thomson One, Bloomberg, Dundee Capital Markets

Figure 1.1: Graph illustrates the volatility of uranium market price relating to global current events from February 2011 to February 2012. The black line represents the Ux Consulting Company (UxC) broker average price of uranium. It is an average of the best bids and offers reported by the brokers. The orange line represents the uranium stock market trend.

They have made their living by hunting, fishing, agriculture, and small to large placer gold and diamond operations. Alluvial gold and diamond production is completed by hand and small dredging operations. The transportation network is not highly developed with river transport the most common. Numerous falls and rapids require portaging. Air transport relies on small airfields and rivers within the geographic interior.

1.3 Location, Property Description and Access

Uranium exploration is focused within the Mazaruni Mining District of the interior (Figure 1.3). The area can be accessed by land, water and air travel. International air travel to Guyana arrives at Timehri, a 45 minute drive from the capital Georgetown. The flight to the Aricheng base camp from the local Ogle airstrip on the northwest edge of Georgetown, takes about 1 hour and 15 minutes. The remote Aricheng airstrip was constructed by Cogema in 1983 and is 2000 feet long (Davis, 2006). The airstrip and adjoining Aricheng base camp are situated within the heavy canopy of tropical rainforest and this occurs centrally to the uranium prospects forming the basis of this study (Figure 1.4). The airstrip is in constant use by U3O8 Corp. and local populace, providing other exploration companies with a major fuel depot and way station for further plane access into the interior. Tractor roads provide easy ATV access to most of the historical and current drill sites. Numerous rivers in the area make boat access the preferred means for reaching remote areas.

Due to local political demands, U3O8 Corp's interests within Guyana are carried out by Prometheus Resources Inc. The concessions are held by Prometheus Resources Guyana which is a wholly-owned subsidiary of Prometheus Resources Barbados, which is a wholly-owned subsidiary of U3O8 Corp. Prometheus Guyana holds a 100% title to the concessions, although upon mining, royalties and other taxes will have to be paid to the Guyana government. The exploration property currently encompasses six granted prospecting licenses and four prospecting license applications totalling approximately 47,923 ha (118,420 acres) (Workman and Breede, 2012).

All exploration properties are held for uranium, other radioactive minerals, rare earth metals and zirconium. The project covers portions of the Kurupung batholith and

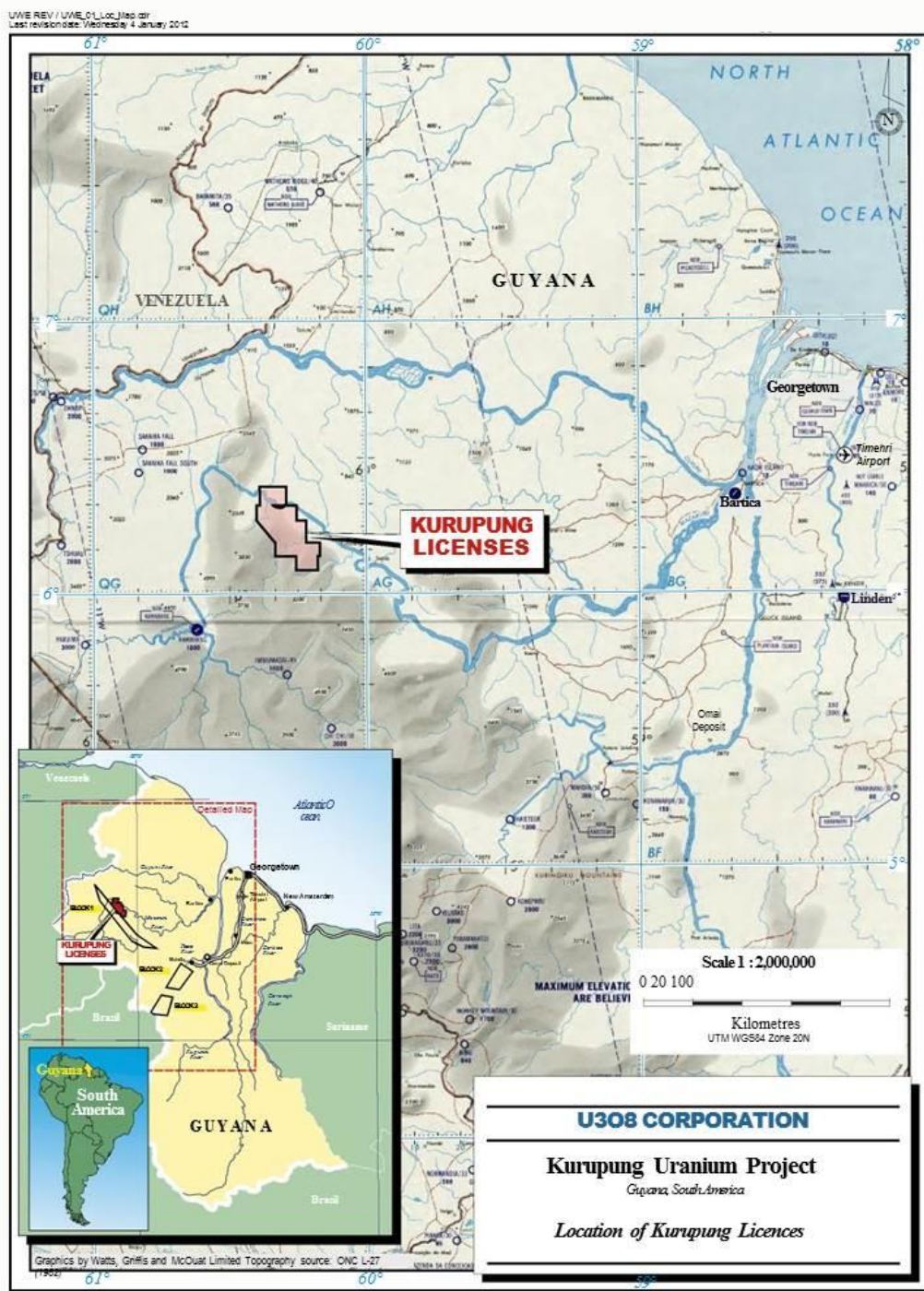


Figure 1.2: Map illustrating the exploration property. The property encompasses six granted Prospecting Licenses and four Prospecting License applications totaling approximately 47,923 ha (118,420 acres) (from Workman and Brede, 2012).

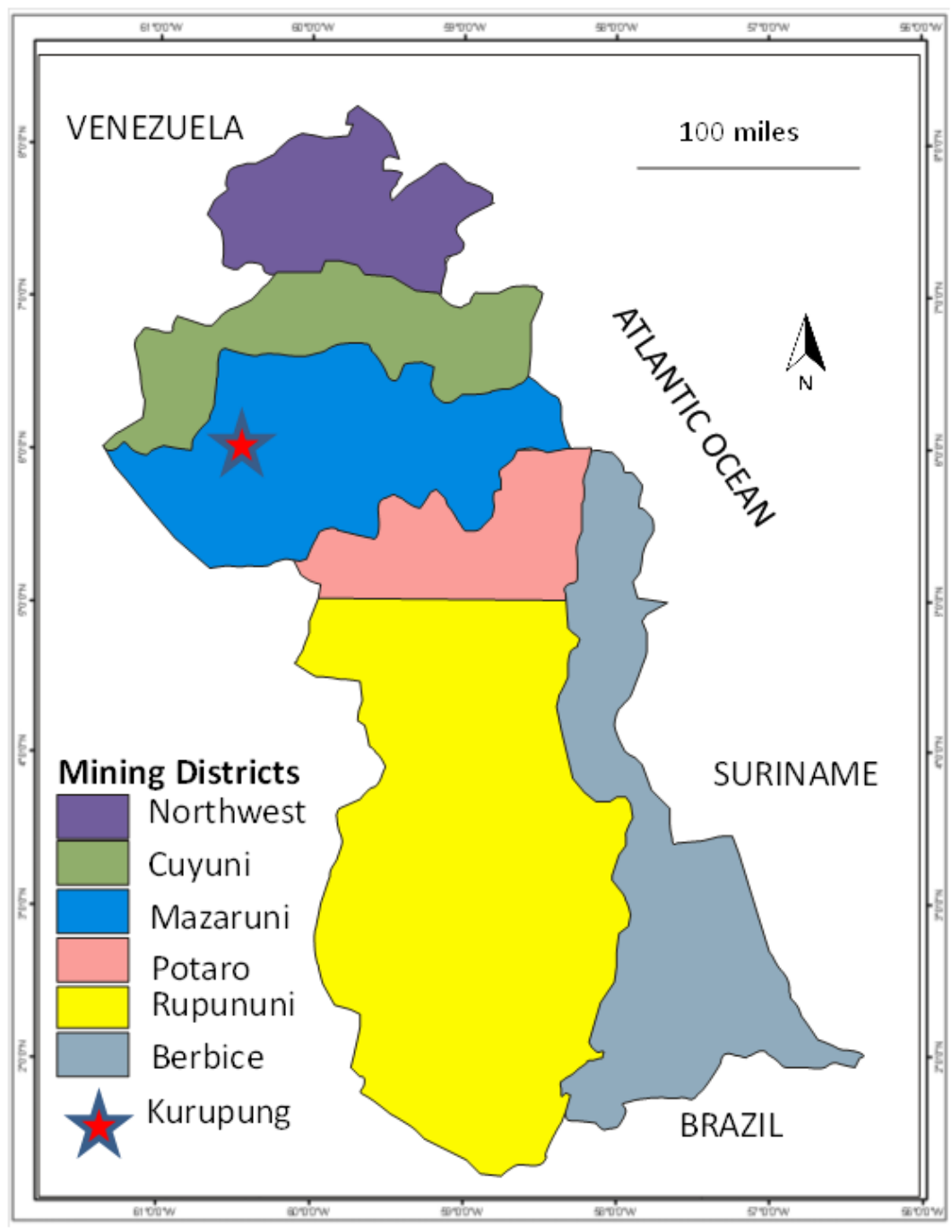


Figure 1.3: Map outlining the mining districts within Guyana. Note the Kurupung batholith is within the Mazaruni mining district. Modified after a map created by Sacre Coeur Minerals (www.scm minerals.com).



Figure 1.4: Aerial view illustrating the Aricheng airstrip, and U3O8 Corp's Aricheng base camp, including an office, core shed, accommodations, kitchen, and storage.

adjacent country rocks (greenstone), in addition to portions of the Roraima basin (epiclastic sedimentary strata). The interior of the Roraima basin is considered too thick for conventional exploration so has not been covered by permits. Both permit areas are mainly covered by tropical rainforest. The permit areas occurring east of the Pakaraima escarpment cover low-lying terrain, with relief 80-100 meters above sea level. The scarp face along the NE edge of the Pakaraima Plateau is a chain of vertical cliffs up to 1000 meters high (Workman and Breede, 2012). Topography increases through a series of benched mesas to the interior of the Pakaraima Plateau. The high scarp at the southern side of the Pakaraima Mountains is over 3000 meters high, the highest point in Guyana.

The Guyana shield is covered by one of only four intact rainforests left on the planet. Recently, there has been international agreement to place financial value on rainforests paying for their upkeep as "utilities" that provide vital services such as rainfall generation, carbon storage and climate regulation. This agreement secures the future of one million acres of pristine rainforest in Guyana. As the first move of its kind, it opens the way for financial markets to play a key role in safeguarding the fate of the world's forests. The initiative follows Guyana's extraordinary offer in November 2011 to place its entire standing forest under the protection of a British-led international body in return for development aid (Howden, 2008).

Guyana is vibrant with abundant and unique species of plants and animals. The coastal region of Guyana is covered by swampy mangrove plantations, whereas the inland is covered by equatorial rainforests. Guyana supports 25,000 species of floras. Rainforests host 5,000 different varieties of medicinal plants, along with lianas and vines used for constructing beautiful furniture. Native birds of the region include flycatchers, tanagers, gulls, egrets, parrots and hummingbirds. The local rainforest of Aricheng is home to birds like the Toco Toucan, Cock-of-the-Rock and King Vulture (Smock, 2008). Aside from such beautiful creatures as exotic birds and howler monkeys, there are giant insects, poisonous toads, and numerous poisonous snakes including the coral, labaria, bushmaster, and the anaconda, which all make their home in the vicinity of the Aricheng basecamp (Figure 1.5 a-f). Poisonous and carnivorous animals and fish are a threat to the human habitants and visiting geologists. Malaria carrying mosquitoes are a significant

health hazard. Routine fogging of the Aricheng base camp keeps the mosquito population to a minimum.

1.4 Previous Work

There is no history of hard rock mining within the Prometheus permit areas. However, there is prolific alluvial diamond and gold exploration and exploitation along the Kurupung and Mazaruni Rivers (Davis, 2006). These are worked by the local mining populace known as `Porkknockers`. Cominco Ltd. first reported highly uraniferous boulders of lateritized conglomerate in the Muruwa River on exploratory work carried out between 1967 and 1975, but had poor follow-up results (Donnerstag, 1976). Denison Mines Ltd. were active in the area between 1968-1970 and identified the basal Roraima conglomerate as an analogue to Elliot Lake-type paleoplacer mineralization. Eleven anomalies were outlined, four were drilled, and radiometric signatures attributed to the thorium concentration in fluvial conglomerate.

Some of the current U3O8 Corp. claim blocks were explored by Cogema of France between 1979 and 1984. Their work resulted in delineating numerous uranium prospects over an area about 70 kilometers in length. Helicopters set-out sampling crews equipped with scintillometers to cover the area around the Mahdia and Kurupung rivers. The Aricheng and Anarabisi areas demonstrated 3.5 and 4 times background radiation respectively. Further stream sampling of the area yielded up to 50 ppm uranium, highest ever reported in the country. Cogema discovered anomalous uranium in outcrops between the Merume river in the south to Anarabisi River in the north. Ground scintillometer readings reported up to 7000 cps and helped vector toward uranium bearing outcrops in 1980. Follow-up work included the drilling of 253 holes (32000 meters) (Davis, 2006).

An assay of vein-type uranium hosted within basement Haimaraka shale in the Merume area was reported as 3040ppm uranium by Davis (2006). When airborne surveys were flown after discovery, no anomaly was detected because the area was then flooded by a



Figure 1.5: (a) Black and yellow butterfly (b) Howler monkey range in size from 22 to 36 inches (c) Smooth-sided toad (*Bufo guttatus* ~5 inches in length) (d) Dynastinae or Rhinoceros Beetle climbing a handrail (~6 inches in length) (e) Anaconda crossing the road (~30 feet long) (f) Coral snake (~5 feet long).

meter of water. These prospects were never followed up with drilling. In 1981, Cogema applied for a detailed exploration permit over the Kurupung-Aricheng-Anarabisi area.

Numerous drilling programs, trenching, mapping, and ground-truthing of geophysical surveys were conducted between 1982 and 1984. The Cogema project ended on November 1984, the exploration program deemed unsuccessful. Their assay records, rock chip sample maps, and trench maps were never surrendered to the Guyanese government (Davis, 2006). The bulk tonnage/low grade uranium resource of the Kurupung batholith is currently being explored by U3O8 Corp. Published grades and tonnages of 8.4 mlb at an average grade of 0.09% U_3O_8 (indicated) and 7.7 mlb at an average grade of 0.08% U_3O_8 (inferred) is reported for the deposit (Workman and Breede, 2012). Mineralization extends from approximately 10m below surface to 220m and is open at depth (U3O8 Corp. website).

1.5 Objectives and Methods of Study

The thesis research was based on four weeks of field work over the 2009-2010 field seasons. Field work consisted dominantly of logging drill core from the various Aricheng prospects and visiting poorly exposed outcrops within the area. Drill core logging was supplemented with scintillometer readings to establish the degree of radioactivity from background unaltered batholith into high grade mineralized segments of drill core.

The surface exploration carried out by Prometheus Resources to date for uranium in the Pakaraima Escarpment area of the Roraima basin has established a geological analogue to the Athabasca basin in Saskatchewan. There has been recent discovery of both basement-hosted and unconformity-related uranium mineralization. The basement-hosted uranium prospects proximal to the Pakaraima escarpment occur in albitized granite breccia. These occurrences are fault-controlled and have associated zircon veining in zones of intense hematite-chlorite-albite alteration. The sodic alteration, hydrothermal zircon, and U-mineralization at Aricheng share characteristic features with the Valhalla U-deposit, Australia (Polito et al., 2009), as well as similarities to the Lagoa

Real deposit, Brazil, the Elkon deposit, Russia, and the Michelin deposit, Canada. Both alteration assemblages and U-mineralogy of these deposits relate to pervasive K- and Na-alteration common to IOCG-style mineralization. Using Olympic Dam as an example, the uranium mineralization might be expected to bridge granite/rhyolite interfaces where deeper levels are characterized by pervasive K-feldspar alteration with associated magnetite-chalcopyrite, and shallower levels by albitization with associated hematite-bornite (Williams, 2010).

In IOCG deposits related to alkaline metasomatic alteration, the mineralization and alteration is generally associated with deep-rooted structural zones and faults. For example, the Lagoa Real deposit in Brazil, is associated with a continental-scale fault. In the Kurupung, uranium-bearing structures have lamprophyre dyke associations attesting to the deep-seated nature of the fault system. The Aricheng district is characterized by deep K-alteration to shallow Na-alteration, consistent with IOCG systems. The timing of alkaline metasomatic activity is late magmatic and signifies the potential for regional 1995 +/- 15 Ma IOCG systems. The working hypothesis is that the alkaline metasomatism and associated uranium mineralization relates to rapid unroofing of a K-rich granitoid along a mylonitic strike-slip fault active during the transition from Rhyacian (2.26-2.08 Ga) to the post-collisional Orosirian (2.07-1.96 Ga) stage of the Transamazonian orogenic cycle.

The economic mineral inventory of the Guyana shield is dominated by bauxite, and placer mining of gold and diamonds. Uranium exploration has also intensified since Cogema's exploration activity in the early 1980's. Although the Kurupung batholith is currently being explored for its uranium potential, it is also a prospective setting for lode gold and diamond sources. The batholith sits within the Kurupung mylonite zone, a deep-seated sinistral strike-slip fault system which was active between the 2103 +/- 3 Ma age of the batholith and the 1995 +/- 15 Ma age of uranium mineralization. Such deep-seated shear systems are somewhat analogues to mid-Tertiary detachment systems documented in the southwest United States Cordilleran (Davis et al., 1983; Reynolds and Lister, 1987). These host significant gold mineralization within detachment fault

breccias. Although sources of gold have been well established in the Guyana shield (Lowe, 2013), the location and age of the source of diamonds in the northern Amazon craton remains unknown (Santos et al., 2003). The source of alluvial diamonds in conglomerates at the base of the Roraima remains a quandary since Paleoproterozoic kimberlites and lamproites are not known in northern South America and rare in West Africa. Those that are known are either younger than the Roraima or are geographically located in an area that did not contribute to Roraima sedimentation.

The essential hypothesis of this thesis proposes that shear-hosted uranium mineralization is linked to post-collisional extension that characterized the terminal 1.96 Ga Orosirian phase of the Transamazonian orogenic event. Mylonitic shears in the basement were U-mineralized well before Roraima deposition. This study will therefore refute the original working hypothesis that U, P, Ti, and Zr were transported in oxidized basinal brines that precipitated U in basement faults well below the unconformity. Recognition of pre-Roraima uranium enrichment has significant ramifications for current interpretations regarding the unconformity related U-mineralization as best represented by the Athabasca basin in Central Canada and the McArthur Basin of Northern Australia. The unconformity-type deposit may have reworked older uranium concentrations that existed in underlying basement prior to the deposition of continental sandstone successions. The following are the specific objectives of this research study: (1) detail the importance and significance of the Cr-rich sanukitoid-type Kurupung batholith using petrography and mineral chemistry; (2) establish the host rock mineralogy and the degree of alteration related to uranium mineralization by coupling mineral chemical investigations with detailed petrographic textural relationships at numerous mineralized zones; (3) establish the timing of uranium mineralization and hydrothermal zircon veining by documenting the detailed paragenetic relationships of zircon veins in uranium mineralized zones; (4) detail deposit scale elemental zoning in the Kurupung batholith by utilizing whole and trace element geochemistry; (5) constrain timing of mineralization and alteration using geochronology; (6) establish a working metallogenic model to apply in future exploration at both property and regional scales.

Chapter 2: Regional and District Geology

2.0 Introduction

This chapter addresses the geological evolution of the South American craton, the evolution of the Guyana shield, the Transamazonian orogenic cycle, and introduces the local geology of the Aricheng uranium district.

2.1 Geology of the South American Craton

The South American continent has an active mountain chain on its west and northwest coasts. Archean-Proterozoic shields and Phanerozoic sedimentary cover sequences occur throughout the interior and comprise the South American platform. Guyana lies within the Amazonian craton, forming the Precambrian basement to Brazil, French Guiana, Guyana, Suriname and Venezuela (Figure 2.0). The Amazon craton is subdivided into two geographic shields, the Guyana shield in the north and the central Brazil or Guapore shield to the south. The Amazon craton was formed as a result of progressive Proterozoic crustal accretion onto an older Archean nucleus that stabilized around 2.5 Ga. As a result, this craton has been subdivided into six geochronological provinces (Santos et al., 2003). These provinces are illustrated in Figure 2.1 and include: Imataca (3.10-2.53 Ga); Trans-Amazon (2.25-2.00 Ga); Tapajos-Parima (2.10-1.87 Ga); Central Amazon (1.87-1.78 Ga); Rio Negro (1.83-1.52 Ga); and the Sunsas (1.33-1.00 Ga).

The Guyana shield is mostly composed of Paleoproterozoic-aged supracrustal rocks that are dominated by the Barama-Mazaruni Supergroup, a sequence of 2.25-2.0 Ga Transamazonian greenstone belts (Figure 2.2). It is essentially comprised of east-west trending folds of mafic through felsic volcanic assemblages with intercalated clastic sediments (Gibbs, 1979; Gibbs and Barron, 1993). The juvenile Barama-Mazaruni Supergroup assemblages amalgamated through ocean closure between the northern Amazonian Archean shield and the West African Archean shield between 2.18-2.13 Ga (Delor et al., 2003). They reflect the consumption of oceanic crust during early Rhyacian

CRUSTAL PROVINCES OF SOUTH AMERICA

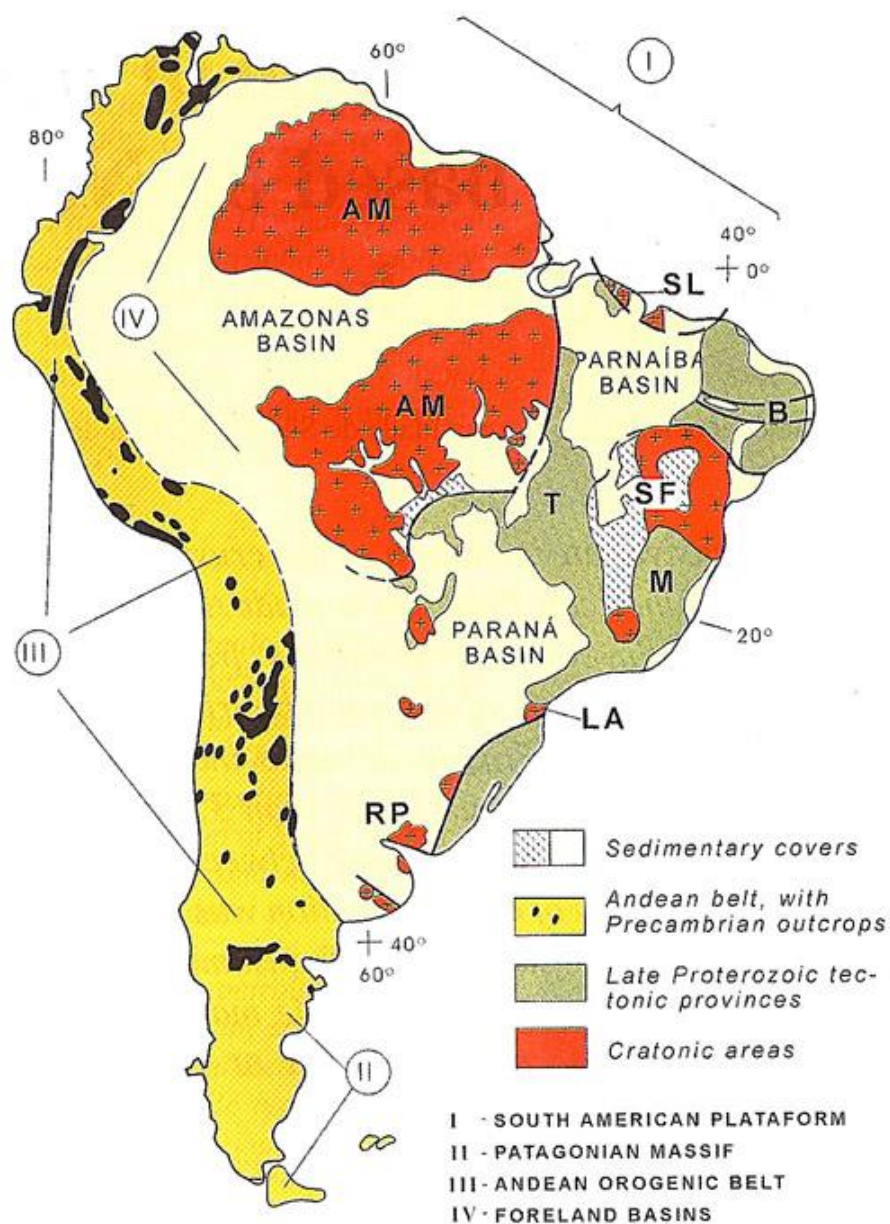


Figure 2.0: Crustal provinces of South America: AM – Amazonian craton; SF - Sao Francisco craton; RP – Rio de la Plata craton; SL- Sao Luis, and LA-Luiz Alves. Figure is from Cordani and Sato, 1999.

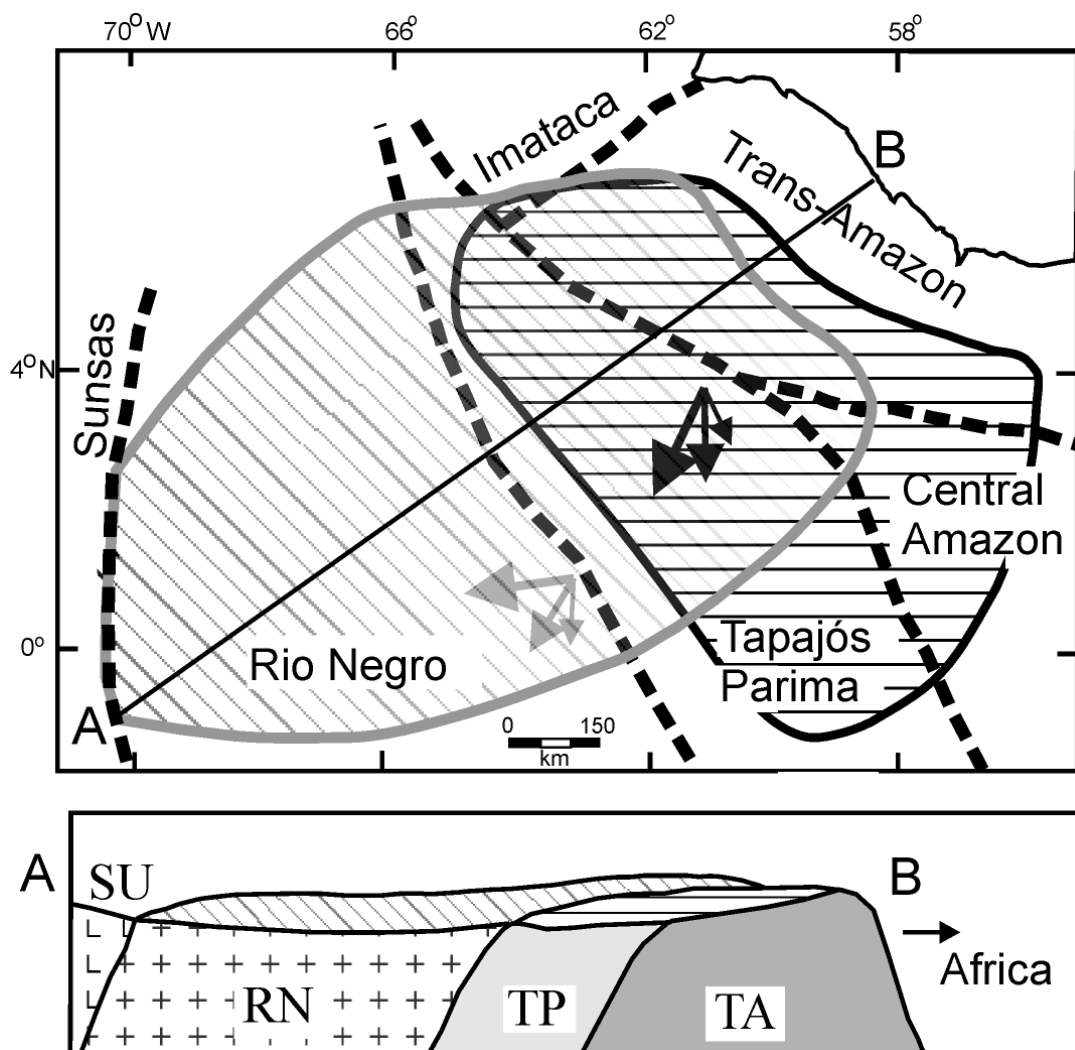


Figure 2.1: Tectonic provinces of the Amazon craton illustrating a progressive younging of accreted terranes to the west. The Roraima basin (inclined gray lines) and Neblina (parallel black lines) sedimentary basins in relation to the geologic provinces of the Amazon craton: Imataca (Archean); TA-Trans-Amaزون (2.25–2.00 Ga); TP-Tapajós-Parima (2.1–1.88 Ga); Central Amazon (1.87–1.78 Ga); RN-Rio Negro (1.83–1.52 Ga); and SU-Sunsás (1.33–1.00Ga). Arrows indicate the main paleocurrent directions (as measured in the field, Reis et al., 1990) and as inferred from ages of zircons. The schematic section A–B shows the relationship between the two basins and the provinces of the craton. The figure is after Santos et al., 2003. The Aricheng District is situated below the Neblina basin within the TA.

north-south collisional stages of the Transamazonian cycle (Delor et al., 2003). The supracrustal rocks have been tightly folded and metamorphosed to lower greenschist facies.

2.2 Geology of the Transamazonian Orogen

The Kurupung batholith intrudes the Mazaruni Supergroup, a granitoid-greenstone terrane dating between 2.25 and 2.0 Ga in age (Gibbs and Olszewski, 1982; Cox et al., 1993; Santos et al., 2000). The Transamazonian orogenic cycle (2.2-1.9 Ga) defines the accretionary history of the Guyana shield. This cycle originally defined the tectonic history between 2.1-2.0 Ga within the Amazon craton but has been redefined to include the 1.9-1.7 Ga Orosirian cycle (Gibbs and Writh, 1986; Delor et al., 2003). The collisional Rhyacian (2.26-2.08 Ga) stage of the Transamazonian involved the consumption of juvenile oceanic crust during convergence between the Amazonian and African blocks (Delor et al., 2003). The related subduction was marked by development of the volcano-sedimentary arcs of the Barama-Mazaruni Supergroup overlapping with tonalite-trondjemite-granodiorite (TTG) plutonism (Figure 2.3). These greenstone belts show typical volcanic successions from lower mafic through middle intermediate to upper felsic extrusives capped by clastic and chemical sediments.

The transition from collisional (Rhyacian) to post-collisional (Orosirian) tectonics is represented by the emplacement of a primitive 2.11-2.08 Ga Mg-K granitoid suite representing onset of Orosirian A-type magmatism (Figure 2.3). The Orosirian (2.07-1.96 Ga) post-collisional stage of the Transamazonian is marked by the formation of granulite-facies metamorphism and emplacement of granites related to continental-scale sinistral shearing (Delor et al., 2003). Sinistral strike-slip faulting and related mylonitic shearing is important as it facilitates the unroofing of the Rhyacian infrastructure (Figure 2.4). This post-collisional extensional shearing event is represented at surface by Haimaraka sedimentation in strike-slip related fault basins (Baker, 2008). The Orosirian is characterized by post-collisional A-type magmatism

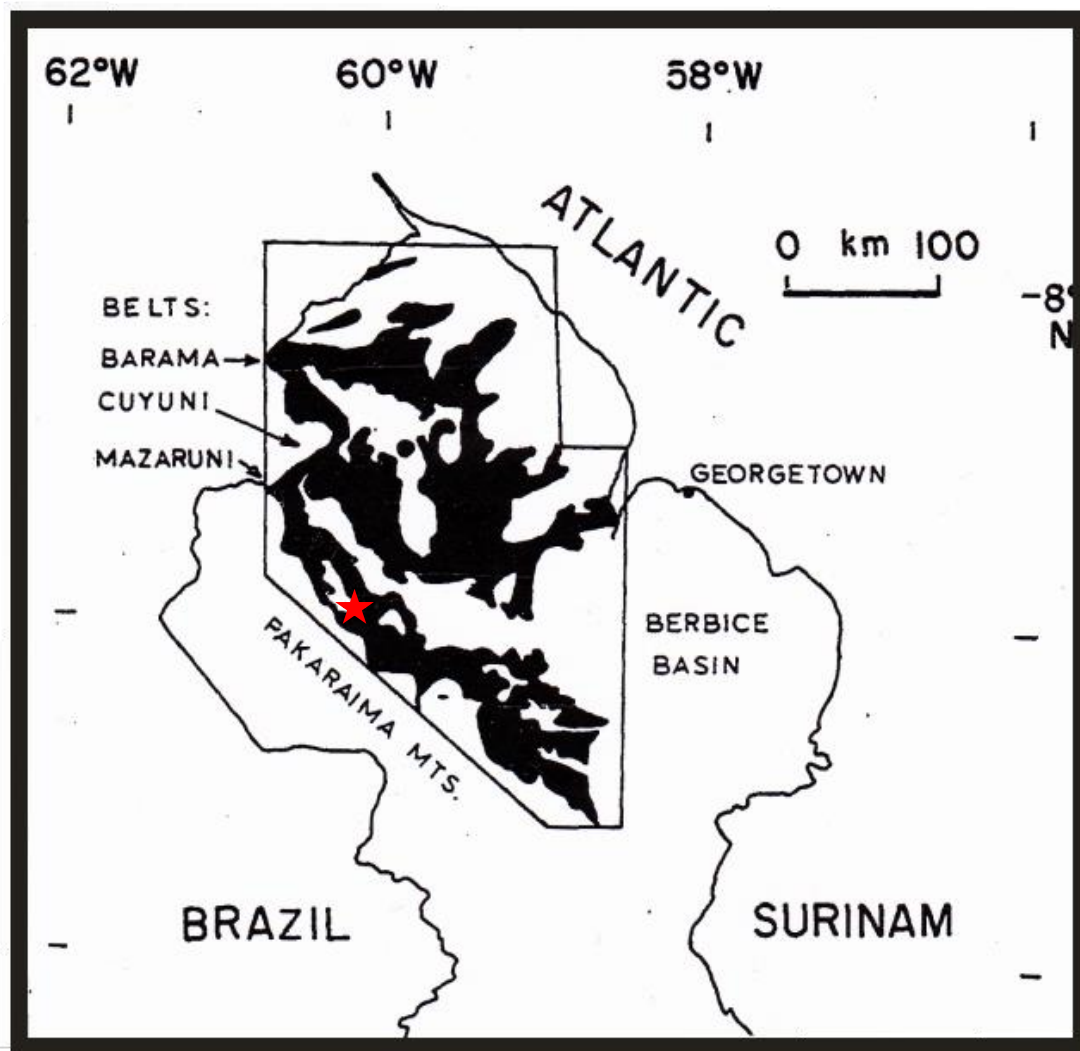


Figure 2.2: A sketch map of Guyana illustrating the locations, extent, and names of the granite-greenstone belts. The Kurupung batholith (red star) is located with the Mazaruni greenstone belt at the edge of the Pakaraima Mountains (From Gibbs, 1979).

across the Guyana shield between 2.01-1.96 Ga (Delor et al., 2003). This event is marked by regional ash tuff volcanic fields and co-magmatic two-mica subvolcanic intrusives of the Uatuma/Surumu formations (1966 +/- 9 Ma) (Delor et al., 2003; Santos et al., 2003; Schobbenhaus et al., 1994). This volcanism marks the period of orogenic collapse prior to the onset of Roraima Supergroup deposition.

The Roraima Supergroup forms the high plateau and hills of the Pakaraima Mountains in west-central Guyana. On its eastern margin it lies unconformably on the Barama-Mazaruni Supergroup. The Roraima Supergroup is up to 2 km thick and composed of unmetamorphosed arkose, shale, quartz arenite and conglomerate. A basal unconformity occurs between volcanic and plutonic basement and overlying Roraima sediments. The age of the basement Surumu Group in Brazil is 1966 +/- 9 Ma (Schobbenhaus et al., 1994) and 1984 +/- 9 Ma along the Uraricaa River, southern edge of the Roraima Basin (Santos et al., 2003), thus marking the maximum age of the Roraima Supergroup. Pyroclastic volcanics interbedded with the middle and upper Roraima sediments at 1873 +/- 3 Ma form marker horizons through the basin. The Younger Basic Group, the Avanavero suite of dykes and sills, dating at 1782 +/- 3 Ma, intrudes the Roraima Supergroup (Santos et al., 2003). These age relations bracket an approximately 180 Ma history for continental sandstone deposition in the Roraima basin.

2.3 Local Geology of the Aricheng District

The regional geology of the Aricheng area is well demonstrated on Baker's geological compilation map (Figure 2.4). Cogema's 1:200,000 scale reconnaissance map of northwestern Guyana was utilized by Baker (2008) to compile a 1:100,000 scale geological interpretation on the basis of RADAR imaging. The simplified geology map presented as Figure 2.5 is modified from Baker (2008) updated on the basis of 1:50,000 airborne magnetic maps supplied by U3O8 Corp. As shown, the Aricheng district is situated within the juvenile Mazaruni granite-greenstone terrane just outboard of the Roraima Basin. In the Aricheng district, the juvenile Transamazonian volcanic and sedimentary arc assemblages are intruded by >2.0 Ga

granitoids. Both the granitoids and bordering volcano-sedimentary lithologies are overprinted by a late 140° SE striking, moderately SW dipping mylonitic fabric related to regional scale sinistral strike-slip faulting. This faulting accounts for the deposition of Haimaraka Formation sediments and accommodated the unroofing of the Kurupung batholith, which is most intensely foliated along its eastern margin. The Haimaraka is poorly exposed in the area, but where it outcrops along the Mazaruni River, preserves primary sedimentary features, thus lacking the mylonitic overprint. The Transamazonian supracrustals, Haimaraka Formation, and the Kurupung batholith are unconformably overlain by the Roraima Supergroup. Unfoliated Avanavero dike swarms transect the study area and focus along major rivers. Avanavero sills are interlayer with and cap Roraima sediments.

An airborne magnetic survey flown in 2006 shows the Kurupung batholith is transected by magnetic patterns defining open "S"-shaped sigmoids (Figures 2.6). Sigmoidal magnetic lows extend from the southwest to northeast margin of the batholith. These sigmoidal structures developed as a result of regional sinistral strike-slip fault movement during the Orosirian period (Baker, 2008). The uranium mineralization at Accori North C and Aricheng South occur at intersections of sigmoids with bounding faults. Consequently, radiometric anomalies that lie on sigmoidal structures are exploration priorities for U3O8 Corp.

VLF survey and drill hole location maps are presented below for the Aricheng South prospect (Figures 2.7, and 2.8). The VLF survey illustrates red conductive areas and blue resistive areas. The figure demonstrates that mineralization at Aricheng South is hosted by a conductive breccia zone. The magnetic surveys illustrate that shears are locally defined by magnetic highs, but the elevated uranium concentrations are located in many of the magnetic low areas. This is attributed to the fact that uranium mineralization occurs in zones where crustal fluids responsible for chlorite-hematite development caused demagnetization of magnetite and provided a reducing environment for uranium precipitation. Individual shear strands are discontinuous and form en-echelon shear systems. Individual anastomosing shear strands are ductile where they

converge, but feather out into brittle fault fracture sets. Where ductile the shears have broad Ba-Kfeldspar envelopes, where brittle, albitite displays cataclasis and microbrecciation textures (Figure 2.9). A drill section of the Aricheng South prospect (Figure 2.10) illustrates uranium concentration within the shear. It is important to note that mineralized zones within shears comprise demagnetized cataclastic albitite breccia. The reasons for uranium enrichment in magnetic lows will be explored in the thesis.

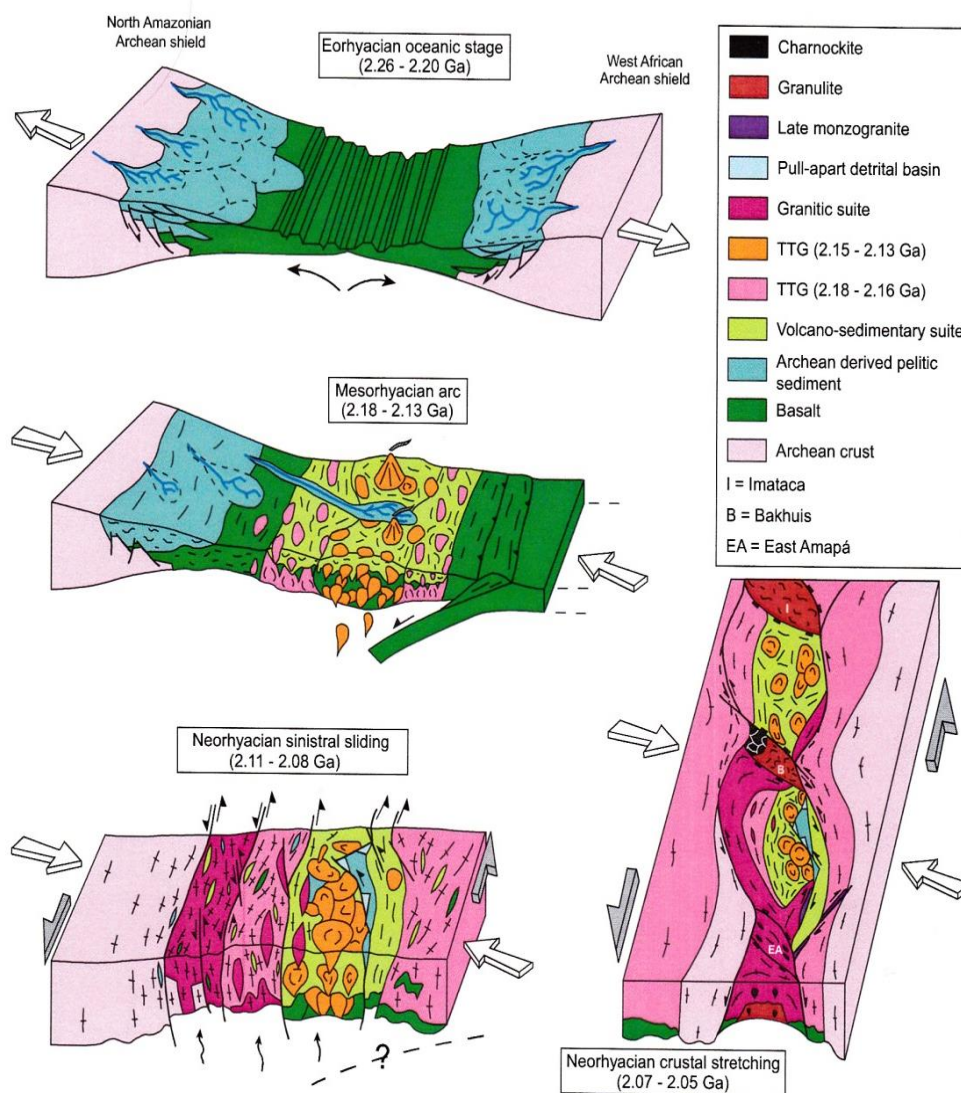


Figure 2.3: Geotectonic evolution of the Guyana shield from the collisional Rhyacian to post-collisional Neorhyacian-Orosirian periods (Delor et al., 2003). Note the importance of sinistral strike-slip and transpressional tectonics between 2.11-2.08 Ga.

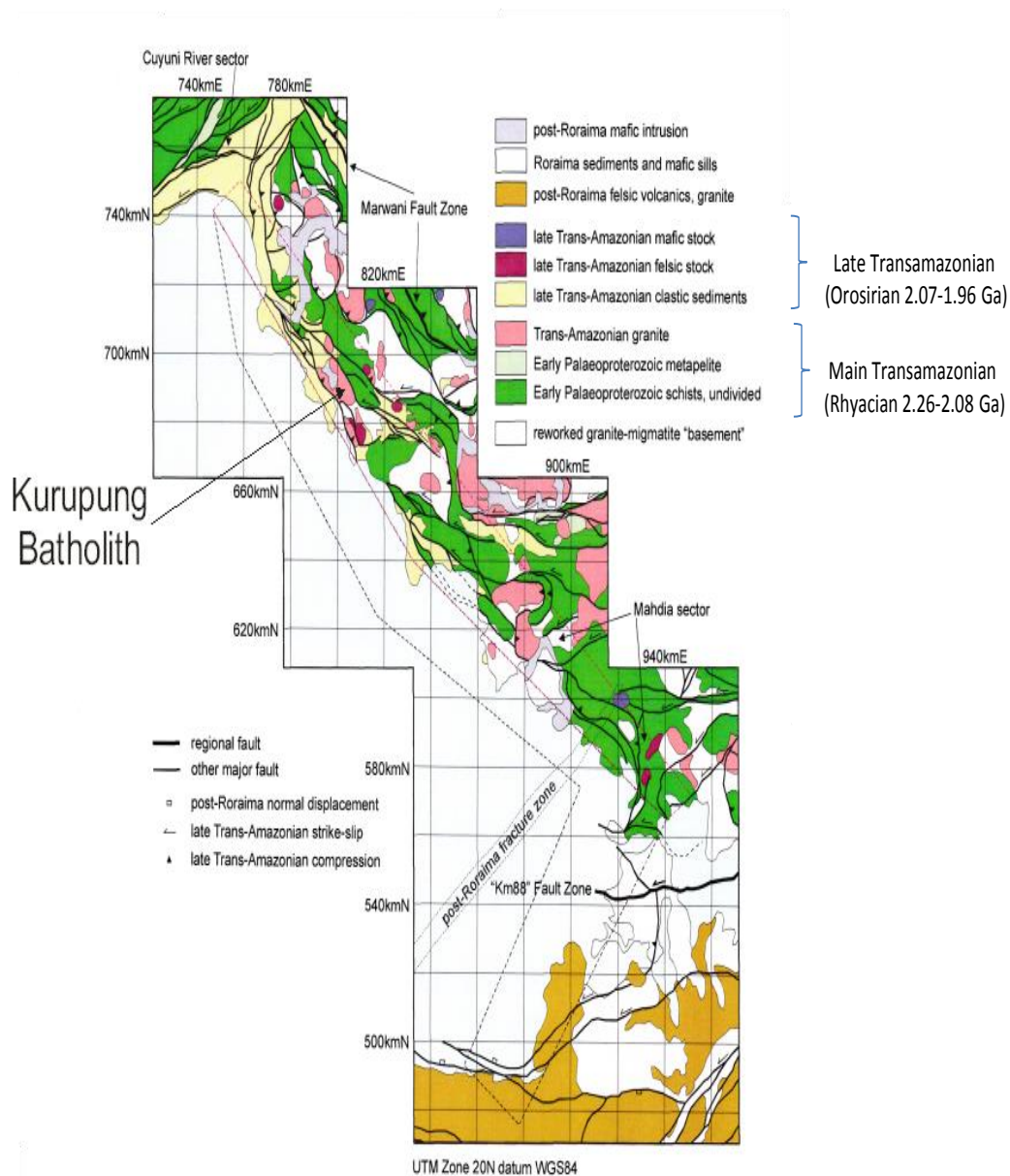


Figure 2.4: Regional map illustrating the location of the Kurupung batholith in Transamazonian volcanics (From Baker, 2008; age constraints added from Delor et al., 2003).

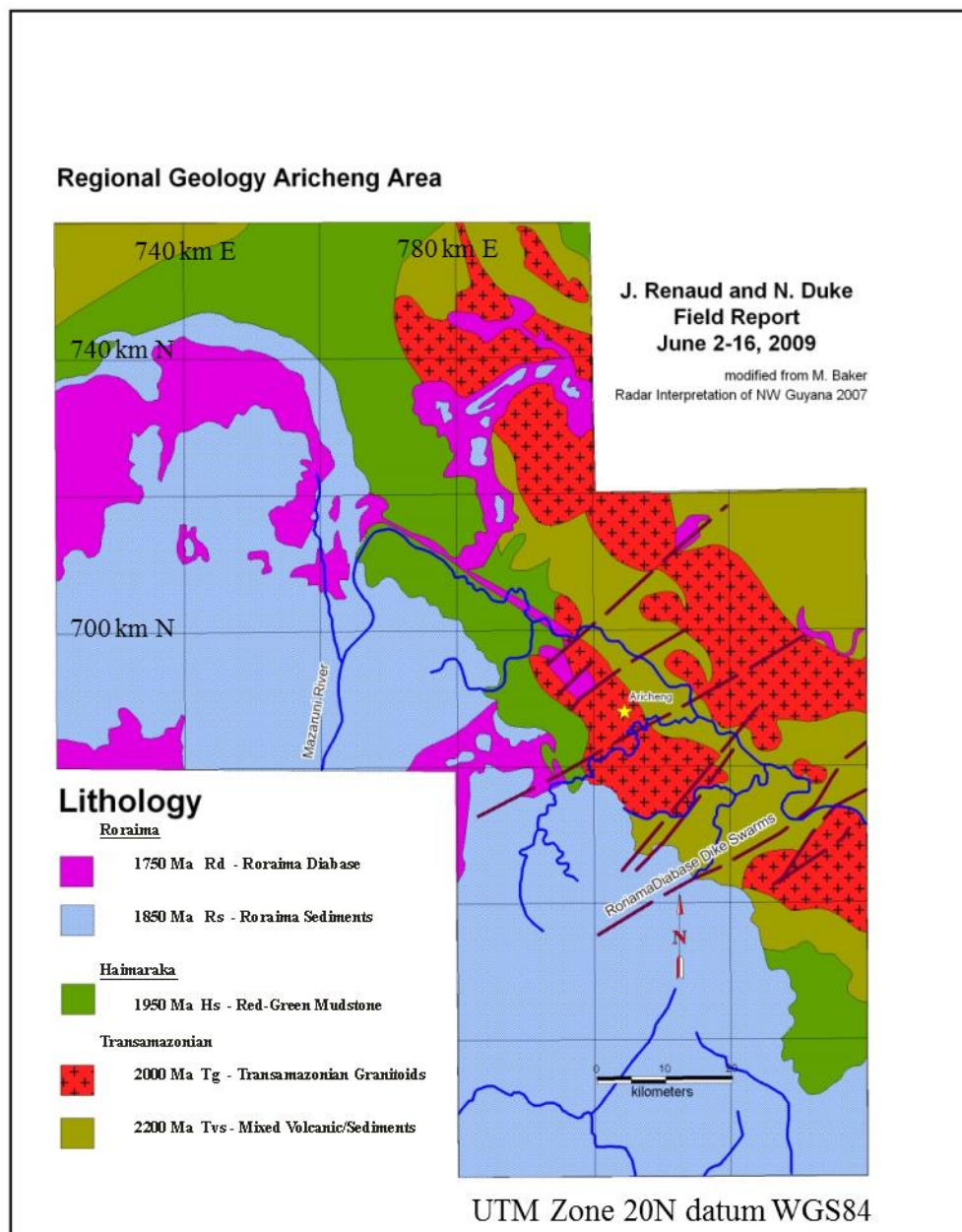


Figure 2.5: Simplified geological map of the Aricheng district (Modified after Baker, 2008).

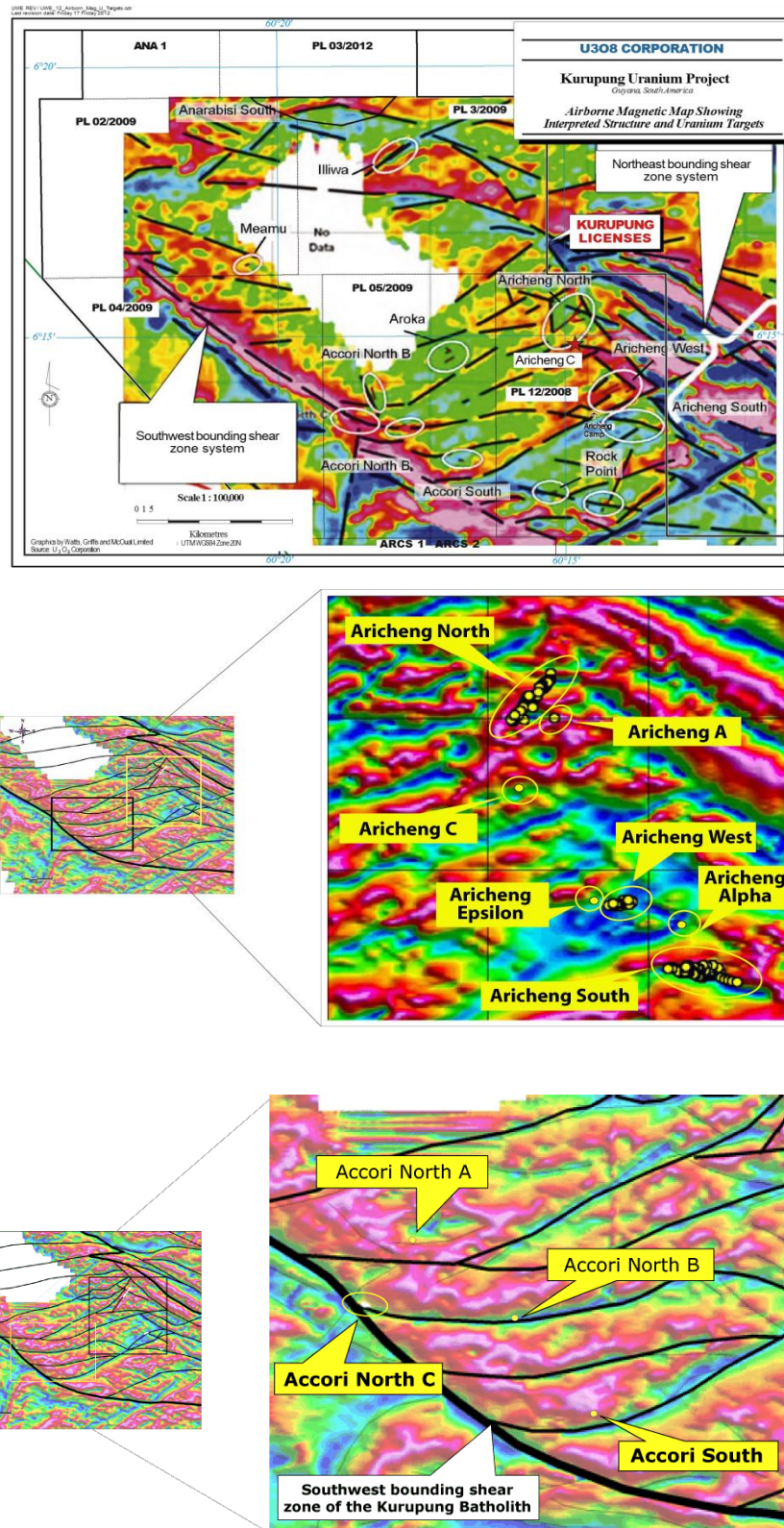


Figure 2.6: Airborne magnetic surveys delineating sigmoidal shears and illustrating uranium prospects within the Kurupung batholith within cooler blue areas of shears. (modified after image from U308 Corp. website (from www.u3o8corp.com), and Workman and Brede, 2012).

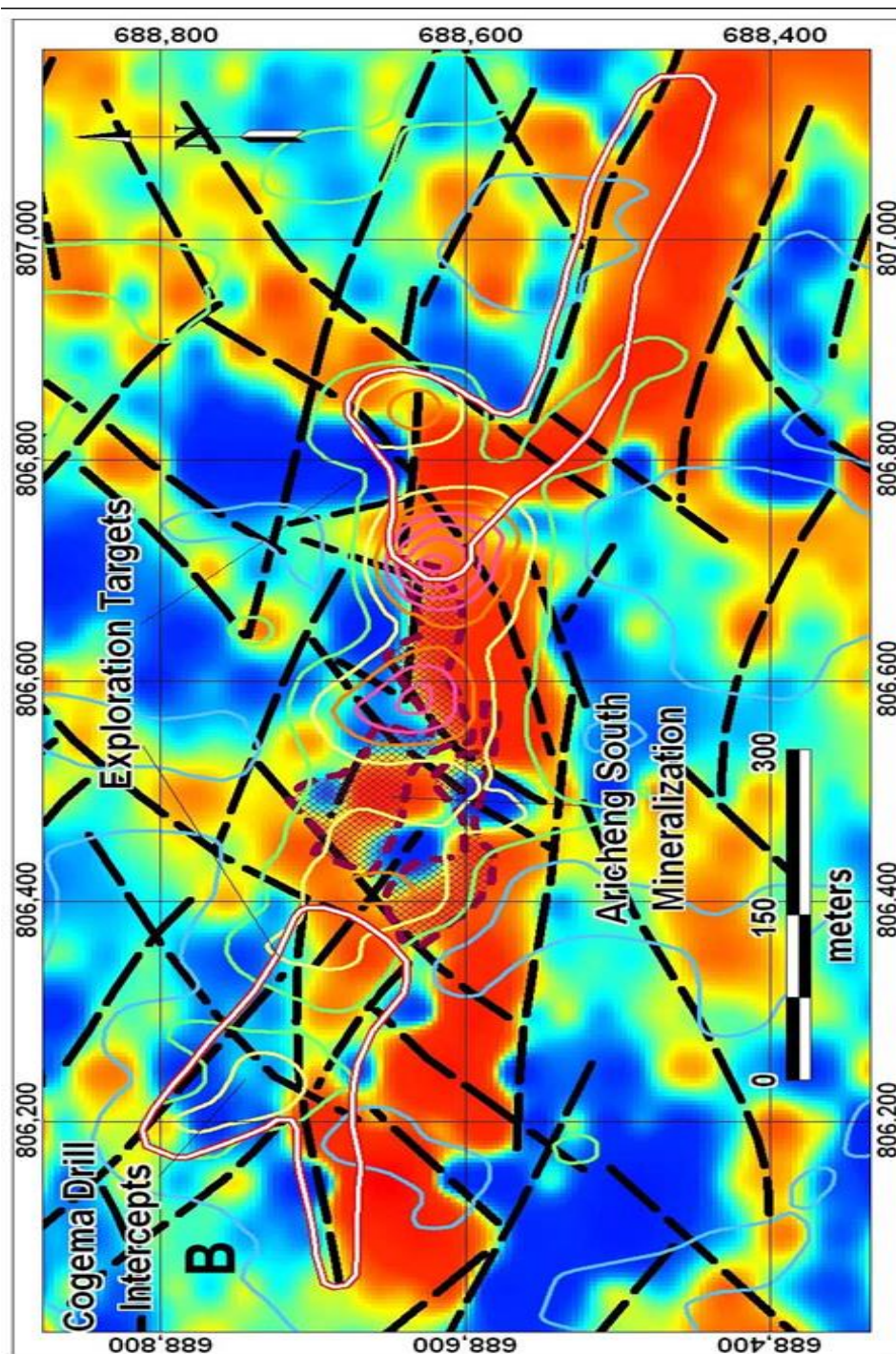


Figure 2.7: VLF survey: Magnified view of the Aricheng South sigmoid illustrating contours of uranium enrichment. The color scheme is red for conductive areas and blue for resistive areas. The mineralization at Aricheng South is hosted by a conductive fractured/brecciated zone (from Workman and Breede, 2012).

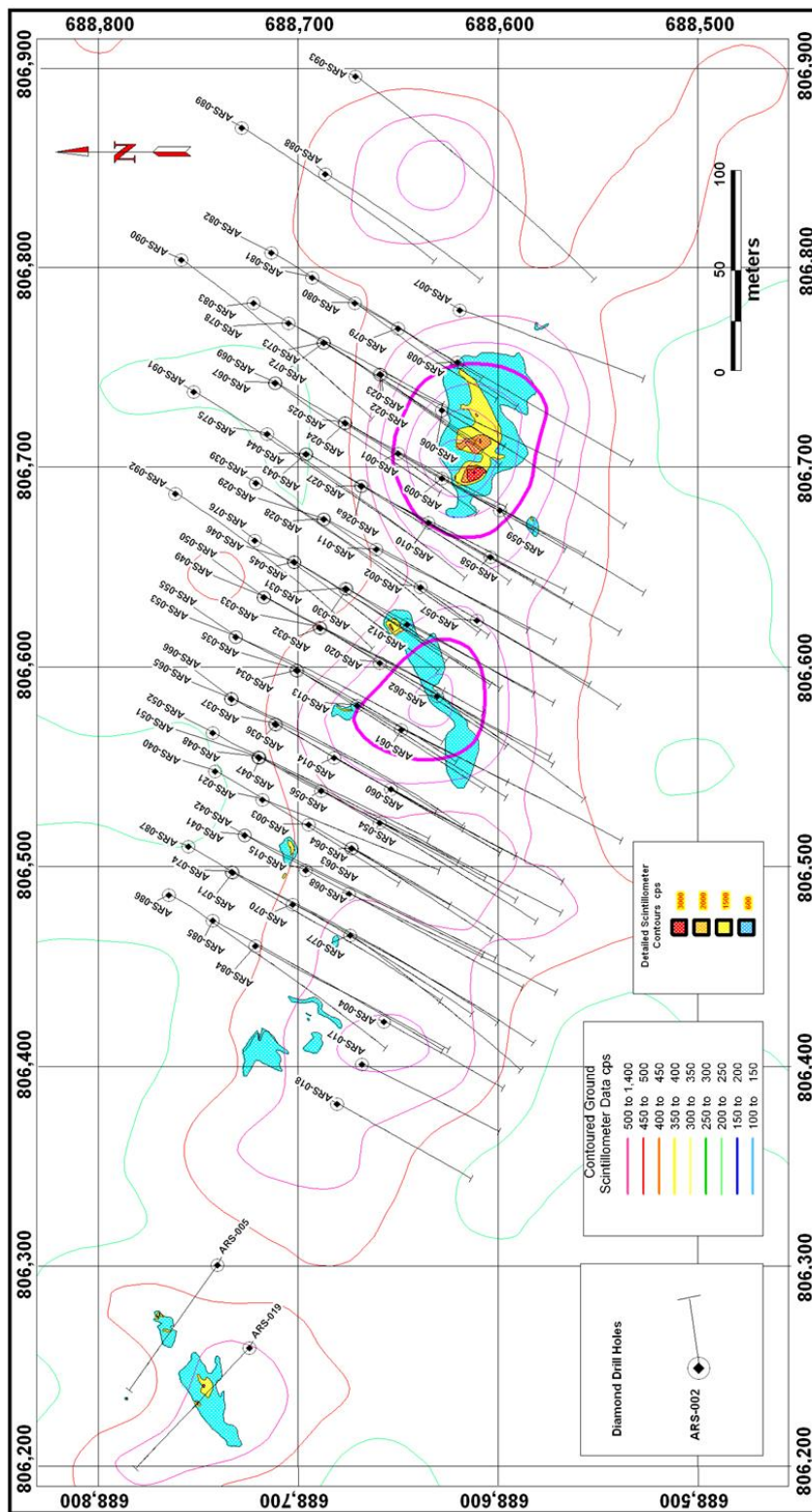


Figure 2.8: The figure illustrates the drill hole locations for the Aricheng South area. Figure from Alexander and Breede, 2009.

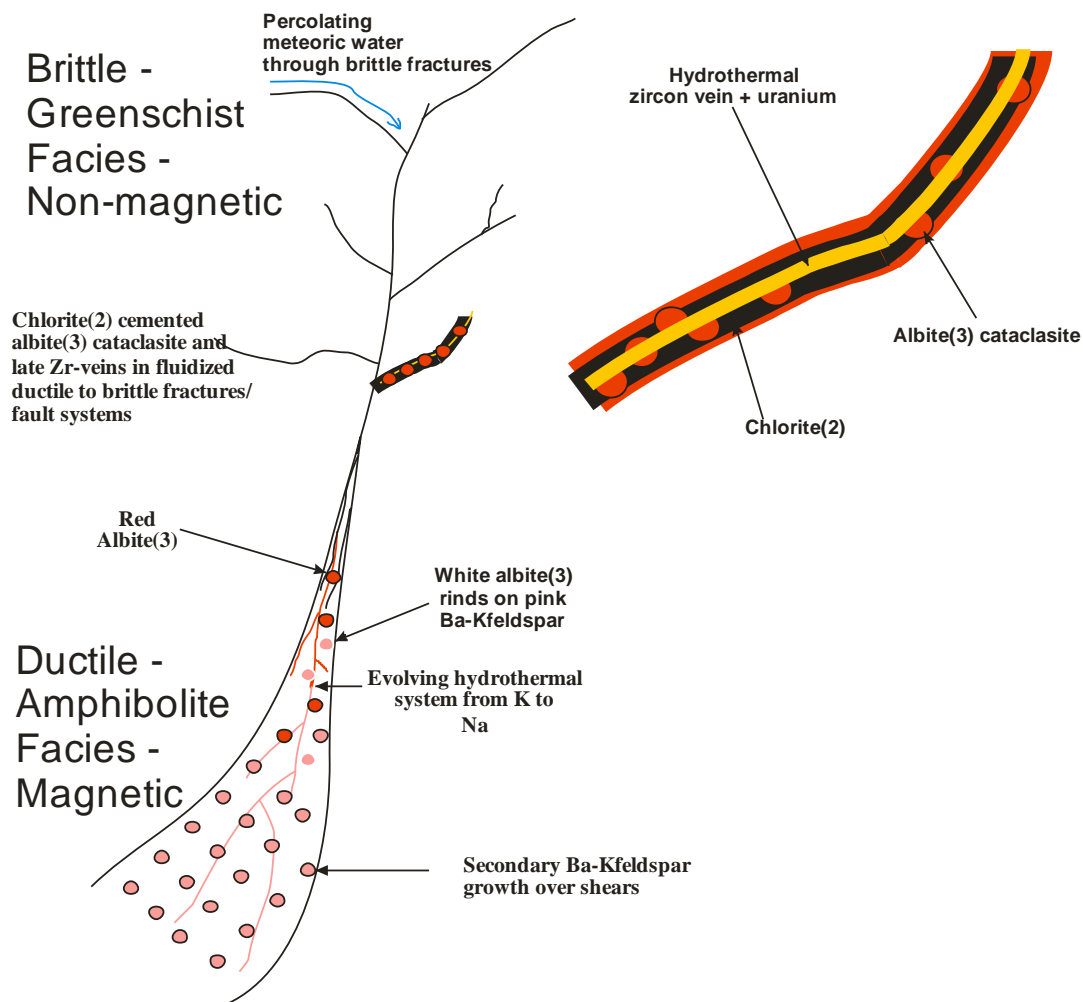


Figure 2.9: Non-magnetic mineralized shears within background magnetic Kurupung. The mylonitic ductile areas of shears are dominated by secondary Ba-Kfeldspar overgrowing chlorite(1) with low grade mineralization (typical of Meamu core). Development of the shear system from ductile to brittle illustrates an evolving hydrothermal fluid from K to Na with development of white albite on Ba-Kfeldspar into complete replacement of Ba-Kfeldspar by red albite(3) towards the top of the system. Shear movement along internal fault fractures causes cataclasis of albitized zones. Black chlorite(2) derived from percolating meteoric waters form black rinds on red albite and seals albite(3) cataclasite. This event is followed by late stage Zr-veining and associated U-mineralization, typical of Aricheng.

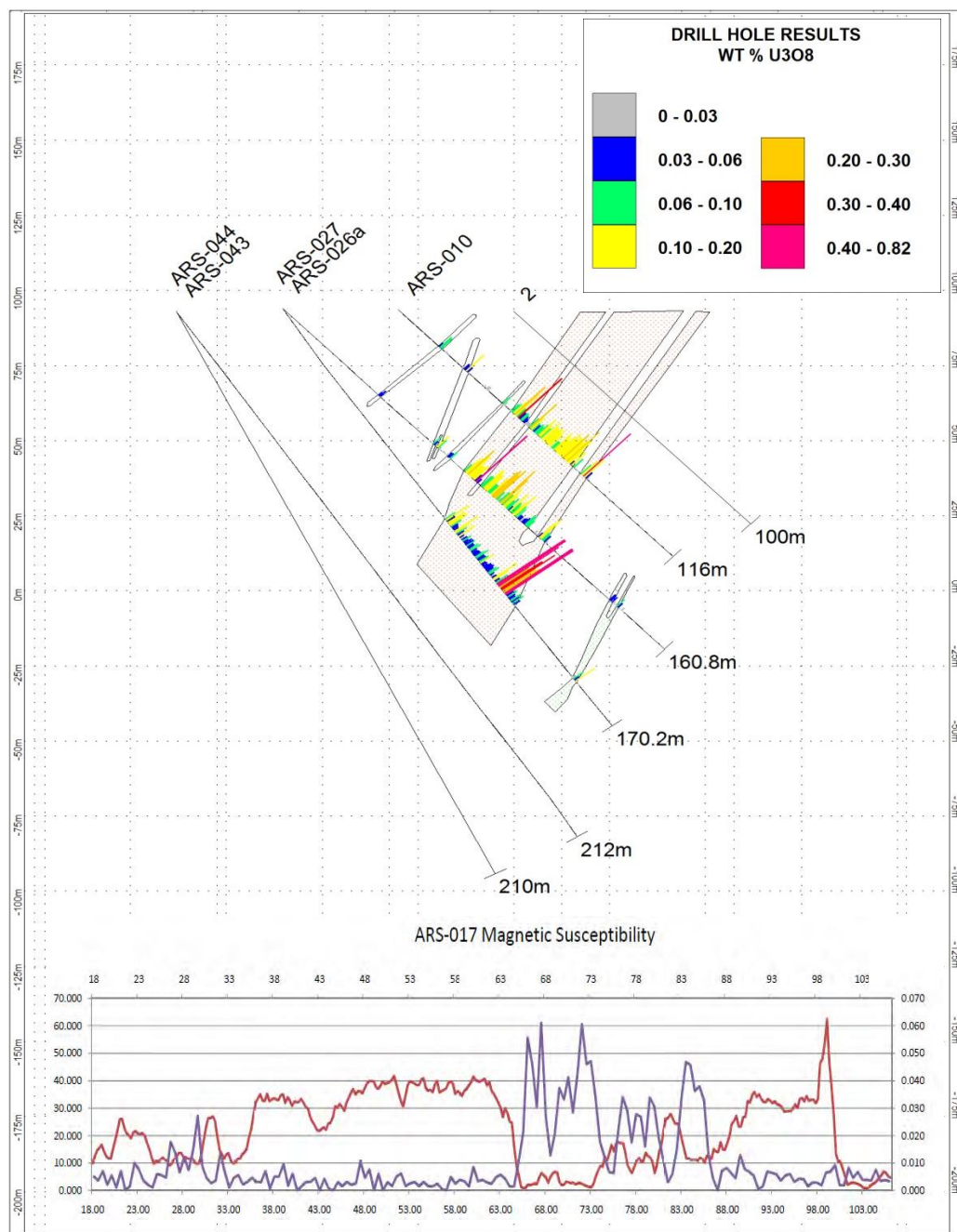


Figure 2.10: Drill section illustrating six holes at Aricheng South. The pink stippled area represents the mineralized sigmoidal shear. The hot and cold histogram colours represent areas of high and low uranium concentrations, respectively. The graph at the bottom of the figure shows measured magnetic susceptibility (red) and gamma radioactivity (purple) in drill hole ARS-017. The two lines demonstrate the reduction of magnetic susceptibility in the demagnetized oxidized zones correlating with elevated uranium mineralization. Figure from U3O8 Corp. internal files. Bottom chart from Workman and Brede, 2012.

Chapter 3: Petrography and Mineralogy

3.0 Introduction

This chapter presents the petrological framework of the Kurupung batholith, supplemented with detailed petrographic descriptions and mineral chemistry. Also described are dikes, including strongly foliated lamprophyres, and the later unfoliated Avanavero diabases. Mineral chemical data of relevant phase and methods are located in Appendix A.

The following text deals specifically with the paragenetic sequence of mineral growth related to the Kurupung batholith, from emplacement through to the uranium mineralization (Table 3.0). Lithologies are described in the following order: 1) unmetasomatized Kurupung batholith and effect of retrograde greenschist facies hydration; 2) chloritic mylonite shear zones; 3) secondary Ba-Kfeldspar growth within chloritic mylonitic shear zones; and 4) the main ore stage that involves development of white to red albite(3) in zones of brittle disaggregation cemented by late chlorite(2) followed by hydrothermal zircon veining and uranium mineralization.

The term ‘background’ is used herein for Kurupung lithologies characterized by magnetometer (25-40 nanotesnells) and scintillometer (<200 counts per second) readings. The range in the magnetometer reading correlates to the abundance of chlorite(1), as the chlorite(1) content of the rock increases the magnetism decreases.

3.1 The Unmetasomatized Kurupung Batholith

The Kurupung batholith, is a foliated monzonite to quartz-monzonite granitoid that has a “background” mineral assemblage of Cr-clinopyroxene, three populations of amphibole, two populations of plagioclase, microcline, titanite, uraniferous zircon and a variety of accessory phases including apatite, epidote, chlorite, biotite, quartz, sericite and serpentine. Interestingly, the background rock contains anomalous values of uranium, well above values expected for granitoids. Mineral textures demonstrate degradation of Cr-bearing clinopyroxene and co-existing Cr-bearing amphibole to actinolite and cores of primary magmatic plagioclase to albite(1)+epidote+titanite.

	KURUPUNG HOST ROCK	LOWER AMPHIBOLITE TO UPPER GREENSCHIST RETROGRESSION	K- METASOMATISM	Na- METASOMATISM	MAIN ORE	POST ORE
Cr-diopside and Cr-augite	██████████					
Cr-Ti-magnetite	██████████					
Cr-edenite and Cr-magnesiohornblende	██████████	██████████				
Ca-plagioclase	██████████	██████████				
Quartz	██████████	██████████				
Microcline(1) (groundmass microcline with Ba)	██████████	██████████				
Primary U-bearing Zircon	██████████	██████████				
Actinolite	██████████	██████████				
Magnetite	██████████	██████████				
Biotite	██████████	██████████				
Cr-epidote	██████████	██████████				
Titanite	██████████	██████████				
Apatite	██████████	██████████				
Albite(1) (retrogression of Ca-plagioclase)	██████████	██████████				
Chlorite(1) (green chlorite mylonite)	██████████	██████████				
Megacrystic Ba-Kfeldspar	██████████	██████████	██████████			
Albite 2 (inclusions in megacrysts)	██████████	██████████	██████████			
Muscovite	██████████	██████████	██████████			
Microcline(2) (local obliteration of Ba-Kfeldspar megacrysts)	██████████	██████████	██████████			
Copper Sulphides	██████████	██████████	██████████			
Epidote	██████████	██████████	██████████			
Rutile	██████████	██████████	██████████			
Albite(3) (main albitization)	██████████	██████████	██████████			
Hematite	██████████	██████████	██████████			
Chlorite(2) (birefringent blue chlorite)	██████████	██████████	██████████			
Hydrothermal zircon	██████████	██████████	██████████			
U-minerals (Uraninite, Brannerite, Coffinite)	██████████	██████████	██████████			
Fluorapatite	██████████	██████████	██████████			
Calcite	██████████	██████████	██████████			
	Relative Mineral Abundance		Temporal Extent			Relative Time
	██████████ Main		██████████	██████████	██████████	██████████
	██████████ Minor		██████████	██████████	██████████	██████████
	██████████ Trace		██████████	██████████	██████████	██████████

Table 3.0: The paragenetic sequence defining a mineralogical continuum from unmineralized Kurupung batholith to post ore alteration.

3.1.1 Cr-bearing Clinopyroxene:

Mafic glomerophyric aggregates of chromian-clinopyroxene and chromian-amphibole comprise about 15% of the rock (Plate 3.1). The Cr-clinopyroxene occurring at the centers of these aggregates form large (2 to 4mm) simply twinned crystals with spectacular compositional zonation. They are composed of Cr-Na-Al-rich Cr-diopside cores which exhibit compositional zonation outward to high-Fe, low-Al-Cr augite margins (Plate 3.2). In addition to the core to margin compositional variation, the Cr-clinopyroxenes also demonstrate well developed growth zonation textures and lozenge-shaped Al-Cr-rich amphibole replacement lamellae. Skeletal Cr-Ti-magnetite defining herringbone texture along lattice planes within the clinopyroxene may be a result of unmixing during ascent or due to hydration and Cr-amphibole replacement (Plate 3.3).



Plate 3.1: Sample # ARN053-108.5m representing background Kurupung with mafic clots of Cr-Clinopyroxene-Cr-amphibole in a more felsic groundmass.

The pyroxenes were analyzed by electron microprobe and the determined compositions are presented in Appendix A Table 1. This data is presented graphically on the Wollastonite-Enstatite-Ferrosilite ternary (Figure 3.0). Primary clinopyroxenes are Cr-diopside with Cr_2O_3 ranging from 0.1 to 1.27 wt%, Al_2O_3 from 1.14 to 5.94 wt% and Na_2O from 0.22 to 1.04 wt%. Core Cr-diopside domains are elevated in Cr-Al-Na while marginal domains are lower in Cr-Na-Al and represent Cr-poor augite. The two populations fall within the Cr-diopside and augite stability fields on the pyroxene ternary. The marginal, lower temperature augite differs compositionally from the core Cr-diopside, showing containing slight enrichment in FeO and TiO_2 , and lower Al_2O_3 , Cr_2O_3 , Na_2O and CaO. Cr-diopsides and augites are replaced by amphibole containing considerably less Cr but more Ti, Al, Fe, Na than the core compositions. Augites are overgrown by Cr-bearing amphiboles which eventually become Cr-depleted due to exsolution of Cr-Ti-magnetite.

The composition and molecular components of pyroxene can be used to relate to pressure conditions during crystallization or recrystallization on the basis of Al^{vi} and Al^{iv} . The ratios of Al^{vi} to Al^{iv} for clinopyroxenes of the Kurupung batholith were plotted in Figure 3.1. The Cr-diopside cores fall dominantly in the field of “granulites and inclusions in basalts and eclogites” while the more augitic compositions fall within the “igneous” field. This supports the interpretation based on petrographic relationships that the Cr-diopsides represent primitive unresorbed mantle derived at elevated P-T conditions and that the Cr-augite overgrowths occurred at lower P-T conditions during ascent of the melt. The mineral chemical studies of these mafic aggregates therefore demonstrate that they have a mantle origin. The lack of textural intergrowths of these mafic aggregates with the surrounding more felsic host coupled with their mantle mineral chemistry suggests that they are not igneous in origin but rather represent unresorbed mantle fragments incorporated into a melt which generated the more felsic host granitoid. A detailed discussion on the origin and implications of Cr-diopside are presented in chapter 6.

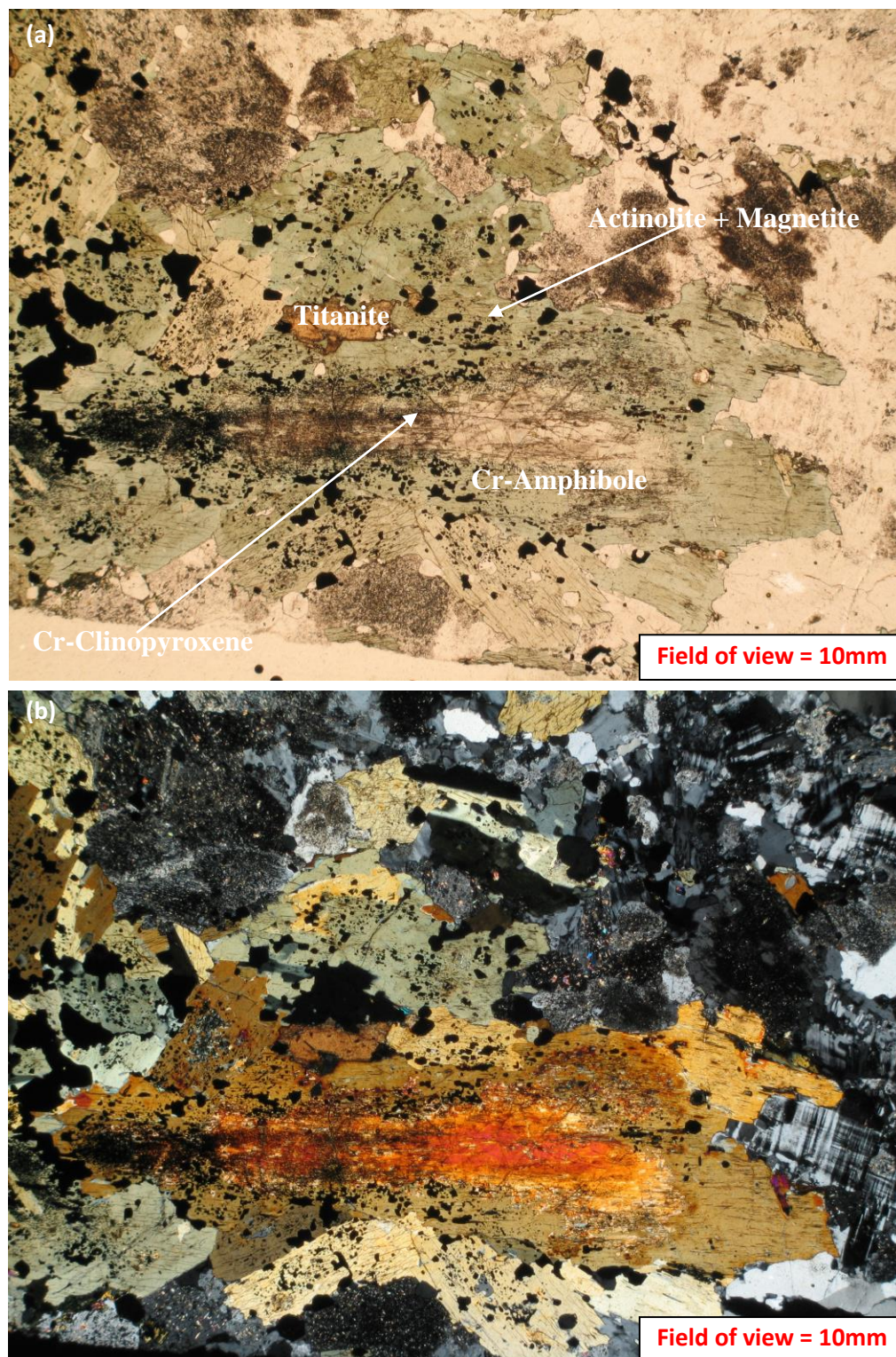


Plate 3.2a,b: Sample #ARN053-108.5m: (a) Plane light image of Cr-clinopyroxene at the centers of the mafic clots form large simple twins and compositional zoning with high Mg,Al,Cr-clinopyroxene cores zoned outward to high-Fe, low-Al,Cr-clinopyroxene margins; (b) crossed polarized image of (a) with bright orange Cr-clinopyroxene core mantled by actinolite+magnetite.

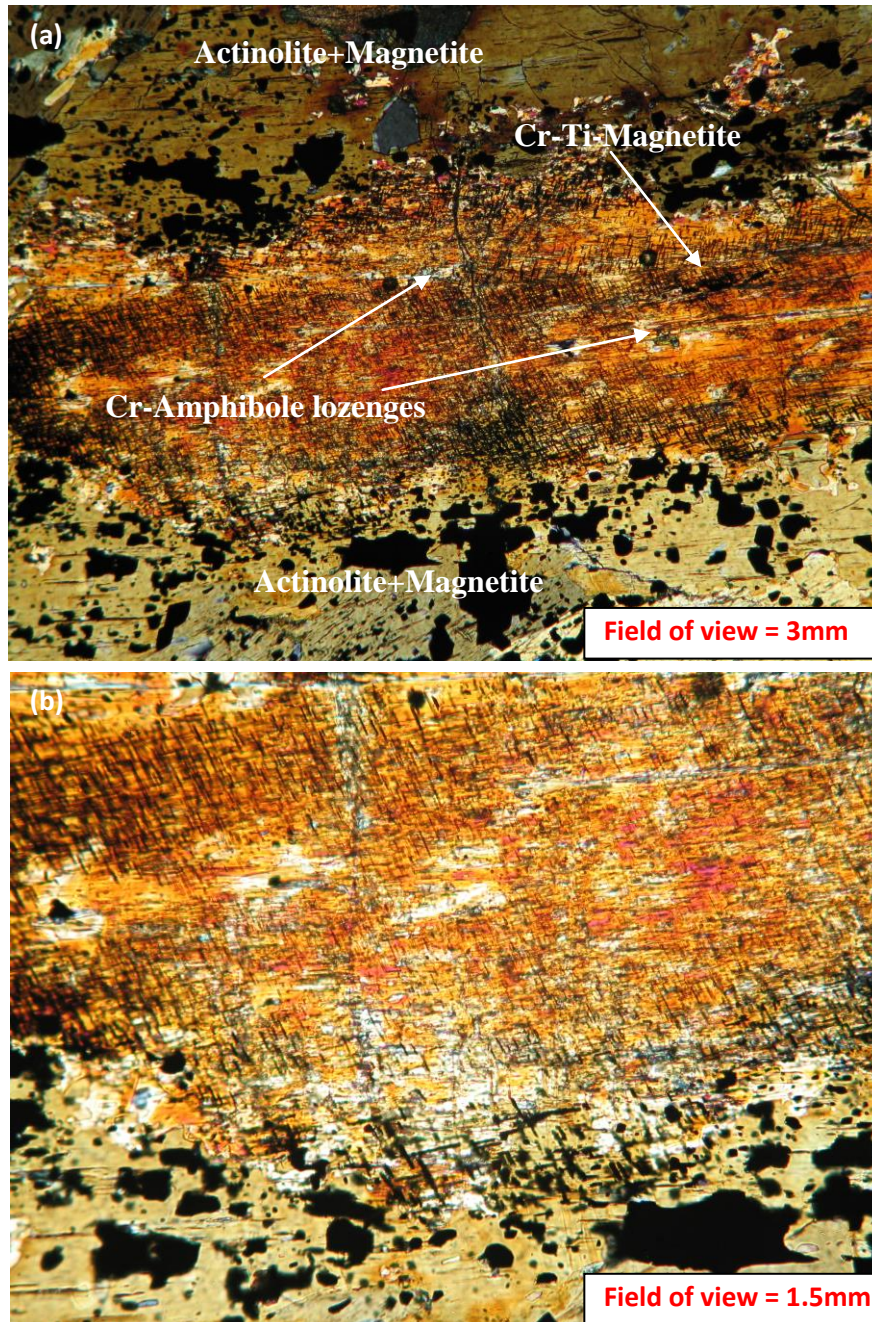


Plate 3.3a,b: Sample #ARN053-108.5m: (a) Crossed polarized light image of lozenge shaped Al-Cr-amphibole replacement lamellae and growth of fine-grained Cr-Ti-magnetite forming herringbone texture along lattice planes within the clinopyroxene; (b) higher magnification of (a) illustrating the delicate exsolution texture which is crystallographically controlled by the clinopyroxene crystal structure.

Clinopyroxene Ternary Diagram

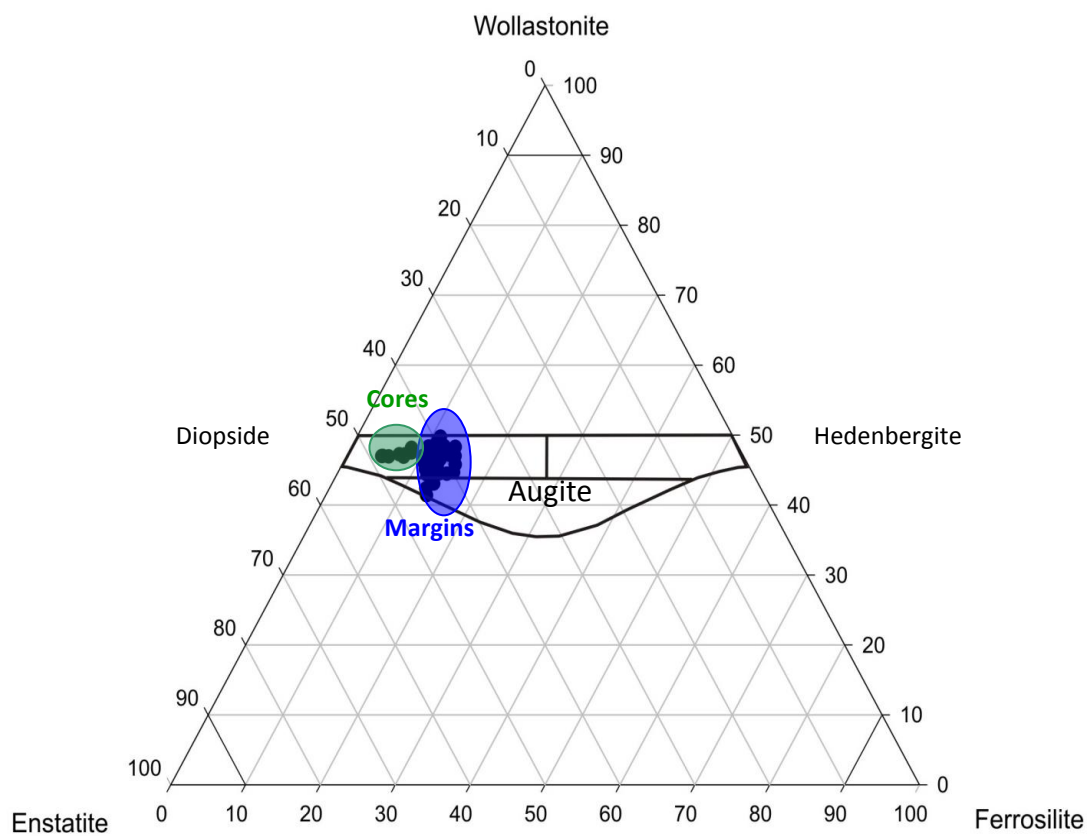


Figure 3.0: Clinopyroxene ternary illustrating the compositional variation between Cr-diopside cores and Cr-augite margins within mantle aggregates. Modified after Klein and Hurlbut, (1985).

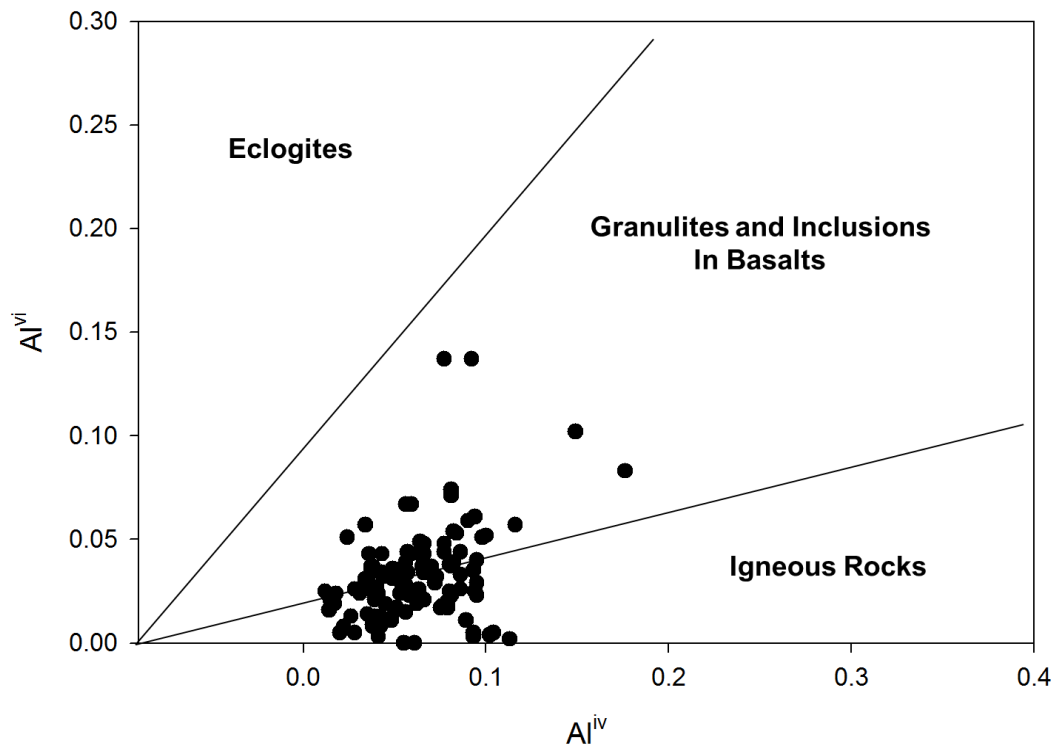


Figure 3.1: Graph illustrating ratios of Al^{vi} to Al^{iv} for clinopyroxenes. Data points falling within the “granulites and inclusions in basalts” field support the interpretation that Cr-diopside represents primitive mantle compositions derived at elevated P-T conditions and that the Cr-augite overgrowths plotting in the “igneous rocks” field formed at lower P-T conditions during ascent of the melt. Figure modified after Aoki and Shiba, 1973.

3.1.2 Amphibole:

Three populations of amphibole are recognized: (1) lozenge-shaped Cr-amphibole forming submicroscopic exsolution lamellae within Cr-clinopyroxene (Plate 3.3); (2) coarse-grained anhedral Cr-amphibole mantling the glomerophyric Cr-clinopyroxene (Plate 3.4); and (3) retrogressive hydrothermal/metamorphic actinolite developed on the outer margins of Cr-clinopyroxene and Cr-amphibole aggregates (Plate 3.2). In domains of intense retrogression the mafic aggregates have been completely retrogressed to actinolite and epidote (Plates 3.5). Amphibole mineral chemistry can be found in Appendix A Table 2. Amphibole compositions are plotted on Figure 3.2a, a binary of SiO_2 versus $Mg/(Mg+Fe)$ illustrating Ca-amphibole classification (Leake et al., 1997). The more primary edenite to Mg-hornblende show low Si and high $Mg/(Mg+Fe)$ relative to actinolite. The Al^{iv} versus total alkalis binary (Figure 3.2b) also illustrates the

compositional variation from magmatic to retrogressive amphibole chemistry; magmatic amphibole have higher total alkalis and higher Al^{IV} relative to actinolite.

Submicroscopic lozenge-shaped replacement lamellae of Cr-amphibole within Cr-clinopyroxene exhibit a primary zonation from Na+K-Ti-Fe-Al-rich edenite cores to intermediate domains of magnesiohornblende to outer margins of Fe-rich and lower Na+K, Mg, Al, Ti-magnesiohornblende (Plate 3.3). The edenite cores contain up to 44.13 wt% SiO_2 , 1.51 wt% TiO_2 , 8.96 wt% Al_2O_3 , 0.34 wt% Cr_2O_3 , 13.90 wt% FeO, 13.72 wt% MgO, 12.27 wt% CaO and 1.60 wt% Na_2O . The magnesiohornblende margins are slightly less aluminous and in comparison to the edenite contain 47.38 wt% SiO_2 , 1.15 wt% TiO_2 , 7.29 wt% Al_2O_3 , 0.68 wt% Cr_2O_3 , 11.58 wt% FeO, 15.12 wt% MgO, 12.37 wt% CaO and 1.40 wt% Na_2O .

A population of coarse-grained Cr-amphibole mantles the Cr-clinopyroxene and lozenge shaped Cr-amphibole intergrowths (Plates 3.2 and 3.4). These coarse-grained anhedral Cr-amphiboles constitute up to 15% of the glomerocrystic mafic aggregates. They are Al-rich magnesiohornblende (up to 8% Al_2O_3) which give way to actinolite margins (0.01% Al_2O_3), indicating sub-solidus hydration during cooling.

Non-pervasive hydrothermal retrogression has converted coarse-grained magnesiohornblende to actinolite, commonly associated with chlorite(1) (Plate 3.5). Actinolite associated with chlorite(1) is characterized by elevated silica and low aluminum-titanium contents. This actinolite is characterized by up to 56.19 wt% SiO_2 , 0.01 wt% TiO_2 , 0.44 wt% Al_2O_3 , 0.14 wt% Cr_2O_3 , 9.27 wt% FeO, 18.33 wt% MgO and 13.27 wt% CaO. The actinolite co-exists with coarse-grained honey-yellow epidote and euhedral rhombs of titanite, accounting for the residual calcium from the breakdown of plagioclase, and the iron and titanium components of the primary magnesiohornblende (Plate 3.5). The margins of biotite + actinolite + titanite + magnetite are replaced by

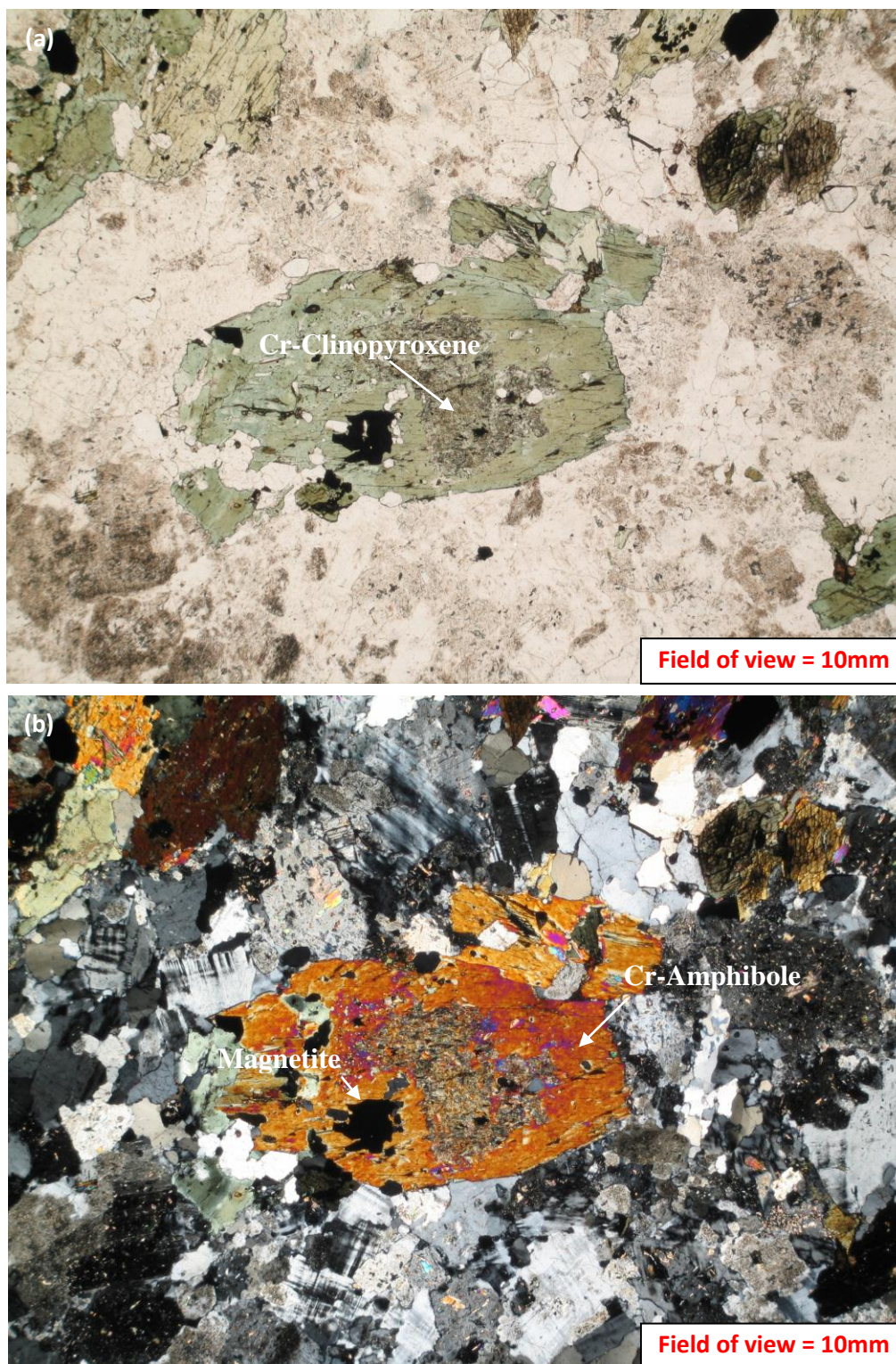


Plate 3.4a,b: Sample #ARN21-117.7a: (a) Plane light photomicrograph illustrating a mafic aggregate with Cr-clinopyroxene cores mantled by Cr-amphibole (dark green) and retrogressive actinolite (light green) in a groundmass dominated by quartz and microcline; (b) Crossed polarized image of (a) illustrating the birefringent orange-red Cr-amphibole and magnetite growth within domains of actinolite.

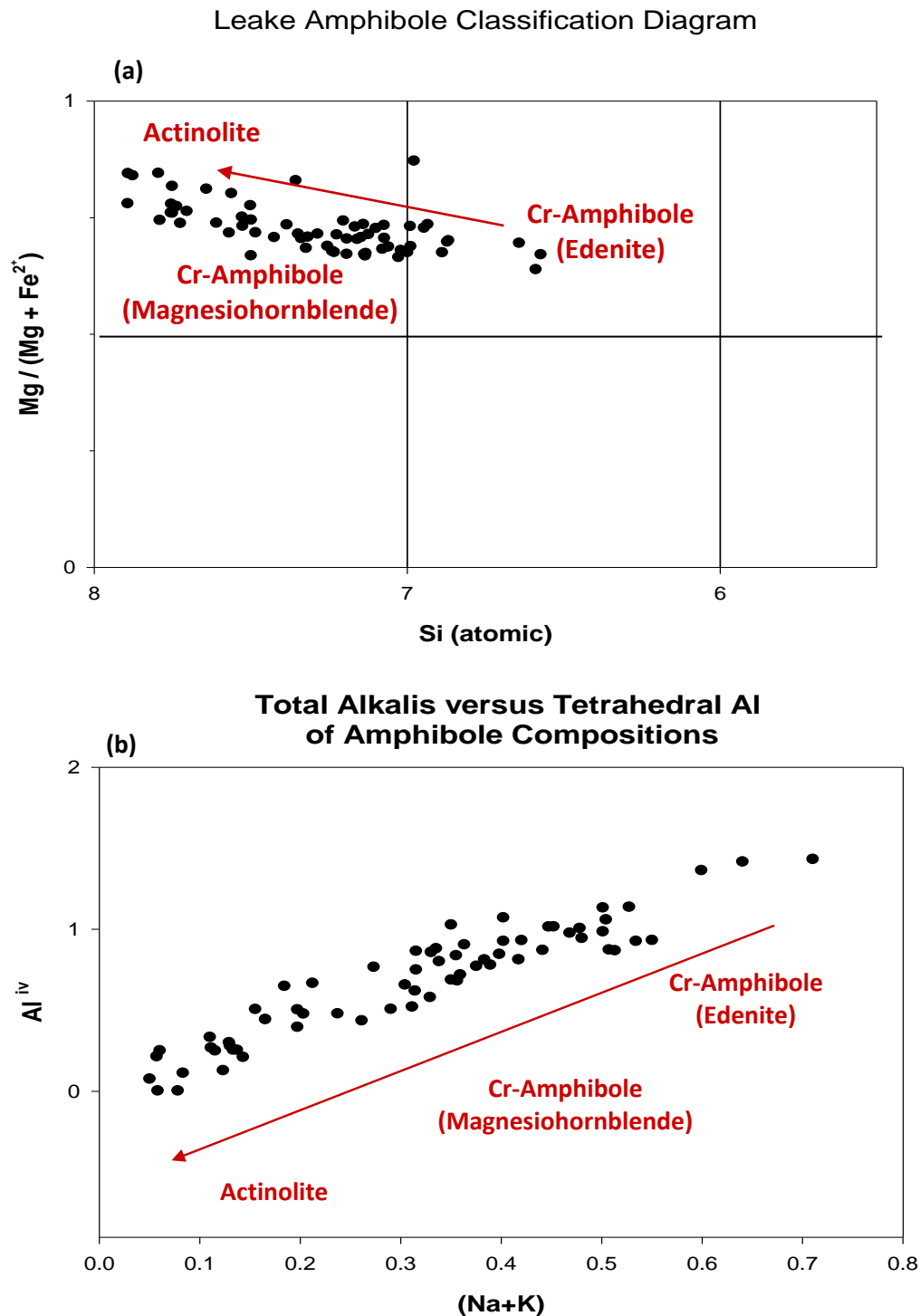


Figure 3.2a,b: (a) Leake et al., (1997) classification diagram for amphiboles illustrating the progression from most primitive Cr-edenite through Cr-magnesiohornblende to low temperature retrogressive actinolite; (b) a plot of total alkalis versus Al^{iv} illustrating the more elevated alkali and tetrahedral Al content of most primitive amphibole compared to the more depleted alkali and tetrahedral aluminum content of the retrogressive actinolites. See analyses Appendix A, Table 2.

green chlorite(1), a product of selective hydration on cooling against the Transamazonian volcanics. Coarse-grained euhedral magnetite inclusions within amphibole are the residual Fe-Ti component liberated during amphibole retrogression (Plates 3.4 and 3.5). The magnetite within these retrogressive margins is what gives the rock its magnetic signature.

3.1.3 Plagioclase:

Coarse-grained, ragged and intensely replaced magmatic primary plagioclase phenocrysts comprise 35% of the rock (Plate 3.6). Non-pervasive replacement of Ca-plagioclase cores by albite(1), epidote, muscovite/sericite, and titanite are a result of retrogression. Relict plagioclase in cores have contents up to 4.07% CaO (An₂₁). Where alteration is most intense, twinning is obliterated by insipient saussuritization forming clouded domains encapsulating Fe-oxide that is partially replaced by unclouded domains of Kfeldspar.

Of particular interest are grains of Ca-plagioclase that underwent pervasive Ba-Kfeldspar replacement and subsequent albitization as in sample ANC011-120. Detailed petrographic investigation of megacrysts in this sample revealed an approximately 300micron patch of relict primary Ca-plagioclase that survived both K- and Na-metasomatic processes. Microprobe analyses determined that this relic phase has a composition of An_{19.5} (Plate 3.7). Plagioclase mineral chemistry is located in Appendix A Table 5.

3.1.4 Microcline(1):

Anhedral white microcline(1) makes up 35% of a groundmass which shows no preferred orientation (Plates 3.2 and 3.4). It is coarse to medium-grained and displays both albite and pericline twinning, the combination leading to the typical tartan gridiron twinning of microcline. The individual lamellae are discontinuous and form pinch and swell

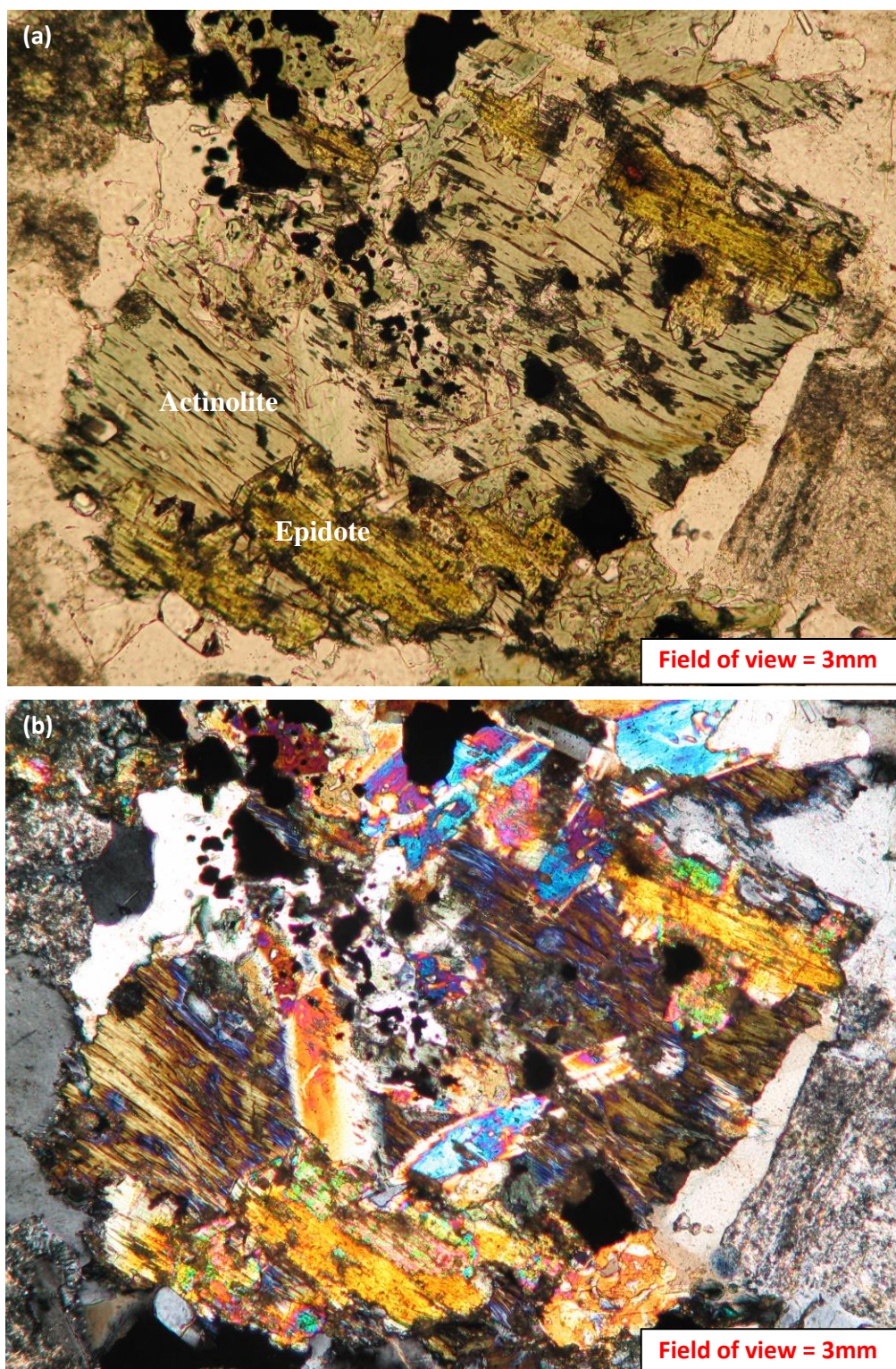


Plate 3.5a,b: Sample #ANC011 120m: (a) Plane light photomicrograph illustrating relict Cr-clinopyroxene core with pervasive honey-yellow epidote growth with actinolite; (b) Crossed polarized light image of (a) illustrating the pervasive birefringent yellow epidote growth on feathery to fibrous chlorite altered actinolite.

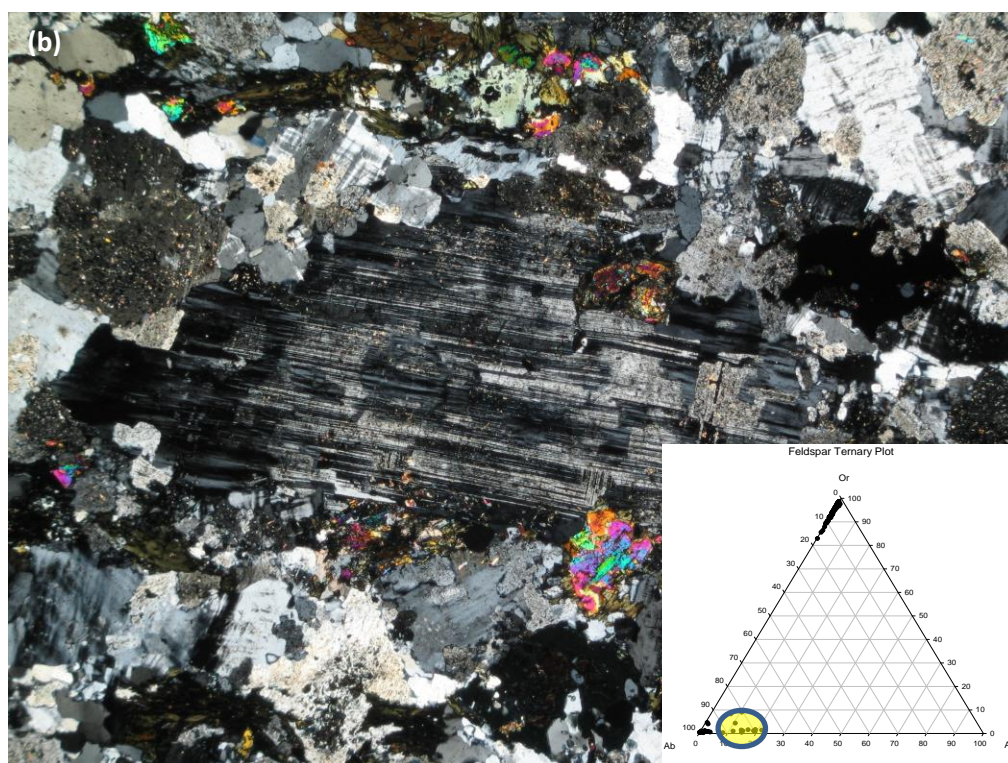
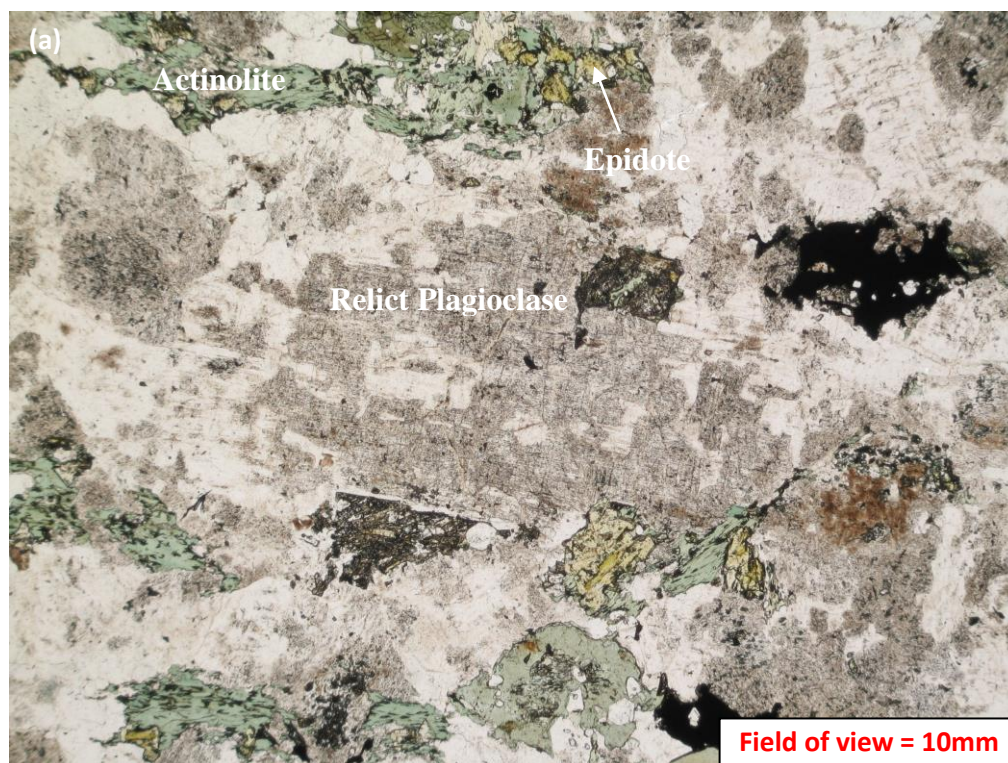


Plate 3.6a,b: Sample #ARN053 108: (a) Plane light image depicting ragged and intensely replaced coarse-grained primary magmatic plagioclase with remnant oscillatory growth zones hosted within a groundmass dominated by microcline, quartz and mafic enclaves now actinolite, chlorite(1) and epidote. The inset ternary plot illustrates that the relict plagioclase grains fall along the base of the ternary between An10-An21.

dislocations. Microcline mineral chemistry indicates that microcline(1) contains up to 0.30 wt% BaO.

3.1.5 Titanite:

Orange-brown titanite is quite common throughout sections of the Kurupung and comprises 2% of the rock. It occurs as high relief, fine- to coarse-grained rhombohedrons up to 2mm in length on the margins of actinolite (Plate 3.2). Coarse-grained titanites commonly host inclusions of magnetite. These coarse-grained rhombs are unaltered and product of late retrogressive growth with actinolite-epidote (Plate 3.8). Titanite is locally altered to rutile.

3.1.6 Accessory Phases:

The accessory phases occur interstitial to the dominant mineralogy. Fine-grained (not exceeding 0.5mm) polygonal quartz exhibiting undulose extinction comprises about 10% of the rock. Polygonal quartz most commonly occurs on the sutured and embayed grain margins of microcline. Accessory laths of fine- to medium-grained biotite show retrogression to green chlorite(1) along grain margins and cleavage planes (Plate 3.9). Ti-biotite laths on actinolite margins are characterized by up to 3.03 wt% TiO₂, 19.07 wt% Al₂O₃, 17.02 wt% FeO, and 18.88 wt% MgO (Appendix A Table 3). Inclusions of zircon and apatite(1) are common within biotite. Yellow crystalline Cr-epidote can be quite pervasive in some sections, most commonly occurring on the margins of retrogressed amphibole where mineral assemblages form an outward continuum from actinolite to biotite to green chlorite(1) to yellow epidote (Plate 3.5 and 3.6). The mineralogical continuum of biotite to actinolite+epidote to chlorite(1) represents a change in mineral phase stability with ever increasing hydration of the batholith during emplacement against the Transamazonian volcanics.

The unaltered background Kurupung is also characterized by anomalously elevated uranium contents. Interestingly, primary isolated euhedral zircon granules with well-defined crystal boundaries are disseminated throughout the groundmass. These

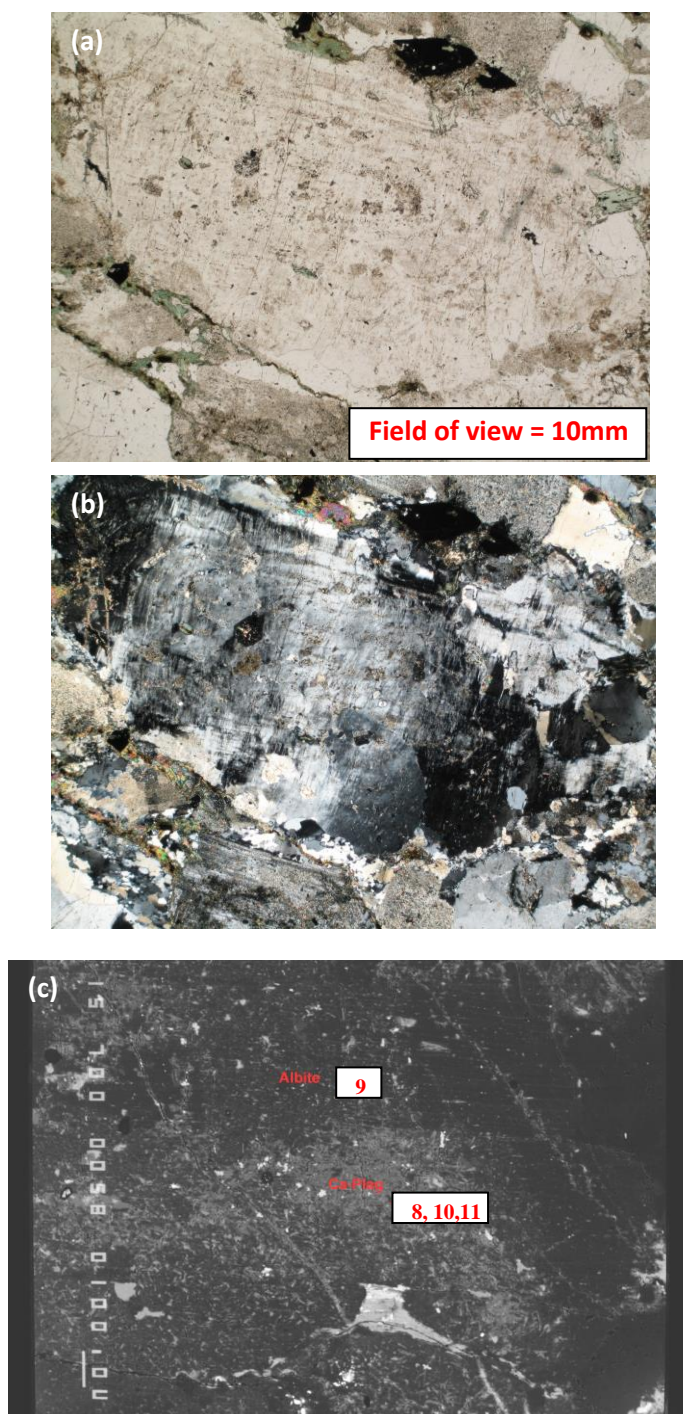


Plate 3.7a-c: Sample ANC011-120m: (a)-(b) Relict plagioclase phenocrysts show a rhythmic concentric zoning formed during Ba-Kfeldspar metasomatism; (c) Backscatter electron image illustrating the alternating rhythmic growth zones and the relict Ca-plagioclase domain preserved after both K- and Na-metasomatism. Numbers represent analysis locations relating to analyses 44-48 in Appendix A Table 5. The 100 micron scale bar for the backscatter image is located along the left margin of the image.

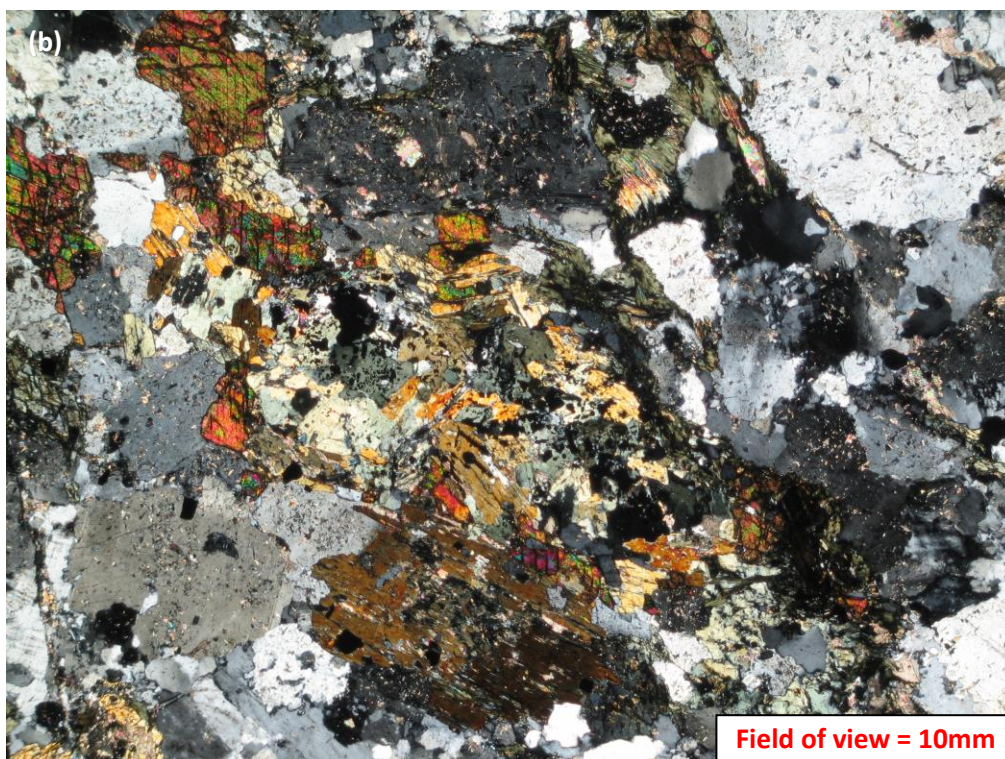
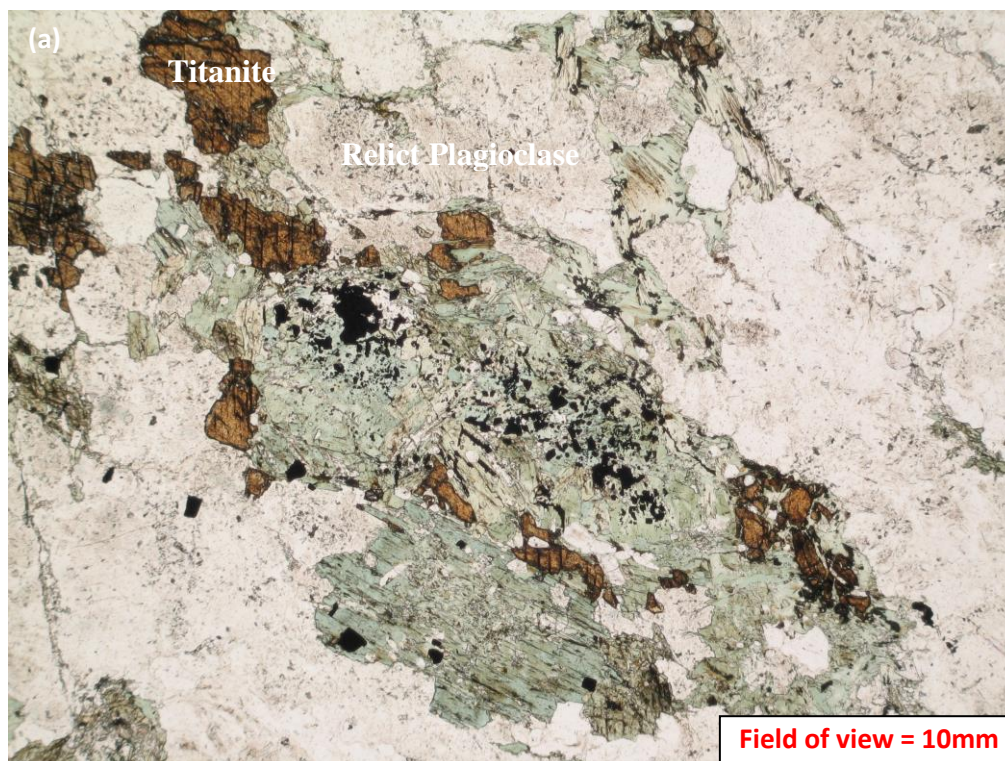


Plate 3.8a,b: Sample #ARN003-43.4m: (a) Plane light image illustrating coarse-grained brown titanite growing on margins of late retrogressive amphibole and magnetite; (b) Crossed polarized image illustrating strongly birefringent titanite on actinolite margins.

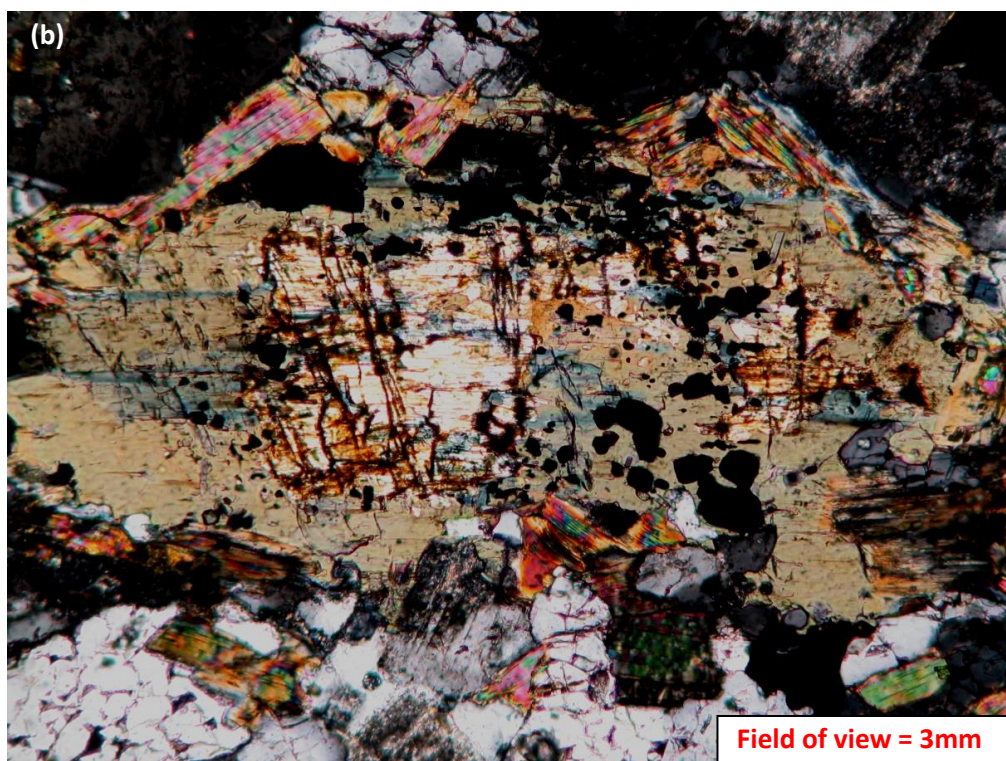
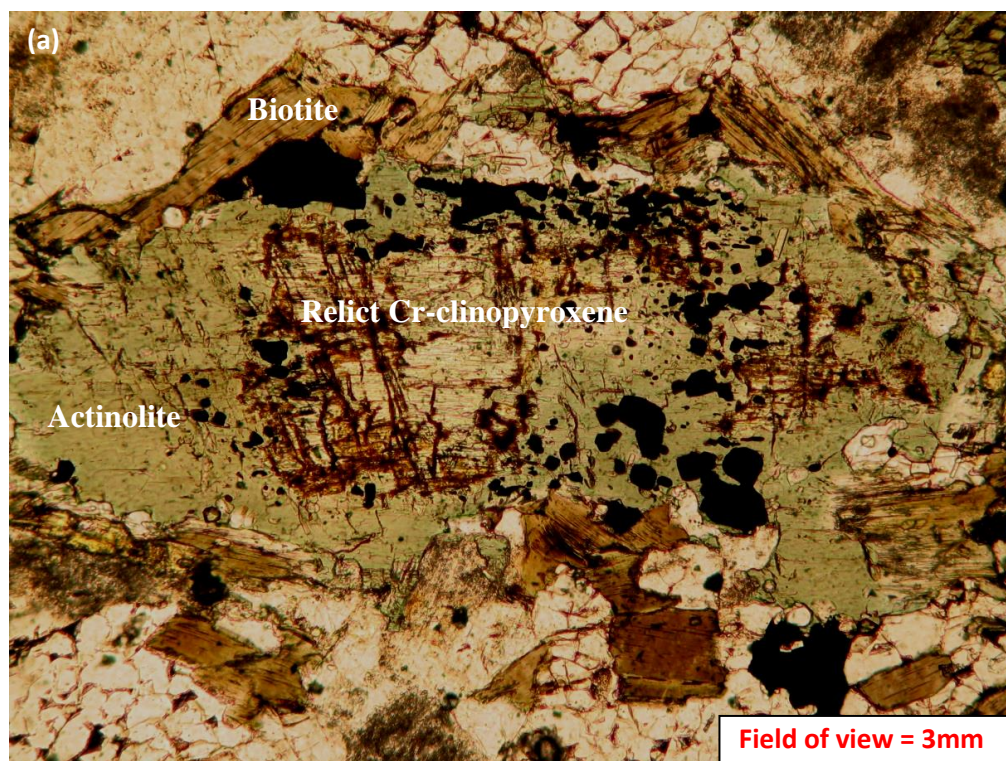


Plate 3.9a,b: Sample #ARN003-53m: (a) Plane light image of remnant Cr-clinopyroxene core with retrogressive growth of actinolite and magnetite replaced by medium-grained laths of biotite; (b) Crossed polarized image illustrating the highly birefringent biotite laths on actinolite.

primary zircons were dated by Davis (2006) and relate to the crystallization of the Kurupung batholith.

They display well preserved crystal faces, with multiple growth zones and sharp crystal boundaries. Grains were analyzed for chemical comparison to the veined zircon and their compositions detailed in Appendix A Table 4. These U-bearing zircon granules account for the anomalously elevated uranium content of the batholith (Plate 3.10).

3.2 Chloritic Shear Zones

Mylonitic shear zones accommodated the uplift of the Kurupung batholith. The emplacement of the still hot Kurupung batholith against the cold Transamazonian footwall resulted in hydration of the intrusive and retrograde reactions forming biotite-actinolite-chlorite(1) alteration on Cr-amphibole. The magnetic signature of the Kurupung is partially to completely eradicated within chlorite(1) altered mylonitic shears, giving rise to magnetic lows (Figures 2.5 and 2.6). The chlorite(1) laths commonly contain extremely fine-grained inclusions of magnetite. Chlorite(1) occurs as dark green, fine- to medium-grained feathery laths with low birefringence (Plate 3.11). This first generation chlorite(1) is characterized by iron contents ranging from 10.29-19.07 wt% FeO, magnesium contents between 18.78-25.37 wt% MgO, aluminum contents between 17.06-24.08 wt% Al₂O₃, and manganese contents between 0.22-0.50 wt% MnO. Chlorite mineral chemistry is located in Appendix A Table 4. When plotted on the chlorite classification diagram of Zane et al (1998), the chlorite(1) compositions plot as pycnochlorite (Figure 3.3).

3.3 Ba-Kfeldspar Metasomatism

Three populations of feldspar are noted: (1) primary Kfeldspar that exhibits microcline twinning is a major part of the groundmass in the unaltered Kurupung batholith; (2) zoned Ba-rich Kfeldspar growth overgrowing Ca-plagioclase; and (3) a late stage microclinization which causes replacement of oscillatory zoned Ba-Kfeldspar. The mineral chemistry of the Ba-Kfeldspars is located in Appendix A Table 5.

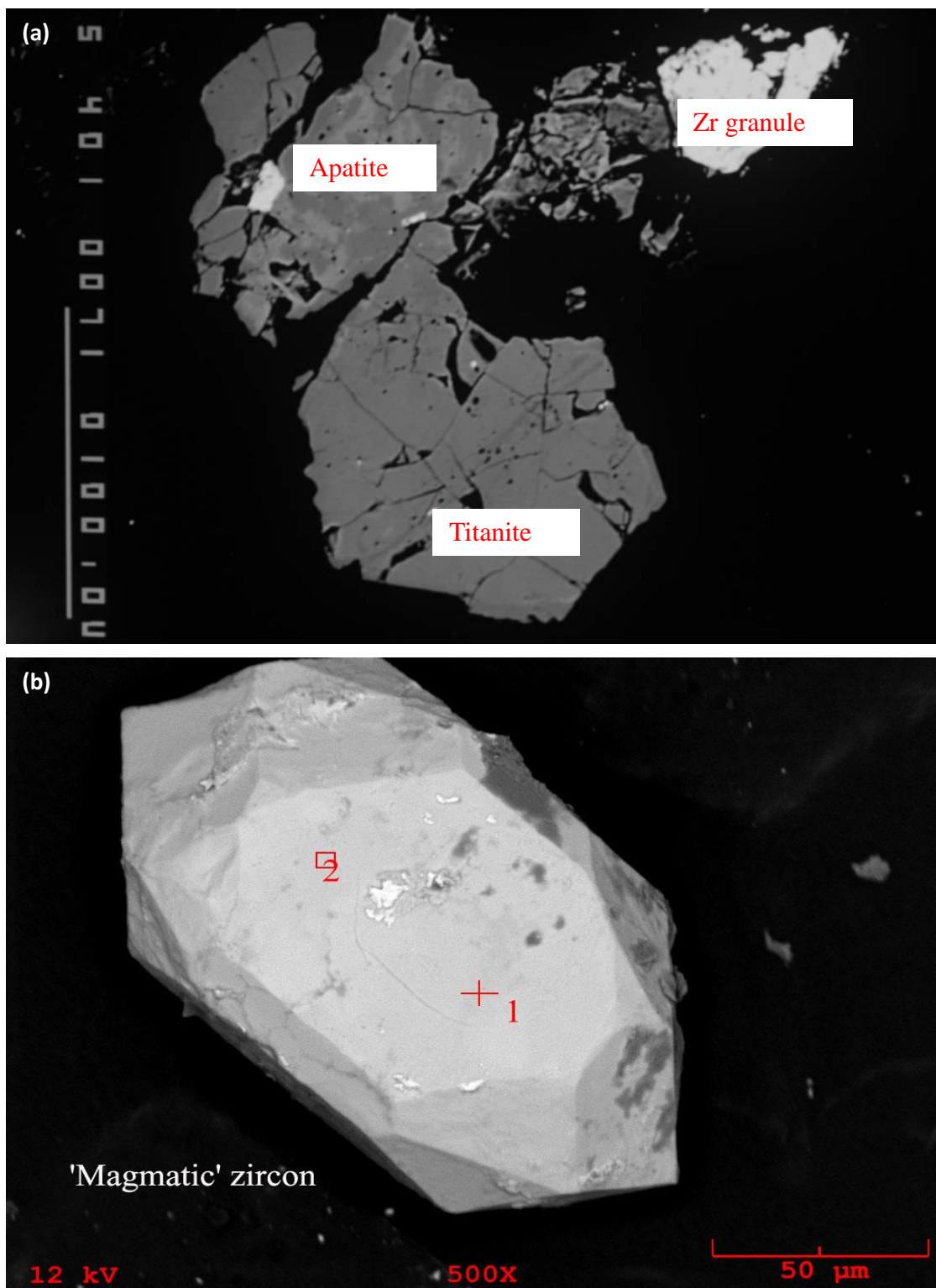


Plate 3.10a,b: (a) Backscatter electron image illustrating a zircon grain with quite well-defined crystal outline with adjacent titanite and apatite. The 100 micron scale bar is located on the left margin of the image; (b) SEM image of a magmatic zircon used for age determination of the Kurupung batholith (Davis, 2006).

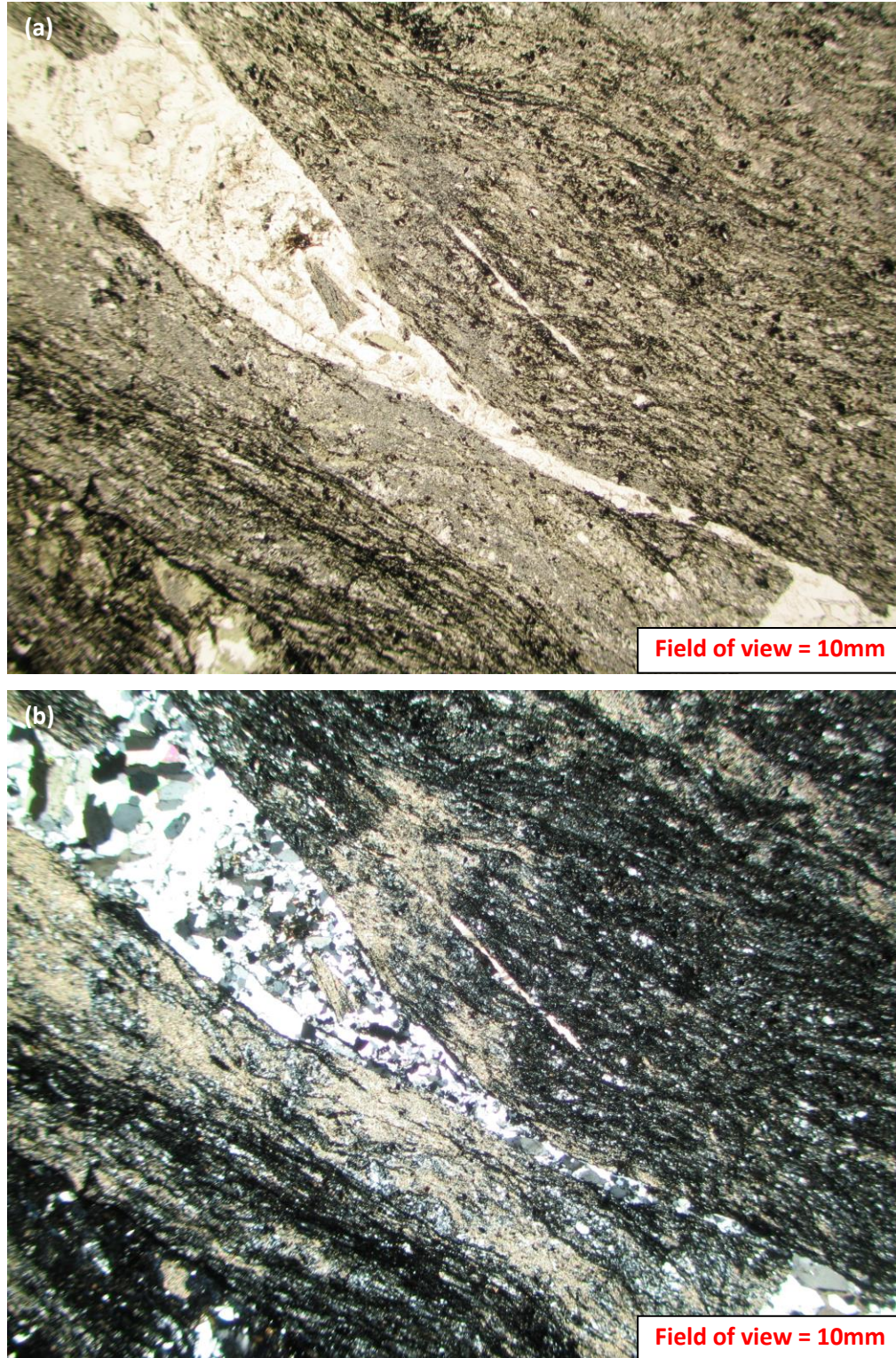


Plate 3.11a,b: (a) Plane light image illustrating the mylonitic shear fabric defined predominantly by chlorite(1) and domains of quartz and carbonate; (b) Crossed polarized image illustrating the low birefringence of chlorite(1), multigranular quartz and microcrystalline calcite.

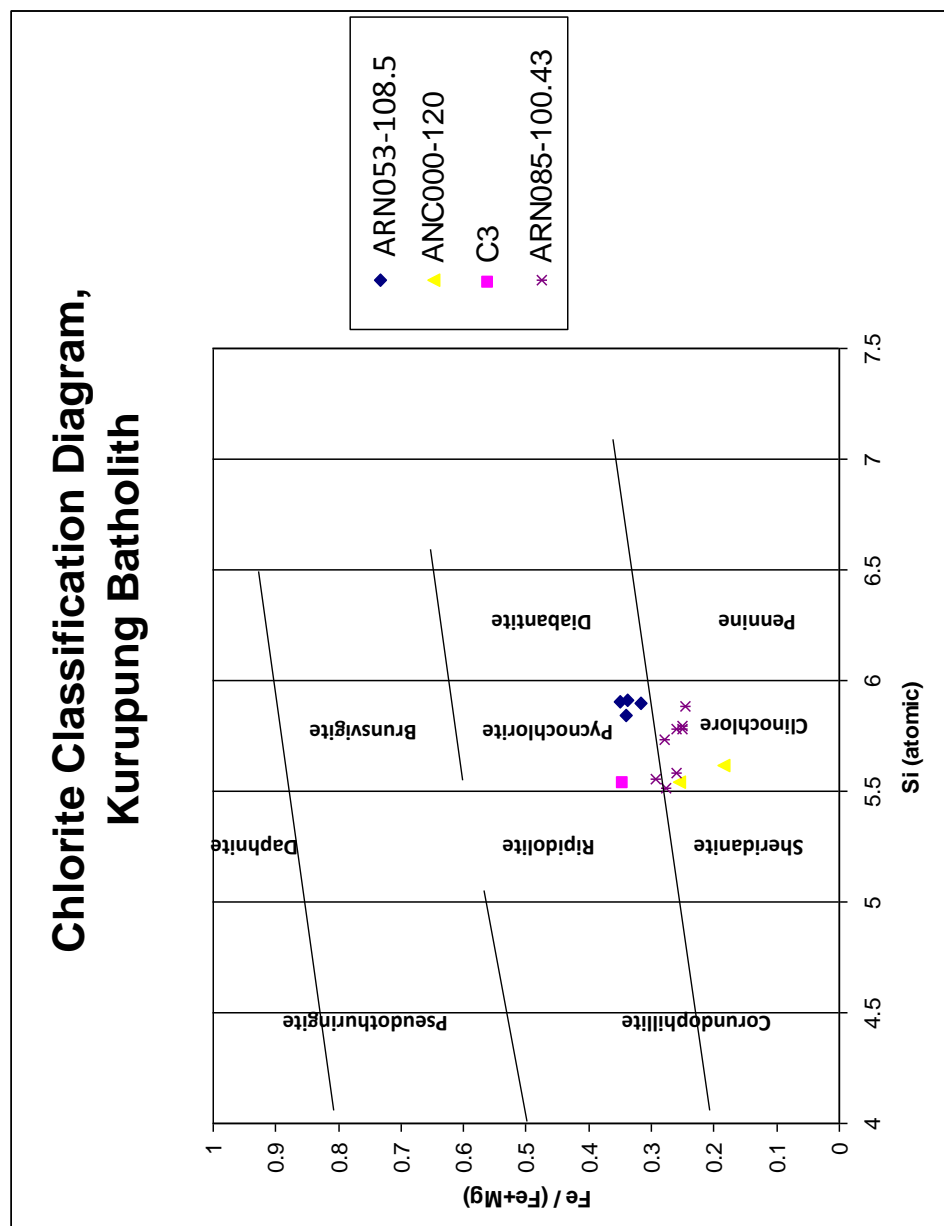


Figure 3.3: Chlorite classification diagram illustrating chlorite(1) compositions plotting in the pycnochlorite field and chlorite(2) compositions plotting as clinochlore. Diagram modified after Zane et al., 1998.

The lithology described here provides evidence for widespread secondary potassium metasomatism of the Kurupung batholith. Secondary Ba-Kfeldspar megacrysts show rhythmic concentric/oscillatory zoning of alternating Ba-Kfeldspar and albite, perhaps indicating growth on either side of the Kfeldspar-albite immiscibility gap (Deer et al, 2001). This secondary stage of potassium metasomatism also gives rise to veinlets of Ba-Kfeldspar + REE bearing minerals+barite crosscutting relict zones of magmatic oscillatory zoned plagioclase (Plate 3.12). These plagioclase phenocrysts (described in section 3.1.3) are the sites of nucleation for growth of Ba-Kfeldspar. Secondary Ba-Kfeldspar overgrows the chlorite(1) fabric of the Kurupung batholith but predate chlorite(2) cementing late albitite breccia.

The sample suite consists of various examples demonstrating infiltration of Ba-K-rich fluids, to form late stage microveinlets. Hydrothermal Ba-Kfeldspar growth in fracture systems cross-cut primary magmatic plagioclase and pervasively alter it to Ba-rich Kfeldspar (Plate 3.13 and 3.14a,b). Backscatter electron images of these microfracture/microveinlet sets show dark, intermediate, and bright domains reflecting the barium content of the Kfeldspar (Plate 3.14c,d). The dark domains have 0.25%-0.55% BaO, intermediate domains have 1.01-1.85% BaO, and the brightest domains have 2.83-3.88% BaO. The brightest barium-rich domains parallel the vein walls and parallel a bright white domain of REE phosphates (Plate 3.14e). Small veinlets off the main vein host crystals of barite. These microveinlets crosscut plagioclase and are overgrown by secondary Ba-Kfeldspar. The Ba-Kfeldspar overgrowing plagioclase is also domainal as backscatter imaging again reveal areas of dark, intermediate, and bright barium zones. The dark zones are 0.45-0.98% BaO; intermediate zones are 6.45-6.58% BaO; and the brightest zones up to 7.27% BaO.

The secondary Ba-Kfeldspar megacrysts are up to 2cm in diameter and demonstrate strong oscillatory zoning of alternating Ba-Kfeldspar and albite. The first stage of megacrystic growth is consumption of primary plagioclase phenocrysts (Plates 3.13 and 3.14a,b).

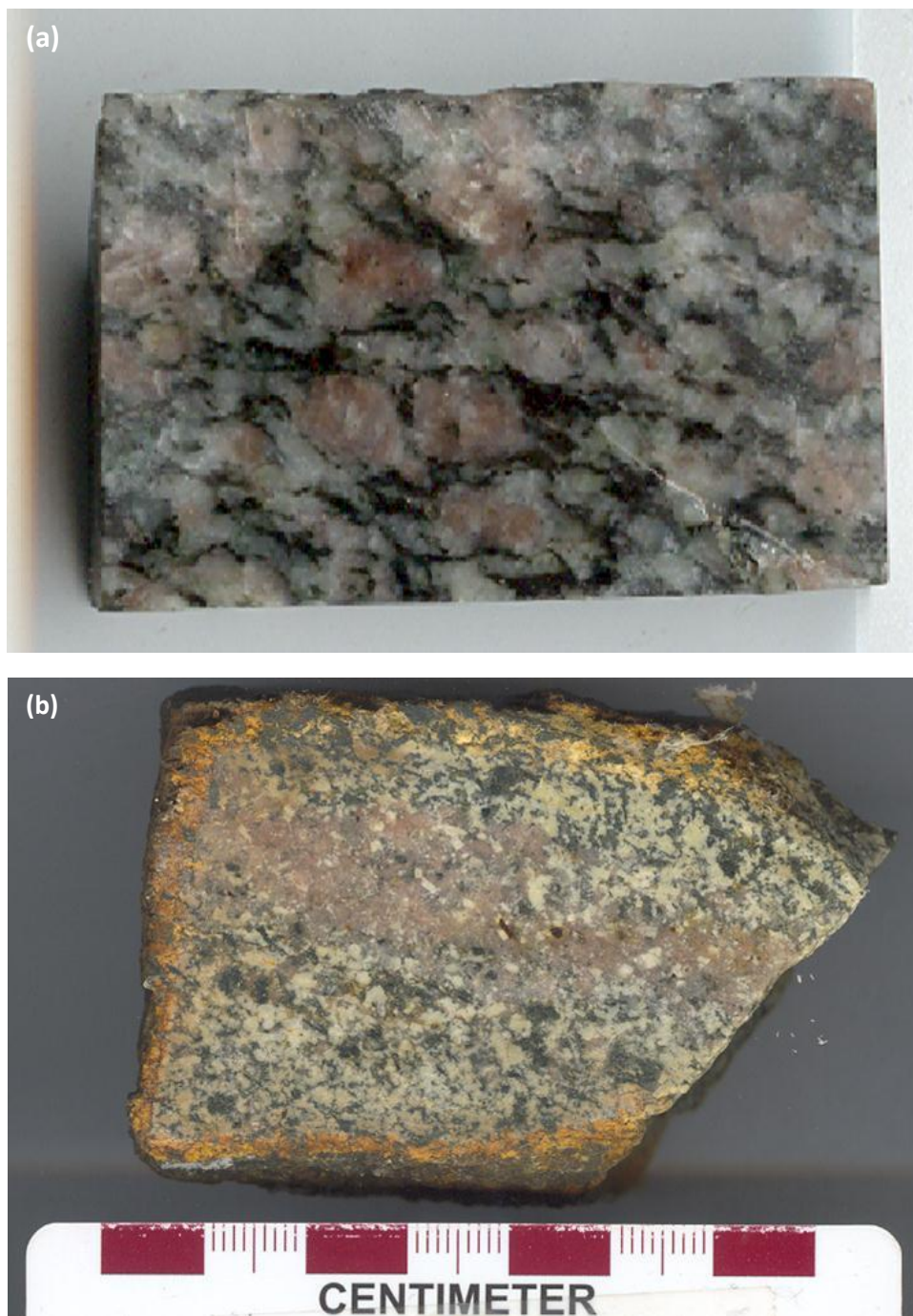


Plate 3.12a,b: (a) A section of drill core illustrating megacrystic Ba-Kfeldspar overgrowing the dominant fabric defined by chlorite(1) indicating secondary growth (Sample #ANC011-120m); (b) Hand specimen illustrating the infiltrating pink Ba-Kfeldspar fluids along site specific zones of fluid ingress (Sample Pere 11).

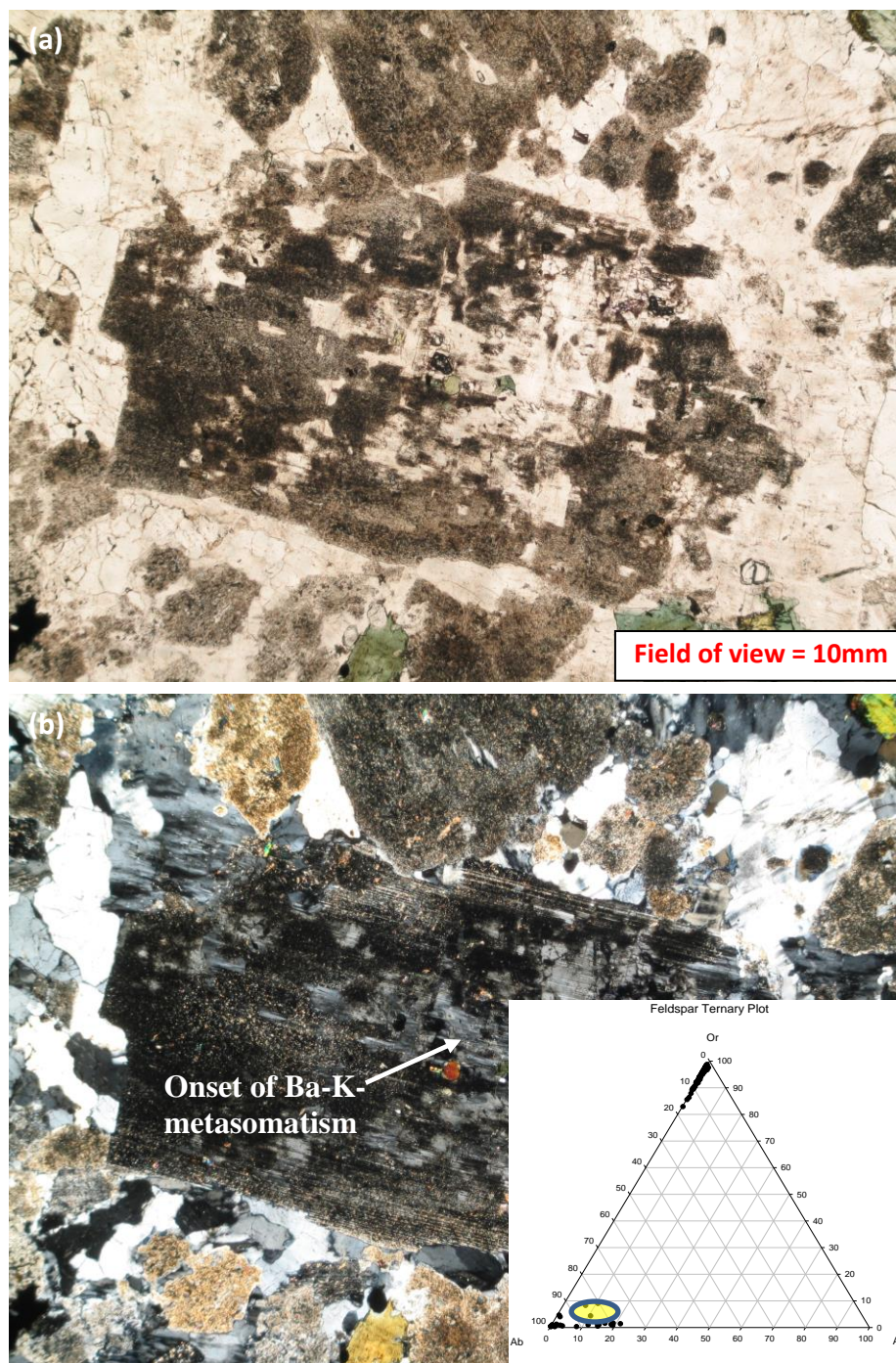


Plate 3.13a,b: Sample #ARN063-128.8m: (a) Plane light photomicrograph illustrating the early onset of the Ba-K-metasomatic event beginning with degradation of the primary plagioclase; (b) Crossed polarized image of first order grey Ba-K-feldspar within plagioclase noted as patchy replacement domains. The inset of the feldspar ternary diagram illustrates the location of the early Ba-K-feldspar mineral chemical compositions. The data points are within the circle (bottom left area of the ternary).

The concentric growth of megacrystic Ba-Kfeldspar replaces the earlier primary mafic mineralogy and retrogressive chlorite(1). As the megacrysts grow, layers of mineral inclusions, principally albite(2), biotite and chlorite(1) are oriented parallel to the Ba-Kfeldspar growth zones (Plate 3.15a-c). The albite inclusions are micron to millimeter sized and have their long axes preferentially aligned parallel to the growth zones. These features indicate the Kfeldspar megacrysts permitted mineral inclusions of albite with compositions near An1.37, to periodically attach themselves to the faces of the growing crystal. The included biotite-chlorite(1) assemblage are associated with the amphibole replacement. The cores of megacrystic Ba-Kfeldspar are dominated by albite-epidote-titanite-muscovite indicative of a relict magmatic Ca-plagioclase kernel which acted as a nucleating site for growth of alternating Ba-Kfeldspar+albite during metasomatism. The brighter oscillatory Ba-Kfeldspar bands are up to 50 microns thick and generally show a strong Ba-zonation from 1.36% at the core to 0.16% at the outermost band (Plate 3.16a). The darker albitic bands are narrow (~20 microns) and generally show a fine-grained intergrowth of Ba-Kfeldspar+albite (An0.47).

Sample DOME 1A,B well illustrates the alternating oscillatory banding with grey Ba-Kfeldspar bands and alternating darker albitic bands. Some Kfeldspar grains demonstrate a less dramatic decreasing barium content systematically outward from the core (0.67% BaO) to the outer most margin of the grain (0.29% BaO). In other cases, brighter Kfeldspar bands are up to 1.02% BaO near the core region and progress outward to more Ba-poor bands as low as 0.14% BaO. This variation in barium content indicates diminishing barium content in metasomatic fluids over the course of secondary Ba-Kfeldspar growth. There is also a late stage of microclinization which involves the replacement of Ba-Kfeldspar (Plate 3.16b). The final stage of K-metasomatism is the localized degradation of oscillatory zoned Ba-Kfeldspar to microcline(2) by late stage microclinization. Within these grains, the ghostly remnants of rhythmic oscillating growth zones are overprinted by microcline twinning. Commonly, primary oscillatory zonation is destroyed by the subsequent growth of late hydrothermal microcline characterized by cross-hatched twinning (Plate 3.17).

3.4 Main Ore Stage

The main ore stage involves a complex paragenetic sequence of white to red albite(3) replacement in zones of brittle cataclasis. These zones of disaggregation, are cemented by birefringent blue chlorite(2). The chlorite(2) cemented albitite breccia hosts hydrothermal zircon veins with associated uranium mineralization. Late Na-metasomatism and subsequent development of albite(3) is evidenced by white albite rinds on pink Ba-Kfeldspar megacrysts (Plate 3.18a). In thin section, the albite rinds on Ba-Kfeldspar display characteristic albite twinning (Plate 3.18b). This progresses towards complete red-albitization of the rocks where earlier textures are still locally preserved, however the rock is completely composed of red-albite(3). Where pervasive, the Ba-Kfeldspar and plagioclase textures have been completely replaced by red-albite(3) (Plate 3.19). The Ba-Kfeldspars megacrysts with albite(2) inclusions oriented parallel to growth faces are easily distinguishable from Ca-plagioclase phenocrysts which lack these albite(2) inclusions. The process of albitization is synchronous with early hematization where Fe^{3+} enters the albite crystal structure resulting in red albite(3). Microprobe investigations of the red albite(3) demonstrates iron contents up to 0.13 wt% FeO.

Domains of hydrothermal albitization are disaggregated, resulting in reticulate-textured cataclasite wherein blocky red albite(3) is cemented by birefringent blue chlorite(2) (Plate 3.20). This birefringent blue chlorite(2) is part of the early ore stage. It forms fibrous mats and replaces the earlier green chlorite associated with hydrothermal retrogression of amphibole-biotite assemblages (Plate 3.27). Chlorite(2) has similar aluminum and magnesium mineral chemistry as the chlorite(1) with aluminum contents between 19.20-22.49 wt% Al_2O_3 , and magnesium contents between 22.01-24.83 wt% MgO. Chlorite(1) and chlorite(2) species are chemically distinct with respect to the iron and manganese contents: chlorite(1) contains 10.29-19.07 wt% FeO and 0.22-0.50 wt% MnO compared to chlorite(2) with 13.98-16.18 wt% FeO, and 0.13-0.42 wt% MnO. The mineral chemistry of chlorite(1) and chlorite(2) can be found in Appendix A Table 4. When plotted on the chlorite classification plot of Zane et al. (1998), chlorite(2) plot within the clinochlore field indicating a lesser iron component than chlorite(1) (Figure 3.3).

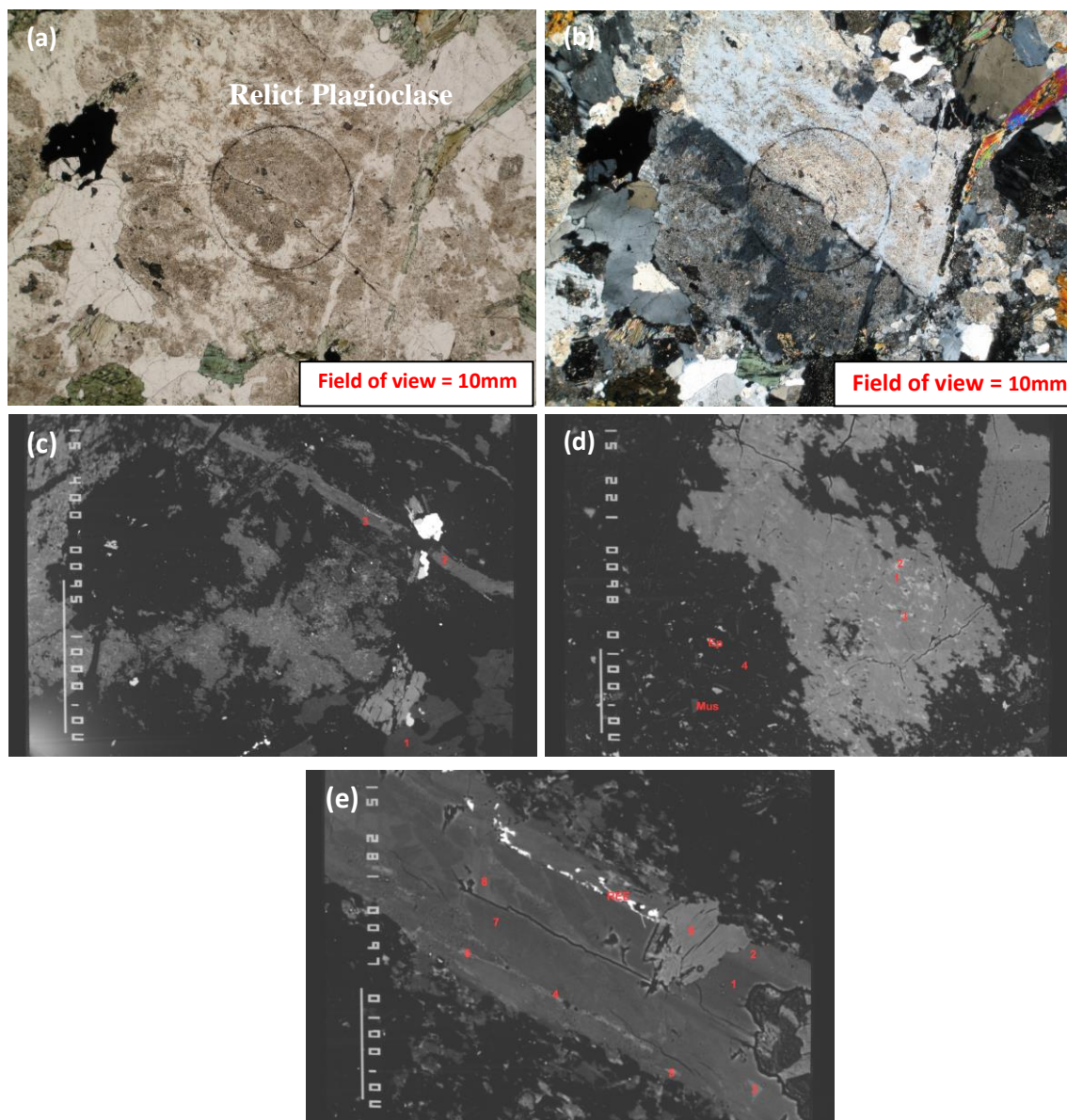


Plate 3.14a-e: Sample #ARN053-108.5b: (a) Plane light image showing a veinlet of Ba-K-rich fluids infiltrating a primary plagioclase and converting it to Ba-Kfeldspar; (b) Crossed polarized image illustrating the relict plagioclase twin with white mica and albite development at the center of the grain and Ba-Kfeldspar growth; (c) Backscatter image of plagioclase grain cut by Ba-Kfeldspar vein and development of Ba-Kfeldspar interior to the plagioclase (see feldspar analyses 113-115); (d) Ba-Kfeldspar domain interior to plagioclase illustrating dark and bright Ba-zones of up to 7.27% BaO (see feldspar analyses 124-128); (e) Dark domains of Ba-poor and bright domains of Ba-rich feldspar. Bright white linear zone of REE development parallel to the bright Ba-rich zone. See feldspar analyses 116-123, mica analysis 6 (low Ti-mica).

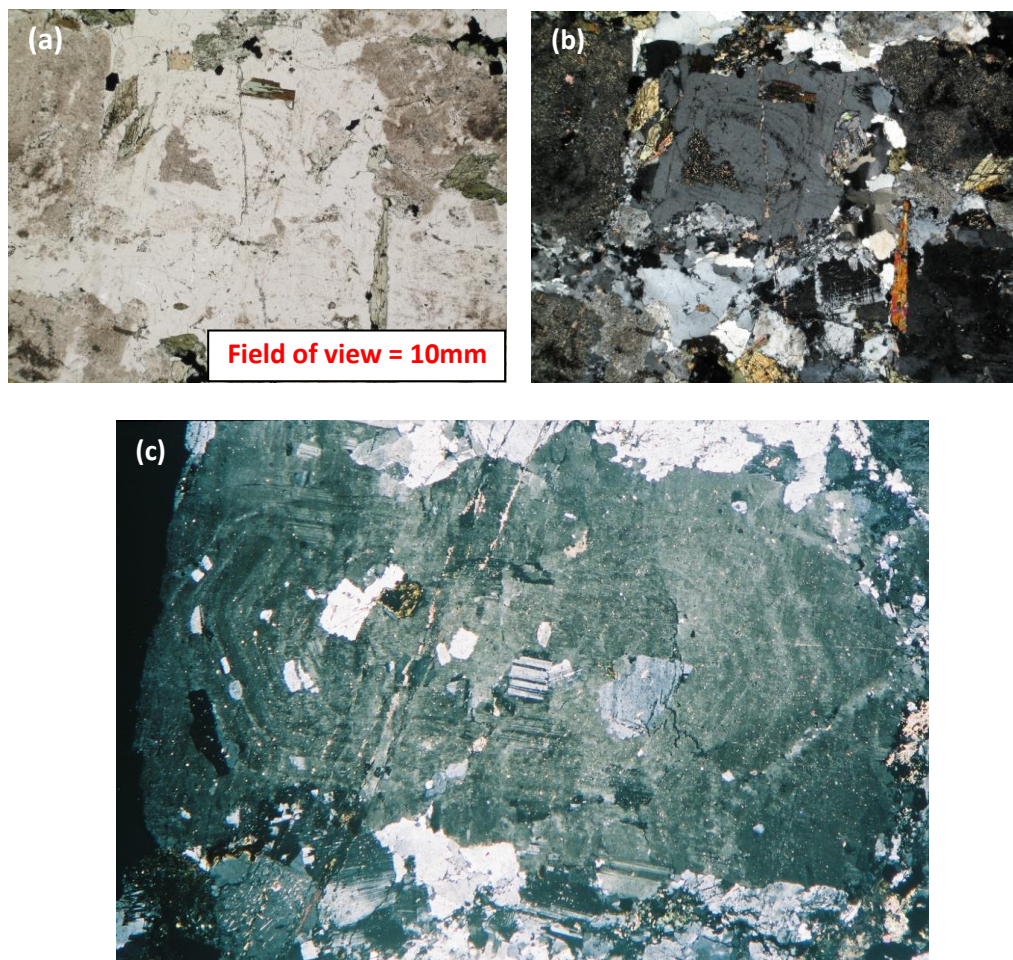


Plate 3.15a-c: Sample #ANC011-120m: (a) Plane light image illustrating inclusions attaching to the growth faces of the evolving Ba-Kfeldspar. The biotite and chlorite(1) inclusions have been incorporated from the matrix material; (b) Crossed polarized image illustrating the highly birefringent biotite laths and darker chlorite(1) laths included within developing Ba-Kfeldspar growth zones; (c) Crossed polarized light image illustrating biotite and chlorite(1) inclusions incorporated from the groundmass whereas the albite(2) inclusions have grown in situ. The feldspar ternary inset illustrates the composition of the albite(2) inclusions within the growing Ba-Kfeldspar megacrysts. Albite(2) data points are within the circle at the albite (Ab) apex of the ternary.

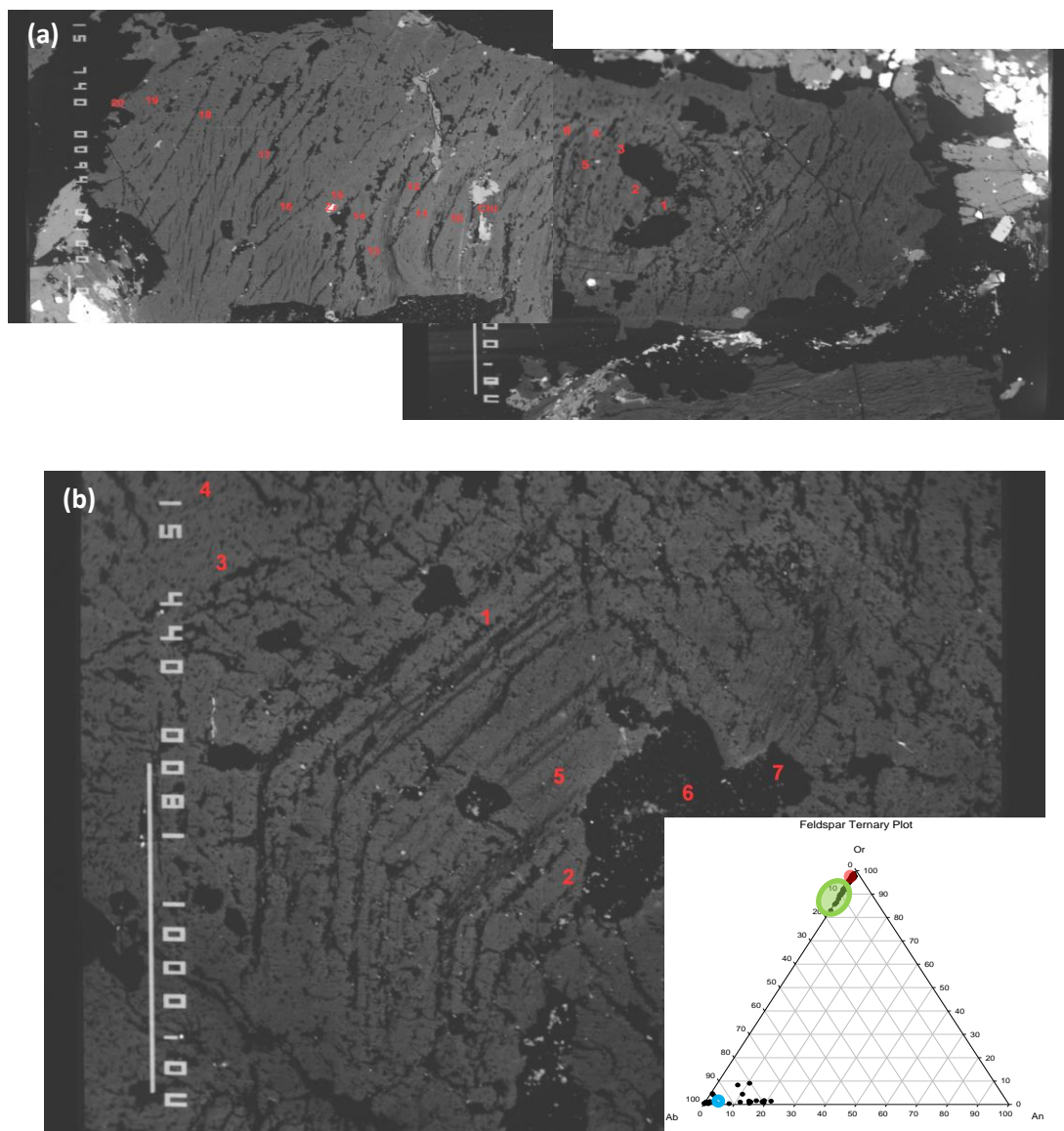


Plate 3.16a,b: Sample #DOME 1b: (a) Merged backscatter images illustrating the concentric zoning of the Ba-Kfeldspars (see feldspar analyses 93-112); (b) Oscillatory zoned feldspar with albite+epidote in core, grey bands of Ba-Kfeldspar, and darker bands of albite (see Appendix A Table 5 analyses 55-64; red numbers correspond to analytical locations). The 100 micron scale bar is located along the left margin of all images. The inset ternary diagram shows a green circle representing the Ba-Kfeldspar core compositions. The red circle nearest the “Or” apex represents Ba-Kfeldspar marginal compositions where all Na has been partitioned out of the megacryst. The blue circle near the “Ab” apex represents the alternating albite growth zones.

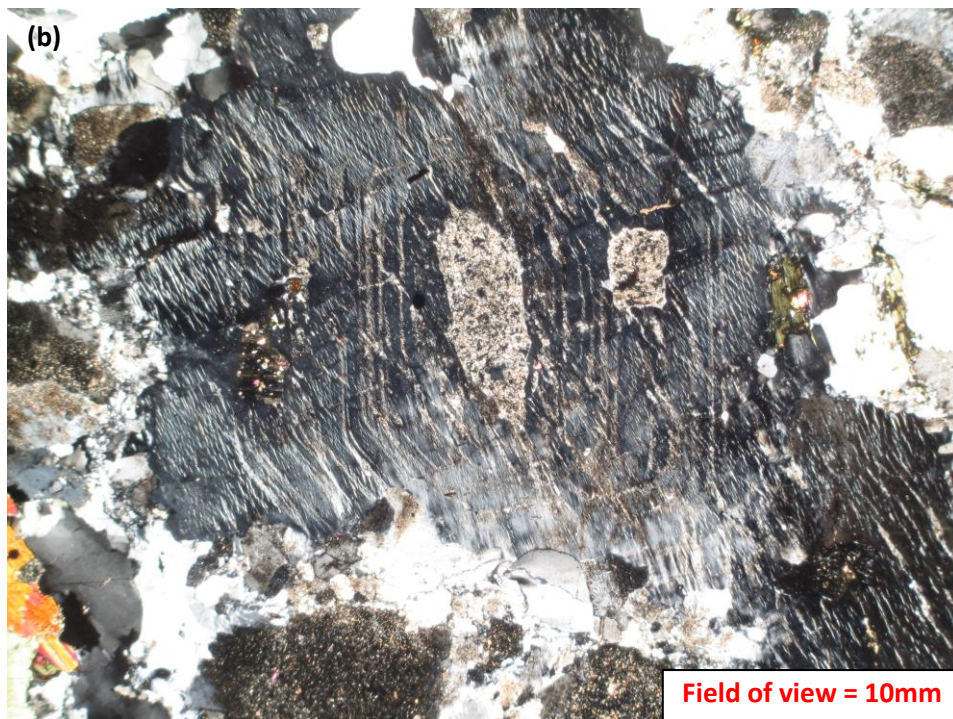
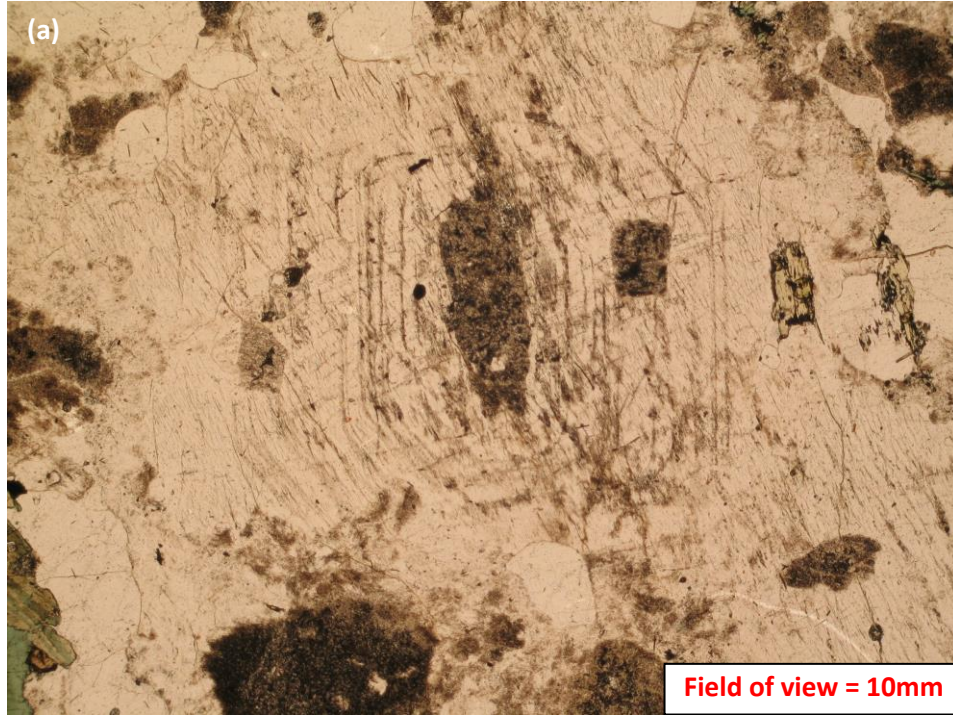


Plate 3.17a,b: Sample #DOME 3: (a)Plane light image of oscillatory zoning of Ba-Kfeldspar obliterated by late hydrothermal microcline evidenced by cross-hatched twinning. Note relict nucleating kernel of primary plagioclase at the center of the grain now albite+epidote; (b) Crossed polarized image defining outlines of relict growth zones and the pervasive microcline(2) twinning.

3.4.1 Main Ore Stage: Calcite, Zircon Veining and Uranium:

The main ore stage is characterized by development of coarse-grained calcite occurring in association with uranium and zircon mineralization. Zircon veins are quite prevalent throughout the mineralized zones. Zircon veinlets are 50-400 microns wide and tend to host the majority of the U-bearing minerals (Plate 3.22a,b). The central part of the zircon veinlets contains zircon+carbonate+hematite+uraninite, coffinite, and brannerite. The margins of the veinlets are commonly comprised of chlorite(2)+calcite+epidote intergrown with uraninite, coffinite, and brannerite. Backscatter imaging of the hydrothermal zircon veins reveals a heterogeneous compositional variation evident by domains of dark, intermediate and bright zones representing the variations in U content within the zircon structure. The dark, intermediate, and bright zones were analyzed by electron microprobe and compositions detailed in Appendix A Table 7. The totals below 100% may reflect hydration/alteration of the zircon and/or the absence of REE's in the analytical schedule.

Electron microprobe analysis reveals compositionally domainal populations of hydrothermal zircon represented by bright, intermediate, and dark domains (Appendix A Table 7). The brightest domains contain up to 5.83% UO₂, intermediate domains 2.01% UO₂, and dark domains 0.79% (Plate 3.23a). The areas from brightest to darkest also show tendencies towards increasing iron, calcium, and decreasing lead. The veined U-bearing zircon is a uranoan-zircon species. These domains represent the changing chemistry of the evolving hydrothermal solution during uranium mineralization.

Within breccia zones, the albitite(3) cataclasite becomes progressively and pervasively reddened due to insipient hematization. The cataclastic red albitite(3) texture is sealed by orange-brown hydrothermal zircon (Plate 3.22a). The ramifying hydrothermal zircon veins sealing larger red albitite(3) breccia fragments form a zircon microbreccia (Plate 3.22b). Zircon can be abundant accounting for up to 80% of the microbreccia rock volume.

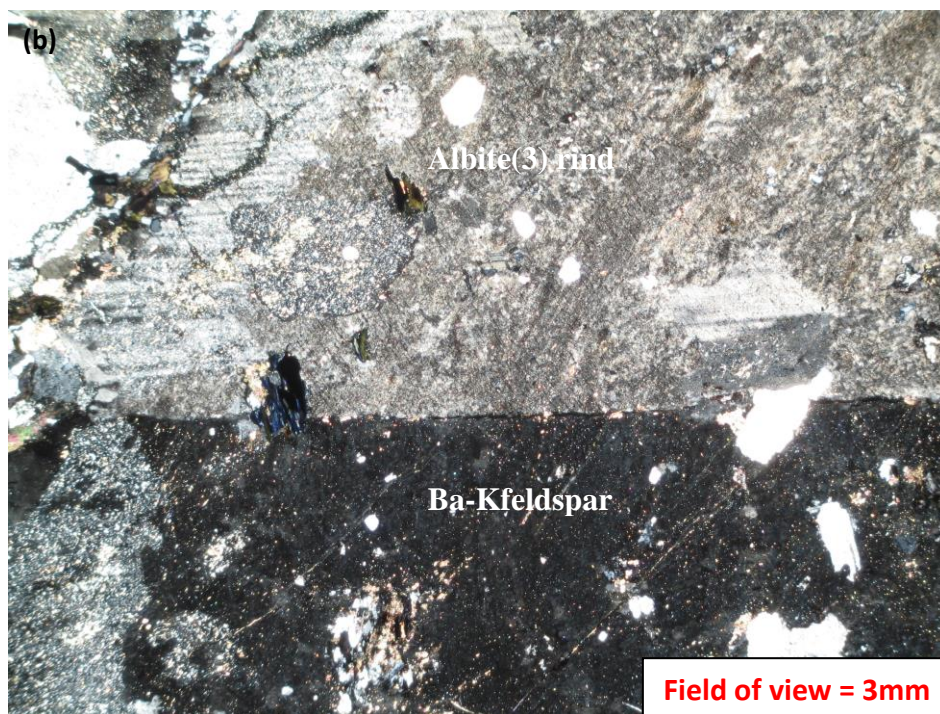


Plate 3.18a,b: Sample #ARS090-209.2m: (a) A section of drill core illustrating the white albite rinds on pink Ba-Kfeldspar, an effect of Na-metasomatism following Ba-K-metasomatism; (b) Crossed polarized photomicrograph of albite rind on secondary Ba-Kfeldspar.

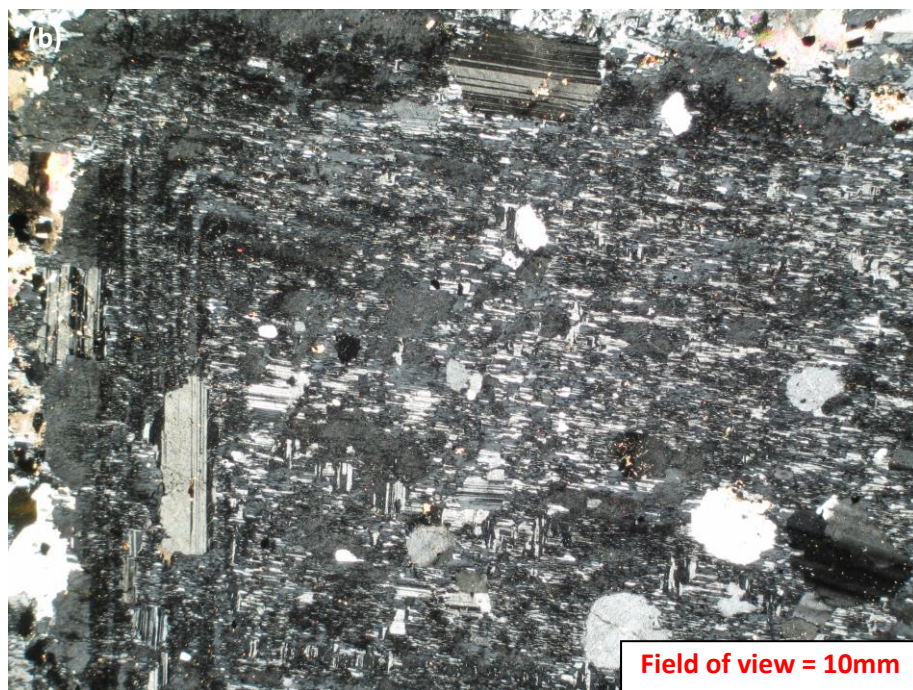


Plate 3.19a,b: Sample #ARS090-209.25: (a) Plane light image illustrating pervasive albitization of a Ba-Kfeldspar megacryst with albite inclusions, however, initial texture still preserved; (b) Crossed polarized image illustrating the pervasive first-order grey albitization of the Ba-Kfeldspar megacryst.



Plate 3.20: Reticulate texture cataclasite where hematite-stained “red” albite is sealed by birefringent blue chlorite(2) as illustrated in Plate 3.21.

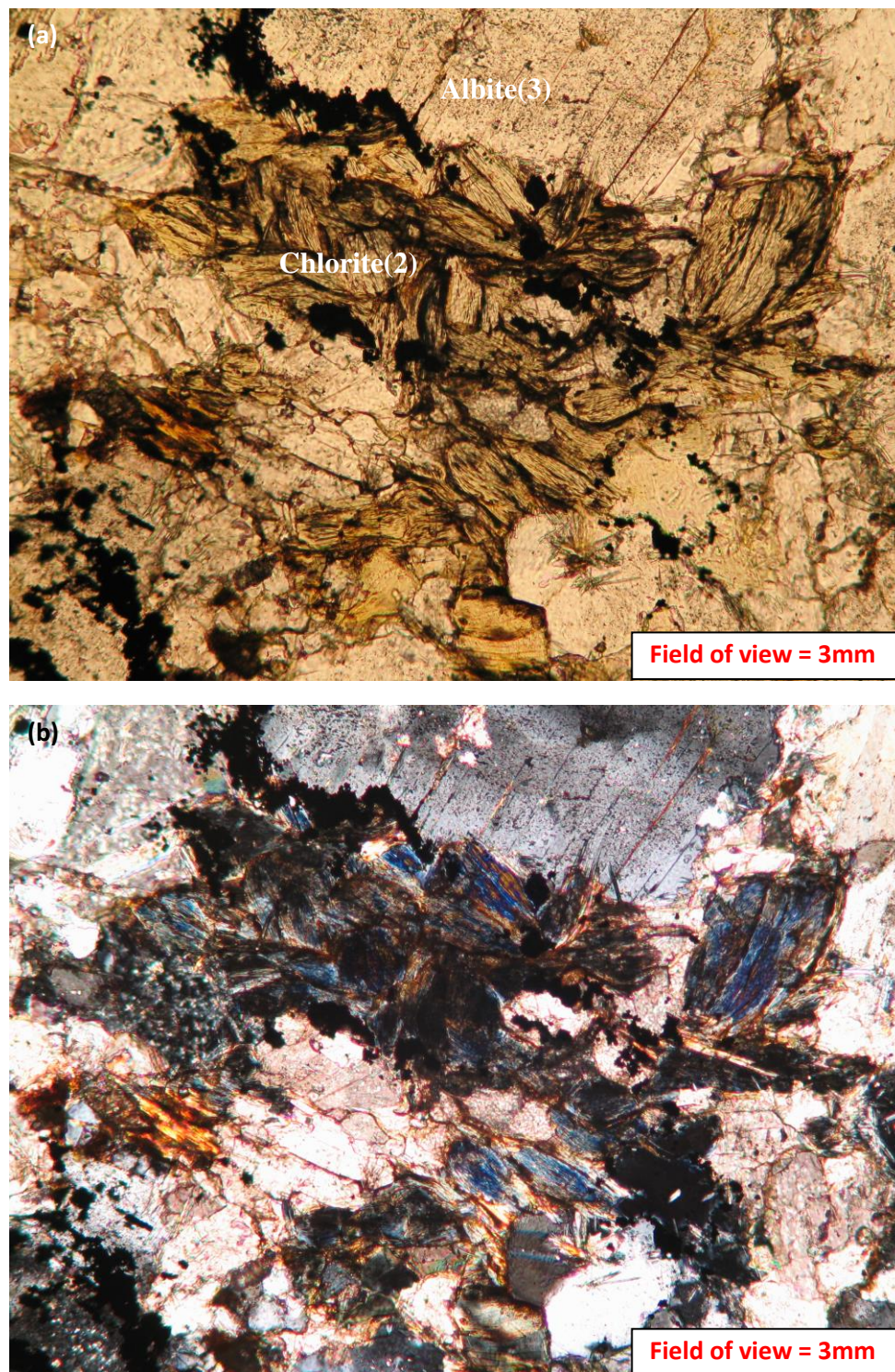


Plate 3.21a,b: Sample #ARS029-90m: (a) Plane light image depicting replacement of green chlorite(1) by birefringent blue chlorite(2) interstitial to and sealing albite cataclasite; (b) Crossed polarized image illustrating birefringent blue chlorite(2) interstitial to first-order grey albite fragments.

A second textural variety of zircon is quite common in areas of strong albitization. It appears that the zircon granules associated with the crystallization of the Kurupung batholith have outer margins characterized by pitted domains which suggest resorption of pre-existing zircon granules by hydrothermal fluids (Plate 3.24). These outer pitted domains commonly have fine-grained inclusions of monazite. Although these granules are lower in uranium than the hydrothermal zircon veins, they still have an appreciable content of uranium. Mineral chemical analysis of these early zircons illustrates an increase in uranium content from 0.10 wt% UO_2 at the core to 0.64 wt% UO_2 at the pitted margin. This implies a diffusion of uranium from the core to the pitted margin during hydrothermal alteration. The porous margins reflect resorption associated with hydrothermal fluids whereby uranium was sequestered from zircon margins and partitioned into the fluid phase.

3.4.2 Main Ore Stage - Uranium Minerals:

The uranium mineralization associated with the main ore stage is commonly hosted within zones of red-albite(3) cataclasite sealed by chlorite(2) and within hydrothermal zircon veins and microbreccia. The analyses of the common U-minerals found during the course of the investigation are displayed in Appendix A Table 7.

In plane light, the uranium minerals occur as yellow-brown and red-brown minerals occurring within zircon veins (Plate 3.25a) closely associated with the late hematite-chlorite(2)-albite(3)-apatite(2) alteration. The grain size of the U-minerals range from 2 to 20 microns. The U-minerals are a combination of uraninite (UO_2), coffinite ($\text{U}(\text{SiO}_4)_{1-x}(\text{OH})_{4x}$), brannerite ($(\text{U,Ca,Y,F,Ce})(\text{Ti,Fe})_2\text{O}_6$), U-silicates and U-oxides, some of which are difficult to classify as they don't stoichiometrically match compositions detailed in the literature. Albite(3) microfractures filled with altered Si-Ca-bearing uraninite were observed in one particular section (Plate 3.25b). Occasional coarse-grained patches of a Th-rich mineral identified as either thorite or ekanite occurs within the Zr-veins (Plate 3.26a). Locally, there are grains of coffinite, brannerite, and Pb-U-Si and Ti-U-Pb minerals which infill microfractures interior to albite grains (Plate 3.26b).

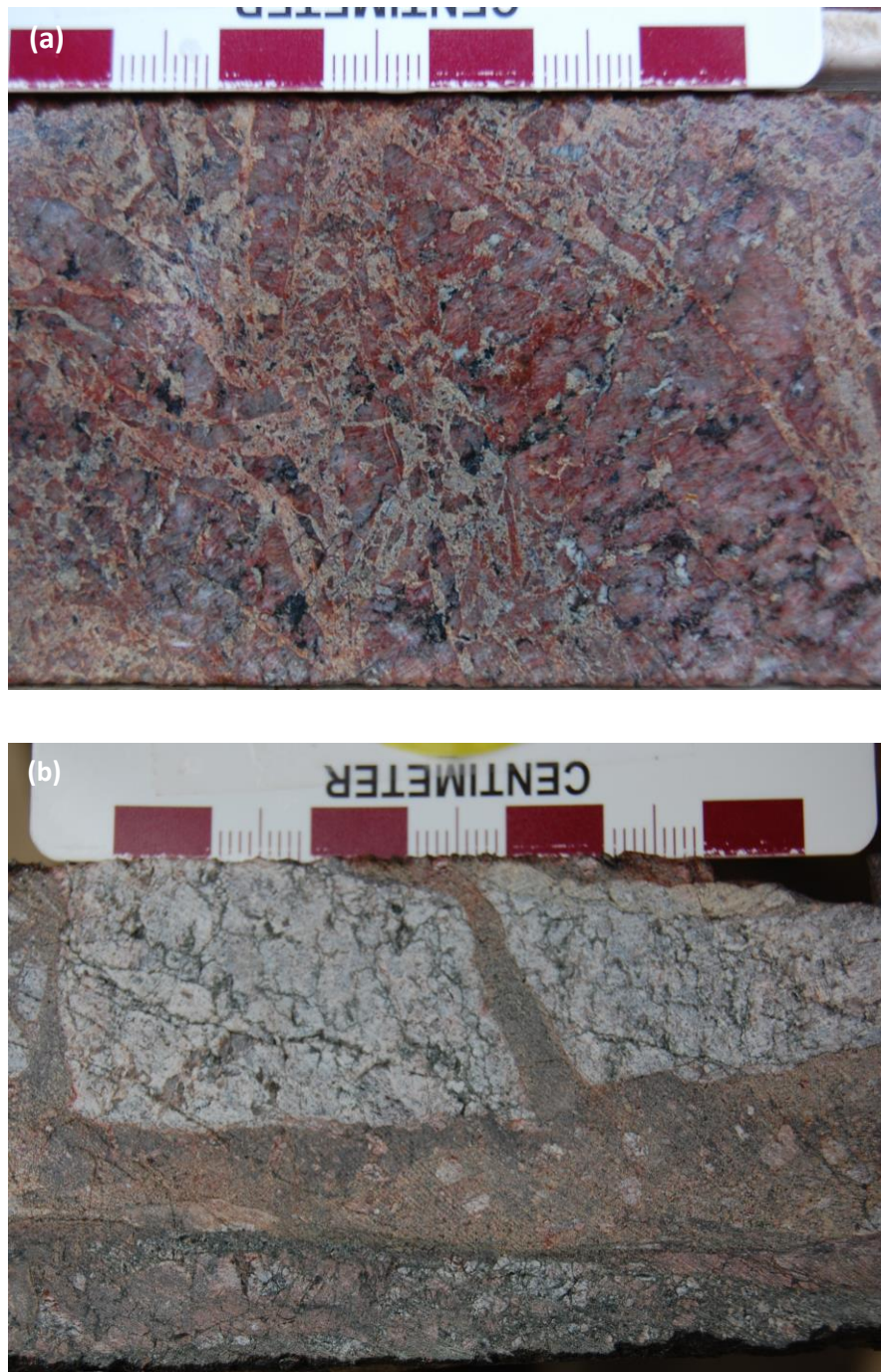


Plate 3.22a,b: (a) A section of drill core representing zircon microbreccia with blocky red cataclasite sealed by orange-brown zircon (Sample #ARN003-98.5m); (b) A section of drill core illustrating zircon breccia where brecciated fragments of cataclasite material is sealed by zircon (Sample #ARS043-146m).

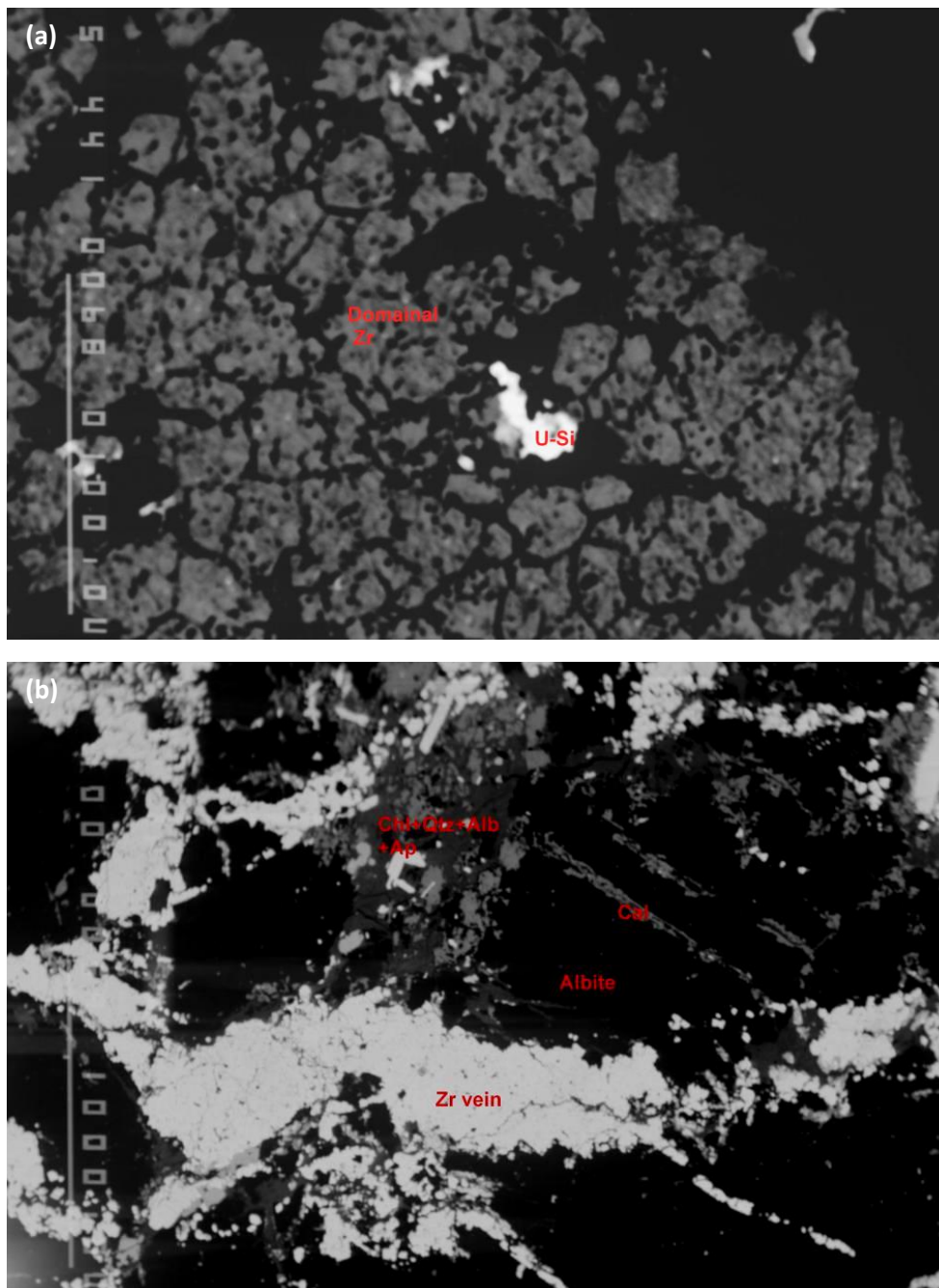


Plate 3.23a,b: Sample #ARS043-146m: (a) Backscatter image of a zircon vein demonstrating the compositional variation of the zircon with darker (low U) domains and brighter (high U) domains. The veins are host to a variety of U-bearing minerals including uraninite, coffinite and brannerite; (b) Backscatter image illustrating the ramifying zircon veining (Chl = chlorite(2); Qtz = quartz; Alb = albite(3); Ap = apatite; Zr = zircon; Cal = calcite). Scale bars are located along the left margin of each image.

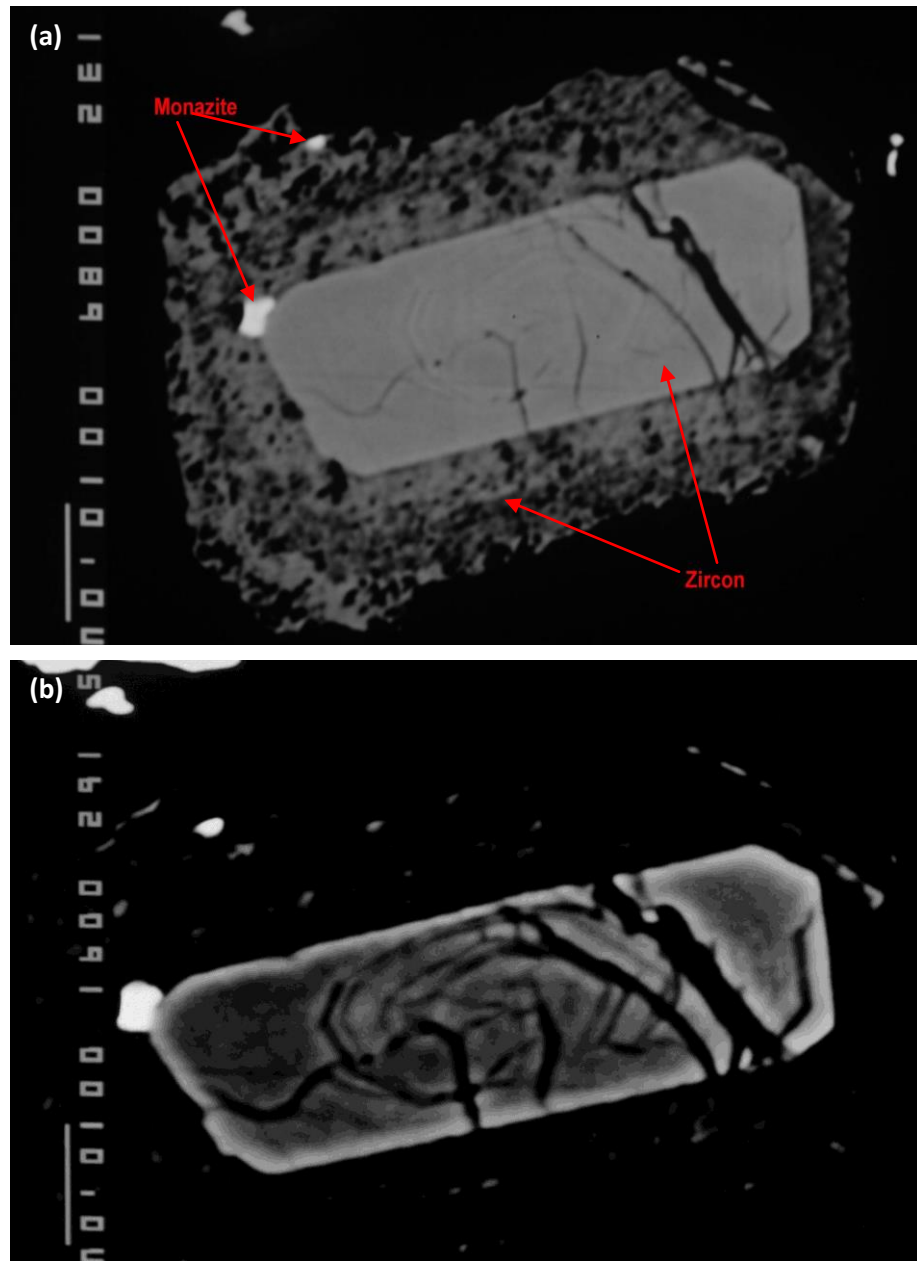


Plate 3.24a,b: Sample #ARN063-113.4m: (a) Backscatter electron image illustrating a zircon grain with quite well-defined crystal outline. The porous outer margin contains less uranium than the core and reflects resorption associated with hydrothermal fluids; (b) A less bright image of (a) illustrating the complex internal zoning of the zircon. The 10 micron scale bar is located on the left margin of both images.

These same mineral species also grow intimately along grain margins of rutile and intergrown with calcite. Hematite commonly contains inclusions of brannerite (up to 20 microns) (Plate 3.26b). A compositionally domainal U-Zr-rich mineral intergrown with apatite was noted in two sections (Plate 3.27). These grains generally reside within zones of albitite(3) outside of the zircon veins. This U-Zr mineral has not yet been identified in the literature and requires further investigation.

3.5 IOCG-style Mineralization at Aricheng

Four segments of drill core hosting copper mineralization from the Aricheng West uranium prospect were investigated petrographically to document IOCG-style mineralization (ARW075-121.1m; ARW075-120.20m; ARW028-207m; ARW054-85.4m). The main purpose is to investigate the sulphide mineral textures and relationships associated with IOCG-style alteration. The sulphide mineralization occurs within anastomosing fractures and veins within albitite host rock consisting of albite(3) + chlorite(2) + epidote + titanite + rutile + calcite. The copper sulphide assemblages occur intergrown with blue-green chlorite(2) which form coarse feathery mats commonly intergrown with fine-grained highly birefringent epidote (Plate 3.28). Magnetite and hematite are commonly present. According to Corriveau and Mumin (2010), common zoning assemblages in IOCG deposits include a chalcopyrite-magnetite association, attributed to an early/deep reducing environment while the bornite + Ag-telluride + galena + hematite associations are indicative of late/shallow oxidative conditions. At Aricheng, the early potassium-magnetite association is linked to an early/deep reducing IOCG setting (Plate 3.29) while the bornite-hematite assemblage is linked to late/shallow oxidative red albitite(3) U-enriched domains, indicative of a shallow oxidative IOCG setting (Plates 3.30, 3.31, and 3.32). The metallic species include bornite (Cu_5FeS_4), chalcopyrite (CuFeS_2), pyrite (FeS_2), galena (PbS), Se-bearing galena, chalcocite (Cu_2S), Ag-telluride, greenockite (CdS), thorite (ThSiO_4), monazite ($(\text{Ce,La,Nd,Th})\text{PO}_4$), hessite (Ag_2Te) and altaite (PbTe).

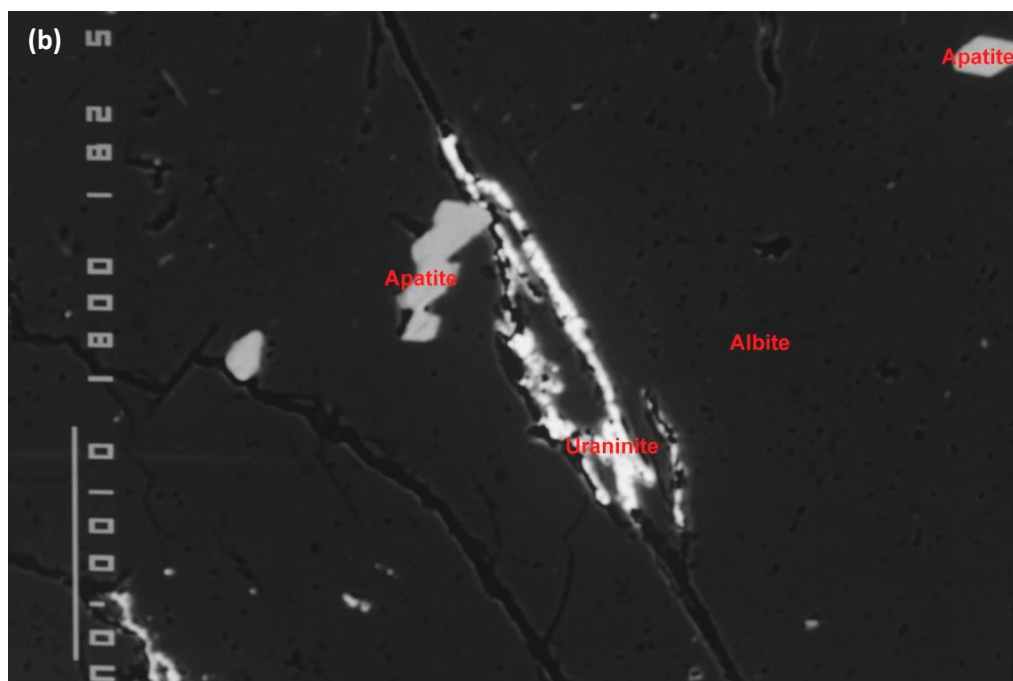
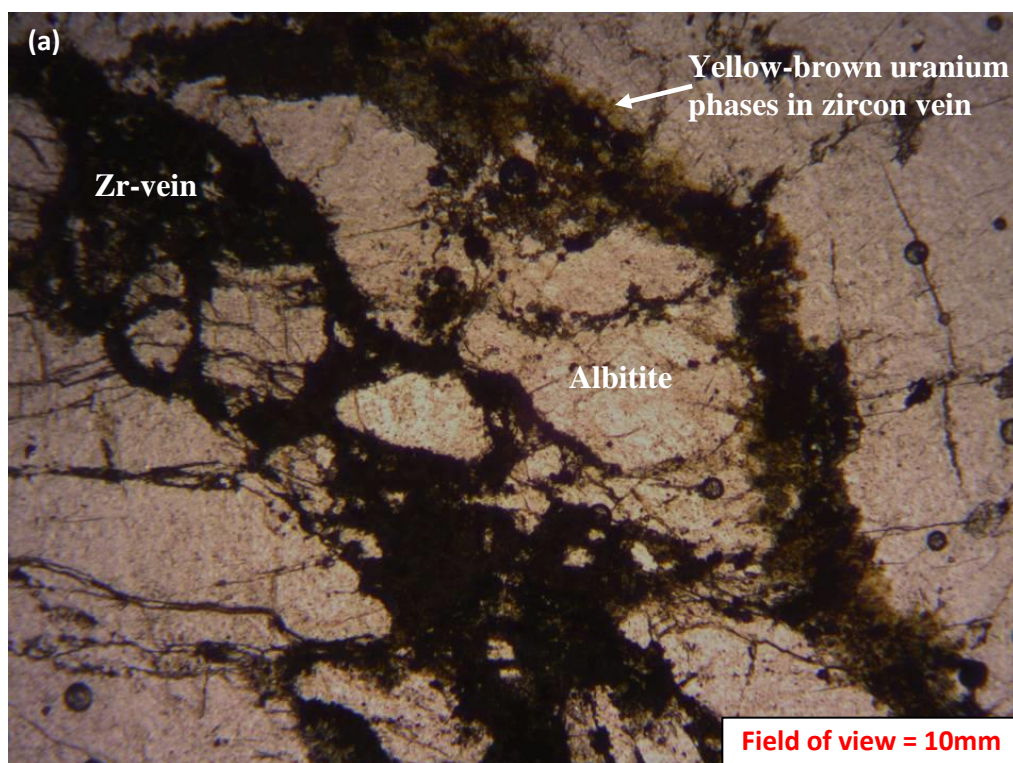


Plate 3.25a,b: Sample #ARS090-209.25m: (a) Plane light image illustrating zircon veins forming a zircon microbreccia and yellow-brown uranium phases intergrown with zircon veins; (b) Backscatter image of altered uraninite filling a fracture in albite. The 100 micron scale bar is located along the left margin.

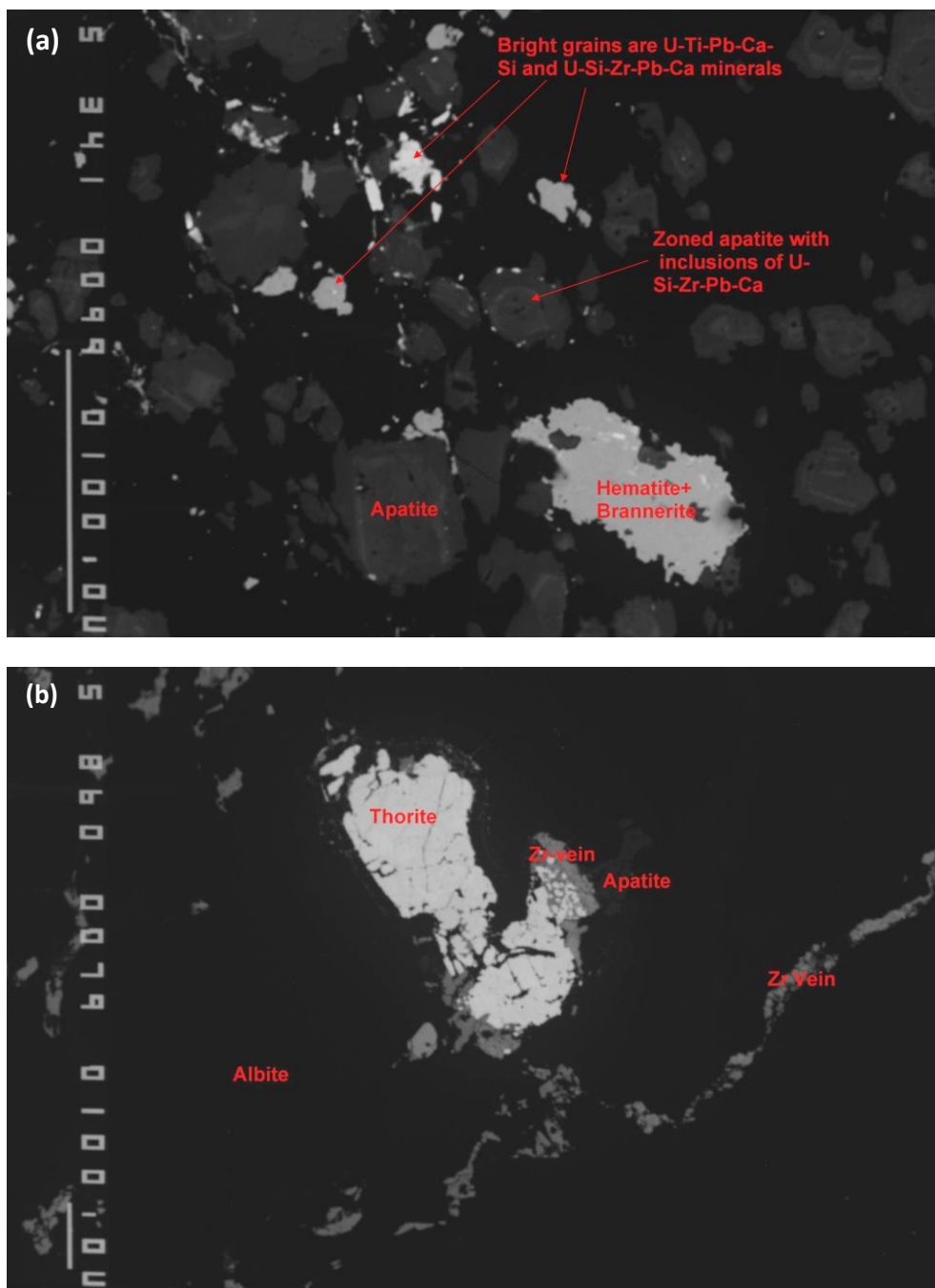


Plate 3.26a,b: Sample #ARN031-98.5m: (a) Backscatter image of a Th-rich grain, potentially thorite/ekranite with 55.31wt% ThO₂ associated with the hydrothermal zircon veins. See Appendix A Table 5 analyses 6 and 7; (b) Backscatter image of U-bearing minerals included within the albite(3) groundmass, intergrown with zoned apatite, and intergrown with hematite. The 100 micron scale bar is located along the left margin of each image.

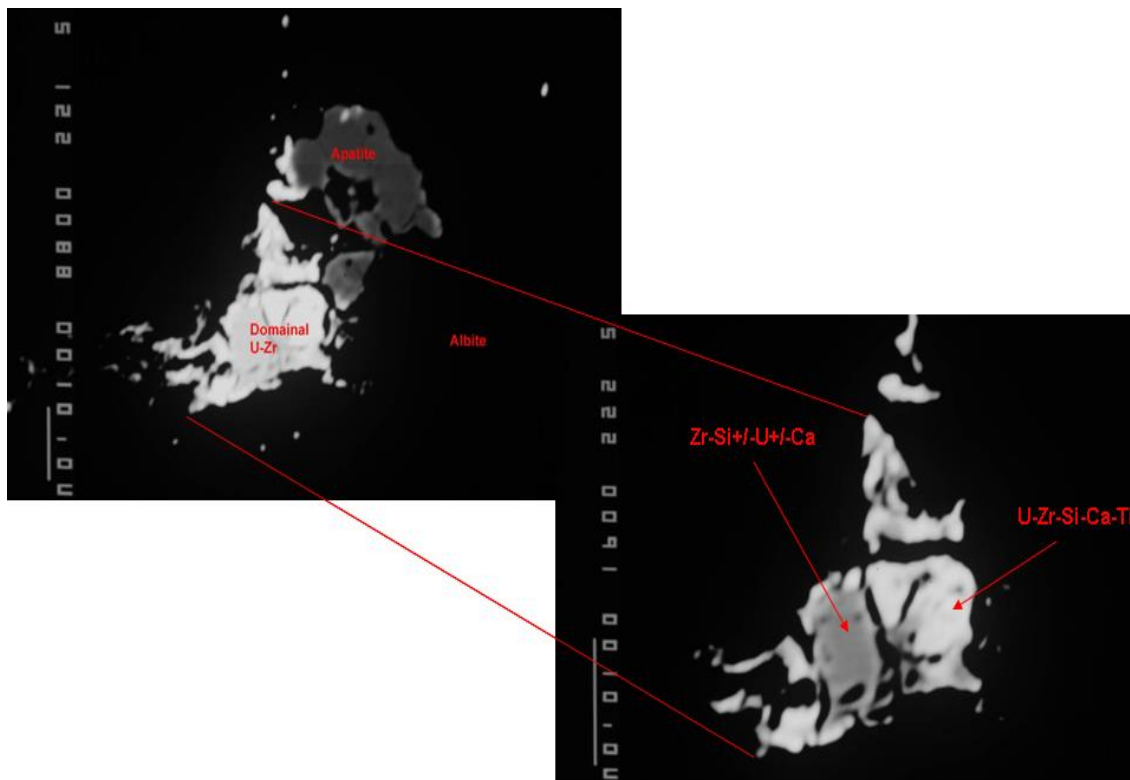


Plate 3.27: Sample #ARS043-146m: Backscatter images showing a zircon with compositional variation evident by dark Zr-Si+/-U+/-Ca and brighter domains of U-Zr-Si-Ca-Ti. These grains tend to be discrete domains outside the zircon veins within zones of intense albitite(3). The 10 micron scale bar is located along the left margin of each image.

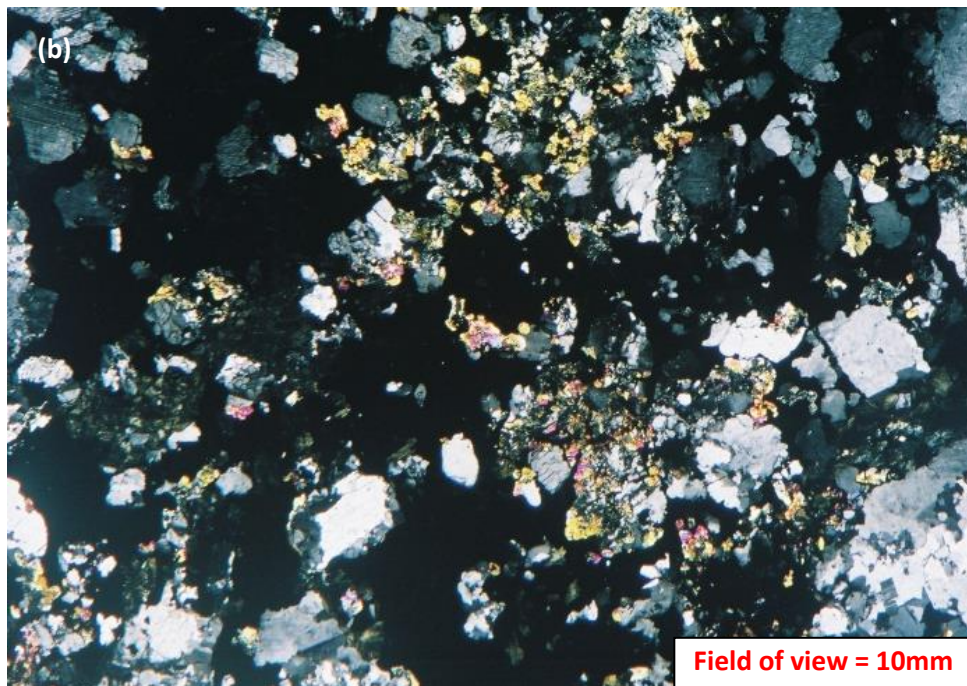
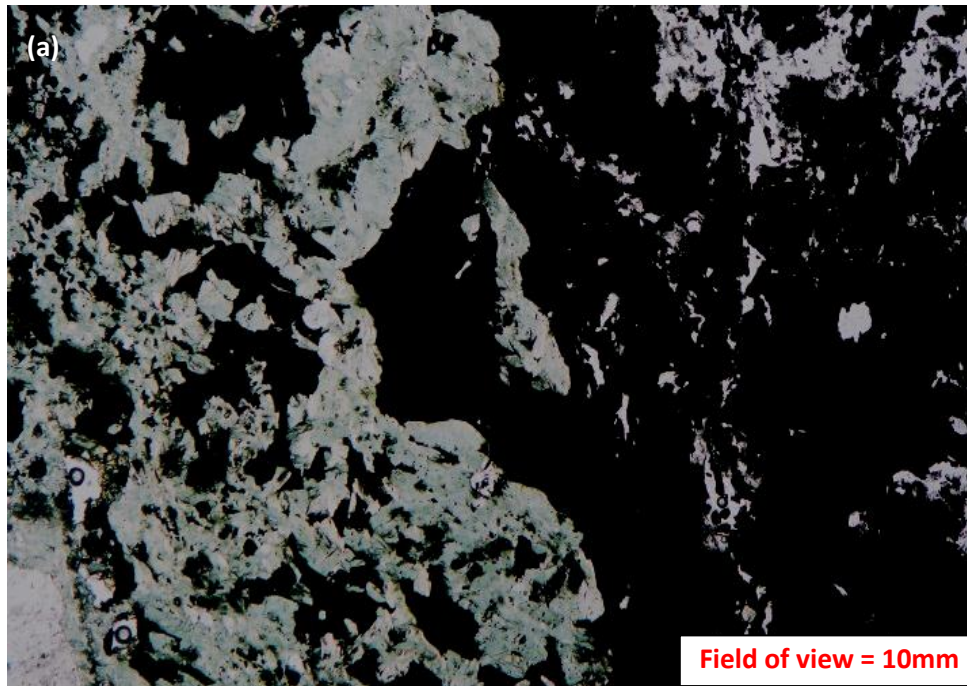


Plate 3.28a,b: Sample ARW075-121.1m: (a) Plane light image illustrating the blue-green chlorite(2) and albite(3) intergrown with sulphides; (b) Crossed polarized image showing birefringent blue chlorite(2) intergrown with highly birefringent epidote and associated opaque areas of sulphides.

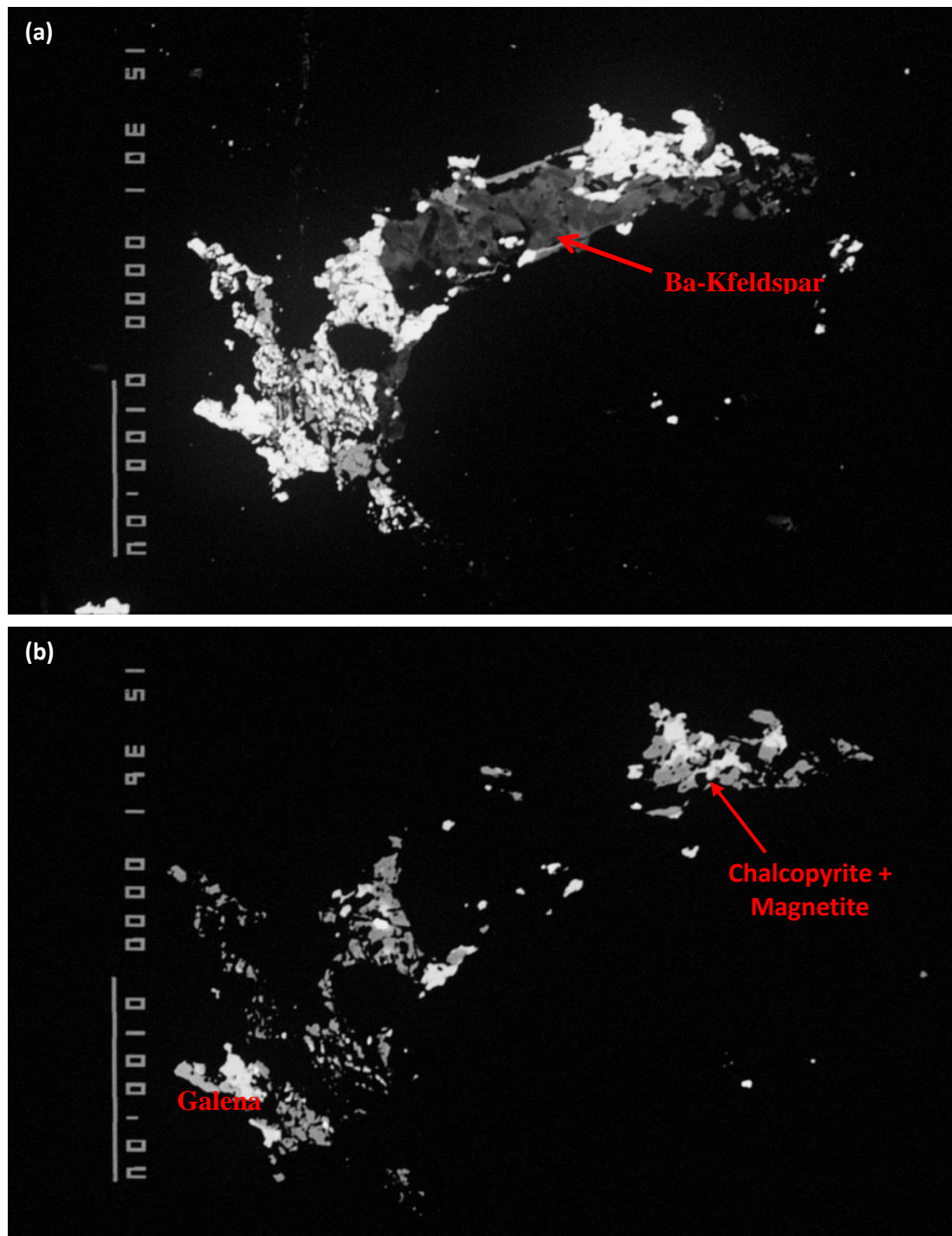


Plate 3.29a,b: Sample # ARW075-120.20m: (a) Backscatter image illustrating a genetic relationship between Ba-Kfeldspar and chalcopyrite-magnetite; (b) Backscatter image of the same field of view as (a) with the brightness intensity reduced to illustrate the sulphide population. This texture is quite interesting as it displays mineralogical characteristics associated with IOCG-type deposits including the deep/early K-metasomatism associated with Cu-mineralization and magnetite. The 100 micron scale bar is located on the left margin of each image.

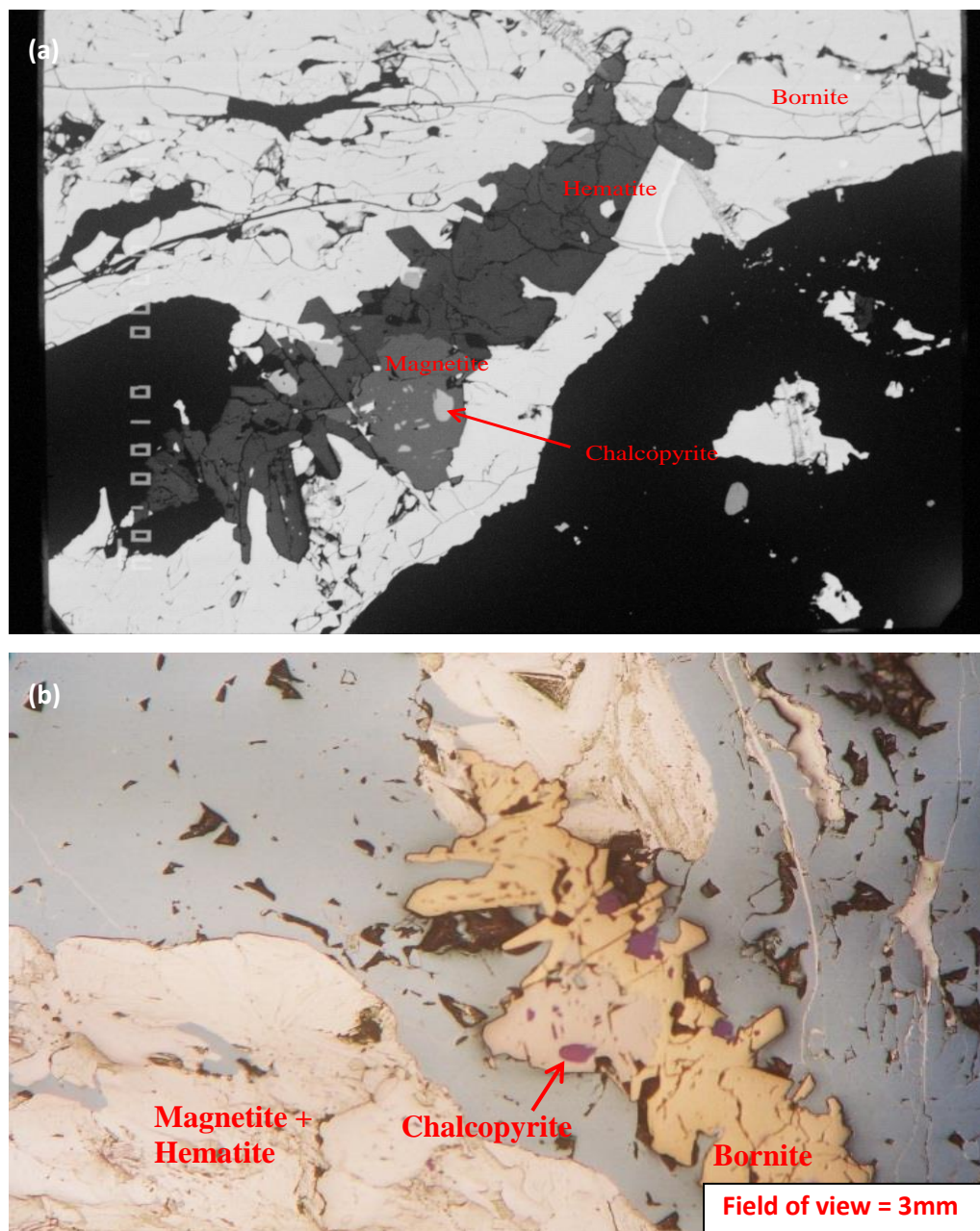


Plate 3.30a,b: Sample # ARW028-207m: (a) Backscatter image illustrating the deep/early chalcopyrite-magnetite association and the late/shallow hematite-bornite association. The 100 micron scale bar is located along the left margin of the image; (b) Reflected light photomicrograph illustrating the oxidation of magnetite to hematite and the development of coarse domains of bornite with inclusions of chalcopyrite.

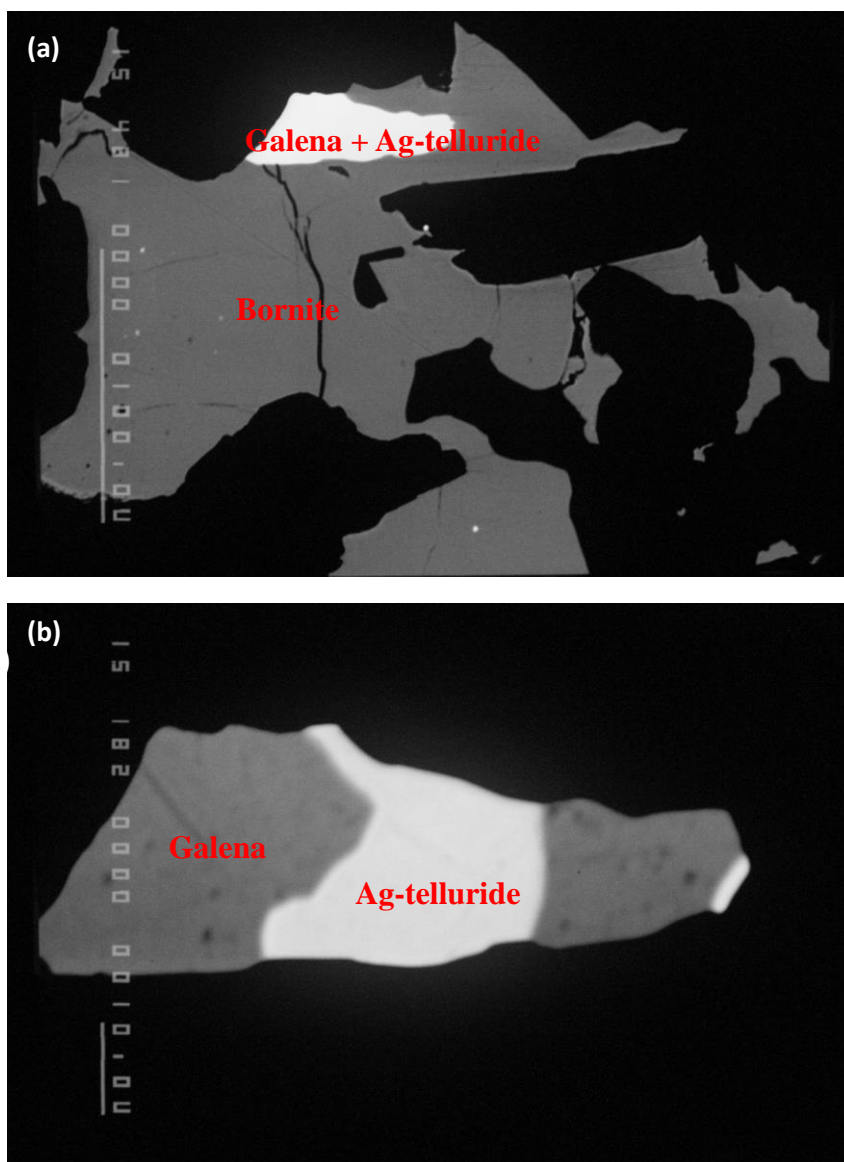


Plate 3.31a,b: ARW028-207m: (a) Backscatter image illustrating an included grain of galena intergrown with Ag-telluride hosted in bornite; (b) backscatter image of (a) with brightness intensity reduced to illustrate the two sulphide domains. Plate 3.32a,b: Sample # ARW054-85.4m: (a) Backscatter image illustrating the albite(3), chlorite(2), and bornite association. Note the bornite development along cleavage planes in chlorite(2). (b) Backscatter image showing the intergrowth of bornite with Se-bearing galena. The 100 micron scale bar is located along the left margin of each image.

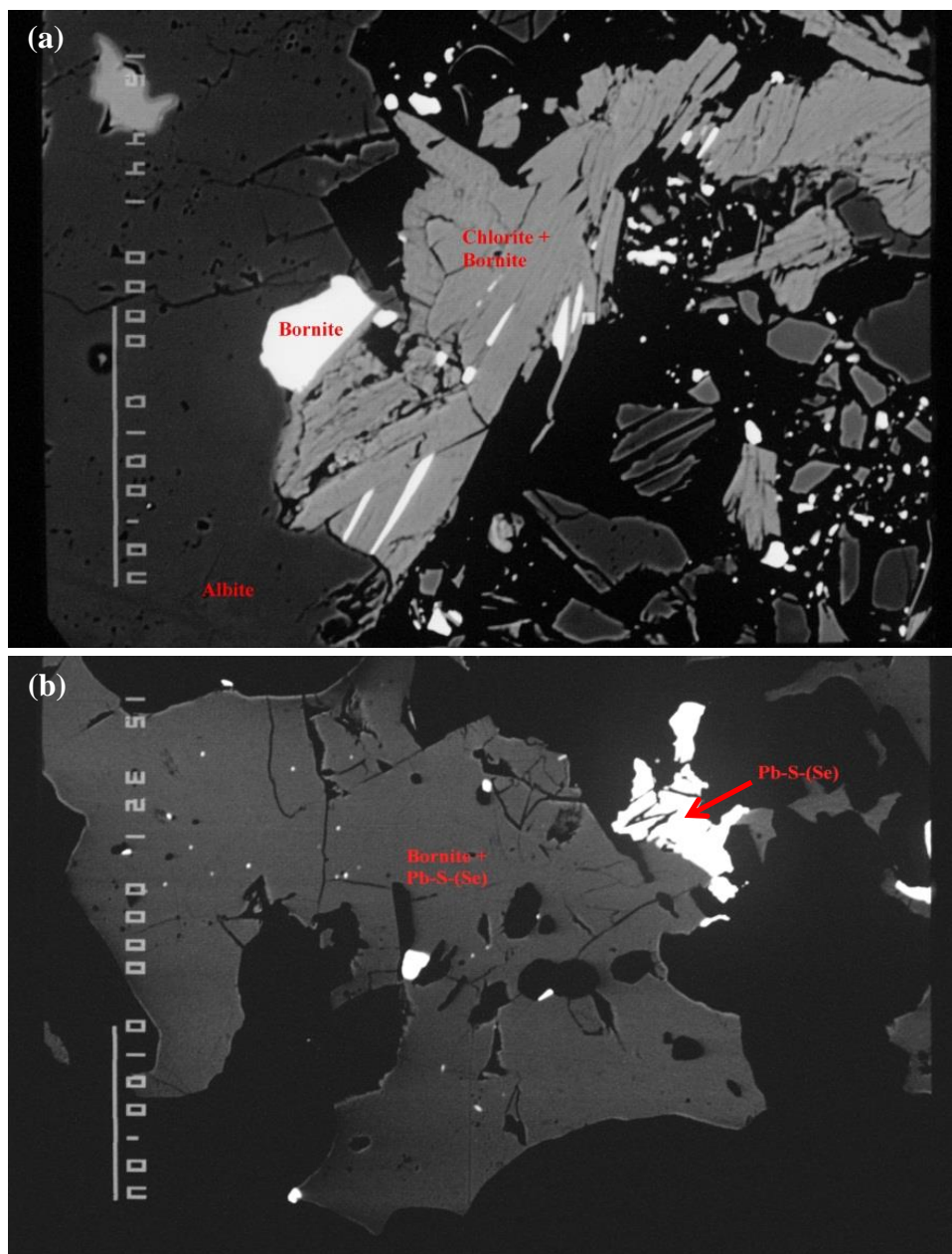


Plate 3.32a,b: (a) Backscatter image illustrating the albite(3), chlorite(2), and bornite association. Note the bornite development along cleavage planes in chlorite(2). (b) Backscatter image showing the intergrowth of bornite with Se-bearing galena. The 100 micron scale bar is located along the left margin of each image.

3.6 Avanavero Dikes

A suite of rocks were chosen from Cow Landing as representative samples of the late Avanavero dike swarm. These dikes are non-foliated and all have a well preserved primary igneous texture with minor retrogression. The Avanavero diabase dikes are characterized by coarse-grained interior domains and fine-grained chill margins (Plates 3.50 and 3.51). The coarse interiors to these diabases have low magnetism whereas the aphanitic margins are highly magnetic. Samples are coarse-grained and subophitic. Thin section investigation reveals a primary texture consisting of labradorite, clinopyroxene, primary igneous amphibole, and Ti-magnetite (Plate 3.33). Clinopyroxenes can be easily recognized in crossed-polarized light by second order interference colours. Secondary mineral assemblages include retrogressive amphibole, chlorite, albite, epidote, Kfeldspar, and ilmenite (Plate 3.34a). Coarse domains of euhedral Fe-Ti oxide occur within chill margins. Retrogression has caused exsolution of ilmenite needles within bright coarse-grained Ti-magnetite (Plate 3.34b). There is trace chalcopyrite disseminated throughout the rocks.

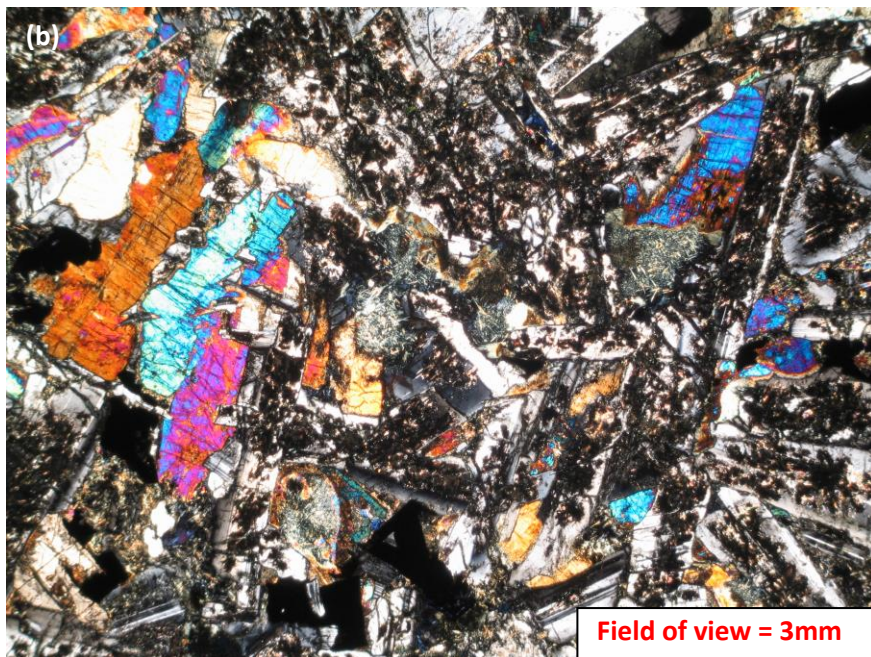
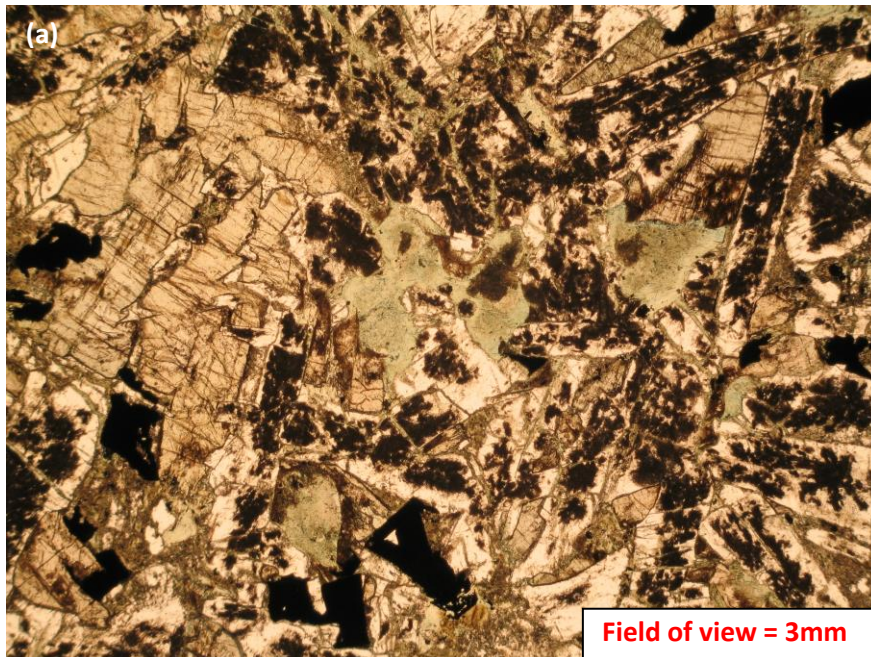


Plate 3.33a,b: Sample # RP11: (a) Plane light image of the coarse-grained interior of late Avanavero diabase dikes; (b) Crossed polarized light image of coarse-grained highly birefringent clinopyroxene intergrown with amphibole, chlorite, plagioclase, quartz, and minor magnetite.

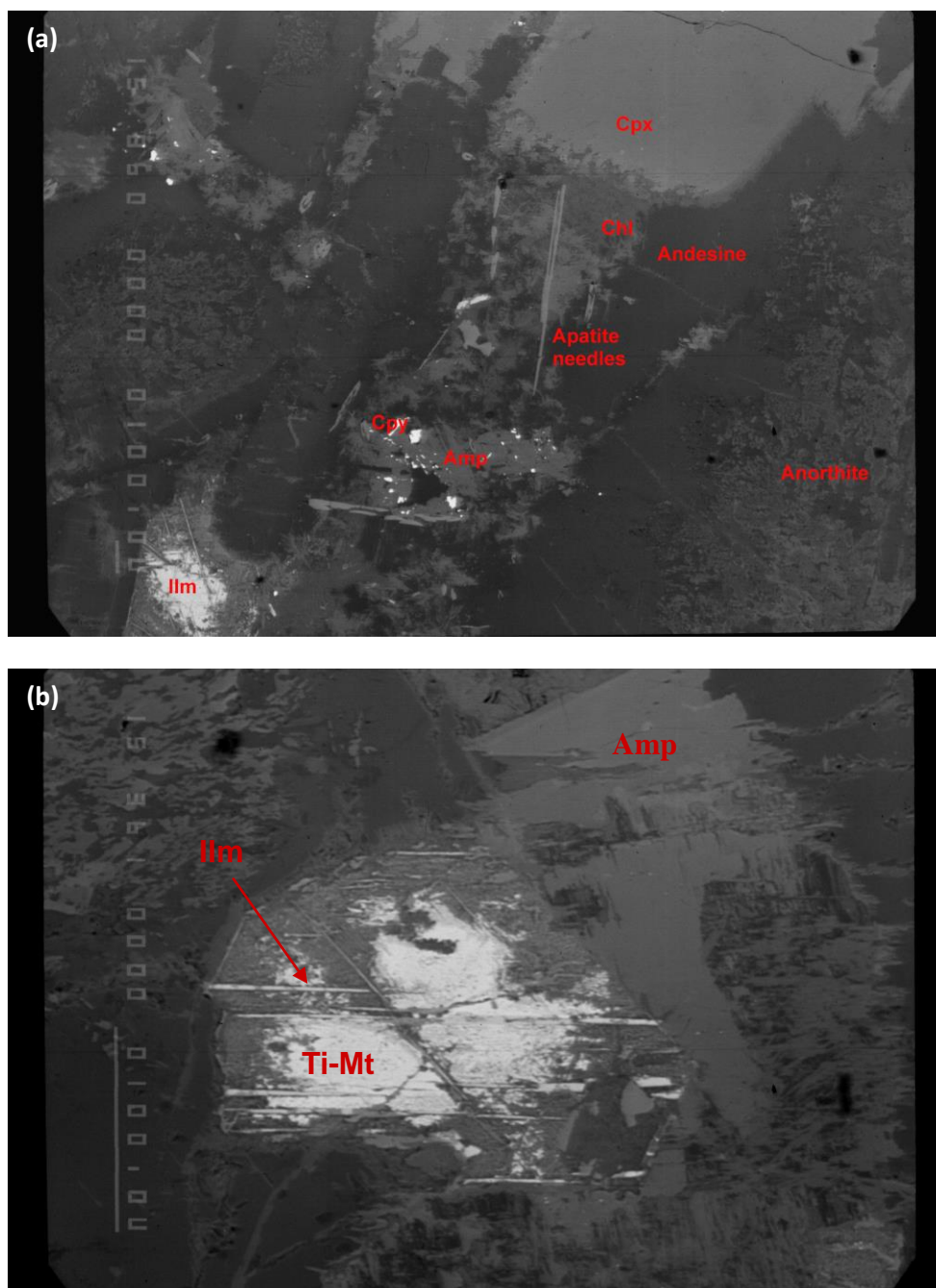


Plate 3.34a,b: Sample #RP11: (a) Backscatter image of coarse clinopyroxene grains with development of retrogressive chlorite, amphibole, and apatite. Relict primary andesine laths penetrate clinopyroxene suggesting primary equilibrium mineral growth; (b) Backscatter image of relict coarse Fe-Ti oxide with crystal faces still evident. Retrogression has caused exsolution of ilmenite needles out of bright coarse-grained Ti-Mt. The 100 micron scale is located along the left margin of each image. (Ilm = ilmenite; Ti-Mt = Ti-magnetite; Amp = amphibole; Cpy = chalcopyrite; Cpx = clinopyroxene).

Chapter 4: Geochronology

4.0 Introduction

Several age dates have been reported by various authors relating to the development of the Guyana shield that help to constrain the time of emplacement of the Kurupung batholith, the most recent by Santos et al., 2003 and Davis, 2006 (Appendix E). A Pb/Pb date on magmatic zircon of 2103 \pm 3 Ma was reported for the Kurupung batholith from the Aricheng area (Davis, 2006). A U/Pb date on hydrothermal zircon of 1995 \pm 15 Ma is reported for the age of U-Zr mineralization within the Kurupung batholith (Davis, 2006). U/Pb age dates of between 1984 \pm 9 Ma to 1966 \pm 9 Ma for the basal Roraima, the 1873 \pm 3 Ma for the ash tuff interlayers, and the 1782 \pm 3 Ma for intrusion of Avanavero suite dikes and sills constrains deposition of the Roraima Supergroup (Santos et al., 2003).

The Kurupung mylonite zone terminates in large 2-mica granite bodies exposed to the northwest and southeast of the Uatuma ash tuff field. These are the intrusive/extrusive counterparts defining the post-collisional peraluminous 2.1-1.96 Ga Orosirian magmatic episode. These mid-crustal peraluminous melts developed within the thick orogenic infrastructure, were rapidly unroofed, and vented voluminous ash tuff deposits. The 2.1-1.96 Ga ash tuffs are conformably overlain by 1873 \pm 3 Ma vitric tuff interlayered with the Roraima continental sandstone. Although there are no 2-mica granitoids or alkaline volcanics exposed in the study area, there is a potential for a deep-seated alkaline intrusive associated with mineralization relating to degassing of 2-mica granites, however, there are no magnetic anomalies representing these 2-mica granites within the study area.

A further four radiometric dates are reported here to establish a more critical temporal constraint on uranium mineralization at Aricheng. U/Pb dating was carried out on coarse-grained titanites on retrogressive margins of amphibole signifying post-magmatic hydrothermal metamorphism. Ar/Ar dating was completed on Ba-Kfeldspar megacrysts in altered Kurupung to date the K-metasomatism. The age of the pegmatites was established by U/Pb dating of zircon inclusions within Kfeldspar. Ar/Ar dates on biotite

phenocrysts in a lamprophyre dike were carried out to establish its timing relative to mylonitic shearing and uranium mineralization. In order to capture mineralogical and textural relationships for a specific age, all samples submitted for geochronological determination were collected from drill core. Age dates are discussed in the following order: 1) U/Pb dates of titanites; 2) Ar/Ar dates for pegmatite dikes and Kfeldspar megacrysts; and 3) Ar/Ar dating of biotites in lamprophyres.

4.1 Radiometric Dates

A summary of radiometric age dates listed in order of younging is presented in Table 4.0 below. This table provides an overview of events and their relationship to the emplacement and unroofing of the Kurupung batholith. Radiometric methods and data are located in Appendix B. The age dates reported in the table as ActLabs, 2012 (Appendix B) are discussed in further detail below.

Sample (Sample #)	Method	Mineral Dated	Radiometric Age (Error Ellipse)	Reference
Kurupung batholith emplacement age (#U308-06-1)	ID-TIMS	Magmatic zircon	2064-2103 +/- 3 Ma (2 sigma)	Davis, 2006 (Appendix E)
Retrograde overprint on Kurupung (#ARN-022 141.9-142.1m)	ID-TIMS	Titanite	2094 +/- 5 Ma (2 sigma)	ActLabs, 2012 (Appendix B)
Pegmatite dikes (#ARN-005 42.7-42.85m)	SHRIMP	Zircon inclusions in Ba-Kfeldspar	2085 +/- 9 Ma (2 sigma)	ActLabs, 2012 (Appendix B)
Ba-Kfeldspar megacrysts (#ACCON-B 34.75-35.18m)	Ar-Ar	Ba-Kfeldspar	2071 +/- 13 Ma (1 sigma)	ActLabs, 2012 (Appendix B)
Lamprophyre dikes (#ARN-053 89.3m)	Ar-Ar	Biotite phenocrysts	2011 +/- 11 Ma (1 sigma)	ActLabs, 2012 (Appendix B)
U-Zr mineralization (#U308-06-1)	ID-TIMS	Hydrothermal zircon	1995 +/- 15 Ma (2 sigma)	Davis, 2006 (Appendix E)
Basal Roraima (Orosirian Uatuma/Surumu 2-mica granites and acid volcanics)	SHRIMP and conventional U/Pb	Zircon	1984 +/- 9 Ma and 1966 +/- 9 Ma	Santos et al., 2003; Schobbenhaus et al., 1994
Roraima Formation (ash tuff interlayers)	SHRIMP	Zircon	1873 +/- 3 Ma	Santos et al., 2003
Upper Roraima Formation (Avanavero dikes)	SHRIMP	Zircon	1782 +/- 3 Ma	Santos et al., 2003

Table 4.0: Summary table of geochronological data specifically related to the Kurupung batholith, age of mineralization, and overlying stratigraphy. Samples designated “ActLabs, 2012” were completed as part of the current thesis investigation.

4.2 U/Pb Geochronology of Titanite

Sample ARN-022 141.9-142.1m was collected from the Aricheng North area of the Kurupung district. This rock exhibits mylonitic foliation and retrogression to greenschist facies mineralogy that is typically associated with upper crustal conditions. Idioblastic titanite replaces retrogressive actinolite and biotite on magmatic Cr-bearing hornblende. These coarse-grained idioblastic titanites are up to 1cm in length and form red-brown irregular transparent or semi-transparent grains rich in magnetite inclusions (Plate 4.0). This sample was submitted for titanite separation and U-Pb dating by TIMS. Two handpicked aliquots consisting of 12 and 14 clean titanite grains were analyzed (Table 4.1a). A concordia age calculation of 2094 ± 5 Ma was obtained (Figure 4.0). U-Pb dating of titanite crystals was chosen to date the uplift event that unroofed the Kurupung to greenschist facies metamorphic conditions. Uplift accommodated by mylonitic shears resulted in rapid exhumation of the batholith. This unroofing event juxtaposed the still hot Kurupung against cool Transamazonian metavolcanics along its eastern margin. Rapid decrease in pressure promoted the greenschist facies overprint along the eastern margin of the batholith. The 2094 ± 5 Ma date on titanite ties the unroofing of the 2103 ± 3 Ma Kurupung batholith to post-collisional Orosirian-stage of deformation.

4.3 U/Pb in Pegmatite Dikes and Ar/Ar in Metasomatic Ba-Kfeldspar

Undeformed pegmatite dikes occur occasionally in the drill logs at Aricheng and these are observed cross-cutting mylonitic shears. In outcrop, the dikes are up to 1m wide and strike 140° , often paralleling the mylonitic fabric. These pegmatites are mineralogically dominated by Ba-Kfeldspar. The rapid decompression of the batholith caused devolatilization, giving rise to pegmatite dikes and pervasive Ba-K-feldspar metasomatism. The age of the pegmatite dike is therefore compared to the Ar/Ar date of the megacrystic Ba-Kfeldspar in the Kurupung.

Pegmatite dikes are comprised of coarse Ba-Kfeldspar and quartz with accessory zircon. Petrographic examination and microprobe analyses were completed on Ba-Kfeldspar in

the pegmatite dike. The Ba-Kfeldspar phenocrysts have multiple growth zones that are defined by the alignment of albite inclusions along crystal faces (Plate 4.1). The growth zones are not well defined in backscatter as the compositions of the growth zones are similar. However, an overall general trend toward decreasing barium content towards the margins of grains was established with the electron microprobe. Core compositions



Field of view = 10mm

Plate 4.0: Sample #ARN022-141.9-142.1m: Plane light photomicrograph illustrating the coarse-grained population of red-brown titanite growth on amphibole margins.

(a)

N	Ident	Weight, mg	Concentration, ppm		Isotopic ratios						Age, Ma		
			Pb	U	$^{206}\text{Pb}/^{206}\text{Pb}$	$^{207}\text{Pb}/^{206}\text{Pb}$	$^{208}\text{Pb}/^{206}\text{Pb}$	$^{206}\text{Pb}/^{238}\text{U}$	$^{207}\text{Pb}/^{235}\text{U}$	$^{206}\text{Pb}/^{238}\text{U}$	$^{207}\text{Pb}/^{235}\text{U}$	$^{206}\text{Pb}/^{238}\text{U}$	$^{207}\text{Pb}/^{235}\text{U}$
1	50 mkm, 12	0.15	139.6	282.6	1768	0.1298±1	0.3337±1	6.8604±137	0.3832±8	0.98	2094±4	2091±4	2096±1
2	50 mkm, 14	0.17	165.5	334.1	1826	0.1298±1	0.3033±1	6.9430±139	0.3880±8	0.95	2104±5	2114±6	2095±1

Note: a—isotopic ratios corrected for blank and common Pb (Stacey and Kramers, 1975). Errors (2σ) are given in last decimal places.

(b)

Spot	% $^{206}\text{Pb}_c$	ppm U	ppm ^{232}Th	ppm ^{238}U	ppm $^{206}\text{Pb}^*$	(1) $^{206}\text{Pb}/^{238}\text{U}$ Age	(1) $^{207}\text{Pb}/^{206}\text{Pb}$ Age	% Dis-cordant	(1) $^{206}\text{Pb}^*/^{238}\text{U}$ ±%	(1) $^{207}\text{Pb}^*/^{235}\text{U}$ ±%	(1) $^{206}\text{Pb}^*/^{238}\text{U}$ ±%	err				
YK-407_1.1	0.11	130	208	1.66	42.8	2094 ±23	2091 ±16	0	2.605 1.3	0.1295	0.89	6.85	1.6	0.3838	1.3	.819
YK-407_2.1	0.11	141	169	1.23	46.6	2094 ±23	2110 ±16	1	2.605 1.3	0.1309	0.89	6.92	1.6	0.3837	1.3	.819
YK-407_3.1	0.15	212	355	1.73	68.5	2055 ±21	2089 ±13	2	2.662 1.2	0.12931	0.74	6.695	1.4	0.3755	1.2	.855
YK-407_4.1	0.15	119	141	1.23	39	2076 ±23	2080 ±19	0	2.631 1.3	0.1287	1.1	6.74	1.7	0.3799	1.3	.778
YK-407_5.1	0.16	282	521	1.91	91.3	2060 ±21	2095 ±12	2	2.655 1.2	0.12979	0.67	6.738	1.4	0.3765	1.2	.870
YK-407_6.1	0.09	240	392	1.69	77.1	2049 ±22	2105 ±16	3	2.672 1.3	0.1305	0.93	6.73	1.6	0.3742	1.3	.807
YK-407_7.1	0.08	252	462	1.90	79.8	2021 ±21	2096 ±12	4	2.715 1.2	0.12984	0.69	6.594	1.4	0.3683	1.2	.866
YK-407_8.1	0.36	86	94	1.13	28	2064 ±25	2098 ±22	2	2.647 1.4	0.13	1.3	6.76	1.9	0.3774	1.4	.738
YK-407_9.1	0.08	82	109	1.36	26.9	2073 ±25	2113 ±20	2	2.636 1.4	0.1311	1.1	6.86	1.8	0.3793	1.4	.779
YK-407_10.1	0.09	251	336	1.38	81.1	2055 ±21	2097 ±12	2	2.663 1.2	0.12993	0.71	6.726	1.4	0.3754	1.2	.861

Errors are 1-sigma; Pb_c and Pb* indicate the common and radiogenic portions, respectively.

Error in Standard calibration was 0.46%

(1) Common Pb corrected using measured ^{204}Pb .

Table 4.1a,b: (a) A summary data table for U/Pb age dates on titanites; (b) A summary data table for U/Pb age dates on zircon.

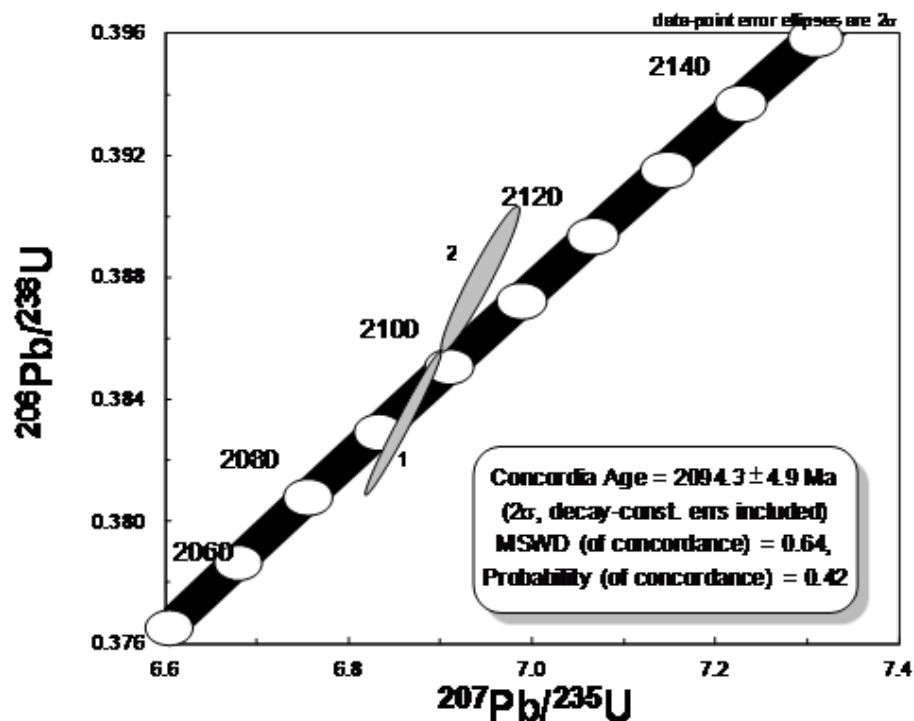


Figure 4.0: Concordia diagram for titanite with axes of the ratios of the radiogenic daughter Pb isotope divided by their respective parent U isotope. A Concordia age of 2094 \pm 5 Ma was calculated for the titanites (Appendix B, from ActLabs, 2012, unpublished).

approximate 0.68 wt% BaO while marginal compositions approximate 0.20 wt% BaO (Appendix A Table 5).

What is interesting to note is that these are petrographic and mineral chemical characteristics that are in common with the secondary Ba-Kfeldspars. Both populations of Ba-Kfeldspars have albite inclusions paralleling the growth face, suggesting insitu growth of albite during Ba-Kfeldspar growth. This indicates simultaneous albite-Kfeldspar growth across the alkali feldspar miscibility gap. The other common characteristic of the two Ba-Kfeldspar populations is the decreasing barium content from core to margin suggesting a reduction in barium content during crystallization of the grain. One main petrographic difference between the two Ba-Kfeldspar populations is that the metasomatic megacrysts contain alternating growth zones of Ba-Kfeldspar and albite, while the Ba-Kfeldspar of the pegmatite lack the albite growth zones. The reason

for this is that the metasomatic Ba-Kfeldspar growth is occurring at the expense of primary plagioclase where a higher sodium budget exists to generate albite growth zones.

One sample of a pegmatite dike (ARN005 42.7-42.85m) was submitted for U-Pb zircon grain analysis by SHRIMP (Table 4.1b and Plate 4.2). Zircon inclusions from within Ba-Kfeldspar were separated, these are depicted in Plate 4.3 and a concordia diagram of data is presented in Figure 4.1. The 2085 +/- 9 Ma age date of the pegmatite dike just postdates the 2094 +/- 5 Ma date on metamorphic titanite. The rapid unroofing event during the Orosirian gave rise to decompressive melting of the orogenic infrastructure resulting in widespread K-metasomatism and local pegmatite generation. The age of the pegmatite dike is then compared to the age of Ba-K-metasomatism. The origin of Ba-Kfeldspar megacrysts within the Kurupung batholith has proven to be a controversial topic. The growth of megacrystic Ba-Kfeldspar eradicates the original chlorite(1) foliation, forming a lithology that appears as porphyritic monzonite and identified as such in core logs. The purpose of dating these Ba-Kfeldspar megacrysts was to confirm their secondary metasomatic origin.

Megacrystic Ba-Kfeldspar (Sample ACCON-B 34.75m-35.18m) was submitted for mineral separation and Ar-Ar dating (Plate 4.4). The mineral separate consisted of 100% Ba-Kfeldspar (SEM confirmed at Activation Laboratories). The sample yielded a saddle shaped age spectrum with a three step plateau characterized by 71 % of ^{39}Ar . An age of 2071 ± 13 Ma was calculated for the megacrystic Kfeldspar (Figure 4.2). The 2071 +/- 13 Ma Ar/Ar date of the megacrystic Ba-Kfeldspars in the altered Kurupung is 32 Ma younger than the reported age for Kurupung emplacement which supports a secondary hydrothermal origin for the megacrysts. The pegmatite age of 2085 +/- 9.2 Ma is comparable to the 2071 +/- 13 Ma date of the megacrystic Ba-Kfeldspar in the altered batholith, indicating that the pegmatite dikes are associated with the pervasive K-metasomatic event that overprints the Kurupung.

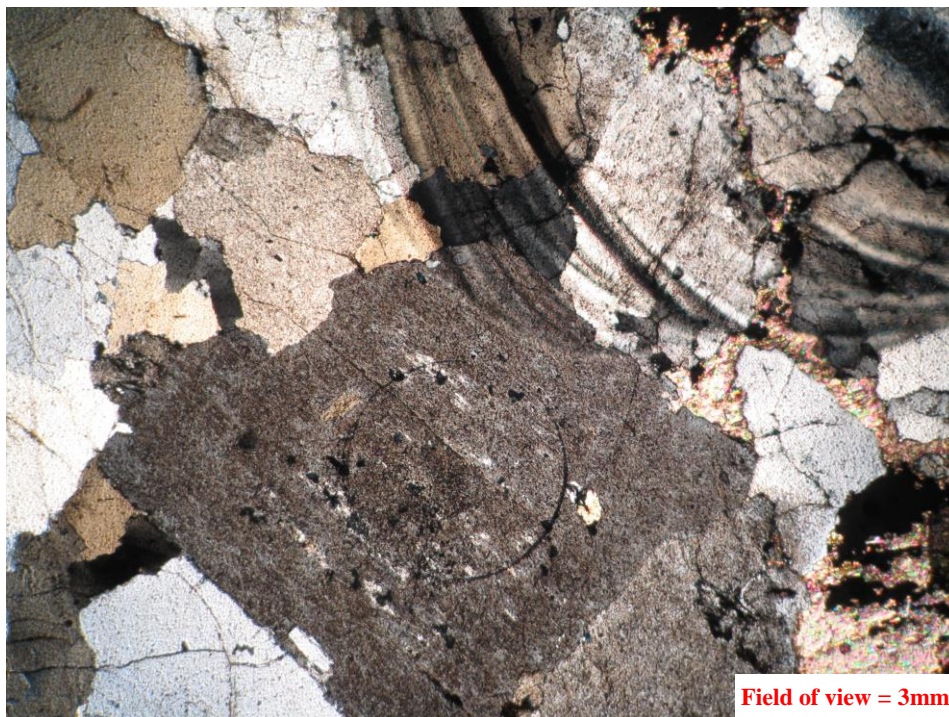


Plate 4.1: Sample #ARN005-42.7-42.85m: Crossed polarized photomicrograph of the pegmatite dike with Ba-Kfeldspar intergrown with quartz and carbonate. Note the growth zones in the Ba-Kfeldspar defined by alignment of inclusions parallel to the growing crystal face.



Plate 4.2: The image illustrates a box of drill core containing the pegmatite dike selected for radiometric dating. The pegmatite dike is enclosed within the red box.

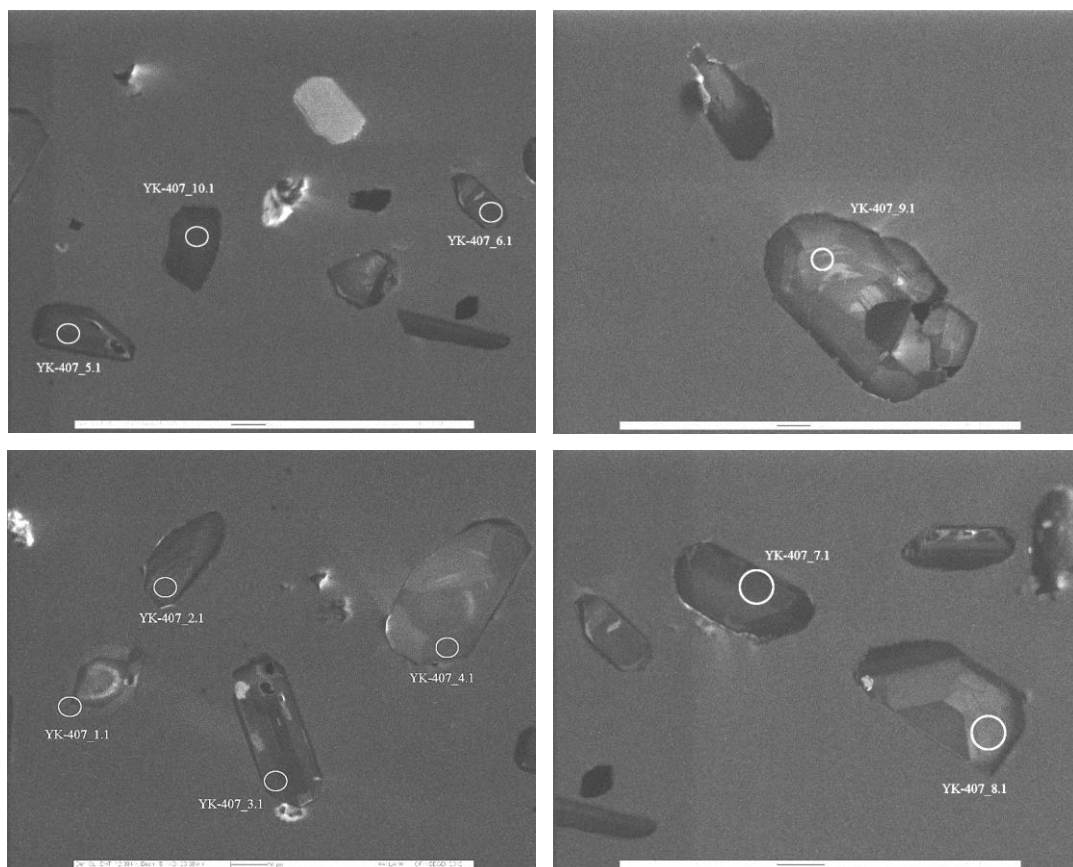


Plate 4.3: Backscatter images of the zircon grains extracted from Ba-Kfeldspar in a pegmatite dike (Sample #ARN005 42.7-42.85m). These zircons were selected for radiometric age dating. Backscatter images provided by ActLabs, 2012, unpublished.

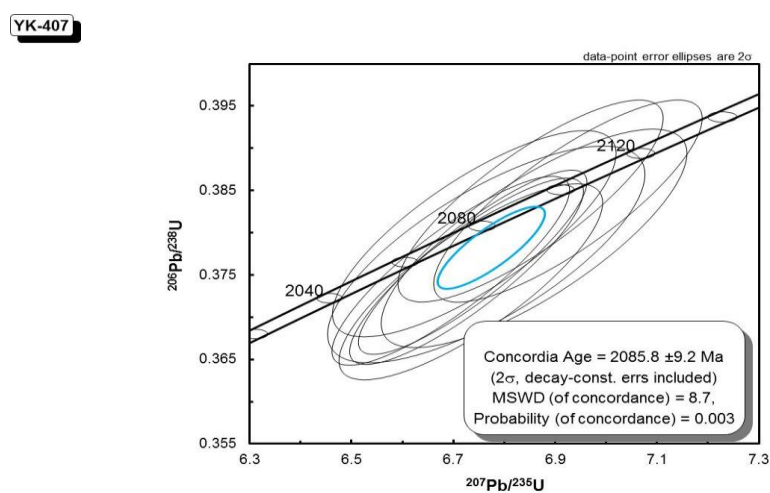


Figure 4.1: Concordia diagram for zircon in pegmatite dike with axes of the ratios of the radiogenic daughter Pb isotope divided by their respective parent U isotope. A Concordia age of 2085 \pm 9 Ma has been calculated for the age of the pegmatite dikes.

4.4 Ar/Ar Geochronology of Foliated Lamprophyre Dikes

Sample ARN053-89.3m is a lamprophyre dike located within well foliated Kurupung near the eastern margin of the intrusion. This sample is strongly foliated with a fabric defined by the alignment of ferro-magnesian minerals. The section consists of biotite-epidote-phengite-chlorite(1)-chlorite(2)-plagioclase-albite (Plate 4.5). Relict mm-scale Ti-biotite phenocrysts have well preserved fresh biotite relics within domains altered to chlorite(1). Ti-bearing biotite phenocrysts have a faint orientation. These phenocrysts occur within a fine-grained groundmass dominated by chlorite(1)-epidote-quartz-

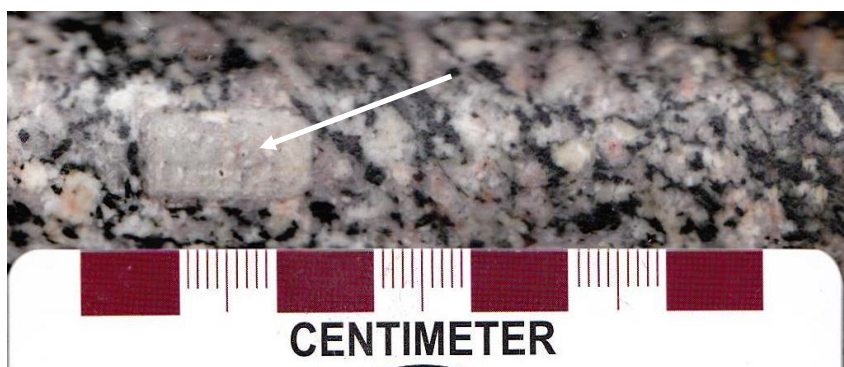


Plate 4.4: Drill core sample #ACCON-B 34.75-35.18m illustrating the growth of secondary Ba-Kfeldspar megacrysts (white arrow).

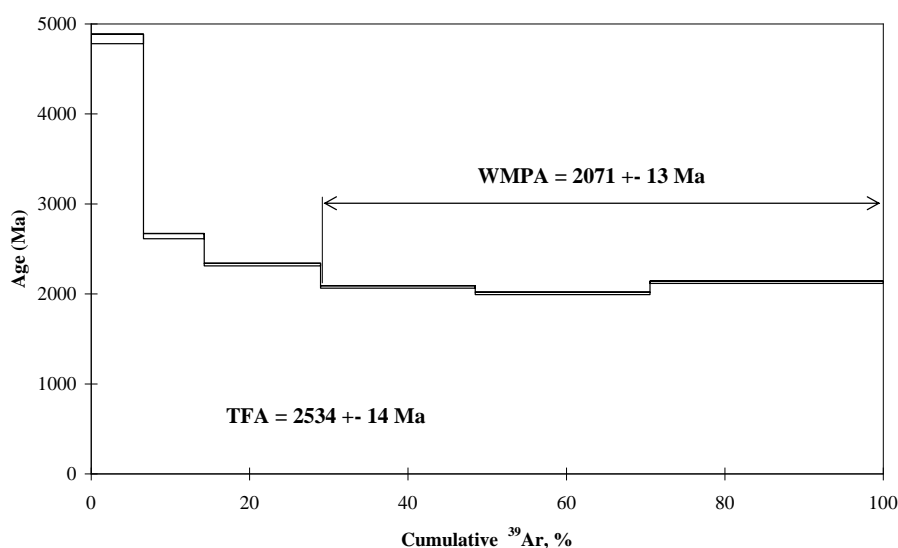


Figure 4.2: Cumulative ^{39}Ar step-heating results. Reheating events yield a staircase-like profile; the 0% value is the age of the reheating event, and the 100% value is the minimum age of initial crystallization of the sample.

plagioclase. The Ti component of the biotite was depleted during retrogression to form Ti-magnetite.

Fine to coarse domains of Ti-magnetite replace Ti-biotite and phengite along cleavage planes and grain margins. The majority of oxides exterior to the micas are non-titaniferous magnetite (Plate 4.6). Fine-grained monazite occurs randomly throughout the section. Areas of coarse epidote show domainal compositional variation in backscatter. Bright epidote domains have 10.51 wt% FeO and 0.27 wt% MnO. Dark epidote domains have 8.73 wt% FeO and 1.07 wt% MnO. It is apparent in backscatter that these darker zones are associated with chalcocite. Coarse-grained apatite(2) measuring up to 1mm in diameter are host to fine-grained U-Pb-Si, possibly kasolite, disseminated throughout their interior (Plate 4.7). All fine-grained bright domains within the apatite are U-Pb-Si minerals. In other areas of the thin section, fine-grained U-Pb-Si are also hosted within birefringent blue chlorite(2), albite(3) and apatite(2) (Plate 4.8). What is interesting to note is that associated with a major oxide-bearing veinlet is Berlin blue chlorite(2), the same chlorite noted in the mineralized zones.

Sample ARN053-89.3m was submitted for age dating of biotite by the Ar/Ar method. The biotite mineral separate was SEM confirmed at Activation Laboratories. A summary table of data is presented below in Table 4.2. An age date of 2011 ± 11 Ma was obtained for the lamprophyre dike (Figure 4.3).

There are two interesting points to consider: (1) the lamprophyres are ~90 Ma younger relative to the age of the Kurupung batholith; (2) the lamprophyres are 15 Ma older than the age of U-mineralization. In general, lamprophyres are ultra-potassic igneous rocks formed deep in the mantle. This yields mafic magmas through low degrees of partial melting resulting in magma rich in the alkalis, lithophile elements (K, Ba, Cs, Rb), and elevated Ni and Cr. There is also volatile enrichment to provide the biotite (phlogopite) and amphibole mineralogy. The mylonitic fabric and the same chlorite(2) alteration, and



Plate 4.5a,b: Sample #ARN053-89.3m: (a) Plane light photomicrograph illustrating the faint alignment of biotite phenocrysts; (b) Crossed polarized light image of the dark vein hosting birefringent blue chlorite(2), U-Pb-silicates (kasolite), and Ti-magnetite-hematite.

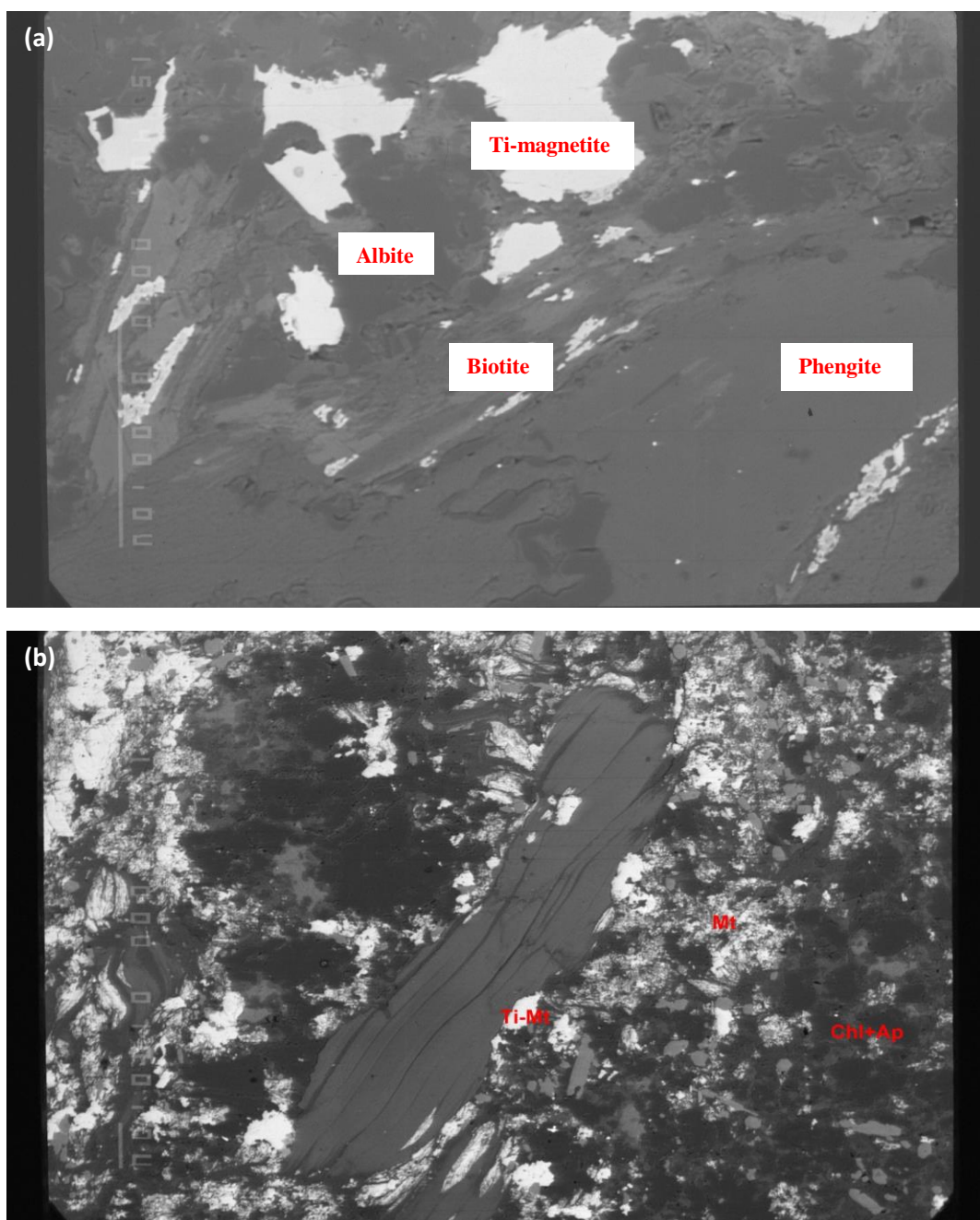


Plate 4.6a,b: Sample #ARN053-89.3m : (a) Backscatter image showing intergrowth of phengite-biotite-albite. Micas have internal zones of Ti-magnetite developed along cleavage planes; (b) Backscatter image illustrating a biotite phenocryst with Ti-magnetite development along cleavage planes and grain margin. The majority of oxides exterior to the micas are simple magnetite. Ti-Mt = Ti-magnetite; Mt = magnetite; Chl = chlorite; and Ap = apatite.

uranium mineralization associated with the lamprophyres indicates these have undergone mylonitic deformation, the same chlorite(2) alteration, and have been U-Zr mineralized. The lamprophyres therefore participated in the mylonitic shearing and the same alteration and mineralizing events that followed.

The age of the lamprophyres and their mineralogical textures supports the interpretation that the mylonitic shearing is long lived and allowed for episodic fluid migration. The age determination of the lamprophyre supports the interpretation that ductile deformation occurred from the 2103 +/- 3 Ma age of the batholith through to the 2011 +/- 11 Ma age of the lamprophyre dikes. Textural observations reveal that chlorite(2) development in the lamprophyres is contemporaneous with chlorite(2) sealing albitite cataclasite (Plate 4.8a,b). Therefore, the transition from ductile deformation to more brittle cataclastic deformation occurred between 2011 +/- 11 Ma and the 1995 +/- 15 Ma age of mineralization. Lamprophyre injection was accompanied by mantle devolatilization whereby fluorine and CO₂-rich fluids migrated upwards through the shear system. These fluids acted as remobilizing agents for uranium and zircon and precipitated uranium and hydrothermal zircon veins in albitite breccia cemented by chlorite(2).

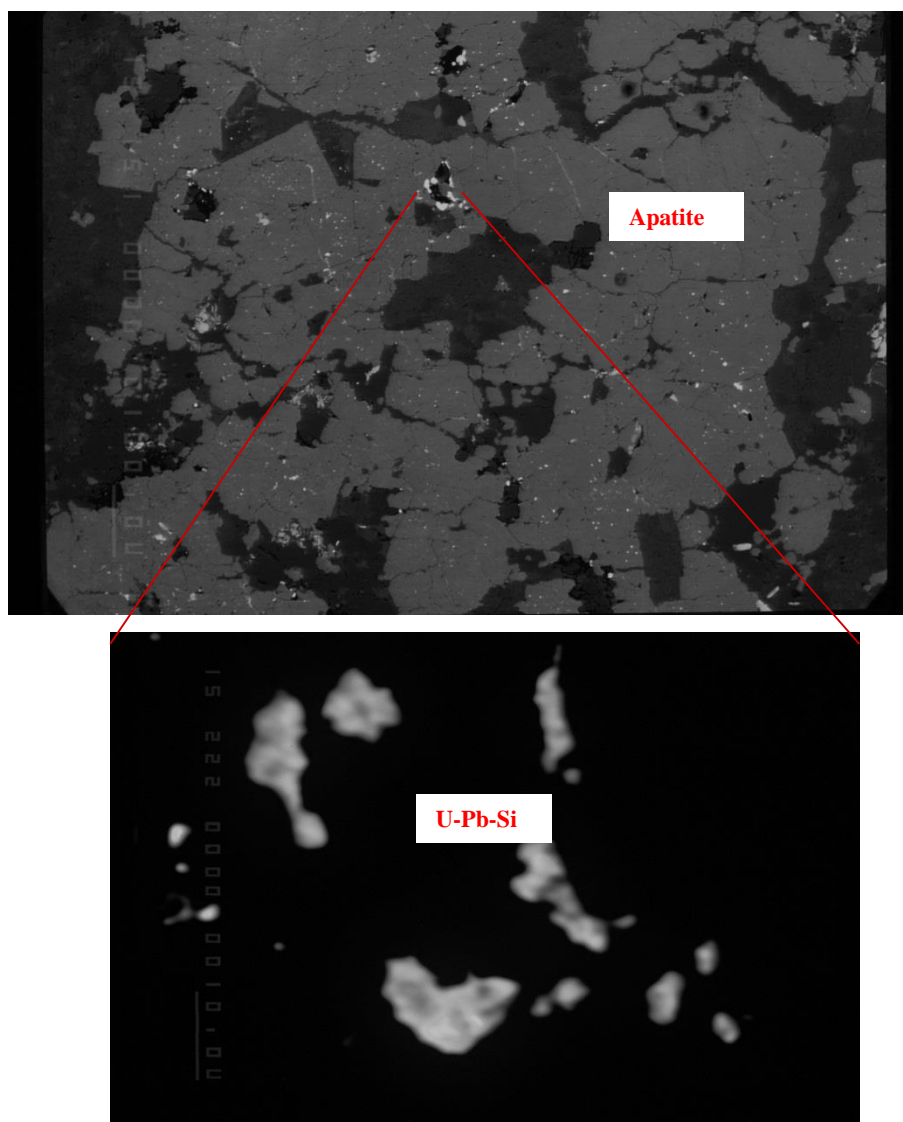


Plate 4.7: Sample #ARN053-89.3m: Retrogressive chlorite–apatite intergrowths with fine-grained U-Pb-Si (kasolite) disseminated throughout the apatite. All fine-grained bright domains within the apatite are U-Pb-Si minerals. A higher magnification image is also presented here to establish grain size of these U-minerals.

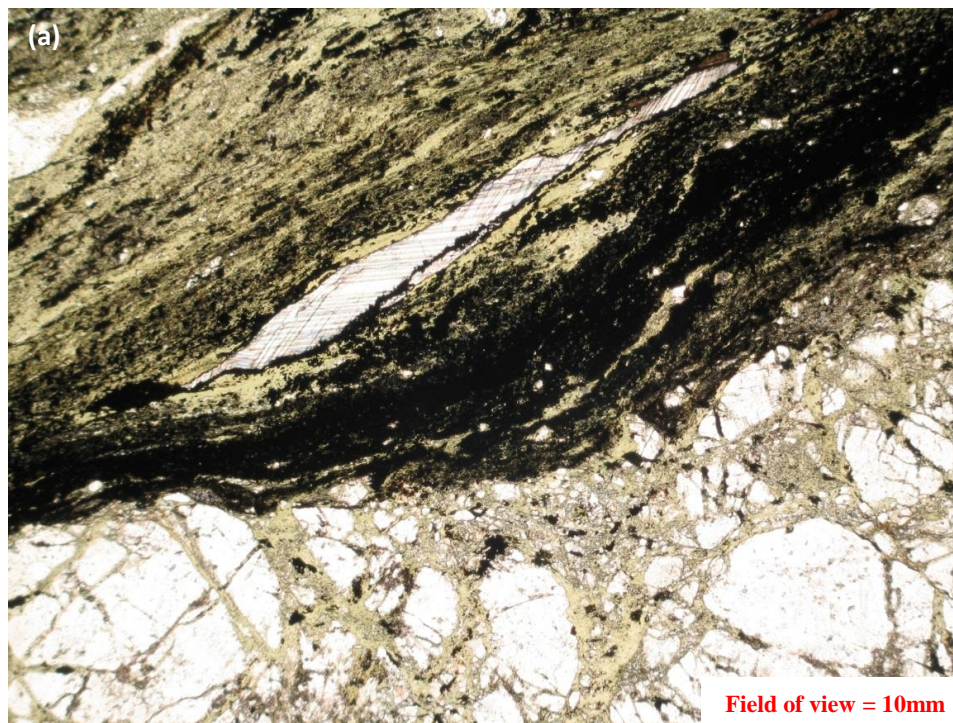


Plate 4.8a,b: Sample #ARN053-89.3m (a) Plane light photomicrograph illustrating the contact between the lamprophyre dike and albite cataclasite. Note the chlorite(2) and carbonate veinlets hosting U-Pb-silicates (kasolite) in the lamprophyre, the same chlorite(2) noted in the adjacent cataclasite; (b) Crossed polarized image showing the birefringent blue chlorite(2) and associated calcite.

Tabulated data

Sample: **YK-281 biotite** $J=0.003355 \pm 0.000030$

T°C	$^{40}\text{Ar}/^{39}\text{Ar}$ (STP)	$^{40}\text{Ar}/^{39}\text{Ar}$	$\pm 1\sigma$	$^{38}\text{Ar}/^{39}\text{Ar}$	$\pm 1\sigma$	$^{37}\text{Ar}/^{39}\text{Ar}$	$\pm 1\sigma$	$^{36}\text{Ar}/^{39}\text{Ar}$	$\pm 1\sigma$	Ca/K	$\Sigma^{39}\text{Ar}$ (%)	Age (Ma)	$\pm 1\sigma$
500	6.8×10^{-9}	154.70	2.97	0.0280	0.0228	0.0781	0.3217	0.1343	0.0190	0.281	0.4	588.7	26.6
600	63.5×10^{-9}	80.65	0.21	0.0204	0.0014	0.2960	0.0626	0.0226	0.0025	1.066	8.0	399.9	4.9
700	504.3×10^{-9}	532.18	1.91	0.0151	0.0023	0.1651	0.0325	0.0256	0.0034	0.594	17.2	1831.6	11.3
750	777.0×10^{-9}	577.26	1.17	0.0229	0.0016	0.0218	0.0208	0.0543	0.0020	0.078	30.2	1910.2	10.9
800	945.3×10^{-9}	596.61	0.82	0.0177	0.0005	0.0614	0.0016	0.0246	0.0014	0.221	45.5	1968.3	10.9
850	252.6×10^{-9}	606.77	1.73	0.0196	0.0039	0.0131	0.0804	0.0257	0.0028	0.047	49.5	1988.2	11.4
950	858.7×10^{-9}	612.22	1.24	0.0191	0.0024	0.0522	0.0392	0.0224	0.0020	0.188	63.1	2001.0	11.1
1000	707.0×10^{-9}	616.18	0.89	0.0188	0.0012	0.0806	0.0092	0.0200	0.0014	0.290	74.2	2010.3	11.0
1065	943.8×10^{-9}	621.38	0.65	0.0138	0.0013	0.0986	0.0173	0.0176	0.0010	0.355	88.9	2022.0	11.0
1130	656.1×10^{-9}	570.56	1.18	0.0294	0.0016	0.1435	0.0180	0.0730	0.0021	0.517	100.0	1884.3	10.8

Table 4.2: Lamprophyre dike Ar/Ar age data on biotite phenocrysts.

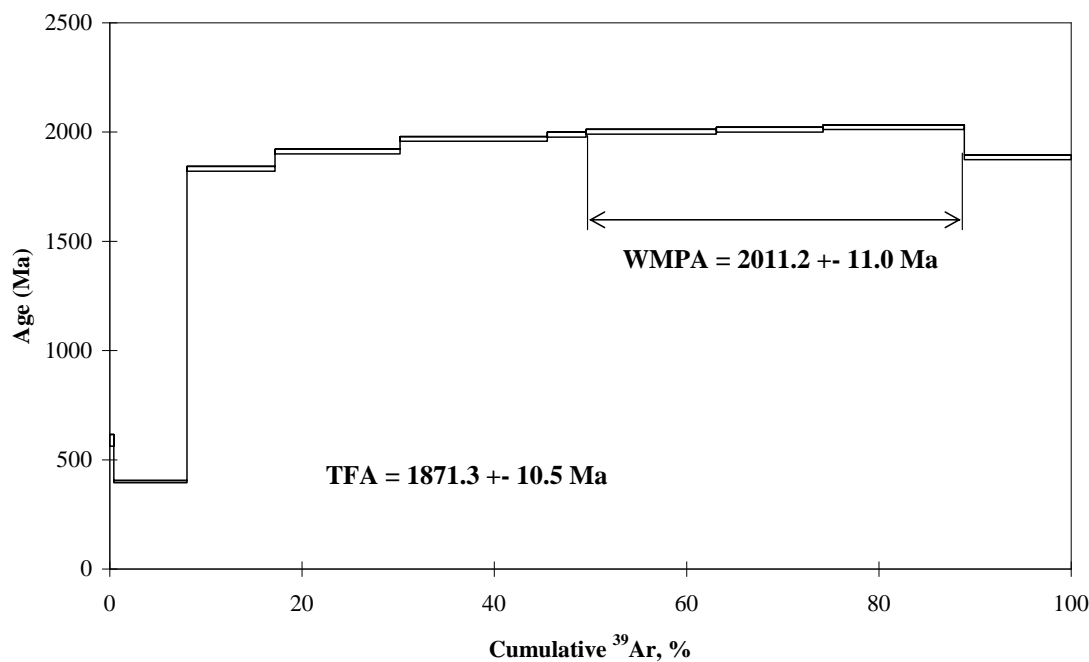


Figure 4.3: Cumulative ^{39}Ar step-heating results of biotite in the lamprophyre dike. Reheating events yield a staircase-like profile; the 0% value is the age of the reheating event, and the 100% value is the minimum age of initial crystallization of the sample.

Chapter 5: Geochemistry

5.0 Introduction

Junior mining companies exploring in areas of limited outcrop exposure base drilling programs on the interpretation of geochemical assay results. In this chapter major and trace elements trends are investigated to determine elemental patterns that may be used to vector potential drill targets. U3O8 Corp supplied a geochemical database in excess of 22,000 analyses for such an investigation. In addition, a suite of 112 samples representing lithological and textural variations were collected by the author from drill core. Of these, twenty-one samples of relatively unaltered and pervasively mineralized samples were submitted to Activation Laboratories (ActLabs) for major and trace element geochemistry (Appendix C, Table 1.0). These samples were used to identify and characterize geochemical variations related to host lithology and mineralization. This geochemical database was then applied to the 22,000 analyses to classify the petrological affinity of the host Kurupung batholith and to characterize the nature of any district scale alteration patterns. Geochemical variations are documented across altered and mineralized zones in an effort to identify specific element associations with U-enrichment.

The first step in this process is to classify the igneous lineage of the unaltered Kurupung batholith. A selected suite of least altered, least weathered drill core was submitted to ActLabs for “Research Grade” whole rock, trace element and REE geochemical analyses. The list of samples submitted and whole and trace element geochemical data are presented in Table 5.0.

To consider these rocks “unaltered” is not correct as even the least altered samples have undergone some degree of alteration. However, this comparison is sufficient to distinguish background bulk rock chemistry from that directly related to the mineralization event. Altered samples were then compared to a base population of least altered samples. In addition to classifying the igneous lineage, a series of mass balance and factor analysis computations were utilized to assess chemical variations and trends as

a consequence of alteration and mineralization. The results of these investigations are presented in the following order: 1) igneous lineage of the unaltered Kurupung batholith;

Analyte Symbol	Unit Symbol	Detection Limit	Analysis Method	PERE 12	ARN 019 40.15-40.78m	ARN021 117.70-117.90m	ARN022 141.90-142.0m	ARN 023 108.5m	ARN 100 164.5m	ARN 085 96.5m	ARN 063 128.6m
SiO ₂	%	0.01	FUS-ICP	59.91	59.69	59	58.42	63.73	56.95	57.22	60.7
Al ₂ O ₃	%	0.01	FUS-ICP	15.86	14.41	14.65	14.76	14.47	14	14.75	14.14
Fe ₂ O ₃ (T)	%	0.01	FUS-ICP	6.01	6.04	6.07	6.07	6.21	6.18	5.8	4.96
MnO	%	0.01	FUS-ICP	0.09	0.09	0.08	0.09	0.06	0.09	0.09	0.08
MgO	%	0.01	FUS-ICP	4.1	4	3.41	3.96	2.65	3.99	3.49	3.12
CaO	%	0.01	FUS-ICP	4.44	4.8	4.59	5.21	3.05	5.5	4.75	4.1
Na ₂ O	%	0.01	FUS-ICP	3.79	4.04	3.83	3.79	4.78	3.91	4.52	3.87
K ₂ O	%	0.01	FUS-ICP	3.7	4.19	4.43	3.8	3.8	4.07	3.44	4.72
P ₂ O ₅	%	0.01	FUS-ICP	0.69	0.73	0.68	0.77	0.55	0.78	0.76	0.68
LOI	%	0.01	FUS-ICP	0.46	0.6	0.5	0.58	0.38	0.66	0.56	0.5
Total	%	0.01	FUS-ICP	1.65	1.42	1.1	1.08	1.52	2.96	3.65	1.14
A/CNK		0.01	FUS-ICP	100.7	97.97	97.97	98.88	99.19	99.08	99.02	98.02
K ₂ O-CaO		0.01	FUS-ICP	0.92	0.77	0.78	0.86	0.73	0.81	0.81	0.77
Na ₂ O+K ₂ O-CaO		0.01	FUS-ICP	-0.74	-0.61	-1.31	-1.31	-1.43	-1.43	-1.31	0.62
FeO/FeO+MgO		0.01	FUS-ICP	3.05	3.43	3.67	2.74	5.53	2.48	3.21	4.49
Mg# = (Mg/(Mg+Fe))*100		0.01	FUS-ICP	0.9446093	0.60559625	0.62568059	0.60518447	0.61370624	0.60766917	0.62432724	0.613861386
Au	ppb	0.01	INAA	72.49773295	72.4888945	70.3327069	72.0811988	71.3826865	71.89821914	70.4532707	71.3689855
Ag	ppm	0.01	MULT INAA / TD-ICP	<0.5	<0.5	<0.5	<0.5	<0.5	<0.5	<0.5	<0.5
As	ppm	0.01	INAA	6	5	6	4	6	<1	6	8
Ba	ppm	0.01	FUS-ICP	982	1260	1219	1250	1249	1195	1383	1216
Be	ppm	0.01	FUS-ICP	2	3	3	3	4	3	3	3
Bi	ppm	0.01	TD-ICP	2	<2	<2	<2	<2	<2	<2	<2
Br	ppm	0.01	INAA	<0.5	<0.5	<0.5	<0.5	<0.5	<0.5	<0.5	<0.5
Cd	ppm	0.01	TD-ICP	<0.5	<0.5	<0.5	<0.5	<0.5	<0.5	<0.5	<0.5
Co	ppm	0.01	INAA	23.5	20	18.3	20.2	13.6	22.4	20	17.2
Cr	ppm	0.01	INAA	208	349	143	160	109	156	148	125
Cs	ppm	0.01	INAA	0.7	1.4	1.8	1.8	3.2	2.7	2.6	2.1
Cu	ppm	0.01	TD-ICP	165	73	90	66	70	76	101	116
Hf	ppm	0.01	INAA	6	6.7	6.8	6.1	5.9	6.1	7.9	7.1
Hg	ppm	0.01	INAA	<1	<1	<1	<1	<1	<1	<1	<1
Ir	ppb	0.01	INAA	<1	<1	<1	<1	<1	<1	<1	<1
Mo	ppm	0.01	TD-ICP	<2	<2	3	<2	<2	<2	2	2
Ni	ppm	0.01	TD-ICP	113	74	68	75	60	75	79	66
Pb	ppm	0.01	TD-ICP	30	34	12	16	20	14	15	17
Rb	ppm	0.01	INAA	90	110	150	110	110	110	80	140
Sb	ppm	0.01	INAA	0.7	0.8	0.6	0.6	0.8	0.6	0.8	1.3
S	%	0.01	TD-ICP	0.01	0.01	0.01	0.01	0.01	0.01	0.02	0.01
Sc	ppm	0.01	INAA	12.3	11.2	10.2	11.5	7.7	12.4	10.5	9.17
Se	ppm	0.01	INAA	<0.5	<0.5	<0.5	<0.5	<0.5	<0.5	<0.5	<0.5
Sr	ppm	0.01	FUS-ICP	734	1351	1158	1282	916	1122	1088	1196
Ta	ppm	0.01	INAA	1.9	<0.3	1.8	1.3	1.6	2.3	<0.3	1.3
Th	ppm	0.01	INAA	12.6	20.7	20.1	18.8	22	19.8	20.9	21.5
U	ppm	0.01	INAA	3.9	4.8	7.1	4.8	11.5	5.2	5.4	9.1
V	ppm	0.01	FUS-ICP	122	109	101	115	78	121	106	96
W	ppm	0.01	INAA	<1	<1	2	<1	<1	<1	<1	4
Y	ppm	0.01	FUS-ICP	22	23	23	24	17	27	24	22
Zn	ppm	0.01	MULT INAA / TD-ICP	61	64	59	62	56	70	72	63
Zr	ppm	0.01	FUS-ICP	242	290	287	295	228	251	316	284
La	ppm	0.01	INAA	77.7	300	88.2	98	96.6	99.4	98	90.3
Ce	ppm	0.01	INAA	145	392	172	189	172	193	188	172
Nd	ppm	0.01	INAA	92	99	102	104	98	106	98	113
Sm	ppm	0.01	INAA	11.1	14.7	13.9	14.6	11.5	15.1	13.8	12.9
Eu	ppm	0.01	INAA	3.31	3.86	3.95	3.91	3	4.19	3.86	3.65
Tb	ppm	0.01	INAA	0.7	1	0.9	0.8	0.8	1	0.8	0.8
Yb	ppm	0.01	INAA	1.75	1.78	1.82	1.86	1.72	2.16	1.78	1.64
Lu	ppm	0.01	INAA	0.27	0.26	0.26	0.26	0.21	0.26	0.23	0.27
Miss	g	0.01	INAA	1.15	1.37	1.37	1.34	1.34	1.27	1.13	1.19

Table 5.0: Whole rock and trace element geochemistry of a representative sample suite of unaltered Kurupung batholith. See Appendix C for data tables from ActLabs. Yellow highlighting represents calculations performed by the author.

and 2) characterization of the intensely altered and mineralized Kurupung. Step two is further subdivided into the following steps: 1) factor analysis of the Accori and Aricheng prospects to evaluate element correlations to U and elemental trends down a drill hole as they relate to IOCG-style alteration and mineralization; and 2) mass balance computations to establish gains and losses of elements related to IOCG-style mineralization in mineralized and non-mineralized zones to vector towards ore shoots.

5.1 Classification of the Kurupung Batholith

The first objective is to classify the igneous lineage of the Kurupung batholith. In previous studies, the Kurupung is classified as a porphyritic monzonite, implying an igneous origin for Ba-Kfeldspar megacrysts. As detailed in earlier chapters, petrological and geochronological studies reveal evidence for the secondary growth of Ba-Kfeldspar. As geochemical evidence outlined below demonstrates, the Kurupung is here classified as a sanukitoid intrusion. This is consistent with whole rock and trace element geochemistry, and elevated Cr- contents in clinopyroxene, amphibole, and Cr-Ti-magnetites. This geochemical signature illustrates that the Kurupung belongs to a high-K calc-alkaline to shoshonitic series and shares features with “low-Ti sanukitoids”. Laurent et al. (2013), has separated sanukitoids into two groups: (1) low-Ti sanukitoids have moderate Ti, Fe, HFSE and REE contents, high Mg# (0.55–0.70) and elevated concentrations of Ni and Cr; and (2) high-Ti sanukitoids are elevated in Ti, Fe, HFSE and LREE, with low Ni, Cr, and Mg# (0.45–0.55).

Based on the molecular ratio of $Al_2O_3/CaO+Na_2O+K_2O$, granitic rocks are classified as strongly peraluminous if the ratio is greater than 1.1, peraluminous if the ratio is greater than 1, and metaluminous if the ratio is less than 1 (Shand, 1927). For the Kurupung, the ratios of A/CNK range between 0.73-0.92, and based on these calculations the Kurupung is metaluminous (Figure 5.0a). When plotted on the SiO_2 versus $FeO/FeO+MgO$ binary (Figure 5.0b), the Kurupung falls within the magnesian domain of sanukitoids and “post-collisional” plutons. This makes the Kurupung a post-collisional sanukitoid.

The petrogenesis of sanukitoids has been studied by Laurent et al. (2013) who compiled a geochemical database of more than 200 sanukitoid samples worldwide. They have shown that suites of mafic to intermediate sanukitoids plot as mostly monzodiorite, quartz-diorite, and quartz-monzonites with SiO₂ contents between 45-62%. The petrogenesis of sanukitoids and of closely related closepet-type granites is generally interpreted to be very similar. By definition, intrusion of sanukitoid and closepet-type granites are commonly late- to post-kinematic (e.g., Shirey and Hanson, 1984; Stern et al., 1989; Evans and Hanson, 1997; Beakhouse et al., 1999; Smithies and Champion, 2000) and not temporally associated with TTG magmatism. Moyen et al (2001) relate TTG to slab melts, sanukitoids to hybridized slab melts, and closepet granites to remelting of previously enriched mantle. They constitute one of the last magmatic events in a stabilizing orogenic crust. Sanukitoid suite compositions range from dioritic to granodioritic, whereas closepet-type can evolve to monzogranitic compositions. In contrast to the TTG series, sanukitoid and closepet-type granite can be rich in mafic minerals, commonly including biotite-hornblende-clinopyroxene associations, on rare occasions even orthopyroxene can be present (Martin and Moyen, 2005). The total alkalis versus SiO₂ diagram of Middlemost (1994) was used to further classify the unaltered Kurupung granitoid (Figure 5.2a). The binary illustrates that the unaltered Kurupung sample suite plot as alkaline monzonite to quartz-monzonite.

The data from the Kurupung are compared to the specific geochemical characteristics of TTGs, adakites, sanukitoids and closepet granites (Table 5.1). The Mg numbers (Mg/Mg+Fe) were calculated for the Kurupung data and found to be between 0.70 and 0.72, matching values akin to a sanukitoid (Table 5.1). The Ni concentrations are between 60-113 ppm and Cr contents between 109-203 ppm, slightly lower than the typical values accepted for sanukitoids and closepet granites (Ni>100 ppm and Cr>200 ppm), however still above TTG values. The Na₂O+K₂O are well above 3 wt%; high Ba contents range from 982 to 1383 ppm; and high Sr contents range from 734-1282 ppm, again supporting sanukitoid affinity. The trace element contents of the Kurupung batholith share characteristics of sanukitoids worldwide.

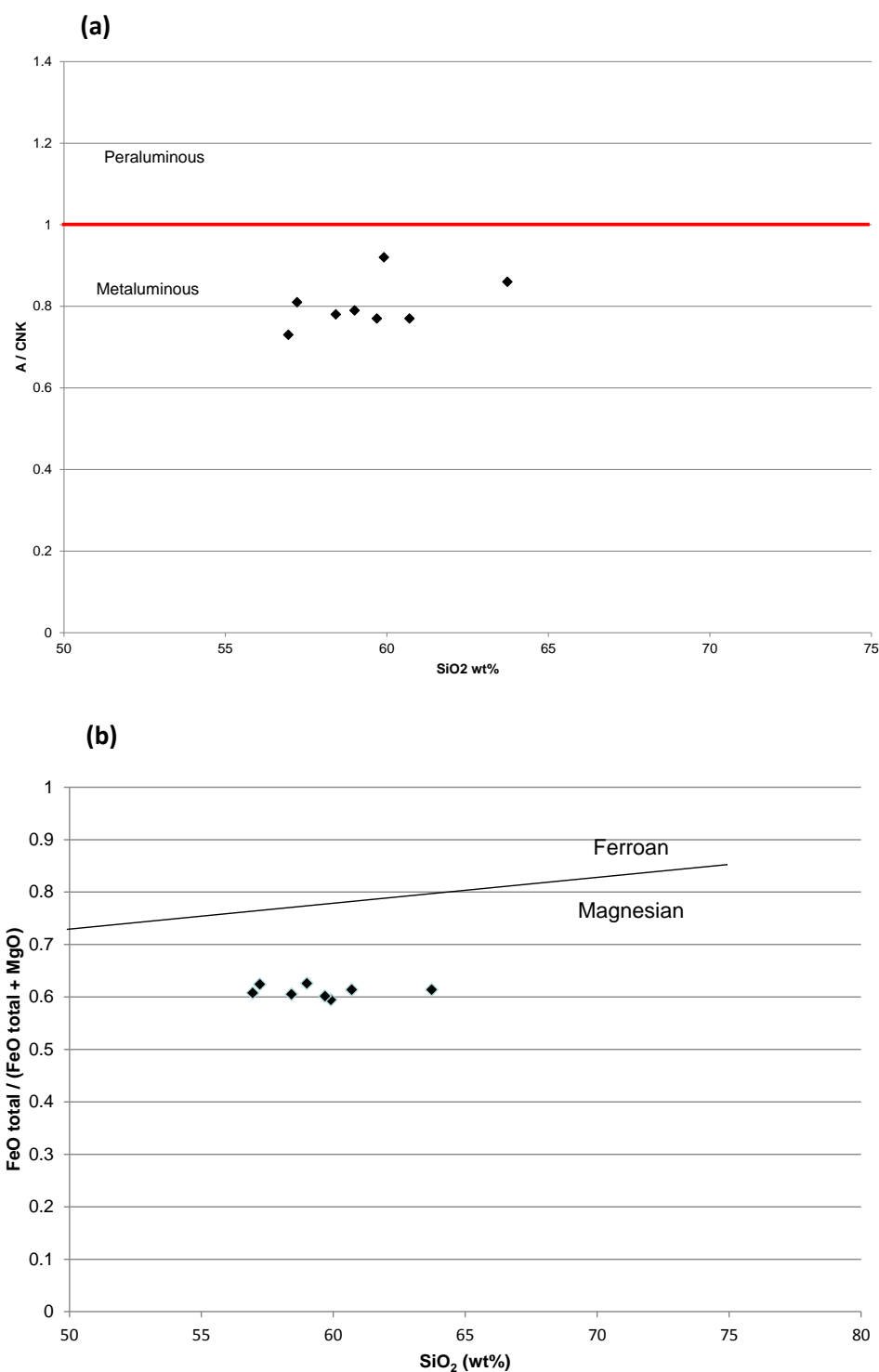


Figure 5.0a,b: (a) A/CNK versus SiO₂ wt% illustrating the metaluminous character of the unaltered Kurupung batholith (after Shand, 1927); (b) Binary diagram illustrating the Kurupung dataset within the magnesian post-collisional A-type granite field (after Frost et al., 2001).

When plotted on a CaO-K₂O-Na₂O ternary diagram, the points fall within the sanukitoid field (Figure 5.2a). On the SiO₂ versus K₂O Harker diagram, they signify high-K shoshonitic to calc-alkaline series and follow a calc-alkaline trend in the Na-K-Ca triangle of Irvine and Baragar (1971) (Figure 5.2b).

These geochemical signatures clearly demonstrate that the Kurupung batholith does not have the geochemical characteristics of tholeiitic or TTG series granitic suites. The Kurupung shares geochemical affinities with shoshonites, but lack the mineralogical characteristics of a true shoshonite such as the presence of sanidine in the groundmass phases and plagioclase rimmed by alkali-feldspar (Mitchell and Bergman, 1991). In essence the shoshonitic classification of the Kurupung on the SiO₂ versus K₂O binary indicates that the Kurupung is the mafic end-member of the sanukitoid suite that is lacking the sanidine and plagioclase rimmed by alkali-feldspar (Stevenson et al., 1999). However, Archean sanukitoids share major element characteristics with differentiated shoshonitic rock series including high K₂O, high total alkalis (Na₂O + K₂O > 5%), high K₂O/Na₂O ratio, low total Fe, low TiO₂, and high Al₂O₃. The trace element abundances of sanukitoids are also of shoshonitic affinity with strong LILE enrichment compared to HFSE (Stevenson et al., 1999). The shoshonitic signature is possibly related to melting of a very phlogopite-rich mantle source. Post-orogenic suites are often attributed to crustal thickening accompanying accretion. Anatectic granites are products of melting of thickened crust while mantle-derived melts are products of transition to an extensional regime produced by failure of the thickened crust (Sonder et al., 1987). Post-collisional extension may have produced shoshonitic-like suites in the form of sanukitoids. Chondrite and primitive mantle normalized REE spider diagrams and MORB normalized trace element plots were constructed for the unaltered Kurupung data (Figure 5.3). REE and trace element spider diagrams representing the characteristic signatures of

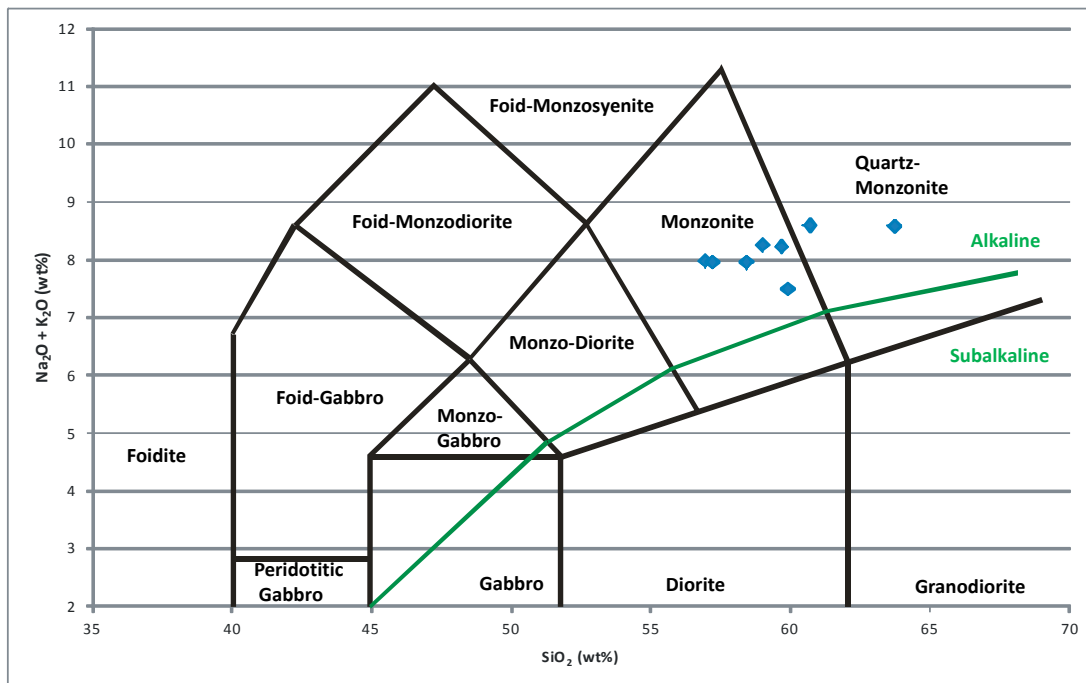


Figure 5.1: Total alkalis vs SiO₂ diagram for the Kurupung batholith. The rock classification is after Middlemost (1994). The line separating the alkaline and subalkaline fields is after Miyashiro (1978). The samples plot as alkaline monzonite to quartz-monzonite.

	TTG	Adakite	Sanukitoid	Closepet	Kurupung
SiO ₂	>67%	~56%	<64%	<62%	<64%
Na ₂ O	4.84%	4.11%	4.39%	4.03%	4.78%
K ₂ O	1.55%	2.37%	2.96%	4.09%	3.80%
Cr	16 ppm	157 ppm	130 ppm	100 ppm	203 ppm
Ni	24 ppm	103 ppm	72 ppm	36 ppm	113 ppm
Sr	648 ppm	2051 ppm	866 ppm	1040 ppm	1282 ppm
Ba	570 ppm	1087 ppm	974 ppm	1300 ppm	1383 ppm
Na ₂ O + K ₂ O	6.60%	>6%	5.92%	8.36%	~8.50%
K ₂ O/Na ₂ O	0.21	0.58	0.51	0.71	~0.79
A/CNK	1	0.45	0.86	0.89	~1.04
Mg#	35-50	61	45-75	35-70	70-72

Table 5.1: A comparative table of characteristic whole rock and trace element data for TTG, adakite, sanukitoid, closepet granitoids, and the Kurupung batholith.

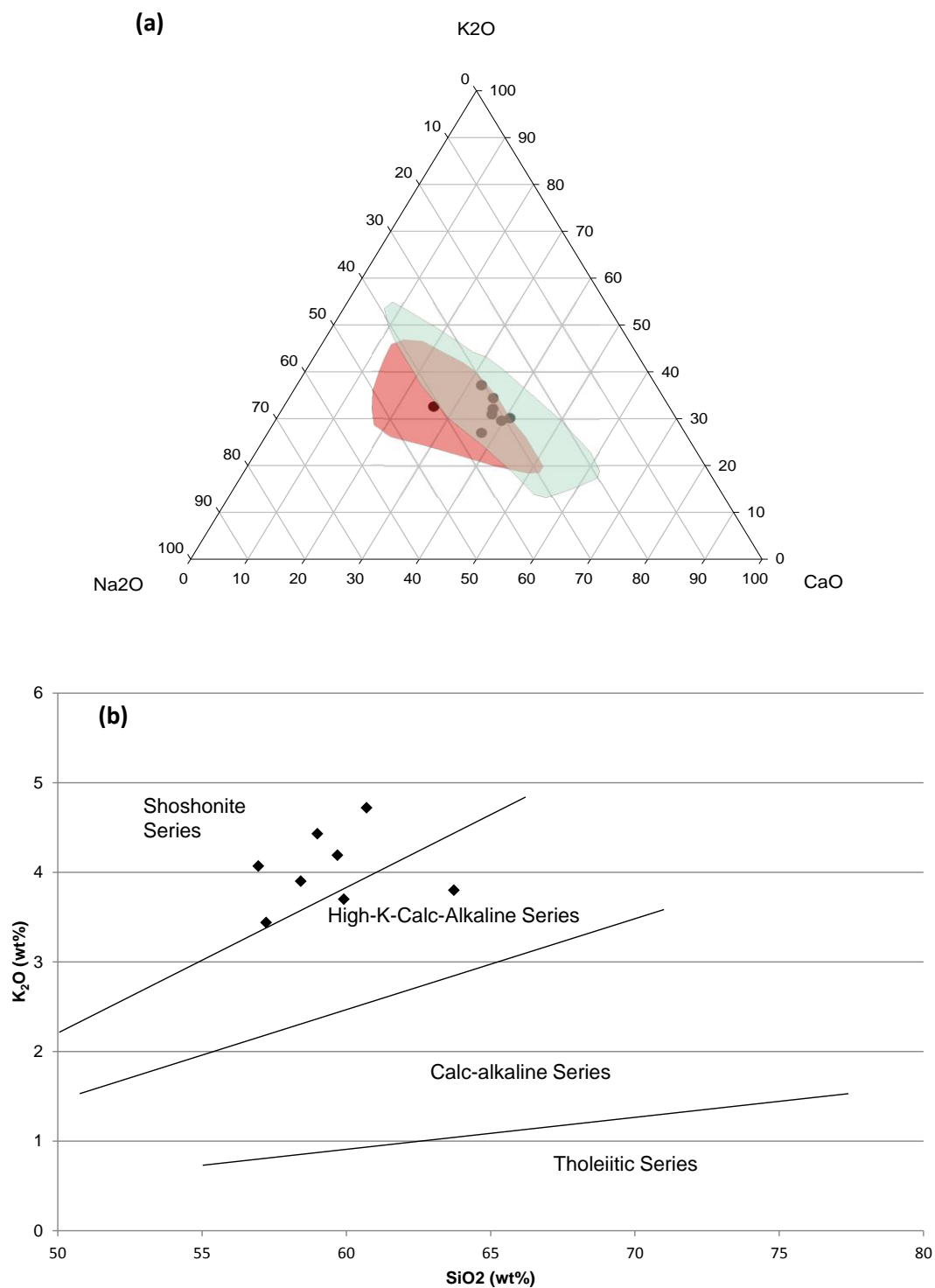


Figure 5.2a,b: (a) Ternary diagram illustrating the red and green sanukitoid and closepet granite fields, respectively. The data points of the unaltered Kurupung batholith fall within the sanukitoid field (after Moyen et al., 2003); (b) Harker diagram showing data points falling within the high-K calc-alkaline to shoshonite series.

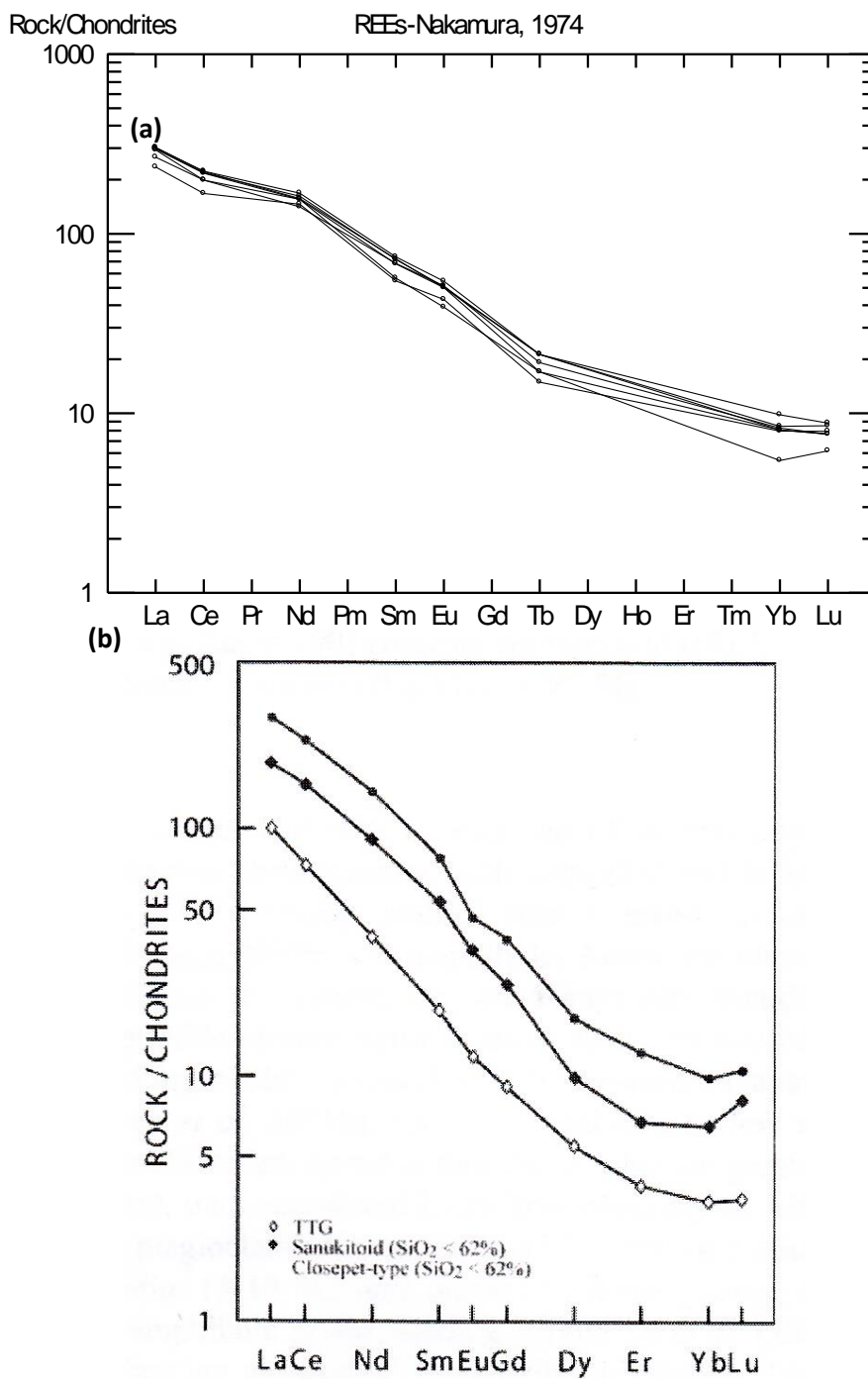


Figure 5.3a,b: Chondrite normalized REE patterns for the unaltered Kurupung. The pattern illustrates high LREE contents and low HREE contents resulting in strongly fractionated patterns; (b) Typical chondrite normalized REE patterns of TTG, sanukitoid, and closepet granitoids (Martin and Moyen, 2005).

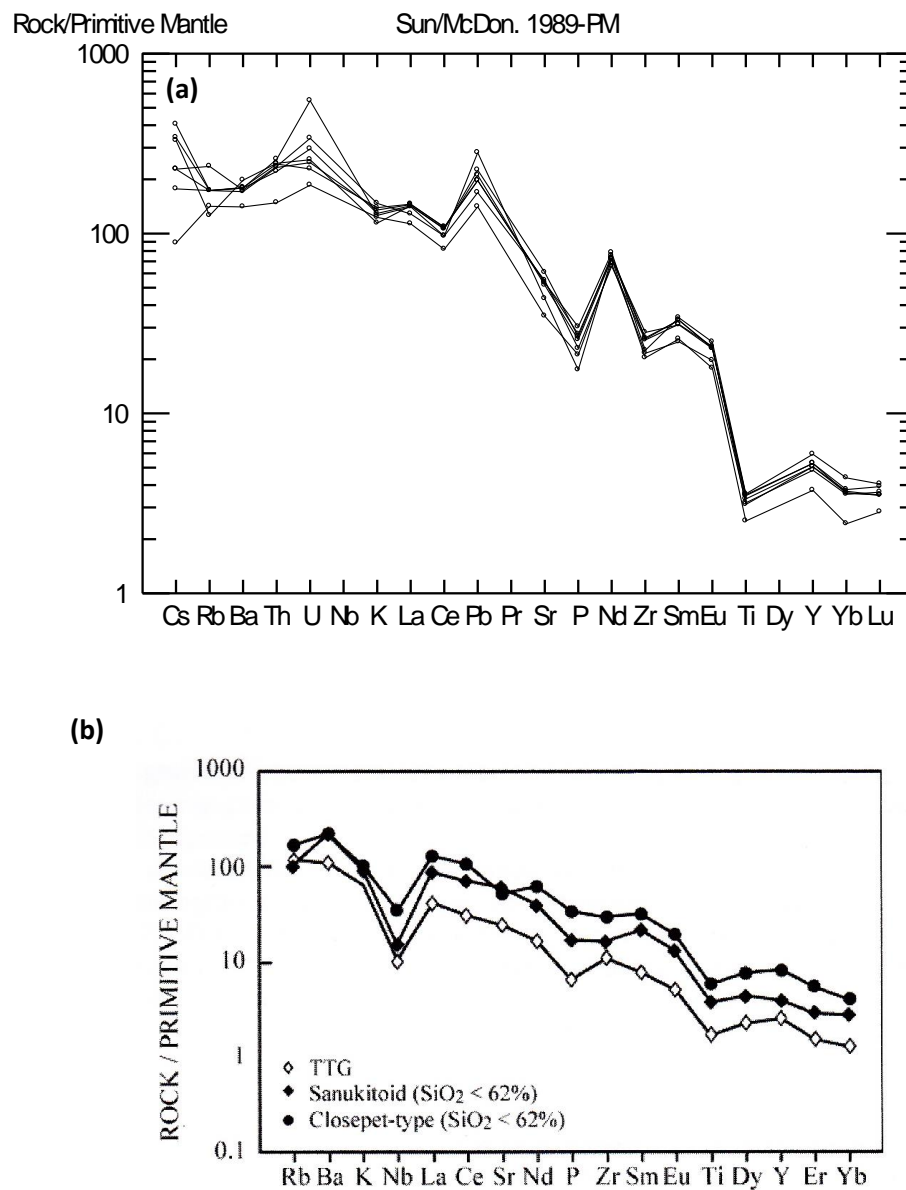


Figure 5.4a,b: (a) Primitive mantle normalized multi-element diagram for the Kurupung; (b) Primitive mantle normalized multi-element diagram for TTG, sanukitoid, and closepet granitoids.

sanukitoids and TTGs are also presented for comparison (Figure 5.4). Chondrite-normalized rare earth element patterns show no Eu anomaly, and a strong enrichment in the incompatible trace elements (LREE) while the heavy rare earth element (HREE) contents are low, resulting in fractionated patterns typical of TTG, sanukitoid and closepet granitoids. On a normalized REE plot, TTG's start at about 100 times chondrite, sanukitoids start at between 110-200 times chondrite while closepet granites generally start at between 500-600 times chondrite on the Y-axis.

The Kurupung generally occurs at approximately 110 times chondrite on the Y-axis making its REE content similar to a sanukitoid pattern. The similarities in REE patterns of TTG's and sanukitoids worldwide suggests that in some instances slab melts can generate TTG granitoids or alternatively can generate sanukitoids from metasomatized mantle (Moyen et al, 2003). For the Kurupung batholith, the primitive mantle normalized spidergram of Sun and McDonough (1989) indicates an overall enrichment in LILE compared to primitive mantle abundances with marked negative Sr, P, Ti and Zr anomalies and positive Th, U, and Pb anomalies.

The negative Sr anomaly can result from extensive plagioclase fractionation, however, this does not hold as the REE patterns do not display the diagnostic negative Eu anomaly. The Sr trough likely reflects Sr-depletion of the mantle source, where fluids derived from Sr-depleted detrital sediments caused the mantle metasomatism. This interpretation also supports the enhanced K, Th, U, and LREE enrichment of the Kurupung, as these elements are also concentrated in terrigenous crust-derived sediments. The negative P, Ti, and Zr anomalies may represent retention by P, Ti, and Zr-bearing phases in the mantle source during partial melting and fractionation in the source region (Laurent, personal communications, December 8, 2013). The concept of preferential transport of REE over HFSE in a hydrous fluid during mantle metasomatism has been well established, and accounts for negative Nb, P and Ti anomalies, enrichment of LILE over LREE, and the lack of dilution of refractory elements such as Mg, Cr, and Ni in these rocks (McCuaig et al., 1994). These anomalies cannot be explained by crustal contamination as the rocks do not show dilution of Mg, Cr, and Ni expected to result

from crustal contamination (McCuaig et al., 1994). Retention of garnet at source due to fractionation is another plausible mechanism to account for the spidergram pattern. Any partial melt with a garnet-rich residuum, or with significant garnet fractionated from it would generate trace element patterns demonstrating LREE enrichment, have a fractionated REE pattern, negative P, Zr and Hf anomalies, and a negative Ti anomaly. The magnitudes of enrichment or depletion would be dependent on the garnet composition, and thus the pressure of melting/crystal fractionation (McCuaig et al., 1994).

5.2 Geochemistry of the Intensely Altered and Mineralized Kurupung Batholith

The mineralized domains in the Kurupung batholith share characteristics of IOCG-style hydrothermal alteration patterns. As such, various metasomatic ion exchanges were expected, most importantly, sodium (Na^+), potassium (K^+), and iron ($\text{Fe}^{2+}/\text{Fe}^{3+}$). Utilizing the geochemical database provided by U3O8 Corp., an effort was made to relate the geochemical data to drill-hole scale and district scale zoning, and to define any unique elemental variations within mineralized domains of the Kurupung batholith as they relate to IOCG-style alteration and mineralization. The following steps were undertaken to manage such an extensive compilation of data:

- 1) a representative suite of 21 rocks were submitted to ActLabs for geochemical analysis to define the compositional trends and element abundances in background to strongly altered Kurupung samples.
- 2) the U3O8 Corp. database was then run through a factor analysis program to establish which elements would correlate positively with U in an effort to define a district scale zoning.
- 3) one drillhole was selected from Aricheng North to demonstrate down hole mass balance variations in an attempt to establish elemental gains and losses related to IOCG-style alteration and mineralization.

The suite of 21 samples submitted to ActLabs are representative of chlorite mylonite, secondary Ba-Kfeldspar megacrystic, and albititic zones in order to define alteration patterns related to mineralization. The following observations were made based on examination of the geochemical results. Within the unaltered Kurupung batholith, the potassium and sodium contents range between 3.70-4.72% K₂O and 3.79-4.78% Na₂O. Within mineralized/altered samples, K₂O ranges from 0.0001-5.62% and Na₂O contents range from 0.0005-9.31%. In samples where K-contents are elevated (5.62%), Ba-Kfeldspar dominates the rock whereas those samples where K-contents are relatively depleted (0.0001%) Na-contents are elevated (9.31%), i.e. the megacrystic Ba-Kfeldspar has been pervasively replaced by albite.

5.2.1 Factor Analysis and Mass Balance (Isocon) Evaluation of IOCG-style Alteration

Two statistical methods were used to treat the extensive geochemical database. The objective of this exercise was two-fold: 1) use Pearson factor analysis (Pearson, 1901) to establish geochemical correlations of key elements associated with IOCG-style alteration to support petrographic and mineral chemical observations outlined in chapter 3; and 2) use mass-balance gains/losses of elements to establish a chemical zoning between a gap in ore shoots in a mineralized area (i.e. does the geochemistry show any zoning that can be used to vector towards mineralization). Methods for both techniques are documented in Appendix C.

5.2.2 Pearson Factor Analysis: Accori and Aricheng Prospects

The Pearson coefficient program was used to establish which elements correlate positively and which correlate negatively with U-Zr mineralization at the various showings comprising the Accori and Aricheng prospects (Figure 5.5). As the alteration assemblages and mineralization within the Kurupung share many characteristics with IOCG deposits, the goal is to establish a correlation of U and Zr with elements commonly associated with the alteration patterns in world class IOCG systems. As these systems are typically associated with intense K- and Na-metasomatism, it would be important to establish a correlation between U and K, Rb, Ba, Na, Sr, Pb, Zr.

The paragenesis of the alteration is important to review at this point. The secondary Ba-Kfeldspar megacrysts are preferentially replaced by later albite growth due to Na-metasomatism accompanying U-Zr mineralization. Inspection of the histogram plots of various elements versus Correlation Indices for the Accori and Aricheng prospects (Figures 5.6 to 5.9a), reveals that U correlates negatively with K, Ba, Al, Rb which are elements associated with Ba-Kfeldspar. In U-mineralized zones where Ba-Kfeldspar is replaced, the elements K, Ba, Al and Rb show a negative correlation with uranium. However, although this negative correlation points to an inverse relationship with the occurrence of U, the degree of negative correlation of K, Ba, Al, Rb does not correlate with a prediction in U grade. That is to say that a greater negative correlation index of these elements does not directly coincide with more uranium.

Na-metasomatism results in the formation of albite(3) within the mineralized zones, accounting for the positive correlation of U with Na. In areas where the K index is negative, the Na index is positive and positively correlates with uranium. Although Na is genetically tied to U mineralogically and temporally, it only demonstrates a weak positive correlation with U on factor analysis plots. The geochemical data are plotted on a U versus Na binary and the results are displayed in Figure 5.9b. It appears that the highest U concentrations are associated with Na values between 1-5%. A number of anomalously elevated ARN, ARS and some ARW samples fall within the ~1 to 5% Na. Here, uranium concentrations reach about 10,000 ppm. An abundant accumulation of data points from all prospects occurs between ~5 to 7% Na. However, uranium concentrations do not exceed ~4000 ppm. It appears that above ~7% Na, uranium concentration drops off. This would suggest that the highest uranium concentrations occur with low Na concentrations (between 1-5%), moderate uranium concentrations occur with more elevated Na concentrations (between 5-7% Na), and low uranium mineralization is tied to high Na concentrations (above 7% Na). These correlations are tied to the degree of cataclasis of the host rocks and the associated abundance of chlorite(2). This phenomena will be discussed further in chapter 6.

At both Accori and Aricheng, there is also a positive correlation between U, Ti, Zr, Pb. The positive correlation of U with Ti accounts for the branneritic ores, the positive correlation of U with Zr accounts for the associated zircon veins found in mineralized zones, and the strong positive correlation of U and Pb is related to Pb being a daughter product of U degradation.

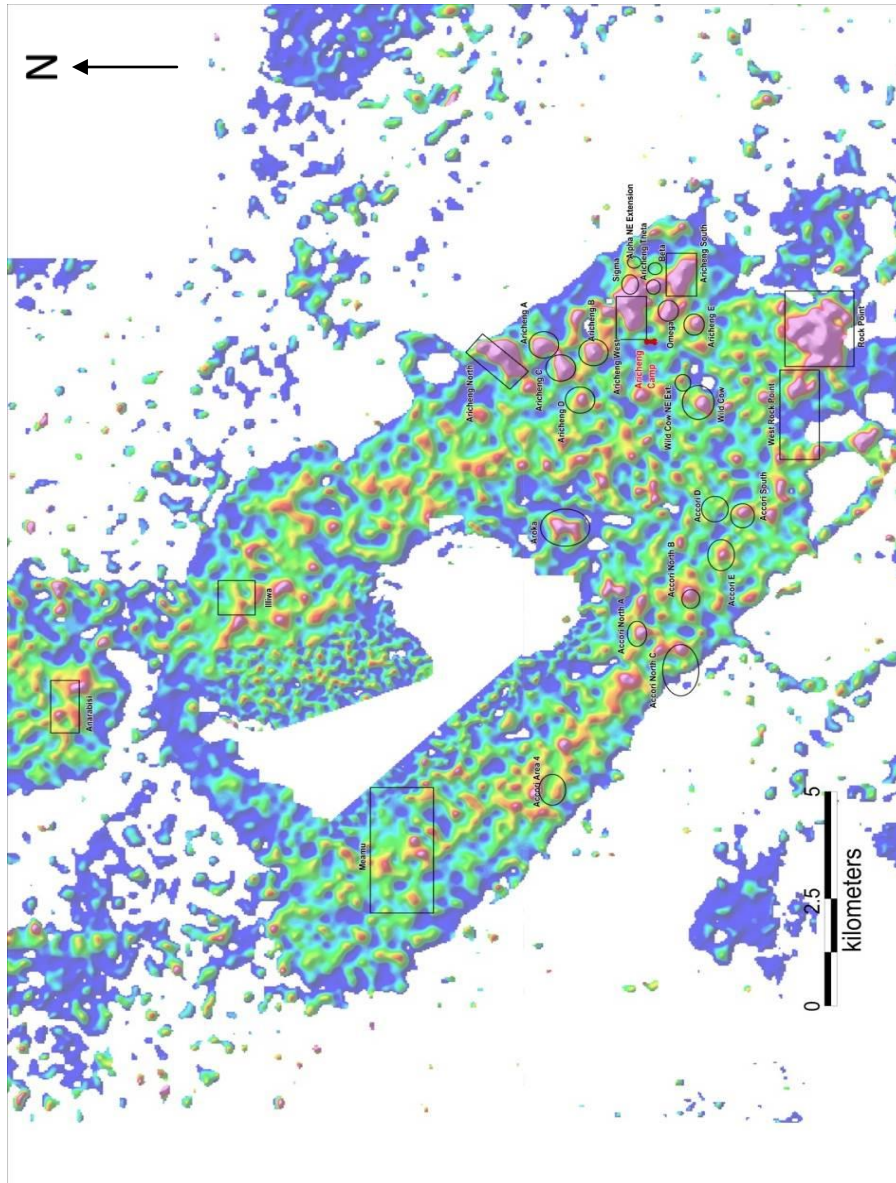


Figure 5.5: A radiometric map of the Kurupung batholith illustrating locations of prospective uranium targets being explored by U3O8 Corp. during this study. From U3O8 Corp., internal files.

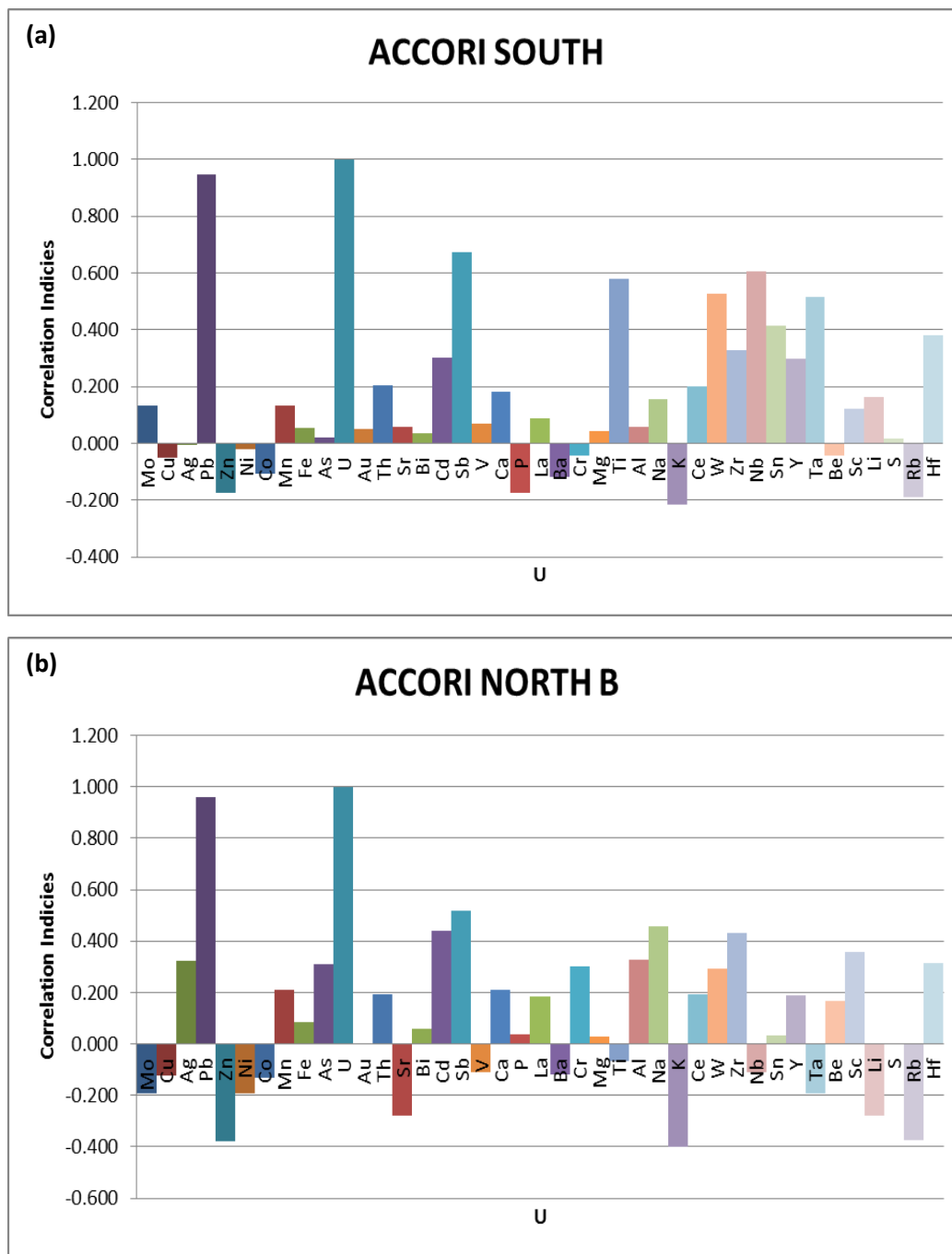


Figure 5.6a,b: (a) Factor analysis diagrams for the Accori South and (b) Accori North B areas.

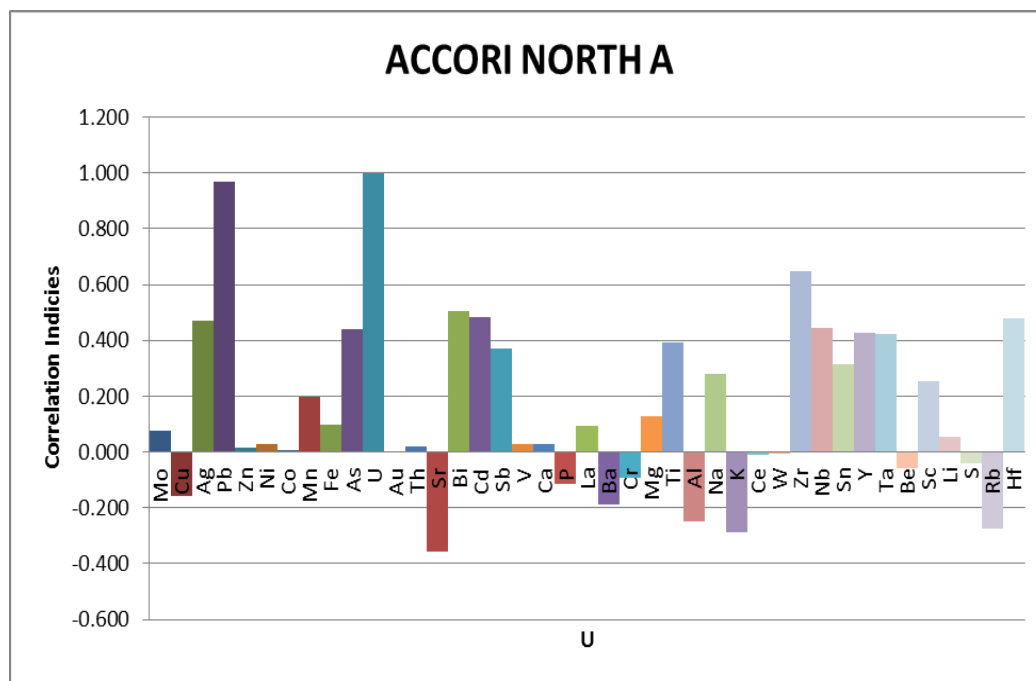


Figure 5.7: Factor analysis diagrams for the Accori North A area.

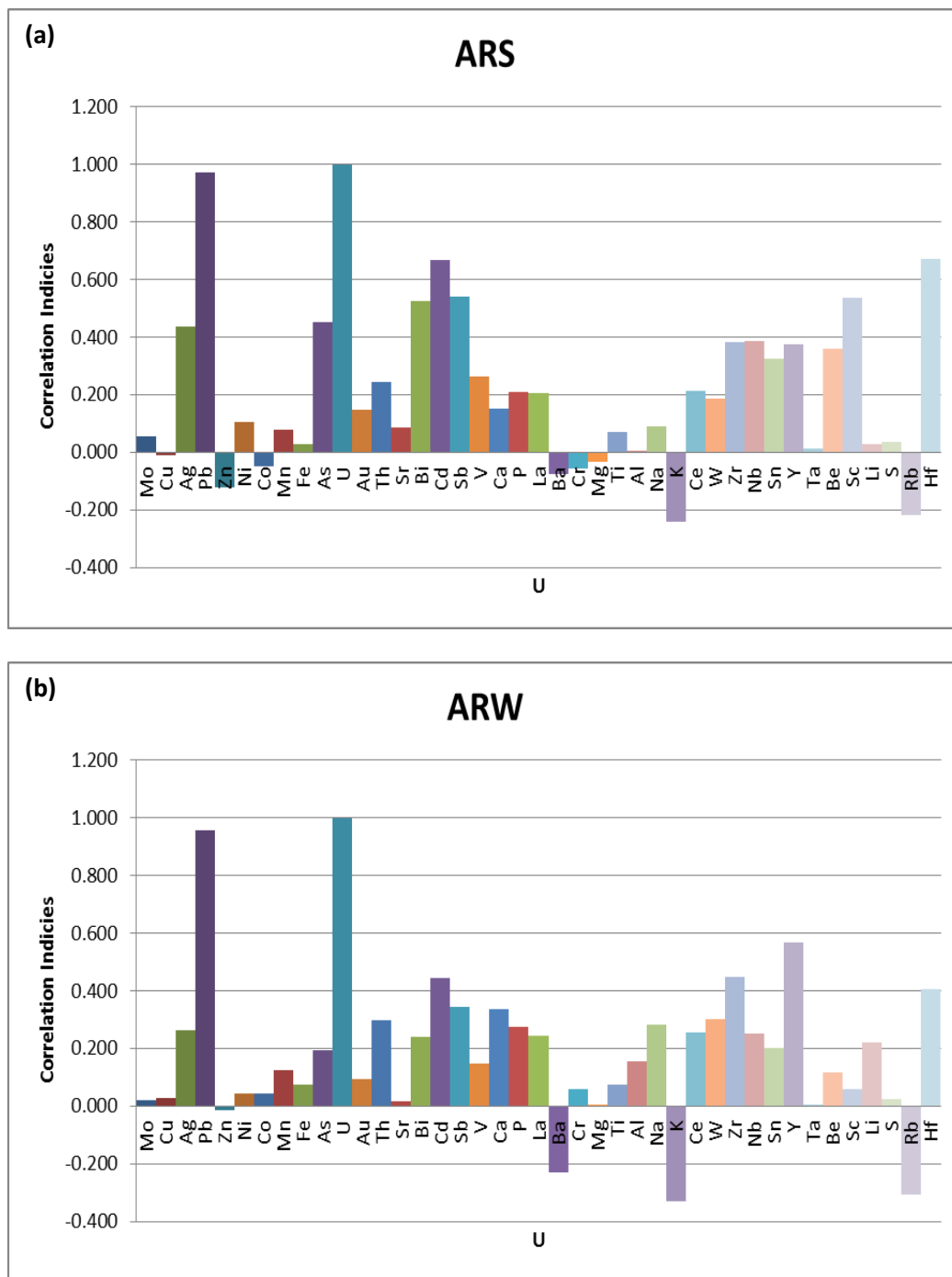


Figure 5.8a,b: (a)Factor analysis diagrams for the Aricheng South (ARS) and (b) Aricheng West (ARW) areas.

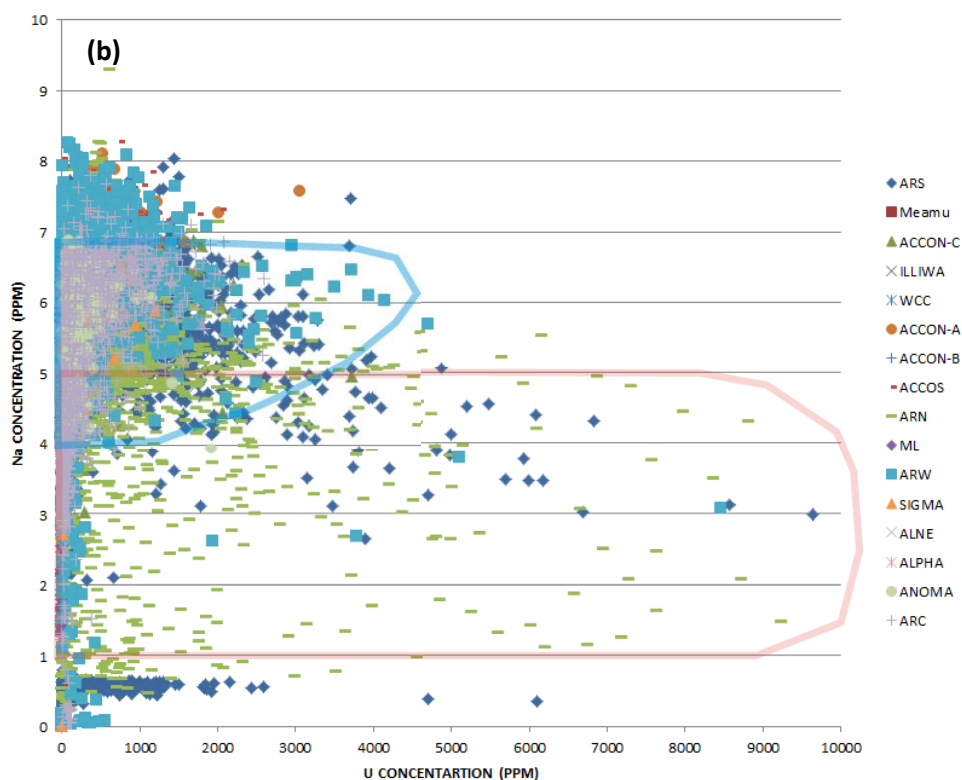
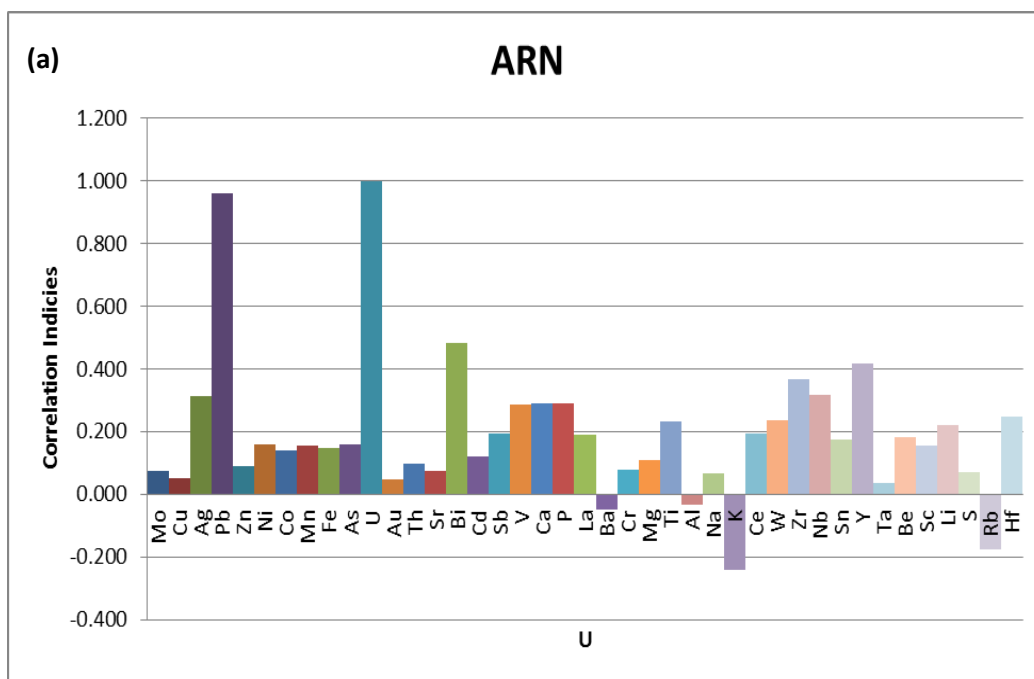


Figure 5.9a,b: (a) Factor analysis diagrams for the entire Kurupung batholith. High U concentrations are associated with low Na concentrations defined by the red loop. The blue loop defines sodium contents between ~4 to 7% Na. Note that above 7 wt% Na, U concentrations diminish.

5.3 Mass-balance Calculations: Drill hole scale analysis

Mass-balance calculations were employed on drill hole ARN-031. The drill log is presented in Table 5.2 and geochemical analyses are presented in Table 5.3. Samples were collected every 2 meters down the drill hole and submitted for geochemical analyses and density measurements. The objective was to identify mass-balance gains and losses of elements (K, Ba, Rb, Na, U, Zr, Pb, Ti) related to alteration patterns associated with IOCG-style deposits. These gains and losses were followed down a drill hole dataset through mineralized and non-mineralized zones. This information could be useful in vectoring drill holes. Mass balance calculations were based on Gresens' statistical computations (Gresen, 1967). The main premise behind Gresens' equation is that some components of the host rock were potentially immobile during metasomatism, and that if these can be identified, they can be utilized to determine the volume change following metasomatism. Gains and losses of elements can then be established assuming the volume change is a factor common to the behaviour of all components (i.e. that the alteration is pervasive and not site specific or localized).

The first aspect in dealing with the altered/metasomatized Kurupung was to establish net gains and losses of elements relative to the unaltered host sanukitoid. Mass balance results in terms of volume and mass change are represented graphically in Figure 5.10. The ore shoots within mineralized shears are highlighted by the yellow boxes. It appears that the alteration and mineralization demonstrate an overall volume gain and mass loss compared to the adjacent bounding, non-mineralized and less altered wall rocks. The volume increase associated with the mylonitic alteration zones is attributed to zones of intense cataclasis and fracturing. A definite trend is noted approaching the mineralized areas with Na₂O demonstrating consistent gain throughout whereas K₂O, Rb, and Ba show a consistent loss. Petrographic examination indicates that these rocks contain abundant albite and hematite and notable lack of Ba-Kfeldspar. In conjunction with gain of Na and loss of K, Rb and Ba, there is an overall mass loss in mineralized zones. The albitization resulted in the demise of primary plagioclase and secondary Ba-Kfeldspar resulting in a loss of Sr with plagioclase and Ba+Rb with Ba-Kfeldspar accounting for

HOLE#		ARN-031		1					
AREA:		Aitching North		CORE DIAMETER:		HQ (0 - 8.70 m) HQ (8.70 - 134.20 mts.)			
COORDINATES:		S04530 E 182252 N		DATE STARTED:		06/06/2008			
INCLINATION:		-80		COMPLETED:		09/05/2008			
AZIMUTH:		140		LOGGED BY:		F. Stearns			
DEPTH:		134.20 mts							

Bar #	From	To	H.Rcv	LITHOLOGY		ALTERATION				MINERALIZATION					CPS	Sample	
				Rock	Texture	Grain S.	Color	Mag Sus	Ab	Chl	SO ₂	Ep	Hem/Il	Spec			Pr
0	1	45	Sh	Phanetic	Medium	Light Green	2	2	1							160	
1	2	55	Sh	Phanetic	Medium	Light Green	2	2	1							160	
2	3	55	Sh	Phanetic	Medium	Light Green	2	2	1							160	
3	4	80	Sh	Phanetic	Medium	Light Green	2	2	1							160	
4	5	85	Sh	Phanetic	Medium	Light Green	2	2	1							160	
5	6	90	Sh	Phanetic	Medium	Light Green	2	2	1							160	
6	7	98	Sh	Phanetic	Medium	Dark Green	2	2	1							160	
7	8	90	Sh	Phanetic	Medium	Dark Green	2	2	1							160	
8	9	95	Sh	Phanetic	Medium	Dark Green	2	2	1							160	
9	10	85	Sh	Phanetic	Medium	Dark Green	2	2	1							160	
10	11	98	Sh	Phanetic	Medium	Dark Green	2	2	1							160	
11	12	98	Sh	Phanetic	Medium	Dark Green	2	2	1							160	
12	13	98	Sh	Phanetic	Medium	Dark Green	2	2	1							160	
13	14	98	Sh	Phanetic	Medium	Dark Green	2	2	1							160	
14	15	98	Sh	Phanetic	Medium	Dark Green	2	2	1							160	
15	16	98	Sh	Phanetic	Medium	Dark Green	2	2	1							160	
16	17	98	Sh	Phanetic	Medium	Dark Green	2	2	1							160	
17	18	98	Sh	Phanetic	Medium	Dark Green	2	2	1							160	
18	19	98	Sh	Phanetic	Medium	Dark Green	2	2	1							160	
19	20	98	Sh	Phanetic	Medium	Dark Green	2	2	1							160	
20	21	98	Sh	Phanetic	Medium	Dark Green	2	2	1							160	
21	22	98	Sh	Phanetic	Medium	Dark Green	2	2	1							160	
22	23	98	Sh	Phanetic	Medium	Dark Green	2	2	2							160	
23	24	98	Sh	Phanetic	Medium	Dark Green	2	2	2							160	
24	25	98	Sh	Phanetic	Medium	Dark Green	2	2	2							160	
25	26	98	Sh	Phanetic	Medium	Dark Green	2	2	2							160	
26	27	98	Sh	Phanetic	Medium	Dark Green	2	2	1							160	
27	28	98	Sh	Phanetic	Medium	Dark Green	2	2	1							160	
28	29	98	Sh	Phanetic	Medium	Dark Green	2	2	1							160	
29	30	98	Sh	Phanetic	Medium	Dark Green	2	2	1							160	
30	31	98	Sh	Phanetic	Medium	Dark Green	2	2	1							160	
31	32	98	Sh	Phanetic	Medium	Dark Green	2	2	1							160	
32	33	98	Sh	Phanetic	Medium	Dark Green	2	2	1							160	
33	34	98	Sh	Phanetic	Medium	Dark Green	2	2	1							160	24230
34	35	98	Sh	Phanetic	Medium	Dark Green	2	2	1							200	24231
35	36	98	Sh	Obiliterate	Medium	Gray	1	3	2							24232	24234
36	37	98	Sh	Obiliterate	Medium	Gray	1	3	2							170	24235
37	38	98	Sh	Obiliterate	Medium	Gray	1	3	2							270	24237
38	39	98	Sh	Phanetic	Medium	Dark Green	2	2	1							180	24239
39	40	98	Sh	Phanetic	Medium	Dark Green	2	2	1							180	24240
40	41	98	Sh	Phanetic	Medium	Gray	1	2	2							180	
41	42	98	Sh	Phanetic	Medium	Gray	1	2	2							2	180
42	43	98	Sh	Phanetic	Medium	Dark Green	2	2	2							2	180
43	44	98	Sh	Phanetic	Medium	Dark Green	2	2	2							2	180
44	45	98	Sh	Phanetic	Medium	Dark Green	2	2	2							2	180
45	46	98	Sh	Phanetic	Medium	Dark Green	2	2	2							1	180
46	47	98	Sh	Phanetic	Medium	Dark Green	2	2	2							1	180
47	48	98	Sh	Phanetic	Medium	Dark Green	2	2	2							1	180
48	49	98	Sh	Phanetic	Medium	Dark Green	2	2	2							1	180
49	50	98	Sh	Phanetic	Medium	Dark Green	2	2	2							1	180
50	51	98	Sh	Phanetic	Medium	Dark Green	2	2	2							1	180
51	52	98	Sh	Phanetic	Medium	Dark Green	2	2	2							1	160
52	53	98	Sh	Phanetic	Medium	Dark Green	2	2	1							1	160
53	54	98	Sh	Phanetic	Medium	Dark Green	2	2	1							1	160
54	55	98	Sh	Phanetic	Medium	Reddish Gray	1	3								2	280
55	56	98	Sh	Phanetic	Medium	Dark Green	2	2	1							1	160
56	57	98	Sh	Phanetic	Medium	Dark Green	2	2	1							1	160
57	58	98	Sh	Phanetic	Medium	Dark Green	2	2	1							230	
58	59	98	Sh	Phanetic	Medium	Dark Green	2	2	1							1	150
59	60	98	Sh	Phanetic	Medium	Green Gray	1	2								1	150
60	61	98	Sh	Obiliterate	Medium	Reddish Gray	1	3								1	400
61	62	98	Sh	Banded	Fine	Reddish Gray	1	3								1	360
62	63	98	Sh	Phanetic	Medium	Reddish Gray	1	2								4	340
63	64	98	Sh	Phanetic	Medium	Dark Green	2	2	1							1	160
64	65	98	Sh	Phanetic	Medium	Reddish Gray	1	3								2	410
65	66	98	Sh	Phanetic	Medium	Reddish Gray	1	2								1	160
66	67	98	Sh	Phanetic	Medium	Reddish Gray	1	3								2	410

67	68	98	Sh	Phanetic	Medium	Reddish Gray	1	3								2	160	24261	24262
68	69	98	Sh	Phanetic	Medium	Reddish Gray	1	2								2	1	190	24263
69	70	98	Sh	Phanetic	Medium	Dark Green	2									1	1	150	24264
70	71	98	Sh	Phanetic	Medium	Dark Green	2									1	1	160	
71	72	98	Sh	Phanetic	Medium	Dark Green	2									1	1	160	
72	73	98	Sh	Phanetic	Medium	Dark Green	2									1	1	160	
73	74	98	Sh	Phanetic	Medium	Dark Green	2									1	1	200	
74	75	98	Sh	Phanetic	Medium	Dark Green	2									2	1	160	
75	76	98	Sh	Phanetic	Medium	Dark Green	2									2	1	170	
76	77	98	Sh	Phanetic	Medium	Dark Green	2									1	1	160	
77	78	98	Sh	Phanetic	Medium	Dark Green	2									2	1	180	
78	79	98	Sh	Phanetic	Medium	Dark Green	2									1	1	150	
79	80	98	Sh	Phanetic	Medium	Dark Green	2									1	1	150	
80	81	98	Sh	Phanetic	Medium	Dark Green	2									1	1	160	
81	82	98	Sh	Phanetic	Medium	Dark Green	2									2	1	180	
82	83	98	Sh	Phanetic	Medium	Dark Green	2									1	1	160	
83	84	98	Sh	Phanetic	Medium	Reddish Gray	1	2								2	1	170	
84	85	98	Sh	Phanetic	Medium	Dark Green	2									1	1	160	
85	86	98	Sh	Phanetic	Medium	Dark Green	2									1	1	170	
86	87	98	Sh	Phanetic	Medium	Reddish Gray	1	2								2	2	160	24267
87	88	98	Sh	Obiliterate	Medium	Reddish Gray	1	3								3	270	24270	24271
88	89	98	Sh	Obiliterate	Medium	Reddish Gray	1	3								3	1	3	270
89	90	98	Sh	Obiliterate	Medium	Reddish Gray	1	3								3	1	3	270
90	91	98	Sh	Obiliterate	Medium	Reddish Gray	1	3								3	2	250	24274
91	92	98	Sh	Obiliterate	Medium	Reddish Gray	1	3								3	2	250	24275
92	93	98	Sh	Obiliterate	Medium	Reddish Gray	1	3								3	2	250	24276
93	94	98	Sh	Obiliterate	Medium	Reddish Gray	1	3								3	2	250	24277
94	95	98	Sh	Obiliterate	Medium	Reddish Gray	1	3								3	2	250	24278
95	96	98	Sh	Banded	Fine	Reddish	1	3								3	3	250	24279
96	97	98	Sh	Obiliterate	Medium	Reddish	1	3								2	2	200	24289
97	98	98	Sh	Obiliterate	Medium	Reddish	1	3								2	2	200	24291
98	99	98	Sh	Obiliterate	Medium	Reddish	1	3								2	2	200	24293
99	100	97	Sh	Banded	Fine	Reddish	1	3								2	2	220	24296
100	101	98	Sh	Obiliterate	Medium	Reddish	1	3								2	1	180	24298
101	102	98	Sh	Phanetic	Medium	Dark Green	2									1	1	170	24300
102	103	98	Sh	Phanetic	Medium	Dark Green	2									1	1	180	24302
103	104	97	Sh	Phanetic															

Sample Interval	1 to 3	3 to 5	5 to 7	7 to 9	9 to 11	11 to 13	13 to 15	15 to 17	17 to 19	19 to 21	21 to 23	23 to 25	25 to 27	27 to 29	29 to 31	31 to 33	33 to 35	35 to 34	
Sample number	50049	50050	50051	50052	50053	50054	50055	50056	50057	50058	50059	50061	50062	50063	50064	50065	50066	24229	24230
Density	2.8125	2.8125	2.8125	2.8125	3.312	3.312	3.312	3.312	3.312	3.312	3.312	3.312	3.312	2.92	2.92	2.92	2.92	2.92	2.92
Element																			
Ti	%	0.457	0.428	0.421	0.383	0.412	0.413	0.405	0.42	0.419	0.403	0.388	0.417	0.35	0.41	0.377	0.377	0.377	0.384
Al	%	7.58	7.5	7.39	7.21	7.25	7.07	7.08	7.4	7.38	7.39	7.16	7.39	6.14	7.21	7.27	7.67	7.67	7.93
Fe	%	3.91	3.69	3.44	3.31	3.21	3.38	3.43	3.27	3.31	3.42	3.21	3.33	2.84	3.32	3.28	3.74	3.74	3.93
Mn	%	0.0698	0.0684	0.0635	0.0603	0.0575	0.0633	0.0671	0.065	0.0642	0.0659	0.0628	0.0607	0.0635	0.0541	0.0638	0.0615	0.0684	0.0697
Mg	%	2.16	2.09	1.88	1.9	1.88	1.92	2.08	2	2.02	1.91	1.88	1.97	1.64	1.89	1.89	2.07	2.07	2.17
Ca	%	2.19	2.28	2.9	2.18	2.76	2.88	3.16	3.11	3.08	3.14	2.99	2.85	2.98	3.04	2.91	3.36	3.36	3.3
Na	%	1.698	2.097	3.048	3.593	3.119	3.13	3.1	3.173	3.111	3.132	3.161	3.469	3.224	3.122	3.4	3.457	3.906	
K	%	3.93	4.04	3.69	2.89	3.59	3.58	3.49	3.66	3.67	3.47	3.77	3.13	3.53	3.17	3.45	3.53	3.03	2.79
P	%	0.225	0.22	0.229	0.232	0.209	0.221	0.237	0.225	0.227	0.229	0.206	0.211	0.227	0.179	0.214	0.204	0.231	0.257
S	PPM	500	500	500	500	500	500	500	500	500	500	500	500	500	500	500	500	500	500
As	PPM	5	6	6	6	5	7	6	6	6	6	6	8	6	6	6	6	6	4
Rb	PPM	97.5	109.6	102.1	107.1	121.7	104.6	107.5	122.9	121.2	123	122.4	106.3	123.1	116.5	111	123.2	127.8	113.1
Ba	PPM	1239	1286	1175	947	1133	1141	1115	1126	1163	1149	1139	1056	1207	967	1115	1099	1110	1280
Sr	PPM	944	969	1169	868	1048	1090	1064	1129	1155	1166	1138	1052	1110	939	1104	1014	1106	1077
Pb	PPM	23.1	23.4	23.2	20.4	23.1	21.7	21.1	21.8	23.1	22.8	23.3	21	22.9	19.9	23.6	23.2	25.3	24.7
Cr	PPM	109	101	90	85	81	95	99	98	96	88	92	94	74	93	87	93	96	
Ni	PPM	79.5	76.4	68.8	65.4	63.1	66.3	69.6	68.9	67.4	68.6	62.5	64.6	65.2	53.5	64.5	60.2	69.2	71.9
V	PPM	102	97	96	91	92	96	96	93	93	94	90	91	94	80	92	91	94	96
Sc	PPM	10	9	8	8	8	8	8	8	8	8	8	8	8	8	8	8	9	8
Zn	PPM	78	71	68	64	63	66	64	65	63	65	63	61	63	55	64	62	70	73
Bi	PPM	0.4	0.5	0.3	0.4	0.4	0.6	0.4	0.4	0.4	0.3	0.2	0.3	0.3	0.2	0.3	0.4	0.8	0.5
U	PPM	3.3	4.9	4.3	23.5	6.8	5.4	6	5.5	5.7	6.3	7.5	13.3	7	5.8	6.4	11.3	6.7	19.6
Zr	PPM	94.3	91.6	92.1	122	84.6	91.1	91.3	77.4	84.1	79.3	82.6	85.7	84.7	76.2	96.2	95.2	100	92.1
Hf	PPM	3	3	3	2.9	2.8	2.8	2.8	2.6	2.4	2.5	2.5	2.7	2.6	2.3	2.9	3	3.5	3
Y	PPM	23.2	20.9	22.8	20.7	21.8	20.8	22.9	22.7	23.2	24.2	22.1	21.2	22.7	19.7	22.4	22.2	22.7	21.3
Nb	PPM	17.7	16.9	17.1	16.3	16.7	15.9	16.2	16.2	17	17.4	17	15.1	17.1	15.2	17.8	15.3	17.5	17.1
Ta	PPM	0.9	0.9	0.9	1	1	0.9	0.9	1	1	1	1	1	1	0.9	1.1	0.9	0.7	0.6
Th	PPM	17.1	19.2	18.6	20.8	21.5	16.7	18.2	21.3	20.6	21.2	18.7	23.1	19.1	21.3	21.7	28.5	24.2	
La	PPM	64	64.9	66.8	66.2	69.5	60.7	68.8	70.1	68.8	74.8	71.7	64.1	74.1	62.6	65.5	70.8	91.6	86.4
Ce	PPM	154	154	156	155	164	145	162	162	166	177	166	154	169	144	151	163	197	194
Mo	PPM	1.7	1.7	2.2	1.7	1.9	2.3	2	2.2	2.3	2.1	2	2.1	2.3	2	2.4	2	1.9	2.2
Cu	PPM	92.5	86.8	98.4	102.4	102.3	85	95.3	81.4	103.3	104.4	85.9	88.8	105	85.3	95.5	97.6	124.3	128.7
Ag	PPM	<0.1	<0.1	<0.1	0.1	0.1	0.1	<0.1	<0.1	<0.1	<0.1	<0.1	0.1	0.1	<0.1	0.1	<0.1	0.05	0.05
Co	PPM	22.5	20	19.3	18.4	16.9	18.7	19.7	18.2	18.3	19.6	17.5	17.7	18	15.2	18	17.6	19.8	19.9
Au	PPM	<0.1	<0.1	<0.1	<0.1	<0.1	<0.1	<0.1	<0.1	<0.1	<0.1	<0.1	<0.1	<0.1	<0.1	<0.1	<0.1	0.05	0.05
Cd	PPM	<0.1	0.2	<0.1	0.1	<0.1	0.1	0.2	<0.1	0.1	0.1	0.2	<0.1	<0.1	<0.1	0.2	0.1	0.2	0.2
Sb	PPM	0.7	1	0.8	0.7	0.7	0.8	0.8	1.1	0.9	0.9	1	1.1	0.9	1	0.9	0.9	0.7	
W	PPM	1.4	1.1	1.1	1.3	1.5	1.5	1.4	1	1.3	1.6	1.4	1.5	1.5	2	1.8	1.7	1.3	
Sn	PPM	1.2	0.9	0.9	0.9	0.9	0.7	0.8	1	0.9	0.9	0.9	0.9	0.8	0.9	0.8	0.9	1.1	1.1
Be	PPM	3	3	4	4	3	3	3	3	3	3	4	4	4	4	4	4	4	4
Li	PPM	29.6	26.8	23.9	41.6	26.2	23	22.2	20.9	22.3	22.4	21.2	23.5	22.3	18.2	20.7	26	28.1	37.5

Table 5.3: A table of geochemical analyses pertaining to drill hole ARN-031. The geochemical data represented here only pertains to the first 34m of drill core. Note that the 2000-series sample numbers are samples originally selected by U3O8 Corp. for geochemical analysis of the prospective areas of the drill core with high CPS. These sample numbers are located on the drill log in Table 5.2. The 5000-series sample numbers were selected for mass-balance calculations and were collected from the various intervals detailed in this table. Density measurements were carried out by U3O8 Corp. See Appendix C for complete analytical package of drill hole ARN-031.

some of the overall mass loss. The pervasive hematization associated with albitization resulted in reddening of albite(3) within ore shoots. The chlorite(1) replacement of early magnetite, the chlorite(2) development in zones of cataclasis, and the pervasive hematization associated with albite(3) development are possibly the most important cause of mass loss within the alteration and mineralized areas. This iron loss is not demonstrated in the mass balance calculations as total iron is presented as Fe_2O_3 . Where the Fe^{3+} component of magnetite has been lost, the Fe^{2+} component of black chlorite(2) and hematite are now present and mask this petrographic observation. The magnetic susceptibility is recorded in Table 5.2. It supports the observation that destruction of magnetite by chlorite(1) and pervasive hematization associated with albite(3) causes a decrease in magnetic susceptibility within mineralized zones.

Adjacent to each yellow box is a red arrow (Figure 5.10). The red arrows point in the direction of volume decrease on either side of the ore shoots. Points of elevated uranium concentrations are represented by the green circles. Uranium mineralization is the highest at the point of dramatic volume increase compared to adjacent rocks. This concentration of U minerals likely represents the presence of abundant chlorite(2) and the magnetite-hematite buffer where redox reactions were most intense as fluids infiltrated the zone of cataclasis. The samples with the greatest uranium concentrations show an overall volume loss and mass loss. The overall volume loss here is potentially due to the sealing of the cataclasite domains with black chlorite(2) and subsequent enrichment of U and Zr. The mass loss in these areas is once again attributed to the oxidation of magnetite to hematite within mineralized zones. Areas between ore shoots demonstrate an overall volume loss and are characterized by few fractures and intense K-metasomatism. Interestingly, the greatest overall mass gains occur between ore shoots and are generally associated with localized U, Pb, Ba anomalies in zones of Ba-Kfeldspar enrichment. The presence of U and Pb in zones of Ba-K metasomatism may simply reflect a localized site specific zone of fluid ingress during the mineralization event.

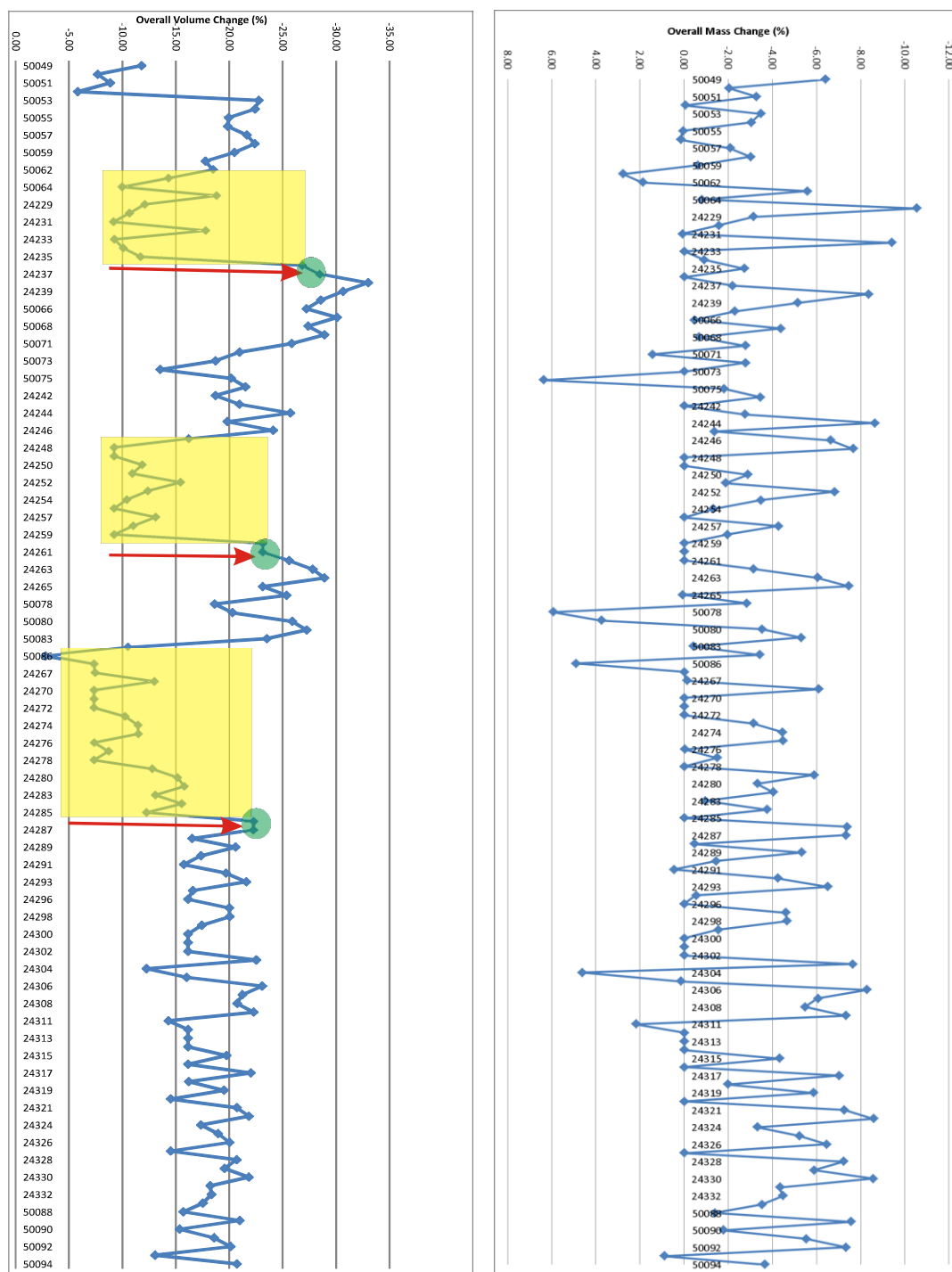


Figure 5.10: Graphical representation of mass balance results from drill hole ARN-031 illustrating overall volume change and overall mass change with respect to sample number. The yellow squares represent the alteration and mineralized zones; red arrows point in the direction of overall volume loss; green dots represent the areas of most elevated uranium concentration down the drill hole. A mass balance summary table is presented in Appendix C, Table 2).

Chapter 6: Discussion

6.0 Introduction

The following discussion synthesizes details presented in chapters 1-5. It first addresses the paleotectonic setting and emplacement of the Kurupung batholith, stressing the importance of Cr-bearing mantle derived mineralogy and its sanukitoid characteristics. The origin and significance of the development of secondary Ba-Kfeldspar and subsequent Na-metasomatism within zones of U-Zr mineralization is then considered. Finally, a discussion is presented identifying the associated sodic alteration and uranium mineralization within the Aricheng district characteristic of albitite-type IOCG uranium deposits.

6.1 Tectonic Setting

The Paleoproterozoic setting of the uranium in the Aricheng district relates to the Transamazonian orogenic cycle (Hurley et al., 1967). The Amazon craton was formed as a result of progressive Proterozoic crustal accretion onto an older Archean nucleus. The oldest parts of the craton demonstrate Archean basement enclaves within juvenile Paleoproterozoic volcano-sedimentary arc assemblages of the Barama-Mazaruni Supergroup. The Transamazonian cycle comprises collisional Rhyacian (2.26-2.08 Ga) and post-collisional Orosirian (2.07-1.96 Ga) orogenic stages. The Late Rhyacian to Early Orosirian transition is marked by continental-scale sinistral shearing with synkinematic emplacement of Mg-K granitoids enriched in uranium (Delor et al., 2003, Baker, 2008). Sinistral strike-slip faulting and related mylonitic shearing facilitated the unroofing of the orogenic infrastructure. The post-collisional strike-slip transpressional shearing event is represented at surface by Haimaraka sedimentation in strike-slip related fault basins (Baker, 2008).

Many Proterozoic mobile belts have deformed sedimentary and volcanic successions occupying narrow troughs (keels) surrounding domes of gneissic basement and granitic plutons (Marshak 1999; Marshak et al., 1997). The sequence from emplacement of calc-alkaline batholiths to uplift and unroofing to alkaline plutonic volcanic complexes occurs

in less than 100 Ma and documents the switch from orogenic to anorogenic conditions (Bonin, 1990). Extensional domains in compressional regimes are important for rapid unroofing. Uplift rates of up to 2-20 kilometres per million years have been documented in places such as the Shuswap and Catalina Core Complexes, North American Cordillera (Fayon et al., 2004). Fault zones accommodating rapid uplift and exposure of the orogenic infrastructure are characteristically mylonitized (Davis et al., 1983). K-bearing fluids commonly modify sheared rocks by growth of secondary Kfeldspar. Well described case histories include the investigation of the Bill Williams Mountains, western Arizona (Collins, 1998) and of several granitic bodies in the Whipple Mountains, southern California (Podruski, 1979).

6.2 Implications Regarding Mantle Source of the Kurupung Batholith

The Kurupung batholith hosts petrographically significant mantle derived aggregates containing Cr-clinopyroxene and Cr-hornblende exsolution lozenges. The simply twinned Cr-clinopyroxene at the centers of these aggregates display spectacular compositional zonation. The Cr-Na-Al-rich clinopyroxene cores are interpreted to represent aggregates preserved during partial melting of slab metasomatized upper mantle. The Cr-rich cores are comprised of 0.1 – 1.27 wt % Cr_2O_3 , 1.14 – 5.94 wt % Al_2O_3 and 0.22 – 1.04 wt % Na_2O . These cores are zoned outwards to Cr-augite which have lower Cr-Na-Al contents. This Cr-augite growth coincides with exsolution of Cr-Ti-magnetite lamellae. Lozenge-shaped lamellae within core Cr-clinopyroxene also demonstrate a zonation from Cr-edenite (up to 0.34 wt% Cr_2O_3) to intermediate Cr-magnesianhornblende (up to 0.68 wt% Cr_2O_3) to outer margins of Cr-depleted magnesianhornblende. The Cr-edenite exsolved out of the Cr-clinopyroxene under more hydrous conditions and generated the lozenge-shaped lamellae. The development of Cr-magnesianhornblende coronas indicate rapid depressurization and more hydrous conditions associated with unroofing. The Cr-amphibole is overprinted by growth of actinolite related to upper greenschist facies metamorphism. The batholith is situated within a regional mylonitic fault. Retrograde metamorphism produced the mineral assemblage biotite, actinolite and titanite replacing the earlier Cr-amphibole. In the

domain of intense shearing along the eastern margin of the batholith, this assemblage has been completely replaced by chlorite(1). Clinopyroxene in ultramafic rocks are characterized by high Cr_2O_3 contents (Aoki and Shiba, 1973). The chemical compositions of Cr-bearing pyroxenes and amphiboles are a sensitive indicator of pressure and temperature conditions during their crystallization. The jadeite component of clinopyroxene is a pressure induced substitution of Na and Al into the pyroxene structure. The pressure induced Na-Cr substitution into the jadeite molecule generates the kosmochlor-euryite molecule. The tschermak molecule is a result of tetrahedral (Al^{IV}) substitution into the clinopyroxene structure and is a sensitive indicator of thermal conditions. Eclogitic clinopyroxenes show a near 1:1 correlation between Na and Al corresponding to accommodation of a jadeite component into the clinopyroxene structure. The jadeite component ($\text{NaAlSi}_2\text{O}_6$) indicates a high pressure substitution into clinopyroxene (Aoki and Shiba, 1973). An excess of Al over Na for Al-rich clinopyroxene is indicative of an additional tschermaks component (Stachel and Harris, 2007). There are numerous clinopyroxene classification diagrams used in diamond exploration. The Al-Cr-Na projection is the most versatile ternary in that a variety of important pyroxenes molecules can be annotated in one plane. Clinopyroxene data from the Kurupung batholith shows the possible molecular allocations for Al, Na, and Cr (Figure 6.0). Notably, the distribution of the majority of clinopyroxenes from kimberlites plot along the compositional line between jadeite and kosmochlor molecules. This indicates that the substitution of Al, Na, and Cr into the clinopyroxene structure at elevated pressures is controlled by these two molecules. It also implies that at elevated pressure, most aluminum enters the clinopyroxene structure as the jadeite molecule and not calcium tschermakite (Morris et al., 2002). The Kurupung batholith clinopyroxene data show two trends on the diagram. The elevated chrome contents associated with mantle-equilibrated aggregates suggests a pressure induced substitution of Al-Cr-Na into the pyroxene structure similarly noted in the jadeite-kosmochlor molecules of clinopyroxenes from kimberlite-hosted xenoliths. The data points falling outside the delineated field suggests that Al and Cr enter the pyroxene structure in the form of calcium tschermakite (CATS) and kosmochlor. It would be expected that the aluminum

associated with the Cr-Al-poor augites would enter the clinopyroxene structure in the form of tschermak molecule. A plot of urreyite substitution versus Ca number for clinopyroxene is presented below (Figure 6.1). This plot illustrates that a strong urreyite component has elevated Al+Cr+Na substitution into the clinopyroxene structure corresponding with a low calcium number at elevated pressures. The plot also illustrates that when Al+Cr+Na substitution decreases the corresponding calcium number increases with decreasing pressure, reflecting a stronger tschermak molecular substitution. The Cr-clinopyroxene microprobe data was used to provide an estimate of the pressure-temperature conditions associated with the origin of mantle derived constituents of the batholith (Figure 6.2). This is demonstrated by the single crystal clinopyroxene geothermobarometer by Nimis and Taylor (2000).

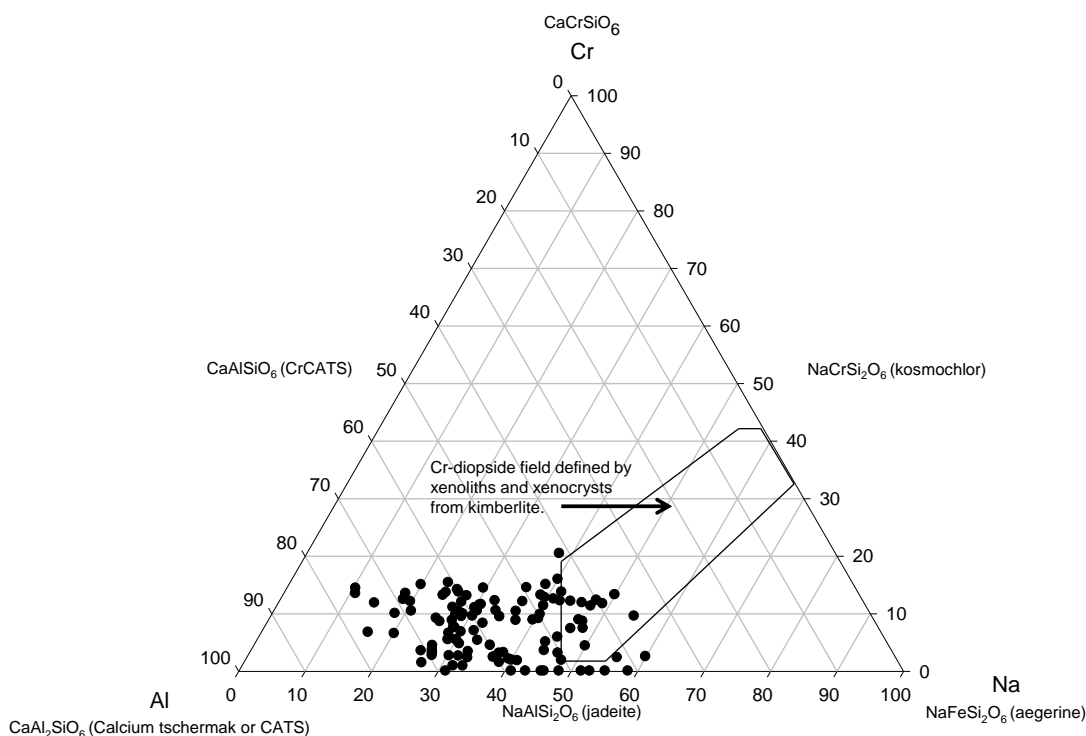


Figure 6.0: Ternary diagram illustrating the substitution of Al, Na, and Cr into the clinopyroxene structure as high pressure jadeite-kosmochlore and lower pressure CATS-kosmochlore.

Ureyite vs. Calcium Number

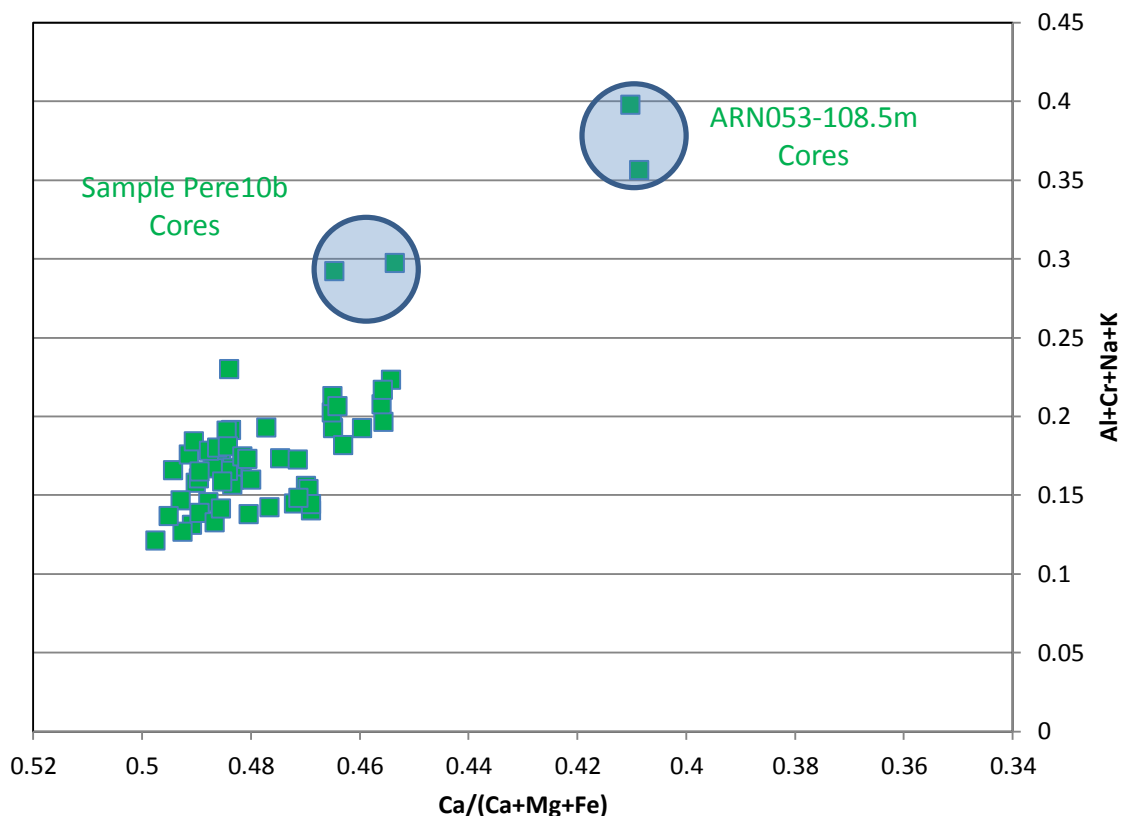


Figure 6.1: A plot of ureyite versus calcium number. The plot illustrates an elevated ureyite component corresponding with a low calcium number at high pressure and a stronger tschermak substitution at lower pressures.

This geothermobarometer is used to estimate P-T conditions for diamond-bearing lherzolite xenoliths in kimberlites which establish the reliability of the thermobarometer. Chromian diopside is defined as a clinopyroxene with greater than 0.5 wt% Cr_2O_3 . They occur as phenocrysts in primitive alkaline magmatic rocks, xenocrysts of mantle origin, or as a constituent of peridotite or pyroxenite xenoliths from the upper mantle (Nimis and Taylor, 2000). It was demonstrated by Nickel (1989) that the Cr-substitution is pressure dependent. The Cr-clinopyroxene data of the Kurupung was plotted on the Nimis and Taylor thermobarometer to evaluate the PT conditions of the earliest stages of partial melting in generation of the sanukitoid melt that generated the Kurupung batholith. Utilizing the methodology of Nimis and Taylor, the clinopyroxene data population from the Kurupung mafic clots was processed through a spreadsheet calculation program

which essentially utilizes the clinopyroxene mineral chemistry and generates a P-T condition using data points containing >0.5 wt% Cr_2O_3 . When plotted on the Nimis and Taylor geothermobarometer, the data points plot from below the 35mW and above the 45mW geotherm. The Kurupung data points form an arcuate trend that spans a temperature range of 98-1133°C and a pressure range of 6-33 Kbar. The points which fall below 500°C are not considered of interest in diamond research and are used here only to display the arcuate trend of data points defining the evolution of the Kurupung batholith. This arcuate trend transects the various geotherms and is clearly a reflection of complex variations in the P-T regime that existed in the generation and emplacement of the Kurupung batholith. This trend is a direct reflection of the core to margin variation of the glomerocystic mafic aggregates.

The core to marginal variation of the clinopyroxene provides further P-T constraints. There is an interesting cluster of points that plot to the far right of the graph above the 45mW geotherm. These 4 points are important as they are the most Al-rich compositions of the entire dataset. These are interpreted to represent the most primitive cores of the clinopyroxenes. It is significant that these 4 data points were derived from clinopyroxenes from two different samples collected from the Kurupung batholith, specifically samples ARN053-108.5m and PERE 10b. Based on detailed petrographic examination and mineral chemical analyses, these two samples represent the most primitive and unaltered rocks of the Kurupung.

Samples ARN053-108.5m and PERE 10b contain excellent examples of simply-twinned Cr-bearing clinopyroxene grains with well-defined core to margin mineral chemical variation. The central core region is accentuated by fine-scale Cr-Ti-magnetite exsolution lamellae. The central clinopyroxene domain was analyzed in detail to establish the most primitive core composition. When plotted on the Nimis and Taylor plot (Figure 6.2), the most primitive Na-Al-Cr-rich core compositions plot furthest to the right at 998-1133°C and 18-23 Kbars while the margins with lower Na-Al-Cr are more

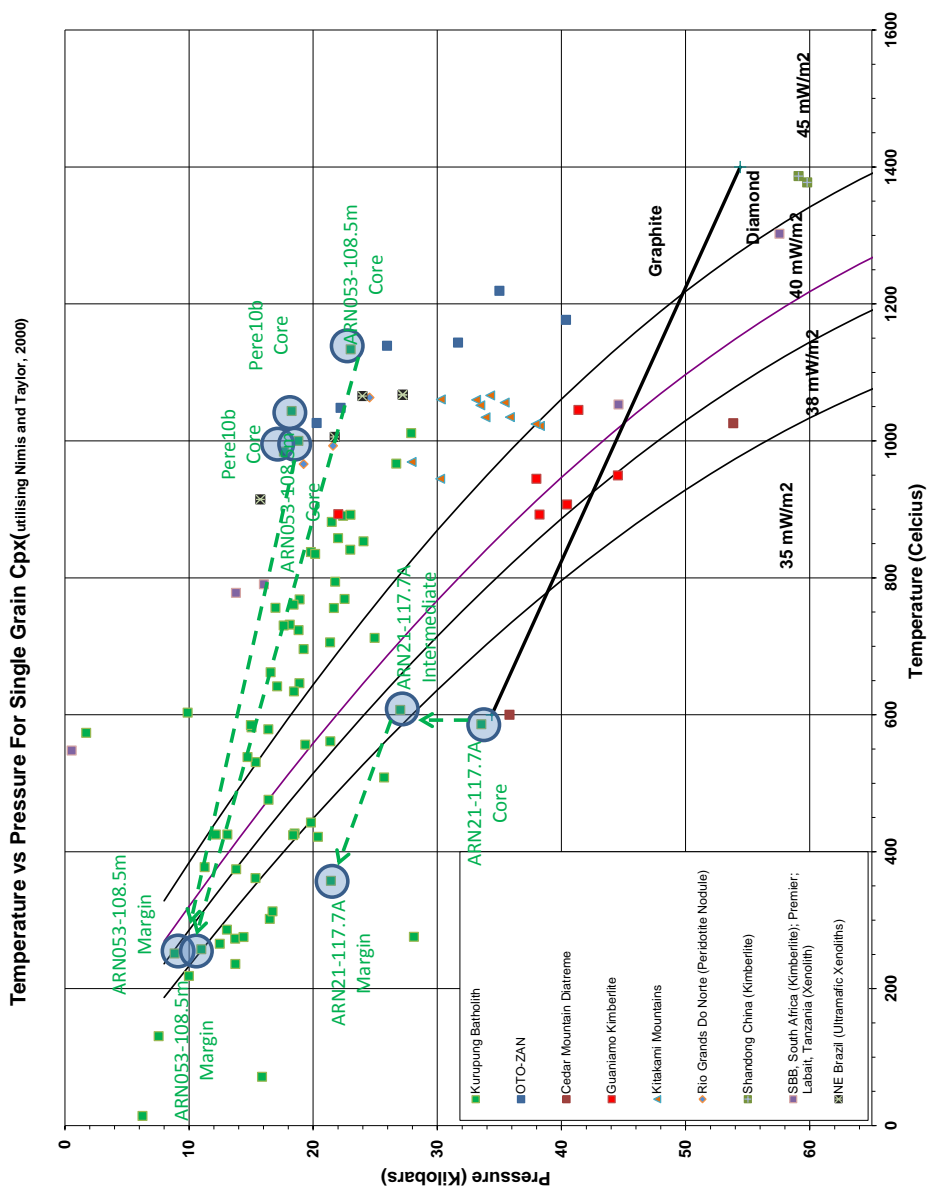


Figure 6.2: The geothermobarometer of Nimis and Taylor (2000) which allows precise determination of P-T conditions of Cr-clinopyroxene with >0.5 wt% Cr₂O₃. Due to the lack of clinopyroxene mineral chemistry of other sanukitoids, the Kurupung batholith dataset is plotted here with Cr-clinopyroxene compositions of xenoliths from various kimberlites worldwide as a comparison.

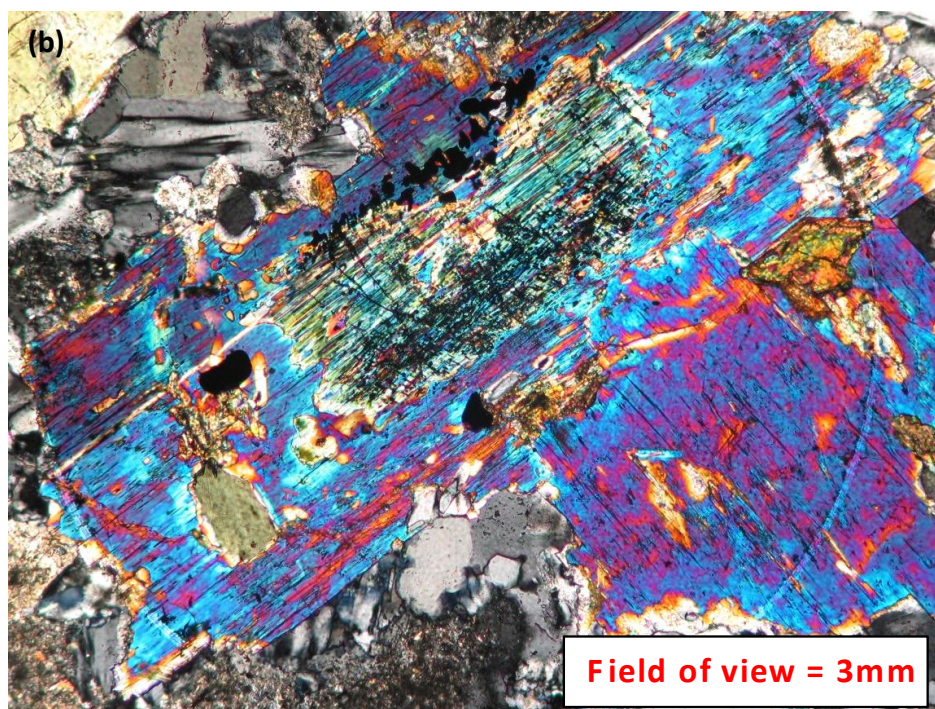
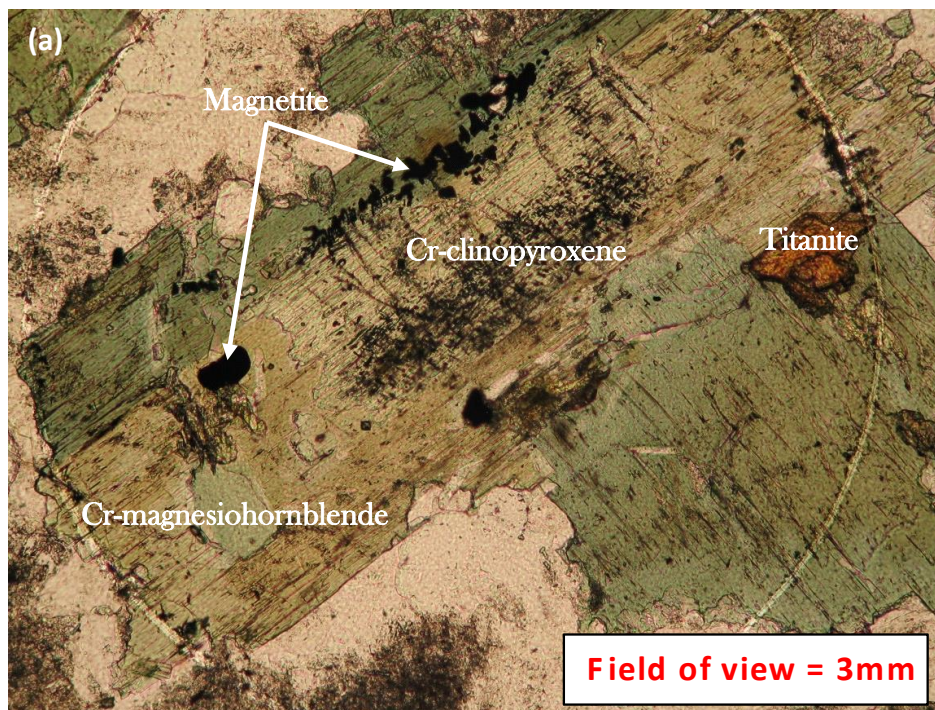


Plate 6.0a,b: Sample #ARN021-117.7A: (a) Plane light photomicrograph illustrating the most primitive relict Cr-clinopyroxene core region in the study accentuated by fine-scale Cr-Ti-magnetite exsolution lamellae; (b) Crossed polarized image illustrating the birefringent Cr-clinopyroxene core mantled by a highly birefringent corona of Cr-magnesiohornblende.

augitic and plot further to the left at 245-268°C and 8-13 Kbars. Another important sample is ARN21-117.7A (Plate 6.0) as this includes numerous aggregates containing simply-twinned Cr-bearing clinopyroxene with well-defined core to margin mineral chemical variation. The central uniform core region is again surrounded by a zone of herringbone texture, accentuated by fine-scale Cr-Ti-magnetite exsolution lamellae alternating with Cr-amphibole. The core clinopyroxene composition of this grain provides the deepest pressure condition for the Kurupung batholith. The backscatter image displayed in Plate 6.1 shows analytical locations 4 and 6 which represent the most primitive core compositions along an interior twin plane. This composition of most interest straddles the diamond-graphite line at 33.5Kbars and 589°C along the 35mW geotherm. This particular point is important as it suggests the original partial melt of the Kurupung originated near the diamond-stability field in the mantle at approximately 100Km depth. It is important to compare this data point to the most elevated PT analysis of sample ARN053-108.5m. The P-T condition of sample ARN053-108.5m was 1133°C and 23Kbars, corresponding to elevated P coincident with elevated T. In contrast, the data point from ARN21-117.7A, plots at 33.5 Kbars and 589°C, corresponding to elevated P and low T along a colder geotherm. The implication here is that the partial melt that generated the Kurupung batholith sampled aggregates from a deeper and colder mantle root at approximately 100Km depth, at or near a pressure enabling the stability of diamonds, and also sampled aggregates at shallower depths near the crust-mantle boundary.

The distribution of data points forms an arcuate trend across the array of geotherms on the Nimis and Taylor plot. This arcuate pattern shows a trend from samples with an elevated ureyite-jadeite component in the Cr-clinopyroxene to the far right of the diagram representing mantle conditions, whereas compositions with lesser Cr and octahedral Al and a stronger tschermakitic substitution plot to the far left of the diagram and represents compositions of clinopyroxenes that formed under ever-decreasing PT constraints. For instance, in sample ARN053-108.5m, the grain with the maximum chrome content of 1.27 wt% Cr₂O₃ and aluminum content of 5.66 wt% Al₂O₃ has an octahedral Al

occupancy of .084 which represents simultaneously the highest ureyite-jadeite component of the dataset. The clinopyroxene with the lowest ureyite-jadeite component and strongest tschermakite component plots furthest to the top left and has lower chrome content of 0.60 wt% Cr_2O_3 and lower aluminum content of 1.50 wt% Al_2O_3 with an octahedral Al content of 0.004. The sensitivity of the octahedral Al content of the clinopyroxene is therefore important in establishing the pressure conditions involved in magma genesis through ascent, emplacement, and cooling. The decrease in octahedral Al content from the most primitive clinopyroxene composition to the most evolved composition illustrates the decrease in pressure induced substitutions of Cr and octahedral Al in the clinopyroxene structure from 23Kbars to shallow crustal conditions.

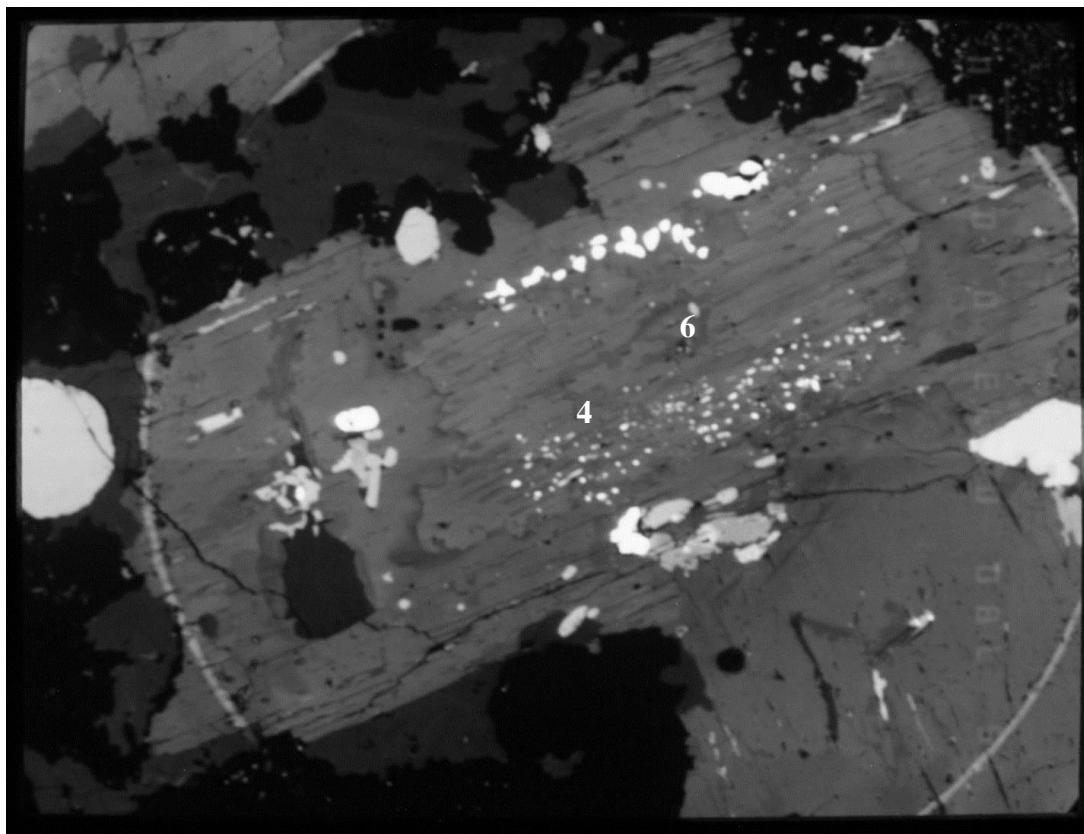


Plate 6.1: Sample #ARN021-117.7A: Backscatter image illustrating the relict Cr-clinopyroxene core representing the most primitive compositions obtained in the study. Numbers 4 and 6 pertain to analytical locations represented in Appendix A Table 1 (analyses 104 and 107).

The Nimis and Taylor geothermobarometer is idealized for mantle conditions between the range 900 to 1600 °C and 0 to 75 Kbars. However, the main purpose of using this diagram is to establish the initial PT melt parameters of the Kurupung batholith. The arcuate pattern of data points in Figure 6.2 defines a transition from higher pressures and temperatures to lower pressures and temperatures from upper mantle conditions to upper crustal conditions. This is also reflected in the mineral chemistry by high Cr-diopsidic cores and Cr-depleted augite mantles. Also plotted on the Nimis and Taylor plot (Figure 6.2) are comparative microprobe analyses of Cr-bearing clinopyroxenes from kimberlites, nodules, and xenoliths from various localities around the world. The sanukitoids from the Kitakami mountains in Japan are also plotted on this diagram and show a similar mantle origin to the Kurupung.

The exact P-T condition of the Cr-poor and Al-poor clinopyroxene grains cannot be established using the Nimis and Taylor plot due to the program's limitations for use in estimating P-T conditions of the mantle and not the crust. As such, the geothermometer of Kretz (1982) was used to estimate the temperature of formation of these more crustal clinopyroxene compositions. The main premise behind Kretz's thermometer is that the difference in the Ca:Mg:Fe ratios of metamorphic and igneous clinopyroxene compositions can be used to establish a temperature. The grain of most elevated Cr-clinopyroxene from the Kurupung batholith was run through Kretz's equation and gave a temperature range of 1104-1174°C compared to the 1133°C from Nimis and Taylor. In an effort to estimate the temperature associated with the formation of the Cr-poor clinopyroxenes, Kretz's equation was used on the lowest Cr-Al composition from the dataset. The Kretz equation yielded a temperature of approximately 536°C for Cr-augite which coincides with onset of Cr-amphibole stability within an environment with increasing water fugacity allowing the stability of aluminous-chrome-rich amphibole coronas.

Although the Nimis and Taylor plot was designed to evaluate P-T of mantle conditions of the source magma, it is used here to illustrate the unroofing history of the Kurupung.

Since the geothermobarometer is not intended for estimating crustal conditions, data points plotting below $\sim 500^{\circ}\text{C}$ are considered suspect by researchers. However, it illustrates the unroofing history of the Kurupung from upper mantle conditions ($\sim 33\text{Kbars}$ and 11330°C) to upper crustal conditions ($\sim 9\text{Kbars}$ and 536°C). This unroofing and cooling history is also reflected in the mineral chemistry from high Cr-diopsidic cores to Cr-depleted augite and Cr-amphibole margins. The Cr+Al versus Na binary plot of Sobolev et al. (1992) illustrates a similar spread in the Kurupung dataset with the most primitive compositions plotting in the spinel peridotite field and the more evolved compositions plotting to left of this field (Figure 6.3).

6.3 The Kurupung Batholith: A Post-Collisional Sanukitoid

Geochemical classification of the Kurupung indicates that it is a post-collisional metaluminous monzonite to quartz-monzonite granitoid belonging to the high-K calc-alkaline to shoshonitic series that captures a hybrid “low-Ti sanukitoid” mantle signature. Laurent et al., (2013) points out that both low- and high-Ti sanukitoid melts are derived from mantle peridotite. Low-Ti sanukitoids are best explained by a “one-step” hybridization of silicate melt and mantle peridotite in equilibrium with clino- and orthopyroxene. Experimental results on low-Ti sanukitoids show they are derived from high-pressure ($> 2.5\text{GPa}$) interactions between high volumes of silicate melt and mantle peridotite. These petrogenetic conditions can be explained by a model which considers the migration of slab-related silicate melts, which progressively consume mantle by melt-rock interactions during their upward percolation. Figure 6.4 illustrates a series of subduction zone cross-sections detailing melting conditions of the subducted slab through time. The Kurupung would appear to model process 3 or 4 on Figure 6.4, where slab melts are consumed in the mantle *or* the slab metasomatizes the mantle.

Classification diagrams presented in earlier chapters identifies the Kurupung batholith as an A-type granitoid. Although the Kurupung is not a typical A-type granitoid due to its mantle characteristics, the classification implies the Kurupung originated in the non-

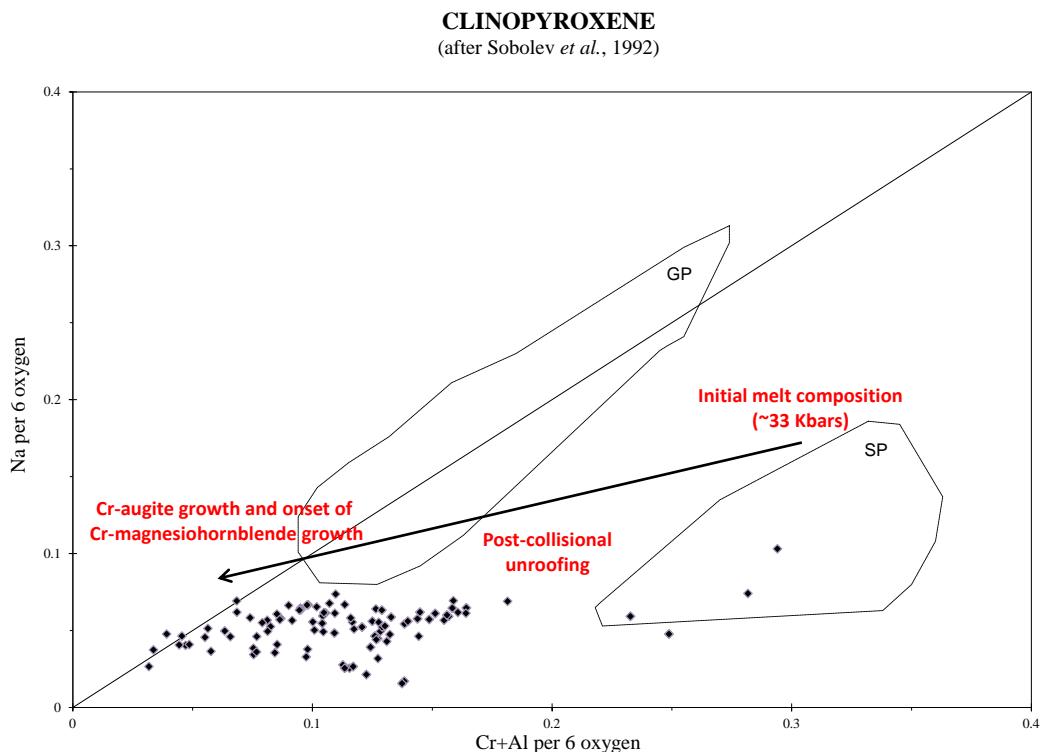


Figure 6.3: Binary plot of Cr+Al versus Na with fields defining “spinel peridotite (SP)” and “garnet peridotite (GP)”. The graph illustrates the Kurupung batholith’s Cr-clinopyroxene trend from most primitive Cr-diopside compositions in the “spinel peridotite” field to more evolved Cr-augite compositions. The diagram is modified after Sobolev *et al.*, 1992. See Appendix A, Table 2 for amphibole compositions.

compressive, post- collisional geological setting that terminated the Transamazonian orogenic cycle. Compositions of A-type magmas range from paraluminous to peralkaline, and these magmas are also quite variable in terms of oxygen fugacity and water content. Their common geochemical characteristics include high FeOt/FeOt + MgO and high contents of K₂O and incompatible elements. Although the Kurupung batholith is geochemically classified as an A-type granite, petrographic and mineral chemical investigations reveal it has an extraordinary Cr-component not accounted for by A-type magmatism. Trace element bulk rock geochemical signatures also indicate that the Kurupung is of sanukitoid affinity. The A-type classification implies a post-collisional emplacement for the Kurupung, the anomalous Cr-content implies incorporation of a mantle signature.

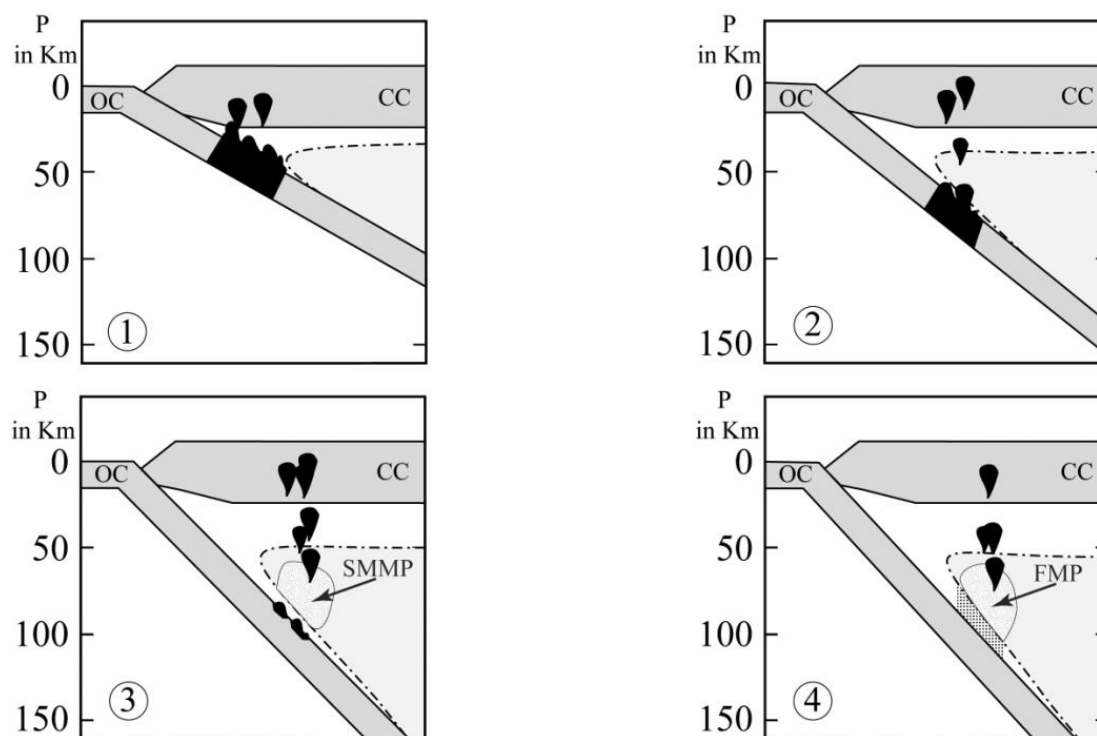


Figure 6.4: Synthetic cross-sections of subduction zones (after Martin and Moyen, 2002). (1) In the Early Archean (4.0 Ga) the geothermal gradient was very high, thus the subducted slab melted at shallow depth. Due to the thinness of the wedge and the low temperature, mantle and melt interactions are limited or absent; (2) After 3.0 Ga, the Earth was cooler, the geothermal gradient was lower and slab melting occurred at greater depth. The overlying mantle wedge is thick and hot, and interactions can occur between mantle and slab melts; (3) At the Archean–Proterozoic transition, geothermal gradients are too low to allow a high degree of slab melting. Slab melts are almost totally consumed in a reaction with the mantle. Low-Ti sanukitoid are assumed to be the result of a single event of contamination of slab melts by peridotite, whereas high-Ti sanukitoids formed through a two-step process where the mantle metasomatized by slab melts is subsequently melted; (4) After 2.5 Ga, geothermal gradients are so low that slab melting is precluded. The oceanic crust dehydrates and the liberated fluids metasomatize the mantle wedge, whose melting produces modern arc magmatism. OC=oceanic crust; C=continental crust; dotted line=solidus of hydrous mantle; black areas=magma; dotted area=fluids; SMMP=slab melt metasomatized peridotite; FMP=fluid metasomatized peridotite. Figure modified after Martin and Moyen, 2002 and Martin et al., 2009.

Sanukitoids represent the oldest high-Mg and high-K magmas identified in all cratonic domains during the 3.0–2.5 Ga Archean (Shirey and Hanson, 1984). Both mantle and arc components play a role in formation of sanukitoids, derived from melting of metasomatized peridotitic source (Smithies and Champion, 1999). Intrusion of sanukitoid and closepet-type granites is commonly late- to post-kinematic (e.g., Shirey and Hanson, 1984; Stern et al., 1989; Evans and Hanson, 1997; Beakhouse et al., 1999; Smithies and Champion, 1999) therefore not temporally associated with early syn-collisional TTG magmatism. Sanukitoids constitute one of the late magmatic events in an orogenic cycle. It is important to recognize that preservation of the Cr-clinopyroxene mantle compositions supports the hypothesis that the Kurupung batholith was unroofed rapidly.

Rapid unroofing is important for two reasons: (1) rapid emplacement from a deep mantle source allows for presentation of high pressure mantle phases, suggests diamond potentiality; and (2) rapid decompression is required to drive degassing of the batholith, accounting for voluminous structurally controlled alkaline metasomatism. Initially, the metasomatism related to uranium mineralization is tied to devolatilization within a strike-slip shear zone.

6.4 Growth of Secondary Ba-Kfeldspar Megacrysts

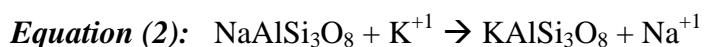
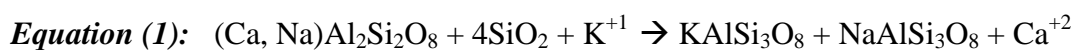
The origin of secondary Ba-Kfeldspar in the Kurupung batholith has been a topic of considerable debate. Microscopic examination clearly shows that the coarse Ba-Kfeldspar overgrows chlorite(1) retrograded shears on the mylonitized eastern margin of the batholith. As the Ba-Kfeldspar overgrows the dominant foliation, they are definitely not primary phenocrysts. Growth of Ba-Kfeldspar megacrysts nucleated on plagioclase, which is relict within the core of many megacrysts. Relict plagioclase is represented by complex intergrowths of albite+epidote+muscovite. Compositional oscillatory growth zoning in the Ba-Kfeldspars is attributed to the variation in barium content. The barium ranges from 1.38 wt% BaO near the core to 0.16 wt% BaO at the outermost margin. The alternating growth zones are a result of the extraction of Na from the plagioclase during

Ba-Kfeldspar growth to form the alternating albitic growth zone, albite(2) laths growing parallel to growth faces, and the balance of Na being partitioned into the fluid phase which gives rise to the domains of pervasive Na-metasomatism.

Coarse-grained orthoclase and microcline occurring in plutonic igneous and metamorphic rocks are generally regarded as primary phenocrysts that have developed during late stage crystallization from a melt, particularly if the megacrysts are zoned (Vernon, 1986). Undoubtedly, many Kfeldspar megacrysts do originate as phenocrysts, however, they can also be formed by secondary replacement processes under subsolidus conditions related to metasomatic fluid migration (Collins, 2002). Collins (2002) showed that megacrysts resulted from K-replacement of broken plagioclase crystals in sites of strong cataclasis. The progressive growth of secondary microcline encompassed broken remnant fragments of groundmass minerals in concentric shells. Veins of microcline penetrating cores of broken zoned plagioclase are clear evidence for K-replacement. K-metasomatism exists in silicate rocks because deformation creates an open system for K and Si ions to mobilize through the rock. Such metasomatism forms mineral assemblages which are stable between 550-350°C (Mariano and Woodard, 1984). Where most intense, K-metasomatism has totally obliterated any evidence of a pre-existing plagioclase. The growth of metasomatic megacrysts is dependent on the ability of K-bearing fluids to reach these nucleating sites. Mylonitic micro-fracturing of plagioclase crystals provided permeability for infiltration of metasomatic fluids. Microfracturing also developed local veinlets precipitating Ba-rich fluids with REE's and calcite.

The continued supply of K-metasomatic fluids from defluidization resulted in near wholesale replacement of primary plagioclase phenocrysts by Ba-Kfeldspar. In primary intrusive rocks, plagioclase is zoned with calcic cores and more sodic rims. Kfeldspar metasomatism occurs from the interior outward, where the Ca-cores are the least stable at low temperatures. Where these zoned grains are deformed and broken, vapor can penetrate causing diffusion of Ca out of the cores. This produces interior sites that are increasingly more sodic and more stable at the lower P-T conditions (Collins, 2002). It is

this altered plagioclase interior that has become more sodic that is most susceptible to being replaced by K to form Kfeldspar. The escape of Ca and Na will drive equations(1) and (2) to the right, as K-metasomatism produces more and more Kfeldspar. In that process, plagioclase grains are eventually completely converted to Kfeldspar (Collins, 1998; Hunt et al., 1992). Any residual Na that has not been partitioned into the fluid phase forms albite(2). Each concentric zone represents another sequence of replacement and megacrystic growth. The final product is a euhedral megacryst with concentric zones of Ba-Kfeldspar with tiny inclusions alternating with a concentric albite(2) growth zone. Successive overgrowth layers on a growing megacryst contain different Ba compositions indicating a fluctuating fluid chemistry. Rhythmic growth zoning of Ba-Kfeldspar shows an overall decrease in Ba from the core toward the outer growth rind. The sodium released during this process results in the formation of albite inclusions. Liberated sodium provides a source of sodium for pervasive albite(3) development associated with the mineralized zones.



Fluid inclusion studies by Smith (1953) and Roedder (1963) have shown that fluids that move upward through deformed plutons likely contain, not only water, but also dissolved brines and various gases, including methane, hydrogen, nitrogen, and carbon dioxide. The principal cations in solution are Na^{+1} , K^{+1} , Ca^{+2} , and Li^{+1} , and the principal anions are Cl^{-1} , SO_4^{-2} , and CO_3^{-2} . These anions can become the components of acids (HCl , H_2SO_4 , H_2CO_3) when coupled with principal cations (Na^{+1} , K^{+1} , Ca^{+2}) from the fluids during metasomatic reactions. The oxidation of methane to carbon dioxide and water may be a primary source of carbonic acid that facilitates metasomatic reactions. On that basis, hot acidic water will dissolve much of the displaced Ca and other extracted metals and carry them out of the system (Roedder, 1963).

The origin of barium within the Ba-Kfeldspar megacrysts of the Kurupung is a topic of debate. Based on research and experimental studies, Kerrick (1969) proposed that the source of Ba in megacrysts was from biotite and that the Ba-zoning of microcline megacrysts could be explained by complete consumption of Ba from the biotite structure. The Ba ion has similar ionic size to the K ion, and Ba⁺² ions have substituted for Ca⁺² ions. Soluble Ca ions with +2 charges removed from plagioclase would be expected to be transported out of the system because the Ca ion does not readily substitute for the K ion in microcline and would not be stable in recrystallized albite. The Ba ions with +2 charges would be expected to combine with K in a growing microcline megacryst because of the similar sizes of the K and Ba ions. According to Kerrick (1969), in late stages of deformation and at cooler temperatures, the fluids causing metasomatism can be expected to carry less Ba because most available Ba would have been removed from the original biotite. Therefore, lower temperature microcline on the outer rims contains lesser Ba.

It is possible that K-metasomatism is an “autometasomatic” process whereby metasomatism is a result of the last water-rich liquid fraction trapped within the rock. Dickson’s (1996) study of the Papoose Flat Pluton in California proposed that the Ba-K oscillatory zoned Kfeldspar with tabular inclusions of plagioclase formed at subsolidus temperature by autometasomatism. In this model the megacryst formation is controlled by internal reactions in a rock under stress (Ortoleva, 1994) and all the Ba and K are derived locally from recrystallization of primary Kfeldspar, plagioclase, biotite, and quartz with no elements derived from outside sources. The heat released during the recrystallization caused dissolution of plagioclase crystals. This dissolution caused a localized fluid from which dissolved plagioclase renucleated on a growing face of the orthoclase megacryst. In this way, the longer dimensions of the renucleating plagioclase crystals were aligned parallel to a former orthoclase face (Collins, 2002).

6.5 Discussion of Factor Analysis and Mass Balance Results

Whole rock geochemical analyses demonstrate elevated Ba (up to 1508ppm) and K (up to 4.72%) in rocks that have been Ba-K-metasomatized. The elevated Ba and K is due to the growth of abundant secondary Ba-Kfeldspar megacrysts. In areas of mineralization, K is diminished and Na is elevated adjacent to ore shoots. The post-magmatic processes associated with potassium and sodium metasomatism include: changes in the structural state of feldspars (primary plagioclase replaced by megacrystic Ba-Kfeldspar); ion exchange reactions in feldspars (K for Na); and albitization with evolution of the hydrothermal system to more Na-rich contents. In rocks that have been mineralized, K is diminished (~0.07%) while Na, Zr and U values are augmented to 6.07%, 83820ppm, and 2050ppm, respectively.

The factor analysis carried out in chapter 5 illustrates correlations between uranium and many of the elements associated with the alteration patterns of IOCG deposits. Uranium is positively correlated with Pb, Zr, Na, Ti and negatively correlated with K, Ba, Rb. The negative correlation is due to the progressive replacement of Ba-Kfeldspar by albite during Na-metasomatism associated with U-Zr mineralization. Although Na is genetically tied to U mineralogically and temporally, it only demonstrates a weak positive correlation with U on the factor analysis plots. It appears that the highest U concentrations are associated with Na values between 1-5%. This weak correlation is counter intuitive and this feature requires some explanation.

The reasoning associated with the above observations is tied to the shear system and the degree of black chlorite(2) cementing albite breccia rather than the abundance of Na. Although sodium alteration was pervasive, the degree of cataclasis and the precipitation of chlorite(2) created a sink for U-mineralization irrespective of Na-metasomatism. This is expressed counter intuitively as lower sodium being favourable to mineralization. High sodium contents (above 7 % Na) point to lesser degree of cataclasis correlating with lesser development of chlorite(2) and therefore, a reduced uranium content. At Aricheng South, the drill core displays broad zones of secondary Ba-Kfeldspar. Aricheng South

has limited albite cataclasite with minor late oxidation with minor hematization. The majority of the data points for ARS plot between 5-7% Na. There are some data points which plot within the 1-5% Na which are dominated by uranium-bearing hydrothermal zircon. Aricheng West is somewhat similar but narrower, with the zone of secondary Ba-Kfeldspar bound by chlorite mylonite, but with more albitic cataclasite and chlorite(2). Aricheng North shows a tight chlorite schist to the north broadening southwestward into albitic cataclasite with substantial oxide microbreccia. The data points for ARN cluster between 4-6% Na for the chlorite(2) sealed cataclasite and the chlorite mylonite schist form a broad domain between 1-5% Na.

In areas where shears are tight and rocks behave more brittle (e.g. Aricheng N), there is greater development of the more cataclastic albite texture, where individual grains of albite become enveloped in black chlorite(2) giving rise to the cluster of data points between 4-6.5% Na. A zone that is more cataclastic and brecciated would have greater area for development and cementing by chlorite(2) with the net effect being less Na in the rock and more chlorite(2) reductant. The breccia domains consisting of both green chlorite(1) and black chlorite(2) are the areas of highest mineralization. Mass balance computations demonstrate an increase in volume approaching ore zones and a decrease in volume leaving the ore zone down hole. The volume increase approaching the ore zone is attributed to increased fracturing and cataclasis permitting secondary fluid migration through the rock in mylonitic zones. Between ore shoots there is a drastic overall volume decrease and mass increase in rocks hosting secondary Ba-Kfeldspar. These domains show increases in K, Ba and Rb relative to the ore zone and the background sanukitoid. K₂O contents within ore zones is typically below 1% while values adjacent to the ore shoots are typically greater than 3%.

6.6 The Kurupung Mineralizing System

Primitive mantle normalized REE signatures of the unaltered Kurupung batholith illustrate a marked U-enrichment, with concentrations of uranium ranging between 3.9-11.5 ppm U. These values are quite elevated relative to typical granitoids which contain

approximately 3.2 ppm U (Flanagan, 1976). Leaching of uranium-fertile granites represents a major source of uranium, as uraninite is easily dissolved in oxygenated aqueous solutions. Archean and Paleoproterozoic granites of the Pine Creek U-district, Northern Australia, have uranium contents which are well above the crustal average of 2.8 ppm U (Wyborn, 1990). Granites and granitic gneisses of the Nanambu complex contain 3–50 ppm U; tonalites, granitic gneisses and granitic migmatites of the Nimbuwah complex have 1–10 ppm U. The Nabarlek granite that has been intersected in drill holes below the Nabarlek deposit has 3–30 ppm U, and the Tin camp and Jim Jim granites also have high uranium contents. The Malone Creek granite (South Alligator Valley) has 11–28 ppm U. Wyborn (1990) suggested that the underlying basement to these uranium fields is enriched in uranium. Uranium is also known to be present in the mantle and it is assumed that 50 wt% of total U in the Earth is stored in the lower mantle (Turcotte et al., 2001). The major and trace element geochemistry presented in chapter 5 illustrated that the batholith has a strong alkaline character with a negative Sr anomaly, and enriched Th, U, and LREE. The preferred interpretation is mantle metasomatism by fluids derived from detrital sediments as these are depleted in Sr and support the K, Th, U, LREE enrichment. This allows for the possibility that the primary U-enrichment in the unaltered Kurupung could be a result of slab metasomatized mantle.

The uranium mineralization at Aricheng is constrained to magnetic lows marginal to the magnetic highs defining sigmoidal shears across the batholith. Drilling has confirmed that these sigmoidal shaped magnetic lows are shear zones, which are bound by the northwest-southeast shears located on the margins of the batholith. Petrographic investigations have shown that these anomalously low magnetic zones result from extensive destruction of magnetite and Fe-Mg minerals to form hematite in alteration haloes that enclose uranium mineralization. It has been shown that uranium mineralization in the Kurupung occurs in shear structures that experienced K- and Na-metasomatism. The questions that remain include: 1) what was the composition of the mineralizing fluid and what were the transport and mineralizing mechanisms; 2) what is the source of uranium; and 3) what is the model that best describes this deposit?

It is clear from isotopic studies completed by Alexandre (2010) that meteoric and magmatic fluids interacted during mineralization. Earlier workers suggested that uranium is sourced from the Roraima basin and percolated downward with oxidizing meteoric fluids. The question remains however, as to when the onset of the Roraima occurred. The contact between Transamazonian basement and overlying Roraima sediments marks a basal unconformity. According to Schobbenhaus et al., (1994) the maximum age of the Roraima is 1966 +/- 9 Ma marking the boundary between the basement Surumu Group and overlying Roraima Supergroup in Brazil. Although the maximum age of the Roraima approximates the 1995 +/- 15 Ma age of mineralization, there is no evidence for Surumu volcanic or plutonic activity at Aricheng. Regional ashtuff volcanism and peraluminous intrusions of the Sumuru exposed along the south margin of the Roraima may have initiated Roraima deposition. However, there is a potential time gap of up to 30 million years between mineralization and the onset of Roraima sedimentation.

The composition of a uranium-bearing fluid can vary greatly. Uranium can occur both in the tetravalent (U^{4+}) valency in reducing environments such as magmatic or metamorphic conditions or in the hexavalent (U^{6+}) state in oxidizing, low temperature near surface conditions. Typical ore minerals of uranium can include U^{4+} -bearing uraninite and pitchblende (UO_{2+x}), coffinite ($USiO_4$), brannerite (UTi_2O_6), and U^{6+} -bearing oxyhydroxides, phosphates, arsenates, vanadates, and silicates. Limited substitution of U^{4+} for Ca^{2+} can occur in some of the common accessory minerals like apatite, titanite and fluorite. The comparable charge and radii of U^{4+} , Zr^{4+} , Th^{4+} , and Ce^{4+} (and other REE) can result in elevated uranium contents in accessory minerals such as allanite, monazite, xenotime and zircon. Notably, uranium mineralization in the Aricheng District includes: uraninite, coffinite, brannerite and occasionally uranium bearing zircon, suggesting a relation to magmatic volatiles. In zones of mineralization, the batholith contains F-bearing apatite and Ca-Y-fluorite intergrown with uranium and zircon minerals. This strongly suggests that F- complexes were prevalent during uranium precipitation and that F-bearing fluids were involved in mobilizing U-Zr. The ions U^{4+} , U^{6+} and Th^{4+} are considered hard acids and tend to couple with hard bases like F-, OH-,

NO_3^- , CO_3^{2-} , HCO_3^- , SO_4^{2-} , HSO_4^- , PO_4^{3-} , HPO_4^{2-} and H_2PO_4^- . Fluoride complexes are more stable than chloride complexes at high temperature conditions (Peiffert et al., 1996). Oxidized magmatic-hydrothermal fluids containing abundant F or Cl are capable of transporting high concentrations of uranium. However, high solubilities are also possible at reducing conditions where pH is low (<3), chloride or fluoride concentrations are high, and temperatures are elevated (Peiffert et al., 1996).

The two key processes involved in uranium precipitation are fluid-rock interactions and fluid mixing. In oxidizing conditions where aqueous uranium species are uranyl complexes, ore minerals containing tetravalent uranium (such as uraninite, coffinite, and brannerite) require reduction of the uranium-bearing oxidized fluids. Reductants may be present in rocks or fluids in the form of reduced carbon (organic matter, hydrocarbons including CH_4 , graphite), iron in Fe^{2+} -bearing minerals (amphibole, chlorite), and reduced sulfur in sulfide minerals, H_2S gas and aqueous H_2S (Skirrow et al., 2009). Regardless of the oxidation state of the uranium bearing fluid, a change in temperature, pH or redox state can promote U-precipitation. At elevated temperatures where chloride and fluoride complexes of U^{6+} and U^{4+} are significant, cooling and/or pH increases results in precipitation of uranium, whether the fluids are oxidized or reduced. Fluoride complexes of U^{6+} or U^{4+} are destabilized to precipitate uranium minerals, with or without a redox step (Peiffert et al., 1996).

Albitite-type uranium deposits are associated with zones of mylonitization and cataclasis. Deposits in the Kirovograd district, Ukraine, are adjacent to deep penetrating faults with associated pegmatite intrusions, cataclasis and mylonitization. The Valhalla deposit in central Australia occurs within the regionally extensive Mt. Isa fault zone where albitites have a temporal relationship to uranium and copper-gold IOCG-style mineralization. Uranium at Lagoa Real, Brazil occurs within albitized shears. In all cases, albitization accompanies mylonitic deformation and uranium is concentrated at the brittle-ductile transition. The mobility of both U and Ti are related to F-rich fluid flux through zones of cataclasis (Gieré, 1990). The common occurrence of brannerite $((\text{U,Ca,Ce})(\text{Ti,Fe})_3\text{O}_6)$

in moderate to high temperature uranium deposits is associated with Na-metasomatism (e.g., at Valhalla, Australia (Polito et al., 2007); at Kirovograd, Ukraine, (Cuney and Kyser, 2008); at Crocker Well, Australia (McKay and Miezitis, 2001))

The original source of uranium at Aricheng remains elusive. However, it is likely that uranium was sourced in the primary igneous U-bearing zircon forming granules in the unaltered Kurupung batholith. Certainly, the resorbed margins of early U-bearing zircon granules supply a ready source of uranium. Acidic F-bearing fluids were released either during rapid depressurization of the batholith or by mantle devolatilization during lamprophyre injection. These fluids formed the resorbed pitted outer margins of zircon granules, and may well have sequestered uranium from the outer margin of the granule and transported uranium in solution. The fluids ponded in zones of brittle albite cataclasite sealed by chlorite(2) and concentrated uranium in shear structures.

Isotopic investigations on the chlorite(2) and albite(3) by Alexandre (2010), demonstrate the oxygen isotope signatures of albite(3) derived through Na-metasomatism is magmatically sourced whereas chlorite(2) is of meteoric origin. Although meteoric water is typically oxidizing and magmatic or metamorphic fluids are dominantly reducing, oxidation state of the two mixing fluids may only be relative. Meteoric fluid percolating downward may interact with reducing wall rock and become progressively reduced. These reduced meteoric waters precipitated chlorite(2) within zones of cataclasis sealing red-albite(3). Conversely, the magmatic signature of red albite(3) supports the interpretation that pervasive hematization is linked to albite(3) development from high temperature magmatic degassing. Uranium precipitation was promoted where oxidized F-rich magmatic fluid carrying U interacted with reduced crustal fluid precipitating chlorite(2). Fluid mixing likely resulted in simultaneous decrease in pH, temperature, and a change in redox state of the mineralizing environment. Fluid inclusion studies indicate low saline fluids and temperatures of 250–350°C for the development of albite(3) and carbonate alteration, whereas temperature of 210–280°C are given for chlorite(2) development (Cinelu and Cuney, 2006).

6.7 Origin of Uraniferous Hydrothermal Zircon Veins

The occurrence of both abundant euhedral U-bearing zircon granules and hydrothermal zircon veins suggests the likelihood of insitu autometasomatic hydrothermal remobilization of uranium. Primary zircon granules display characteristic pitted outer margins within albitized U-mineralized domains. These pitted outer margins generally contain an elevated U-content compared to the core of the granule. This pitted texture is due to resorption of marginal domains during albitization. The granules contain up to 0.26 wt% UO_2 at their core and up to 0.64 wt% UO_2 at their margins, thereby supplying a ready source of uranium in the batholith. Zircon is highly soluble in an oxidizing F-rich neutral-alkaline fluid (Saxena, 1966; Kraynov et al., 1969; Gieré, 1990; Rubin et al., 1993). It is therefore possible that igneous zircons from within the Kurupung were readily dissolved by F-rich oxidizing fluids, thus releasing HREE and U into solution. Similar resorbed porous margins are described by Geisler et al. (2007) as secondary textures. They interpret this as structural damage caused by diffusion-reaction processes in which a hydrous fluid phase causes certain elements to diffuse inward and elements from within the zircon grain to move outward and into the fluid phase. Nano-scale pores develop and elements such as Ca, Al, and Fe are gained, and radiogenic elements (Pb, Zr, Hf, REE, U, Th) are lost to the fluid (Pidgeon et al., 1966; Sinha et al., 1992; Schmidt et al., 2006). A fluid at temperatures above 200°C carrying Ca, Al, Fe, and CO_2 could cause an exchange reaction at the zircon-fluid interface where U, Zr partition into the fluid phase. The dissolved U and Zr precipitated as U-Zr veins. As zircon is not a readily mobile mineral, the fact that it forms hydrothermal veins is highly anomalous. The formation of albite and carbonates implies fluids of neutral to alkaline pH values (Cinelu and Cuney, 2006).

6.8 IOCG Processes Pre-Dating the Roraima Formation

The Kurupung batholith hosts a significant uranium resource with 13-18 million tonnes grading 0.08% to 0.10% U_3O_8 , deriving an estimated 30-35 million pounds (Workman and Breede, 2012). The uranium mineralization is characterized by deep-early K- to shallow-late Na-metasomatism. The origin of uranium remains problematic but evidence

suggests resorption of primary uranium-bearing zircon through magmatic degassing. Precipitation of uranium resulted from interaction between oxidized ascending fluids from depth and reduced meteoric sourced hydrothermal fluid giving rise to chlorite(2).

The Aricheng district was originally targeted as an unconformity type uranium deposit related to the Roraima-basement contact. However, as illustrated in this thesis, uranium mineralization occurred prior to Roraima sedimentation within basement structures. Aricheng West best demonstrates the association of Ba-K-metasomatism, Na-metasomatism, brecciation, copper mineralization, and high grade uranium intersections. Local sulphide mineralization is associated with the K- and Na-metasomatic events which pre-date the uranium mineralization. The sulphide minerals are texturally related to chlorite(1) altered shears and chlorite(2) cementing breccias. This style of mineralization and alteration is characteristic of IOCG deposits worldwide.

The uranium mineralization in the Kurupung batholith has geological characteristics similar to a class of sizeable deposits known as “albitite-hosted uranium”, many of which contain resources in the 60 to 130 million pound range at comparable grades around 0.1% U₃O₈. This group of deposits remains poorly described, however a link to alkaline magmatism and IOCG deposits has been suggested (Wilde, 2013). In both albitite and IOCG-type deposits, there is a long-lived mantle to surface connection expressed by the commonality of extensional zones following compressional tectonics, unroofing of alkaline stocks along crustal scale mylonitic fault zones, intense K-Na metasomatism, and intense cataclasis and brecciation. Deposits which satisfy these characteristics include Canada’s Beaverlodge, Australia’s Valhalla, the United States’ Coles Hill and Brazil’s Lagoa Real deposits (Wilde, 2012).

These deposits all demonstrate intense Na-metasomatism in areas of uranium mineralization. Uranium mineralization is associated with later zircon, hematite, carbonate, quartz, chlorite, and sulphides as at Valhalla. In all cases, U-mineralization is associated with precipitation of brannerite, uraninite, U-Ti minerals, apatite, calcite and

zircon. The Beaverlodge camp north of the Athabasca Basin is associated with the 1.83 Ga Martin Group and shows progressive albitization of the granite gneiss and replacement of Kfeldspar by albite with specular hematite intergrown with chlorite and calcite (Wilde, 2012). The ore is disseminated uraninite and uranophane in albitized brecciated masses.

Available evidence in literature suggests that the uranium grade of IOCG deposits is quite variable and that the deposits usually have a broad halo of low grade uranium mineralization in the alteration zone. At Valhalla, regional albitization is linked with IOCG copper-gold deposits that carry anomalous, but subeconomic uranium. Uranium in IOCG deposits generally occurs as uraninite, although brannerite and coffinite have also been recognized (Reeve et al., 1990; Hitzman et al., 1992). Uranium minerals commonly associated with copper-iron sulfides occur within domains of potassic metasomatism. Anomalous uranium can also occur peripheral to zones of copper mineralization. A-type granites are spatially and temporally associated with many IOCG deposits, such as those of the Gawler craton, Australia (Creaser, 1996), Cloncurry, Australia (Pollard et al., 1998; Wyborn, 1998), and Carajás, Brazil (Lindenmayer, 1990; Barros et al., 1997) districts. These granite types contain relatively elevated uranium relative to other igneous rocks (Keppler and Wyllie, 1991; Keppler, 1993). Interestingly, the Kurupung batholith has elevated U contents of up to 11.5 ppm, which is approximately ten times the background in continental rocks. With the evidence presented above, the Kurupung should be considered a basement-hosted albitite-type uranium deposit that shares mineralogical and structural similarities to IOCG deposits.

Mid-Proterozoic unconformity-related deposits occur close to major unconformities. Basement rocks which host the uranium mineralisation below the unconformity are typically usually faulted and brecciated. The source of uranium in these deposits is from the overlying sandstone which is preferentially leached and deposited in basement structures beneath the unconformity. The overlying Proterozoic continental sandstones are usually undeformed. The largest unconformity-related deposits were formed in the Mid-Paleoproterozoic basins in Canada and Australia (Gandhi, 2005). Formation of

these deposits is related to a reduction fronts near the unconformity (Hoeve and Sibbald, 1978; Sibbald, 1985; Fayek and Kyser, 1997).

More work needs to be carried out on basement-hosted uranium mineralization in the Beaverlodge area, Saskatchewan, Canada, and in the Ranger, Jabiluka, and Koongarra deposits of the Northern Territory, Australia. The mineralization in the Kurupung may pre-date the overlying Roraima sandstone deposition by approximately 30 Ma and should therefore not be considered unconformity-related. This sheds new light on unconformity-related uranium as it suggests that reworking of older basement uranium concentrations may play a key role in concentrating uranium at unconformities.

Chapter 7: Conclusions

7.0 The Metallogenic Evolution of the Kurupung Batholith

The Kurupung batholith is situated in a west dipping mylonite zone within the Transamazonian age Mazaruni granite greenstone terrane. Mylonitic shearing is a result of regional sinistral strike-slip faulting initiating the post-collisional stage of the Transamazonian orogenic cycle. Deformation was active between 2103 \pm 3 Ma, the age of the batholith, and 1995 \pm 15 Ma, the age of hydrothermal uranium and zircon mineralization. Mineral chemical and geochemical characterization of the batholith indicates that it is a low-Ti sanukitoid generated by either partial melting of slab metasomatized mantle or interactions between high volumes of slab melt and mantle peridotite. In either case, Cr-bearing mantle inclusions were unresorbed and provide an opportunity to establish P-T conditions of the source melt region. The partial melt that generated the batholith occurred at depths between 70-100km, at up to 35 kilobars, and at temperatures up to 1130°C. Deep penetrating shears accommodating collapse of the orogen initiated partial melting of the low-Ti upper mantle-lower crust transition generating a low-Ti sanukitoid at 2103 \pm 3 Ma. The partial melt rose along the deformation zone with little to no residence time within the transitional Ti-rich zone of the mantle.

Whole rock and trace element geochemistry of the least altered batholith indicates a strong U-Th-LREE-alkaline enrichment concomitant with depleted Sr-Ti. These characteristics are favoured by models involving mantle metasomatism by detrital sediments (Laurent et al., 2011). This suggests that the Kurupung attained a “primary” U-enrichment within the metasomatized mantle. As identified by the age date on titanite, the batholith underwent upper greenschist metamorphism by 2094 \pm 5 Ma, promoting a retrograde actinolite-biotite-magnetite-chlorite(1)-titanite overprint on the mafic mineral assemblages and minor sausseritization of plagioclase to albite(1). The body attained a gneissic fabric synkinematically with rapid unroofing. Textural relationships clearly demonstrate that the mylonitic fabric pre-dates metasomatic replacement and late cataclastic deformation.

Devolatilization of the batholith during unroofing generated pegmatite dikes at 2085 +/- 9 Ma and initiated nearly contemporaneous Ba-K-metasomatism at 2071 +/- 13 Ma. This initiated the growth of secondary Ba-K-feldspar over chlorite(1) at the expense of primary plagioclase. Recondensation of this magmatic vapour phase formed a lower temperature hydrothermal fluid and Na partitioned into this aqueous phase causing pervasive albitization. The onset of the main mineralizing event is marked by albitite(3) development on margins of Ba-K-feldspar megacrysts. The Na-metasomatic process progressed to the point of complete replacement of Ba-K-feldspar and pervasive albitization of the host rock within shears.

There is a hiatus of approximately 60 Ma between the Ba-K metasomatic event and the injection of lamprophyre dikes. This implies a long lived deeply penetrating fault zone with episodic fluid migration. A suite of 2011 +/- 11 Ma lamprophyre dikes display mylonitic overprints and their emplacement coincides with pervasive structurally controlled chlorite(2) replacement. The injection of lamprophyre dikes marks the transition from ductile to brittle deformation. The albitite domains were exceptionally brittle, forming zones of cataclasis sealed by chlorite(2). Zones of brittle cataclasis are the main control for U-concentration at 1995 +/- 15 Ma. Degassing of mantle fluorine and CO₂ followed structures plumbed by lamprophyres, and synchronous ingress of meteoric waters provided a mixing zone in brittle microbreccia domains promoting U-Zr precipitation.

7.1 Summary

The results of this study maybe summarized according to key events leading to uranium mineralization: (1) magma source; (2) rapid unroofing; (3) uranium concentration; (4) fluid mixing; (5) albitite-type uranium deposits; and (6) exploration potential.

(1) Magma Source:

The Kurupung magma was sourced in deep mantle, metasomatized by fluids or melts derived from subducted detrital sediments. The partial melt ascended rapidly through the Ti-rich zone of the mantle with minimal residence time incorporating Cr-bearing mantle

aggregates and acquiring a low-Ti sanukitoid signature. The melt was emplaced and crystallized at 2103 +/- 3 Ma within the Transamazonian volcanics.

(2) **Rapid Unroofing:**

The batholith was rapidly unroofed along a major “crust to mantle” scale strike-slip mylonitic fault zone. Emplacement of the batholith to high crustal settings gave rise to greenschist facies retrogression at 2094 +/- 5 Ma, deriving an actinolite-biotite-magnetite-chlorite(1)-titanite assemblage. Rapid depressurization caused wholesale devolatilization along active structures forming pegmatite dikes at 2085 +/- 9 Ma. Degassing of K out of the background Kurupung caused the growth of megacrystic Ba-Kfeldspar at 2071 +/- 13 Ma. The Na partitioned into the aqueous phase, giving rise to pervasive albitization. The albitite domains were exceptionally brittle, forming late breccias bodies.

(3) **Uranium Concentration:**

Whole rock and trace element geochemistry show the Kurupung batholith has an enhanced U-Th-LREE content and elevated alkaline signature with uranium-zircon enriched in domains of chlorite(2) sealing albite(3) cataclasite. A hiatus of approximately 60 Ma occurred between the K-Na metasomatic events and injection of lamprophyre dikes at 2011 +/- 11 Ma. Degassing of mantle CO₂-F-rich fluids followed brittle/ductile structures plumbed by lamprophyre dikes.

(5) **Zone of Fluid Mixing:**

The F-rich fluid sequestered uranium out of the marginal domains of the primary zircons. Ingress of meteoric waters ponded in albitite breccia providing a mixing zone for precipitating remobilized U-Zr from primary zircon. The F-rich oxidized magmatic fluids interacted with the chlorite(2) and caused precipitation of F-rich and U-bearing minerals within zones of chlorite(2) sealing albitite breccia at 1995 +/- 15 Ma.

(6) **Albitite-type Uranium Deposits:**

The evidence presented in this thesis indicates that mineralization in the Kurupung predates the overlying Roraima sandstone deposition, by approximately 30 Ma. The mineralization therefore cannot be considered unconformity-related. This sheds new light on unconformity-related uranium as it suggests reworking of older basement uranium concentrations. Evidence presented herein identifies an albitite-type uranium system. Magmatic devolatilization within long-lived basement structures allowed for autometasomatic remobilization of uranium and concentration within albitite breccia.

(7) **Exploration Potential:**

The study has shown that alkaline metasomatism related to mantle-derived granitoids intruding major fault structures are pertinent to forming albitite-type uranium deposits with an IOCG signature. The importance of the elevated uranium content in the host Kurupung batholith melt, and high P-T conditions indicated by Cr-bearing phases provide clues for further exploration in the area. The unique whole rock and trace element geochemistry coupled with mineral chemical data can identify other uraniferous sanukitoid bodies. Notably, such bodies with remnant Cr-clinopyroxene may have a potential to preserve deep mantle phases and may prove to be diamondiferous. Since no primary source has been established for Paleoproterozoic diamonds in the Roraima, the Kurupung batholith and other unrecognized sanukitoids in the South American craton may be a prospective diamond source.

REFERENCES

References

- Alexander, R.B., and Breede, K., 2009. A Technical review of the Aricheng North and Aricheng South uranium deposits, in western Guyana for U3O8 Corp. and Prometheus Resources (Guyana) Inc. (43-101 Report).
- Alexandre, P., 2010. Mineralogy and geochemistry of the sodium metasomatism-related uranium occurrence of Aricheng South, Guyana. *Mineralium Deposita*, 45, p. 351-367.
- Aoki, K. and Shiba, I., 1973. Pyroxenes from lherzolite inclusions of Itinome-gata, Japan. *Lithos*, 6, p. 41-51.
- Baker, M., 2008. U3O8 Corp. Internal Report. Radar Interpretation of Northwest Guyana.
- Barros, C.E.M., Dall'Agnol, R., Barbey, P. & Boullier, A.M., 1997. Geochemistry of the Estrela granite complex, Carajás region, Brazil: an example of an Archaean A-type granitoid. *Journal of South American Earth Sciences*, 10, p. 321-330.
- Beakhouse, G.P., Heaman, L.M. and Creaser, R.A., 1999. Geochemical and U–Pb geochronological constraints on the development of a Late Archean greenstone belt at Birch Lake, Superior Province, Canada; *Precambrian Research*, 97, p.77–97.
- Bonin, B., 1990. From orogenic to anorogenic settings: evolution of granitoid suites after a major orogenesis. *Geological Journal*, 25, p. 261-270.
- Cinelu, S., and Cuney, M., 2006. Sodic metasomatism and U-Zr mineralization: a model based on the Kurupung batholith (Guyana). *Geochimica et Cosmochimica Acta*, 70 (suppl. 1): A103.
- Collins, L. G., 1998. Exsolution vermicular perthite and myrmekitic mesoperthite: Myrmekite, ISSN 1526-5757, electronic Internet publication, no. 32.
- Collins, L.G., 2002. K-metasomatism and the origin of Ba- and inclusion-zoned orthoclase megacrysts in the Papoose Flat pluton, Inyo Mountains, California, USA: electronic publication Myrmekite, ISSN 1526-5757, no. 44.
- Cordani, U, and Sato, K., 1999. Crustal evolution of the South American Platform, based on Nd isotopic systematics on granitoid rocks. *Episodes*, 22, #3, p.167-173.
- Corriveau, L. and Mumin, H., 2010. Exploring for iron oxide copper-gold deposits: Canada and global analogues. Geological Association of Canada, Short Course Volume 20, p. 111-126.

Cox, R.P., Wynn, J.C., Sidder, G.B., and Page, N.J., 1993. "Geology of the Venezuelan Guayana Shield", In: Geology and Mineral Resource Assessment of the Venezuelan Guayana Shield, U.S. Geological Survey Bulletin 2062, p.9-15.

Creaser, R.A., 1996. Petrogenesis of a Mesoproterozoic quartz latitegranitoid suite from the Roxby Downs area, South Australia: *Precambrian Research*, 79, p. 371-394.

Cuney, M. and Kyser, K., 2008. Recent and not-so-recent developments in uranium deposits and implications for exploration. Mineralogical Association of Canada Shortcourse Series, Quebec City, May 2008, Volume 39.

Davis, C., 2006. Technical report on the Prometheus uranium project, Co-operative Republic of Guyana, Mazaruni, Potaro, Cuyuni, & Rupununi Mining Districts Permits A and B. 43-101 Report.

Davis, D., Suppe, J., and Dahlen, F. A., 1983. Mechanics of fold-and-thrust belts and accretionary wedges: *Journal of Geophysical Research*, 88, p. 1153-1172.

Davis, D. W., 2006. Geochronology of magmatic and hydrothermal zircon from an altered granite in Guyana. Unpublished report for U3O8 Corp. 16 pp.

Davis, G. A., Anderson, J. L., Frost, E. G. & Shakelford, T. J., 1980. Mylonitization and detachment faulting in the Whipple-Buckskin-Rawhide Mountains terrane, southeastern California, and western Arizona. *Memoirs Geological Society of America*, 153, p. 79-130.

Deer, W.A., Howie, R. A., Zussman, J., 2001. Framework silicates: Feldspar. *Rock Forming Minerals*, 4A, p. 6-625.

Delor, C., deRoever, E., Lafon, J, Lahondere, D, Rossi, Ph, Cocherie, A, Guerrot, C, and Potrel, A., 2003. The Bakhuis ultrahigh-temperature granulite belt (Suriname): II. Implications for late Transamazonian crustal stretching in a revised Guiana Shield framework. *Geologie de la France*, #2-3-4, p. 207-230.

Dickson, F.W., 1996. Porphyroblasts of barium-zoned K-feldspar and quartz, Papoose Flat, Inyo Mountains, California, genesis and exploration implications; in Coyner, A. R., and Fahey, P. L., eds., *Geology and Ore Deposits of the American Cordillera*: Geological Society of Nevada Symposium Proceedings, Reno/Sparks, Nevada, April 1995, p. 909-924.

Donnerstag, P., 1976. Uranium exploration in Precambrian conglomerates in Guyana, South America. *American Association of Petroleum Geologists*, 60: p.1397 (abstract).

Evans, O.C., and Hanson, G.N., 1997. Late- to post-kinematic Archean granitoids of the S.W. Superior Province: derivation through direct mantle melting. In: de Wit, M.J., Ashwal, L.D. (Eds.), *Greenstone Belts*. Oxford University Press, Oxford, p. 280–295.

Fayek, M., and Kyser, K., 1997. Characterization of multiple fluid-flow events and rare-earth element mobility associated with formation of unconformity uranium deposits in the Athabasca Basin, Saskatchewan. *Canadian Mineralogist*, 35, p. 627-658.

Fayon, A., Whitney, D., Teyssier, C., 2004. Exhumation of orogenic crust: Diapiric ascent versus low-angle normal faulting. *Geological Society of America, Special Paper* 380, p. 129-139.

Flanagan, F. J., 1976. 1972 compilation of data on USGS standards. In: Flanagan FJ (ed) *Descriptions and analyses of eight new USGS rock standards*, USGS professional paper 840, p. 131-183.

Foster, D., Fanning, C.M., 1997. Geochronology of the northern Idaho batholith and the Bitterroot metamorphic core complex; magmatism preceding and contemporaneous with extension. *Geological Society of America Bulletin* 109, p. 379–394.

Frost, B. R., Arculus, R. J., Barnes, C. G., Collins, W. J., Ellis, D. J. & Frost, C. D., 2001. A geochemical classification of granitic rocks. *Journal of Petrology* 42, p. 2033-2048.

Gandhi, S.S., 2005. Significant unconformity-related uranium deposits of the Athabasca Basin region and selected related deposits of Canada and the World: Geological Survey of Canada, Open File CD-ROM.

Gibbs, A.K., 1979. *Geology of the Barama-Mazaruni Supergroup of Guyana*. PhD Thesis, Harvard University.

Gibbs, A.K., and Olszewski, W.J., Jr., 1982. Zircon U-Pb ages of Guyana greenstone-gneiss terrane: *Precambrian Research*, 17, p. 199-214.

Gibbs, A.K., and Wirth, K.R., 1986. Origin and evolution of the Amazonian Craton, in Ashwal, L.D., ed., *Workshop on early crustal genesis; world's oldest rocks: Godthab, Greenland, July 21-30, 1985*, LPI Technical Report, 86-04, p. 46-50.

Gibbs, A.K. and Barron, C.N., 1993. *The Geology of the Guiana Shield*, Oxford University Press, New York, p. 245.

Gieré, R., 1990. Hydrothermal mobility of Ti, Zr and REE: Examples from the Bergell and Adamello contact aureoles (Italy). *Terra Nova*, 2, p. 60-67.

Geisler T., Schaltteger U. & Tomascheck F., 2007. Re-equilibration of zircon in aqueous fluids and melts. *Elements* 3 (1), p. 43-50.

Gresens, P. L., 1967. Composition-volume relationships of metasomatism. *Chemical Geology*, 2, p. 47–65.

Hitzman, M.W., Oreskes, N., and Einaudi, M.T., 1992. Geological characteristics and tectonic setting of Proterozoic iron oxide (Cu-U-Au-LREE) deposits: *Precambrian Research*, 58, p. 241–287.

Hoeve J. and Sibbald T.I.I., 1978. On the genesis of Rabbit Lake and other unconformity-type uranium deposits in northern Saskatchewan, Canada: *Economic Geology*, 73, p. 1450-1473.

Howden, D., 2008. Million acres of Guyanese rainforest to be saved in groundbreaking deal. *The Independent Newspaper*, March 27 2008.

Hunt, C. W., Collins, L. G., and Skobelin, E. A., 1992. *Expanding Geospheres, Energy And Mass Transfers From Earth's Interior*: Calgary, Polar Publishing Company, 421 p.

Hurley, P. M.; Almeida, F. F. M.; Melcher, G. C.; Cordani, U. G.; Rand, J. R.; Kawashita, K.; Vandomos, P.; Pinson, W. H.; Fairbairn, H. W., 1967. Test of continental drift by comparison of radiometric ages. *Science*, 157, p. 495-500.

Irvine, T. N. and Baragar, W. R., 1971. A guide to the chemical classification of the common igneous rocks. *Canadian Journal of Earth Sciences* 8, p. 523–548.

Keppler H., 1993. Influence of fluorine on the enrichment of high field strength trace elements in granitic rocks. *Contributions to Mineralogy Petrology*, 114, p. 479-488

Keppler, H., and Wyllie, P. J., 1991. Partitioning of Cu, Sn, Mo, U, and Th between melt and aqueous fluid in the systems haplogranite-H₂O-HCl and haplogranite-H₂O-HF. *Contributions to Mineralogy and Petrology*, 109, p. 139-150.

Kerrick, D. M., 1969. K-feldspar megacrysts from a porphyritic quartz monzonite, central Sierra Nevada, California: *American Mineralogist*, 54, p. 839-848.

Klein, C. and Hurlbut, Jr., C. S., 1985. *Manual of Mineralogy*, after James D. Dana, 21st edition, revised, John Wiley & Sons, New York, 681 pp.

Kraynov S. R., Mer'Kov A. N., Petrova N. G., Baturinskaya I. V., and Zharikova V. M., 1969. Highly alkaline (ph 12) fluosilicate waters in the deeper zones of the Lovozero massif. *Geochemistry International*, 6, p. 635–640.

Kretz, R., 1982. Transfer and exchange equilibria in a portion of the pyroxene quadrilateral as deduced from natural and experimental data. *Geochimica et Cosmochimica Acta*. 46, p. 411-422.

Laurent, O., Martin, H., Moyen, J.F., Doucelance, R., 2013. Geochemical diversity of late-Archaean Mg-K-rich mafic magmas (sanukitoids) and its implication for metasomatic process between silicate melts and mantle peridotite. *Geophysical Abstracts*, 15, EGU General Assembly.

Laurent, O., Martin, H., Doucelance, R., Moyen, J.F., Paquette, J.L., 2011. Geochemistry and petrogenesis of high-K sanukitoids from the Bulai pluton, Central Limpopo Belt, South Africa : implications for geodynamic changes at the Archean-Proterozoic boundary. *Lithos*, 123, p. 73-91.

Leake, B.E., Woolley, A.R., Arps, C.E.S., Birch, W.D., Gilbert, M.C., Grice, J.D., Hawthorne, F.C., Kato, A., Kisch, H.J., Krivovichev, V.G., Linthout, K., Laird, J., Mandarino, J.A., Maresch, W.V., Nickel, E.H., Rock, N.M.S., Schumacher, J.C., Smith, D.C., Stephenson, N.C.N., Ungaretti, L., Whittaker, E.J.W., and Youshi, G., 1997. Nomenclature of amphiboles: Report of the subcommittee on amphiboles of the International Mineralogical Association, Commission on new minerals and mineral names: *American Mineralogist*, 82, p. 1019–1037.

Lindenmayer, Z.G., 1990. Salobo Sequence, Carajás, Brazil: geology, geochemistry and metamorphism. Ph.D. Thesis, University of Western Ontario, 406 p.

Lowe, S., 2013. An Epoch-based Metallogenic Scheme for Northern Guyana: A Tool for Mineral Resource Assessment. *The West Indian Journal of Engineering*, 35, #2, p.83-88.

Mariano, A., and Woodard, H.H., 1984. Potassium metasomatism of trondhjemites migmatite wallrock, Vermillion Complex, northern Minnesota: Abstracts, Thirteenth Annual Institute of Lake Superior Geology, Wausau, Wisconsin, April 24-28, p. 32-33.

Marshak, S., 1999. Deformation style way back when: Thoughts on the contrasts between Archean/ Paleoproterozoic orogens and modern ones: *Journal of Structural Geology*, 20th anniversary issue, 21, p. 1175-1182.

Marshak, S., Tinkham, D., Alkmim, F.F., Brueckner, H., and Bornhorst, T., 1997. Dome-and-keel provinces formed during Paleoproterozoic orogenic collapse - Diapir clusters, core complexes, or neither? Examples from the Quadrilatero Ferrifero (Brazil) and the Penokean Orogen (USA): *Geology*, 25, p. 415-418.

Martin, H., and Moyen, J.F., 2002. Secular changes in TTG composition as markers of the progressive cooling of the Earth. *Geology* 30 (4), p. 319– 322.

Martin, H. and Moyen, J. F., 2005. The Archaean-Proterozoic transition: Sanukitoid and Closepet type magmatism. *Mineralogical Society of Poland - Special papers Volume 26*, p. 57–68.

- Martin, H., Moyen, J. F., and Rapp, R., 2009. The sanukitoid series: magmatism at the Archaean/Proterozoic transition. *Earth Environmental Science Transactions Royal Society of Edinburgh*, 100 (Special Issue 1–2), p.15–33.
- Martin, H., Smithies, R.H., Rapp, R., Moyen, J.F., Champion, D., 2005. An overview of adakite, tonalite–trondhjemite–granodiorite (TTG), and sanukitoid: relationships and some implications for crustal evolution, *Lithos*, 79, p. 1-24.
- McCuaig, T. C., Kerrich, R. & Xie, Q., 1994. Phosphorus and high field strength element anomalies in Archean high-magnesian magmas as possible indicators of source mineralogy and depth. *Earth and Planetary Science Letters* 124, p. 221–239
- McKay, A.D. & Mieizitis, Y., 2001. Australia's uranium resources, geology and development of deposits. AGSO – Geoscience Australia, Mineral Resource Report 1.
- Middlemost, E. A. K. 1994. Naming materials in the magma/igneous system. *Earth-Science Reviews* 37, p. 215–224.
- Mitchell, R.H., and Bergman, S.C., 1991. *Petrology of Lamproites*. pp.447. New York, London: Plenum Press.
- Miyashiro, A., 1978. Nature of alkaline volcanic series. *Contributions to Mineralogy and Petrology*, 66, p. 91–104.
- Morris, T. F., Sage, R. P., Ayer, J. A., and Crabtree, D. C., 2002. A study in clinopyroxene composition: implications for kimberlite exploration. *Geochemistry, Exploration, Environment, Analysis*, 2, p. 321-331.
- Moyen, J.F., Martin, H. & Jayananda, M., 2001. Multi-element geochemical modelling of crust-mantle interactions during late-Archaean crustal growth: the Closepet granite (South India). *Precambrian Research* 112, p. 87–105.
- Moyen, J.F., Nedelec, A., Martin, H., Jayananda, M., 2003. Syntectonic granite emplacement at different structural levels: the Closepet granite, South India. *Journal of Structural Geology*, 25 (4), p. 611 –631.
- Nakamura N., 1974. Determination of REE, Ba, Fe, Mg, Na, and K in carbonaceous and ordinary chondrites. *Geochimica et Cosmochimica Acta*, 38, p. 757-775.
- Nickel, K.G., 1989. Garnet–pyroxene equilibria in the system SMACCr (SiO₂–MgO–Al₂O₃–CaO–Cr₂O₃): the Cr-geobarometer. In: Ross, J.R. (Ed.), *Proceedings of IVth International Kimberlite Conference*. Special Publication-Geological society of Australia, 14 (2), p. 901–912.
- Nimis, P. and Taylor, W.R., 2000. Single clinopyroxene thermobarometry for garnet peridotites. I. Calibration and testing of a Cr-in-Cpx barometer and an enstatite-in-Cpx

thermometer. *Contributions to Mineralogy Petrology*, 139, p. 541-554.

Orotoleva, P.J., 1994. *Geochemical Self-Organization*. Oxford University Press, Oxford, U.K.

Pearson, K., 1901. On Lines and Planes of Closest Fit to Systems of Points in Space. *Philosophical Magazine* 2 (11), p. 559–572.

Peiffert, C., Nguyen-Trung, C., Cuney, M., 1996. Uranium in granitic magmas: part 2. Experimental determination of uranium solubility and fluid-melt partition coefficient in the uranium oxide-haplogranite-H₂O–NaX (X=Cl, F) system at 770 °C, 2 kbar. *Geochimica et Cosmochimica Acta* 60, p. 1515–1529.

Pidgeon, R.T., O'Neill, J., and Silver, L.T., 1966. Uranium and lead isotopic stability in a metamict zircon under experimental hydrothermal conditions. *Science*, 154, p. 1538-1540

Podruski, J. A., 1979. Petrology of the upper plate crystalline complex in the eastern Whipple Mountains, San Bernardino County, California: unpublished master of science thesis, University of Southern California, Los Angeles, 193 p.

Polito, P.A., Kyser, K. and Stanley, C., 2007. The Proterozoic, albitite-hosted, Valhalla uranium deposit, Queensland, Australia: a description of the alteration assemblage associated with mineralisation in diamond drill hole V39. *Mineralium Deposita*, DOI 10.1007/s00126-007-0162-2.

Polito, P.A., Kyser, K, and Stanley, C, 2009. The Proterozoic, albitite-hosted, Valhalla uranium deposit, Queensland, Australia: a description of the alteration assemblage associated with uranium mineralisation in diamond drill hole V39. *Mineralium Deposita*, 44, p. 11–40.

Pollard, P.J., Mark, G., and Mitchell, L.C., 1998. Geochemistry of post-1540 Ma granites in the Cloncurry district, Northwest Queensland: *Economic Geology*, 93, p. 1330-1344.

Reeve, J.S., Cross, K.C., Smith, R.N., and Oreskes, N., 1990. The Olympic Dam copper-uranium-gold-silver deposit, South Australia, in Hughes, F., ed., *Geology of mineral deposits of Australia and Papua New Guinea: Australian Institute of Mining and Metallurgy Monograph* 14, p. 1009-1035.

Reynolds, S.J., and Lister, G.S., 1987. Structural aspects of fluid-rock interactions in detachment zones: *Geology*, 15, p. 362-366.

Roedder, E., 1963. Studies of fluid inclusions II: freezing data and their interpretation. *Economic Geology*, 58, p. 161-211.

Rubin J. N., Henry C. D. and Price J. G., 1993. The mobility of zirconium and other “immobile” elements during hydrothermal alteration. *Chemical Geology*, 110, p. 29–47.

Santos, J., Hartman, L., Gaudette, H., Groves, D., McNaughton, N., and Fletcher, I., 2000. A new understanding of the provinces of the Amazon Craton based on integration of field mapping and U-Pb and Sm-Nd geochronology, *Gondwana Research*, 3, p. 453-488.

Santos, J., Potter, P., Reis, N., Hartmann, L., Fletcher, I., and McNaughton, N., 2003. Age, Source, and regional stratigraphy of the Roraima Supergroup and Roraima-like outliers in northern South America based on U-Pb geochronology. *GSA Bulletin*, 115, #3, p. 331-348.

Saxena S.K., 1966. Evolution of zircons in sedimentary and metamorphic rocks. *Sedimentology* 6, p. 1-33.

Saywell, T., 2013. Final HEU shipment a catalyst for uranium industry. *The Northern Miner Global Mining Newspaper*. September 4 2013.

Schmidt, C., Rickers, K., Wirth, R., Nasdala, L., Hancher, J.M., 2006. Low-temperature Zr mobility: An in situ synchrotronradiation XRF study of the effect of radiation damage in zircon on the element release in H₂O + HCl ± SiO₂ fluids. *American Mineralogist*, 91, p. 1211-1215.

Schobbenhaus, C., Hoppe, A., Lork, A., and Baumann, A., 1994. Idade U/Pb do magmatismo Uatuma no norte do cráton Amazônico, Escudo das Guianas (Brasil): Primeiros resultados, *in Anais, Congresso Brasileiro de Geologia, 37th, Camboriú, Brazil: Porto Alegre, Brazil, Sociedade Brasileira de Geologia*, 2, p. 395–397.

Shand, S. J., 1927. *Eruptive rocks*. London, p. 51-52.

Shirey, S. B., and Hanson, G. N., 1984. Mantle-derived Archaean monzodiorites and trachyandesites. *Nature*, 310, no. 5974, p. 222-224.

Sibbald, T.I.I., 1985. Geology and genesis of the Athabasca Basin uranium deposits; in *Summary of Investigations 1985, Saskatchewan Geological Survey, Saskatchewan Energy and Mines, Miscellaneous Report 84-4*, p. 133-156.

Sinha, A.K., Wayne D.M., Hewitt D.A., 1992. The hydrothermal stability of zircon: Preliminary experimental and isotopic studies. *Geochimica et Cosmochimica Acta* 56, p. 3551-3560.

Skirrow, R. G., Jaireth, S., Huston, D. L., Bastrakov, E. N., Schofield, A., van der Wielen, S. E. and Barnicoat, A. C., 2009. Uranium mineral systems: Processes, exploration criteria and a new deposit framework. *Geoscience Australia Record 2009/20*. 44 p.

Smith, F.G., 1953. Complex inclusions in pegmatitic minerals. *American Mineralogist*, 38, p. 559 – 560.

Smithies, R.H. and Champion, D.C., 1999. High-Mg diorite from the Archaean Pilbara Craton: anorogenic magmas derived from a subduction-modified mantle. *GSWA Annual Review*, 1998-99, p. 45-49.

Smithies, R.H., Champion, D.C., 2000. The Archaean high-Mg diorite suite: links to tonalite–trondhjemite–granodiorite magmatism and implications for early Archaean crustal growth. *Journal of Petrology*, 41 (12), p. 1653– 1671.

Smock, K., 2008. *Guyana Travel Guide*. *Published by: The Globe Pequot Press Inc.*, ISBN: 978 1 84162 223 1.

Sobolev, N.V., Pokhilenko, N.P., Grib, V.P., Skripnichenko, V.A., Titova, V.E., 1992. Specific composition and conditions of formation of deep-seated minerals in exploration pipes of the Onega peninsula and kimberlites of Zimnii Coast in the Arkhangelsk province. *Geol. Geofiz.* 33 (10), 84– 92 (in Russian). English Translation: *Russian Geology and Geophysics*, 33 (10), p. 71–78.

Sonder, L.J., P.C. England, B. Wernicke, and R.L. Christiansen, 1987. A physical model for Cenozoic extension of western North America, in *Continental Extensional Tectonics*, edited by M.P. Coward, J.F. Dewey, and P.L. Hancock, Geological Society Special Publication, 28, p. 187-201.

Stachel, T., and Harris, J.W., 2007. The origin of cratonic diamonds – constraints from mineral inclusions. *Ore Geology Reviews*, 34, #1-2, p.5-32.

Stern, R., Hanson, G.N., and Shirey, S.B., 1989. Petrogenesis of Mantle derived LILE-enriched Archaean Monzodiorite, Trackyandesites (Sanukitoids) in southern Superior Province. *Canadian Journal of Earth Sciences*, 26, p. 1688–1712.

Stevenson R, Henry P, Gariepy C., 1999. Assimilation–fractional crystallization origin of Archean Sanukitoid Suites: Western Superior Province, Canada. *Precambrian Research*, 96, p. 83-99.

Sun, S. and McDonough, W. F., 1989. Chemical and isotopic systematics of oceanic basalts: implications for mantle composition and processes. In Saunders, A. D. & Norry, M. J. (eds) *Magmatism in the Ocean Basins*. Geological Society, London, Special Publications 42, p. 313–345.

Turcotte, D. L., D. Paul, and W. M. White, 2001. Thorium-uranium systematics require layered mantle convection, *Journal of Geophysical Research*, 106, p. 4265– 4276.

Vernon, R.H., 1986. K-feldspar megacrysts in granites-phenocrysts, not porphyroblasts. *Earth Science Reviews*, 23, p. 1-63.

Wilde, A., 2012. Towards a model for Albitite-type Uranium. *Minerals*, 3, #1, p.36.

Williams, P.J., 2010. "Magnetite-group" IOCGs with special reference to Cloncurry and Northern Sweden: Settings, alteration, deposit characteristics, fluid sources, and their relationship to apatite-rich iron ores. In: Corriveau L, Mumin AH (eds) *Exploring for iron oxide copper-gold deposits: Canada and global analogues*. Geological Association of Canada Short Course Notes, 20, p. 23–38.

Workman, A., and Breede, K., 2012. Technical review and mineral resource estimates of the Aricheng C and Aricheng West structures, Kurupung Uranium project, Mazaruni District, Guyana (43-101 Report).

Wyborn, L.A.I., 1990. High uranium granites of the Kakadu-NW Amhern Land region, are they related to the locally abundant uranium deposits?, *BMR Research Newsletter*, 12, p. 2-4.

Wyborn, L.A.I., 1998. Younger ca. 1500 Ma granites of the Williams and Naraku batholiths, Cloncurry district, eastern Mt Isa Inlier: Geochemistry, origin, metallogenic significance and exploration indicators: *Australian Journal of Earth Sciences*, 45, p. 397-411.

Zane, A., Sassi, R., and Guidotti, C.V., 1998. New data on metamorphic chlorite as a petrogenetic indicator mineral, with special regard to greenschist-facies rocks. *Canadian Mineralogist*, 36, p. 713-726.

Internet Resources:

www.cameco.com/common/.../penny_buyes_text_and_images.pdf

<http://www.scm minerals.com/projects/>

www.u3o8corp.com

www.uxc.com

Appendix

Appendix A

Electron Microprobe Analyses

Appendix A

Electron Microprobe Methods

Electron microprobe analyses were completed by the candidate at the laboratory of Barnett Geoanalytical Consulting Ltd. (formerly Barnett Geological Consulting Inc.), Lambeth, Ontario. Thin sections were covered with a thin film of analytical grade carbon using a vacuum carbon evaporator. The thin sections were analyzed using a JEOL JXA-733 electron microprobe equipped with 5-wavelength-dispersive spectrometers (WDS) and an energy-dispersive spectrometer (EDS). The microprobe is operated using an Advanced Microbeam “Probe for Windows” operating system to drive the Tracor Northern TN-5600 spectrometer and stage automation system.

The chemical compositions were measured using a 15 kV accelerating voltage (20kV for uranium minerals) and 11 nA probe current. Count times for major elements (Fe, Mg, Si) were 20 s on peak and 10 s (on each side) for background measurements. For trace elements (Ti, Ni, Ca, Mn, Co, Na) both peak and background times were 50 s. For calibration a set of microbeam standards (natural minerals) from the Smithsonian Institution were utilized (Jarosewich, 2002). The instrument calibration was deemed successful when the composition of secondary standards was reproduced within the error margins defined by the counting statistics.

Table 1: Mineral Chemical Analyses of Clinopyroxene

Table 1: CLINOPYROXENE, KURUPUNG BATHOLITH, Jim Renaud (Phd Thesis), September 2009-2013

	1	2	3	4	5	6	7	8
STO2	52.41	51.58	52.59	52.39	52.46	51.86	52.24	52.01
TIO2	.41	.33	.35	.44	.45	.29	.34	.32
A2O3	2.31	2.28	2.35	2.47	2.60	2.39	2.05	2.12
C2O3	.85	.60	.64	.65	.68	.71	.50	.29
FeO	5.08	4.87	5.15	4.73	6.48	7.53	6.80	7.27
MgO	15.42	16.06	15.15	15.62	14.46	14.42	14.07	14.07
MnO	.17	.11	.12	.18	.38	.31	.35	.42
CaO	23.60	23.38	22.67	22.67	21.88	22.35	23.25	23.74
K2O	.00	.01	.00	.02	.06	.08	.01	.00
Na2O	.55	.37	.73	.65	.82	.78	.76	.70
NiO	.00	.00	.00	.00	.00	.00	.02	.02
SUM	100.80	99.59	99.75	99.82	100.27	100.72	100.39	100.96
SI	1.921	1.911	1.941	1.930	1.936	1.920	1.937	1.925
AL	.079	.089	.059	.070	.064	.080	.063	.075
AL	.020	*	.043	.037	.049	.025	.026	.017
TI	.011	*	.010	.012	.012	.008	.009	.009
CR	.025	*	.019	.019	.020	.021	.015	.008
FE	.156	*	.159	.146	.200	.233	.211	.225
MN	.005	*	.004	.006	.012	.010	.011	.013
Mg	.842	*	.887	.858	.795	.796	.778	.776
CA	.927	*	.896	.895	.865	.887	.924	.941
K	.000	*	.000	.001	.003	.004	.000	.000
NA	.039	*	.027	.046	.059	.056	.055	.050
NI	.000	*	.025	.000	.000	.000	.001	.001
NI	6.000	6.000	6.000	6.000	6.000	6.000	6.000	6.000
ENST	43.76	45.11	44.12	45.18	42.75	41.54	40.67	39.96
FERR	8.09	7.68	8.42	7.68	10.75	12.17	11.03	11.58
WOLL	48.15	47.21	47.46	47.14	46.50	46.28	48.31	48.46
F/M	.191	.174	.195	.176	.266	.305	.285	.307
F/EM	.160	.148	.163	.150	.210	.234	.222	.235

- 1 *****SAMPLE ARN053-108.5m
- 2 ANOTHER
- 3 ANOTHER
- 4 INT DOMAIN C1
- 5 INT DOMAIN C1
- 6 INT DOMAIN C1
- 7 ADJ CPX DOMAIN TO AMP
- 8 DOM W ORIENT CR-MT LAM, LOWER CR, C-1

CLINOPYROXENE, KURUPUNG BATHOLITH, Jim Renaud (PhD Thesis), September 2009-2013

	9	10	11	12	13	14	15	16
STO2	52.87	52.69	52.63	52.88	53.56	52.09	51.54	51.59
TIO2	.37	.12	.18	.15	.12	.30	.40	.28
A2O3	2.32	.90	1.25	.96	.57	2.73	2.67	2.44
C2O3	.47	.01	.08	.14	.24	.72	.77	.58
FEO	4.83	7.39	7.47	7.26	7.05	3.08	3.07	3.66
WGO	16.05	14.21	13.88	14.08	13.86	17.29	17.62	17.21
MNO	.10	.49	.46	.42	.44	.01	.00	.12
CAO	23.03	23.91	23.63	23.52	24.53	23.45	23.82	23.68
K2O	.00	.01	.01	.01	.02	.01	.03	.04
NA2O	.36	.67	.72	.65	.37	.24	.22	.30
NiO	.02	.02	.02	.02	.14	.00	.00	.00
SUM	100.42	100.42	100.33	100.09	100.90	99.92	100.14	99.90
SI	1.934	1.961	1.959	1.969	1.980	1.905	1.887	1.898
AL	.066	2.000	.039	2.000	.031	2.000	.113	2.000
AL	.034	*	.000	.014	.011	.023	.002	.102
TI	.010	*	.003	.005	.004	.008	.011	.008
CR	.014	*	.002	.004	.007	.021	.022	.017
FE	.148	*	.230	.233	.218	.094	.094	.113
MN	.003	*	.015	.015	.014	.000	.000	.004
MG	.875	*	.788	.770	.782	.943	.961	.944
CA	.903	*	.953	.942	.938	.919	.934	.933
K	.000	*	.000	.000	.001	.000	.001	.002
NA	.026	*	.048	.052	.047	.017	.016	.021
Ni	.001	2.012	.001	2.040	.001	2.034	.000	2.045
O	6.000	6.000	6.000	6.000	6.000	6.000	6.000	6.000
ENST	45.45	39.98	39.59	40.16	39.10	48.20	48.32	47.43
FERR	7.67	11.67	11.96	11.62	11.16	4.82	4.72	5.66
WOIL	46.88	48.36	48.45	48.22	49.74	46.99	46.96	46.91
F/M	.172	.311	.321	.306	.303	.100	.098	.123
F/FM	.147	.237	.243	.234	.233	.091	.089	.110

- 9 POSS CENTRAL TO CPX, C-1
- 10 AT MARGIN ORIGINAL IGN CPX, PT C
- 11 ANOTH RELICT PRIMARY OUTER ZONE CPX, C-1
- 12 SMALL DIFE DOM
- 13 BRIGHT AMP DOMAIN, SPOT I
- 14 CR-CPX
- 15 CR-CPX
- 16 CR-CPX

CLINOPYROXENE, KURUPUNG BATHOLITH, Jim Renaud (Phd Thesis), September 2009-2013

	17	18	19	20	21	22	23	24
STO2	53.12	52.77	52.73	52.30	51.19	51.86	52.77	51.98
TIO2	.31	.25	.32	.28	.14	.25	.08	.55
A2O3	1.97	2.08	2.47	2.00	5.66	2.42	1.55	2.76
C2O3	.41	.61	.68	.59	1.27	.79	.60	.87
FeO	4.26	6.61	6.02	5.97	6.73	4.88	4.52	5.27
MgO	15.83	13.31	14.35	14.41	15.31	15.20	15.18	15.10
MNO	.31	.41	.28	.36	.18	.18	.17	.15
CAO	22.67	22.75	23.11	23.70	18.35	23.76	25.49	23.59
K2O	.04	.01	.09	.05	.08	.02	.01	.02
NA2O	.46	.67	.90	.83	1.04	.69	.50	.65
NiO	.00	.00	.00	.00	.00	.00	.00	.00
STM	99.38	99.47	100.95	100.49	99.95	100.05	100.87	100.94
SI	1.957	1.966	1.935	1.934	1.879	1.917	1.937	1.906
AL	.043	.034	.065	.066	.121	.083	.063	.094
TI	.009	.007	.009	.008	.004	.022	.004	.025
CR	.012	.018	.020	.017	.037	.023	.017	.025
FE	.131	.206	.185	.185	.207	.151	.139	.162
MN	.010	.013	.009	.011	.006	.006	.005	.005
Mg	.869	.739	.785	.794	.838	.837	.830	.825
CA	.895	.908	.909	.939	.722	.941	1.002	.927
K	.002	.000	.004	.002	.004	.001	.000	.001
NA	.033	.048	.064	.060	.074	.049	.036	.046
Ni	.000	.000	.000	.000	.000	.000	.000	.000
NI	2.003	1.997	2.027	2.037	2.015	2.037	2.037	2.030
O	6.000	6.000	6.000	6.000	6.000	6.000	6.000	6.000
ENST	45.86	39.88	41.79	41.41	47.43	43.41	42.12	43.13
FERR	6.92	11.11	9.84	9.63	11.70	7.82	7.04	8.44
WOHL	47.21	49.00	48.38	48.96	40.87	48.77	50.84	48.43
F/M	.162	.296	.246	.247	.253	.187	.173	.201
F/FM	.140	.228	.198	.198	.202	.157	.148	.168

- 17 CR-CPX
- 18 CR-CPX
- 19 C-4 SPOT 1
- 20 SPOT 2
- 21 INTERIOR SPOT 3
- 22 SPOT 3
- 23 SPOT 3
- 24 SPOT 3

	25	26	27	28	29	30	31	32
STO2	51.96	49.11	51.37	52.50	52.67	52.15	52.64	51.24
TIO2	.25	.52	.27	.26	.42	.43	.38	.35
A2O3	1.61	5.94	2.47	1.89	2.23	2.24	2.41	2.21
C2O3	.52	1.16	.84	.56	.59	.66	.83	.54
FeO	4.38	7.63	5.01	4.43	4.12	4.29	3.86	6.64
MgO	15.17	15.17	15.34	15.25	16.13	16.58	16.33	13.97
MnO	.23	.12	.15	.16	.11	.01	.00	.27
CaO	25.38	18.81	23.89	24.95	24.22	24.04	23.76	23.36
K2O	.01	.01	.05	.01	.01	.02	.01	.04
Na2O	.57	1.43	.66	.53	.39	.36	.45	.92
NiO	.00	.00	.00	.00	.00	.00	.00	.00
SiO2	100.19	99.90	100.05	100.54	100.89	100.78	100.67	99.54
SI	1.923	1.824	1.903	1.930	1.921	1.907	1.919	1.920
AL	.070	1.993	.176	2.000	.070	.093	.081	.080
AL	.000	*	.084	*	.017	.003	.023	*
TI	.007	*	.015	*	.012	.012	.010	*
CR	.015	*	.034	*	.017	.019	.024	*
FE	.136	*	.237	*	.126	.131	.118	*
MN	.007	*	.004	*	.003	.000	.000	*
Mg	.843	*	.840	*	.836	.903	.887	*
CA	1.006	*	.749	*	.983	.942	.928	*
K	.000	*	.103	*	.000	.001	.000	*
NA	.041	*	.103	*	.028	.026	.032	*
NI	.000	2.055	.000	2.048	.000	.000	.000	2.023
O	6.000	6.000	6.000	6.000	6.000	6.000	6.000	6.000
ENST	42.47	46.01	43.43	42.75	44.99	45.72	45.90	40.51
FRFR	6.83	12.98	7.96	6.97	6.45	6.64	6.09	10.80
WOHL	50.70	41.01	48.62	50.28	48.56	47.65	48.01	48.69
F/M	.169	.287	.189	.169	.147	.146	.133	.278
F/E/M	.145	.223	.159	.145	.128	.127	.117	.217

- 25 PRIMARY DOMAIN SPOT 6
- 26 SPOT 6
- 27 ANOTHER
- 28 ANOTHER
- 29 UNALTERED PORTION
- 30 ANOTHER
- 31 AGAIN
- 32 NEAR MARGIN

	33	34	35	36	37	38	39	40	
STO2	51.74	52.60	52.95	52.32	51.56	52.63	50.97	51.95	
TI02	.27	.32	.30	.30	.36	.36	.52	.41	
A203	2.48	2.39	1.06	1.01	1.35	1.80	3.47	2.30	
C203	.80	.85	.00	.00	.15	.00	.22	.12	
FE0	3.69	3.89	8.45	8.79	9.07	9.37	8.28	7.96	
MGO	16.25	16.16	13.40	13.57	13.51	13.55	14.20	13.25	
MNO	.15	.04	.20	.26	.37	.44	.32	.37	
CAO	23.67	23.59	23.21	23.34	22.93	21.11	21.04	22.49	
K2O	.00	.00	.00	.00	.00	.05	.00	.06	
NA2O	.60	.63	.55	.56	.69	.76	.96	.85	
NiO	.00	.00	.04	.04	.04	.04	.04	.04	
STM	99.65	100.47	100.16	100.19	100.03	100.11	100.02	99.80	
SI	1.909	1.922	1.975	1.959	1.939	1.964	1.900	1.943	
AL	.091	.078	.025	.041	.060	.036	.100	.057	
TI	.017	.025	.022	.003	.000	.043	.052	.044	
CR	.023	.025	.000	.000	.004	.000	.006	.004	
FE	.114	.119	.264	.275	.285	.292	.258	.249	
MN	.005	.001	.006	.008	.012	.014	.010	.012	
MG	.894	.880	.745	.757	.757	.754	.789	.739	
CA	.936	.924	.928	.936	.924	.844	.840	.901	
K	.000	.000	.000	.000	.000	.002	.000	.003	
NA	.043	.045	.040	.041	.050	.055	.069	.062	
Ni	.000	2.039	.001	.001	.001	.001	.001	.001	
O	6.000	6.000	6.000	6.000	6.000	6.000	6.000	6.000	
ENST	45.99	45.78	38.48	38.46	38.51	39.87	41.80	39.11	
FERR	5.86	6.18	13.61	13.98	14.51	15.47	13.68	13.18	
WOHL	48.15	48.04	47.91	47.56	46.98	44.65	44.52	47.71	
F/M	.133	.136	.362	.374	.392	.406	.340	.353	
F/FM	.117	.120	.266	.272	.282	.289	.254	.261	
33 CENTRAL									
34 CENTRAL									
35 ****SAMPLE ANAR-1A CENTRAL C-2 05-03-4193									
36 CPX CENTRAL, C-2, 05-03-4193									
37 CPX CENTRAL, C-2, 05-03-4193									
38 ****SAMPLE ANAR-1B C-1 CENTRAL 05-02-4196									
39 CPX CENTRAL, SPOT 1, C-3, 05-02-4198									
40 SPOT 2									

	41	42	43	44	45	46	47	48
ST02	51.05	50.92	51.43	53.56	52.52	51.50	52.22	51.35
TI02	.31	.50	.32	.22	.22	.43	.24	.32
A203	2.11	3.51	2.10	1.70	1.73	3.41	2.60	2.85
C203	.22	.20	.10	.01	.03	.52	.53	.66
FE0	8.55	8.77	9.33	8.28	8.60	7.42	7.42	7.80
MGO	13.08	13.74	13.53	13.23	13.51	13.25	14.20	14.16
MNO	.36	.34	.36	.31	.37	.32	.43	.35
CAO	23.22	20.76	22.02	22.16	22.85	22.71	21.73	22.41
K20	.07	.08	.01	.02	.02	.04	.07	.04
NA20	.76	.85	.88	.47	.50	.90	.88	.80
NI0	.04	.04	.04	.00	.00	.04	.04	.04
STM	99.77	99.71	100.12	99.96	100.35	100.54	100.36	100.78
SI	1.924	*	1.929	1.989	1.956	1.910	1.934	1.905
AL	.076	2.000	.094	.011	.044	.090	.066	2.000
TI	.018	*	.061	.063	.032	.059	.048	.029
CR	.009	*	.014	.006	.006	.012	.007	.009
FE	.007	*	.006	.000	.001	.015	.016	.019
MN	.269	*	.275	.257	.268	.230	.242	.242
MG	.011	*	.011	.010	.012	.010	.013	.011
CA	.735	*	.757	.732	.750	.732	.784	.783
K	.938	*	.833	.882	.912	.902	.862	.891
NA	.003	*	.004	.001	.001	.002	.003	.002
NI	.056	*	.062	.034	.036	.065	.063	.058
O	.001	2.046	.001	.000	.000	.001	.001	.001
ENST	6.000	*	6.000	6.000	6.000	6.000	6.000	6.000
ERR	37.84	40.91	39.11	39.14	38.87	39.27	41.79	40.87
WOLL	13.88	14.65	15.13	13.74	13.88	12.34	12.25	12.63
F/M	48.28	44.44	45.76	47.12	47.25	48.39	45.96	46.50
F/M	.382	.372	.402	.364	.373	.328	.310	.323
F/FM	.277	.271	.287	.267	.272	.247	.237	.244

41 POSS BRIGHT MARGIN SPOT 5
 42 SPOT 7, 05-03-4198
 43 CPX CENTRAL, SPOT 5, 06-03-4196
 44 CR-CPX - PIC 1631
 45 CR-CPX - PIC 1631
 46 ***SAMPLE PERE 12 C-1, SPOT 1, 05-04-4202
 47 SPOT 1, C-1, 05-04-4202
 48 SPOT 2 CENTRAL

	57	58	59	60	61	62	63	64
STO2	51.29	52.01	51.62	50.31	50.81	51.54	52.37	53.11
TI02	.52	.47	.37	.54	.47	.50	.38	.16
A203	2.79	2.73	2.99	3.93	2.81	3.35	1.85	.78
C203	.21	.36	.49	.27	.34	.28	.06	.01
FE0	7.57	7.45	7.81	8.19	7.23	7.60	7.06	6.57
MGO	15.05	15.10	14.24	14.62	14.54	14.39	14.57	15.47
MNO	.27	.34	.36	.26	.41	.27	.35	.49
CAO	21.79	21.34	21.69	20.20	22.62	20.88	22.81	23.59
K2O	.04	.06	.02	.10	.02	.14	.03	.00
NA2O	.62	.73	.86	.95	.75	.81	.73	.53
NiO	.04	.04	.04	.04	.04	.04	.04	.04
STM	100.19	100.63	100.49	99.41	100.04	99.80	100.25	100.75
SI	1.905	1.919	1.914	1.884	1.896	1.916	1.942	1.959
AL	.095	.081	.086	.116	.104	.084	.058	.034
TI	.027	.037	.044	.057	.020	.063	.023	.000
CR	.015	.013	.010	.015	.013	.014	.011	.004
FE	.006	.010	.014	.008	.010	.008	.002	.000
MN	.235	.242	.242	.256	.226	.236	.219	.203
MG	.008	.011	.011	.008	.013	.009	.011	.015
CA	.833	.830	.787	.816	.809	.797	.805	.851
K	.867	.843	.862	.810	.904	.832	.906	.932
NA	.002	.003	.001	.005	.001	.007	.001	.000
Ni	.045	.052	.062	.069	.054	.058	.052	.038
O	.001	.001	.001	.001	.001	.001	.001	.001
ENST	6.000	6.000	6.000	6.000	6.000	6.000	6.000	6.000
FERR	43.05	43.62	41.62	43.34	41.71	42.75	41.71	42.84
WOHL	12.15	12.07	12.81	13.62	11.64	12.67	11.34	10.21
	44.80	44.31	45.57	43.04	46.65	44.59	46.94	46.96
F/M	.292	.290	.322	.324	.295	.307	.286	.256
F/FM	.226	.225	.244	.245	.228	.235	.222	.204

57 CENTRAL C-2, 05-04-4203
 58 C-2, CENTRAL, SPOT 1, 05-04-4203
 59 AT MARGIN SPOT 2
 60 SPOT 3
 61 SPOT 4
 62 SPOT 6 AMPH OVER
 63 SPOT 9 AMPH OVER
 64 SPOT 10

	73	74	75	76	77	78	79	80
STO2	52.74	52.61	53.16	51.94	52.02	52.04	52.24	54.14
TI02	.29	.26	.26	.61	.37	.39	.27	.61
A203	1.46	1.72	1.27	3.50	3.17	5.30	4.93	2.76
C203	.07	.09	.09	.09	.64	.68	.65	.31
FE0	6.96	7.03	7.26	7.77	7.39	7.16	7.23	6.99
MGO	14.97	14.61	15.45	15.09	14.41	13.49	12.99	14.30
MNO	.36	.42	.35	.25	.34	.33	.39	.45
CAO	22.58	22.79	22.30	19.85	21.60	20.23	20.59	19.67
K2O	.01	.08	.02	.11	.05	.13	.05	.06
NA2O	.64	.65	.51	.79	.84	.67	.83	.80
NiO	.04	.04	.04	.04	.04	.00	.00	.00
STM	100.12	100.30	100.71	100.04	100.87	100.42	100.17	100.09
SI	1.955	1.950	1.958	1.919	1.916	1.908	1.923	1.982
AL	.045	.050	.042	.081	.084	.092	.077	.018
AL	.019	.025	.013	.071	.053	.137	.137	.101
TI	.008	.007	.007	.017	.010	.011	.007	.017
CR	.002	.003	.003	.003	.019	.020	.019	.009
FE	.216	.218	.224	.240	.228	.220	.223	.214
MN	.011	.013	.011	.008	.011	.010	.012	.014
MG	.827	.807	.848	.831	.791	.737	.713	.780
CA	.897	.905	.880	.786	.852	.795	.812	.772
K	.000	.001	.001	.005	.002	.006	.002	.003
NA	.046	.047	.036	.057	.060	.048	.059	.057
Ni	.001	.001	.001	.001	.001	.000	.000	.000
O	6.000	6.000	6.000	6.000	6.000	6.000	6.000	6.000
ENST	42.64	41.82	43.46	44.75	42.28	42.09	40.79	44.19
FERR	11.12	11.29	11.46	12.93	12.17	12.53	12.74	12.12
WOHL	46.23	46.89	45.09	42.32	45.56	45.37	46.47	43.69
F/M	.275	.286	.277	.298	.301	.312	.329	.292
F/FM	.215	.223	.217	.230	.231	.238	.248	.226

73 SPOT 3
 74 SPOT 4
 75 C-6
 76 C-6, SPOT 1, 05-04-4206
 77 C-1 CENTRAL
 78 ****PERE 10B - CPX CENTRAL GRAIN - PIC 1630
 79 PERE 10B - CPX CENTRAL GRAIN BT- PIC 1630
 80 ****SAMPLE ARM21-117.7A

	81	82	83	84	85	86	87	88
ST02	53.18	53.30	52.55	53.18	53.56	52.29	51.11	52.83
TI02	.29	.33	.36	.27	.24	.16	.21	.18
A203	1.37	1.62	1.50	1.40	1.26	1.14	1.38	1.20
C203	.34	.00	.15	.40	.38	.63	1.01	.55
FE0	6.65	6.82	7.20	6.58	6.16	6.74	8.07	6.52
MGO	13.79	14.21	13.71	13.78	14.21	13.87	13.69	13.85
MNO	.35	.46	.28	.40	.36	.48	.45	.42
CAO	24.07	23.24	24.31	23.99	23.90	24.22	22.57	23.96
K2O	.00	.04	.00	.00	.00	.00	.02	.00
NA2O	.91	.76	.84	.92	.82	.96	.77	.86
NiO	.00	.00	.00	.00	.00	.00	.00	.00
STM	100.95	100.78	100.90	100.92	100.89	100.49	99.28	100.37
SI	1.961	1.963	1.946	1.961	1.969	1.947	1.933	1.961
AL	.039	2.000	.054	.039	.031	.050	.061	.039
TI	.021	*	.034	.022	.024	.000	.000	.013
CR	.010	*	.009	.007	.007	.004	.006	.005
FE	.205	*	.223	.012	.011	.019	.030	.016
MN	.011	*	.210	.203	.189	.210	.255	.202
MG	.758	*	.014	.012	.011	.015	.014	.013
CA	.951	*	.780	.757	.779	.770	.772	.766
K	.000	*	.917	.948	.941	.966	.915	.953
NA	.065	*	.000	.000	.000	.001	.001	.000
Ni	.000	*	.054	.066	.058	.069	.056	.062
O	6.000	*	6.000	6.000	6.000	6.000	6.000	6.000
ENST	39.60	40.90	38.92	39.69	40.78	39.56	39.75	39.88
FERR	10.71	11.01	11.47	10.63	9.92	10.79	13.15	10.53
WOHL	49.69	48.08	49.61	49.67	49.30	49.66	47.11	49.59
F/M	.285	.288	.306	.284	.258	.292	.349	.281
F/FM	.222	.223	.234	.221	.205	.226	.259	.220

- 81 ANOTHER
- 82 SPOT 2, CENTRAL DOMAIN
- 83 SPOT 3
- 84 CENTRAL SPOT 2
- 85 ANOTHER
- 86 CENTRAL SPOT 2 ANOTHER
- 87 ANOTHER CENTRAL
- 88 CENTRAL SPOT 2

	89	90	91	92	93	94	95	96
STO2	54.07	53.11	53.32	54.03	52.76	52.44	51.67	52.31
TI02	.14	.14	.07	.16	.20	.35	.29	.26
A203	.85	.84	.68	.84	1.08	1.88	1.93	1.86
C203	.39	.00	.07	.07	.00	.56	.85	.75
FE0	6.06	6.35	6.72	5.80	6.24	6.26	6.20	6.08
MGO	13.99	14.64	14.07	14.61	15.05	13.77	14.40	14.45
MNO	.44	.43	.39	.38	.36	.42	.45	.40
CAO	24.21	23.89	24.70	24.14	24.34	24.04	23.75	23.23
K2O	.00	.00	.00	.00	.01	.02	.03	.04
NA2O	.64	.72	.68	.68	.69	.93	.85	.92
NI0	.00	.00	.00	.00	.00	.00	.00	.00
STM	100.79	100.12	100.70	100.71	100.73	100.67	100.42	100.30
SI	1.988	1.971	1.974	1.985	1.949	1.940	1.919	1.938
AL	.012	.029	.026	.015	.047	.060	.081	.062
TI	.025	.007	.004	.021	.000	.022	.004	.019
CR	.011	.004	.002	.004	.006	.010	.008	.007
FE	.186	.197	.208	.178	.193	.194	.193	.188
MN	.014	.014	.012	.012	.011	.013	.014	.013
MG	.767	.810	.776	.800	.829	.759	.797	.798
CA	.954	.950	.980	.950	.963	.953	.945	.922
K	.000	.000	.000	.000	.000	.001	.001	.002
NA	.046	.052	.049	.048	.049	.067	.061	.066
NI	.000	.000	.000	.000	.000	.000	.000	.000
O	6.000	6.000	6.000	6.000	6.000	6.000	6.000	6.000
ENST	40.21	41.38	39.53	41.49	41.75	39.84	41.20	41.81
FERR	9.77	10.07	10.59	9.24	9.71	10.16	9.95	9.87
WOIL	50.02	48.54	49.88	49.27	48.54	50.00	48.85	48.32
F/M	.261	.260	.284	.238	.246	.272	.259	.252
F/FM	.207	.206	.221	.192	.198	.214	.206	.201

89 ANOTHER CENTRAL SPOT 2
 90 C-2 SPOT 1 CENTRAL
 91 C-2 SPOT 3 CENTRAL
 92 C-3 DARK SPOT
 93 C-4
 94 C-5
 95 C-5 ANOTHER
 96 C-5 ANOTHER

Table 2: Mineral Chemical Analyses of Amphibole

Table 2 : AMPHIBOLE, KURUPUNG BATHOLITH, Jim Renaud (Phd Thesis), September 2009-2013

	1	2	3	4	5	6	7	8
STO2	47.47	49.01	44.13	47.38	49.32	49.08	50.92	48.35
TIO2	1.12	.86	1.51	1.15	.84	.51	.29	1.08
A2O3	7.19	6.57	8.96	7.29	6.14	5.99	4.83	6.18
C2O3	.69	.57	.34	.68	.49	.14	.08	.04
FE0	11.78	10.74	13.90	11.58	10.56	12.86	11.69	12.16
MGO	15.19	16.31	13.72	15.12	16.22	15.43	16.36	14.92
MNO	.33	.18	.36	.29	.30	.38	.18	.40
CAO	12.18	12.62	12.27	12.37	12.43	12.38	12.35	11.93
K2O	.59	.44	1.01	.73	.49	.64	.44	.73
NA2O	1.40	1.33	1.60	1.40	1.19	1.02	1.01	1.22
F	.76	.73	.67	.61	.63	.68	.68	.67
CL	.02	.02	.03	.03	.02	.02	.00	.03
SUM	98.72	99.38	98.50	98.63	98.63	99.13	98.83	97.71
-O= F+CL	.32	.31	.29	.26	.27	.29	.29	.29
SUM	98.40	99.07	98.21	98.37	98.36	98.84	98.54	97.42
SI	6.870	* 6.988	* 6.524	* 6.866	* 7.072	* 7.077	* 7.284	* 7.058
AL	1.130	8.000	1.012	8.000	1.476	8.000	1.134	8.000
AL	.096	* .092	* .085	* .111	* .110	* .095	* .098	* .121
TI	.122	* .092	* .168	* .125	* .091	* .055	* .031	* .119
CR	.079	* .064	* .040	* .078	* .056	* .016	* .009	* .005
FE	1.426	* 1.281	* 1.718	* 1.403	* 1.266	* 1.551	* 1.398	* 1.484
MG	3.277	* 3.466	* 3.023	* 3.266	* 3.467	* 3.316	* 3.488	* 3.246
MN	.040	* 5.039	* .022	* 5.017	* .045	* 5.079	* .036	* 5.019
CA	1.889	* 1.928	* 1.943	* 1.921	* 1.910	* 1.913	* 1.893	* 1.866
K	.109	* .080	* .190	* .135	* .090	* .118	* .080	* .136
NNA	.393	* 2.390	* .368	* 2.376	* .459	* 2.592	* .280	* 2.253
F	.348	* .329	* .313	* .280	* .331	* .285	* .308	* .309
CL	.005	* .005	* .008	* .007	* .005	* .005	* .000	* .007
O	23.000	* 23.000	* 23.000	* 23.000	* 23.000	* 23.000	* 23.000	* 23.000
FE	30.32	26.98	36.24	30.06	26.76	31.86	28.62	31.38
MG	69.68	73.02	63.76	69.94	73.24	68.14	71.38	68.62
F/M	.447	.376	.583	.441	.376	.482	.407	.473
F/FM	.309	.273	.368	.306	.273	.325	.289	.321

- 1 *****SAMPLE ARN053-108.5m LINEAR DARK AMP INCL CR-MT, C-1
- 2 LINEAR DARK AMP INCL CR-MT, C-1
- 3 AMPH REPL CPX, BRIGHT CENTRAL, C-1
- 4 AT TIP TOWRAD MARGIN, PT F
- 5 DARKER TIP, PT G, C-1
- 6 BRIGHT AMP DOMAIN, SPOT J
- 7 DARK AMP ZONE, SPOT K
- 8 PRIMARY DARK AMP DOMAIN

	9	10	11	12	13	14	15	16
STO2	47.89	50.87	52.46	48.23	51.45	54.18	51.39	48.40
TIO2	1.05	.31	.16	1.02	.17	.01	.18	1.05
A2O3	6.20	4.61	3.42	6.21	4.27	2.38	4.07	5.99
CaO3	.08	.08	.00	.06	.06	.00	.11	.00
FeO	12.65	11.89	11.01	12.99	10.70	9.74	11.93	11.62
MgO	15.00	16.12	16.77	15.07	16.53	17.55	16.69	15.56
MnO	.30	.28	.22	.35	.28	.36	.35	.33
CaO	11.67	12.19	12.23	12.21	12.58	12.41	12.41	11.41
K2O	.73	.41	.27	.70	.34	.11	.32	.71
Na2O	1.29	.99	.68	1.24	.91	.40	.89	1.48
F	.70	.63	.53	.71	.68	.53	.63	.71
CL	.03	.01	.00	.03	.02	.00	.01	.03
SUM	97.59	98.39	97.75	98.82	97.99	97.67	98.98	97.29
-O= F+CL	.30	.27	.22	.31	.29	.22	.27	.31
SUM	97.29	98.12	97.53	98.51	97.70	97.45	98.71	96.98
SI	7.018	* 7.315	* 7.524	* 6.997	* 7.383	* 7.702	* 7.346	* 7.071
AL	.982	8.000	.685	8.000	1.003	8.000	.654	8.000
AL	.088	*	.096	.102	.058	* 0.106	.032	.103
TI	.116	*	.034	.017	.111	* 0.018	.001	.115
CR	.009	*	.000	.007	.007	* 0.000	.012	.000
FE	1.550	*	1.430	1.321	1.576	* 1.284	1.158	1.426
Mg	3.276	*	3.455	3.585	3.259	* 3.536	3.719	3.389
Mn	.037	5.077	.034	5.058	.043	5.054	.043	5.088
Ca	1.832	*	1.878	1.898	1.898	* 1.934	1.890	1.786
K	.136	*	.075	.049	.130	* 0.062	.020	.132
N	.366	2.335	.276	2.229	.349	* 2.376	.247	2.206
F	.324	*	.287	.240	.326	* 0.309	.238	.328
CL	.007	*	.002	.000	.007	* 0.005	.007	.007
O	23.000	*	23.000	23.000	23.000	* 23.000	23.000	23.000
FE	32.12	29.27	26.92	32.60	26.64	23.74	28.63	29.53
Mg	67.88	70.73	73.08	67.40	73.36	76.26	71.37	70.47
F/M	.485	.424	.376	.497	.373	.323	.413	.431
F/FM	.326	.298	.273	.332	.272	.244	.292	.301

- 9 BRIGHT AMP DOMAIN
- 10 DARK MARGIN, C-1
- 11 DARK MARGIN, C-1
- 12 RANDOM AMP, BRIGHT DOMAIN
- 13 RANDOM DARK DOMAIN SAME GRAIN
- 14 DARKEST MARGIN ON AMP
- 15 INTERNAL LINEAR DARK
- 16 PIC 20-100, BRIGHT AMPH, SPOT 1

	17	18	19	20	21	22	23	24
STO2	56.19	58.06	49.83	52.73	57.36	49.87	49.75	49.61
TI02	.01	.03	.90	.20	.01	1.06	.49	.92
A203	.44	.28	7.07	5.77	.29	7.21	7.47	8.37
C203	.14	.06	.00	.00	.00	.00	.14	.78
FE0	9.27	6.63	11.29	9.73	7.39	11.48	10.26	5.00
MGO	18.33	19.28	15.01	15.87	19.62	15.20	15.48	18.83
MNO	.24	.20	.41	.36	.00	.23	.21	.12
CAO	13.27	12.61	11.46	11.87	12.92	11.52	12.15	12.72
K2O	.03	.08	.75	.42	.09	.72	.65	.56
NA2O	.17	.24	1.00	.78	.16	.96	.85	.92
F	.47	.00	.00	.00	.00	.00	.00	.00
CL	.02	.00	.00	.00	.00	.00	.00	.00
SUM	98.58	97.47	97.72	97.73	97.84	98.25	97.45	97.83
-O= F+CL	.20	.00	.00	.00	.00	.00	.00	.00
SUM	98.38	97.47	97.72	97.73	97.84	98.25	97.45	97.83
SI	7.891	* 8.094	* 7.190	* 7.496	* 8.009	* 7.157	* 7.165	* 6.976
AL	.073	7.964	.000	.504	8.000	.843	8.000	8.000
AL	.000	* .046	* .392	* .462	* .048	* .376	* .433	* .363
TI	.001	* .003	* .098	* .021	* .001	* .114	* .053	* .097
CR	.016	* .007	* .000	* .000	* .000	* .000	* .016	* .087
FE	1.089	* .773	* 1.362	* 1.157	* .863	* 1.378	* 1.236	* .588
MG	3.837	* 4.006	* 3.228	* 3.362	* 4.083	* 3.251	* 3.323	* 3.947
MN	.029	4.971	.024	.050	5.130	.028	5.148	.026
CA	1.997	* 1.884	* 1.772	* 1.808	* 1.933	* 1.771	* 1.875	* 1.916
K	.005	* .014	* .138	* .076	* .016	* .132	* .119	* .100
NNA	.046	2.048	.065	1.963	.215	2.099	.237	2.232
F	.209	* .000	* .280	* 2.189	* .043	* 1.992	* .237	* .251
CL	.005	* .000	* .000	* .000	* .000	* .000	* .000	* .000
O	23.000	* 23.000	* 23.000	* 23.000	* 23.000	* 23.000	* 23.000	* 23.000
FE	22.10	16.17	29.68	25.60	17.45	29.76	27.11	12.97
MG	77.90	83.83	70.32	74.40	82.55	70.24	72.89	87.03
F/M	.291	.199	.438	.357	.211	.432	.380	.153
F/FM	.226	.166	.304	.263	.174	.302	.275	.132

17 SPOT 2, MARGINAL ZONE

18 DARK AMP DOMAIN

19 BRIGHT AMP DOMAIN

20 BRIGHT AMP DOMAIN

21 DARK AMP DOMAIN

22 BRIGHT AMP DOMAIN

23 AMP

24 CR-AMP LOZENGER

	25	26	27	28	29	30	31	32
STO2	52.23	50.41	53.29	48.03	49.90	48.93	49.07	53.22
TIO2	.34	.74	.22	.86	.90	.97	1.17	.36
A2O3	5.22	6.45	3.52	6.80	5.23	5.09	5.54	2.45
C2O3	.64	.23	.88	.52	.02	.00	.03	.70
FeO	6.85	9.92	8.06	12.36	13.04	13.12	13.34	10.75
MgO	18.58	15.99	18.16	15.22	15.16	14.98	15.21	16.93
MnO	.14	.31	.32	.34	.46	.54	.45	.46
CaO	13.25	12.87	12.42	12.36	12.17	12.18	11.59	12.50
K2O	.32	.57	.25	.68	.47	.56	.55	.25
Na2O	.47	.85	.44	1.16	1.03	.98	1.46	.55
F	.00	.00	.00	.00	.04	.04	.04	.04
CL	.00	.00	.00	.00	.00	.00	.00	.00
SUM	98.04	98.34	97.56	98.33	98.42	97.39	98.45	98.21
-O= F+CL	.00	.00	.00	.00	.02	.02	.02	.02
SUM	98.04	98.34	97.56	98.33	98.40	97.37	98.43	98.19
SI	7.354	* 7.202	* 7.559	* 6.987	* 7.231	* 7.191	* 7.135	* 7.607
AL	.646	8.000	.798	8.000	.441	8.000	1.013	8.000
AL	.220	* .288	* .147	* .153	* .124	* .073	* .084	* .020
TI	.036	* .080	* .023	* .094	* .098	* .107	* .128	* .039
CR	.071	* .026	* .099	* .060	* .002	* .000	* .003	* .079
FE	.807	* 1.185	* .956	* 1.504	* 1.580	* 1.613	* 1.622	* 1.285
Mg	3.899	* 3.405	* 3.839	* 3.300	* 3.274	* 3.281	* 3.296	* 3.607
Mn	.017	5.049	.038	5.022	.056	5.136	.055	5.189
Ca	1.999	* 1.970	* 1.888	* 1.926	* 1.890	* 1.918	* 1.806	* 1.914
K	.057	* .104	* .045	* .126	* .087	* .105	* .102	* .046
N	.128	2.185	.235	2.309	.289	2.266	.412	2.319
F	.000	* .000	* .000	* .000	* .018	* .019	* .018	* .018
CL	.000	* .000	* .000	* .000	* .000	* .000	* .000	* .000
O	23.000	* 23.000	* 23.000	* 23.000	* 23.000	* 23.000	* 23.000	* 23.000
FE	17.14	* 25.82	* 19.94	* 31.30	* 32.55	* 32.95	* 32.98	* 26.27
Mg	82.86	* 74.18	* 80.06	* 68.70	* 67.45	* 67.05	* 67.02	* 73.73
F/M	.211	* .359	* .259	* .468	* .500	* .512	* .509	* .372
F/FM	.174	* .264	* .206	* .319	* .333	* .339	* .337	* .271

- 25 CR-AMP LOZENGEE
- 26 CR-AMP
- 27 CR-AMP
- 28 INT DOMAIN C1
- 29 ***SAMPLE ANAR-1A AMPH OVERGROWTH SPOT 2, 05-03-4193
- 30 SPOT 3, 05-03-4193
- 31 SPOT 4, 05-03-4193
- 32 CENTRAL, SPOT 1, C-1, 05-03-4194

	41	42	43	44	45	46	47	48
STO2	53.80	48.85	52.15	49.96	51.09	49.87	54.74	52.68
TIO2	1.17	1.11	.28	.78	.68	.50	1.18	.37
A2O3	1.88	5.44	3.56	4.28	5.01	5.50	2.69	3.27
C2O3	.04	.11	.18	.09	.00	.00	.04	.46
FeO	10.65	13.21	13.30	11.92	12.17	12.90	9.82	9.27
MgO	16.72	14.85	14.96	14.44	16.24	15.16	17.31	17.88
MnO	.47	.40	.56	.34	.26	.54	.25	.46
CaO	13.30	12.43	13.31	14.11	12.34	12.59	12.36	12.86
K2O	.12	.53	.21	.30	.18	.45	.21	.21
Na2O	.39	1.21	.42	1.06	.65	.68	.35	.58
F	.04	.04	.04	.04	.00	.00	.00	.04
CL	.00	.00	.00	.00	.00	.00	.00	.00
SUM	97.58	98.18	98.97	97.32	98.62	98.19	97.95	98.08
-O= F+CL	.02	.02	.02	.02	.00	.00	.00	.02
SUM	97.56	98.16	98.95	97.30	98.62	98.19	97.95	98.06
SI	7.723	* 7.132	* 7.497	* 7.321	* 7.315	* 7.237	* 7.748	* 7.499
AL	.277	8.000	.868	8.000	.503	8.000	.679	8.000
AL	.041	* .068	* .100	* .061	* .161	* .177	* .197	* .047
TI	.018	* .122	* .030	* .086	* .073	* .055	* .019	* .040
CR	.005	* .013	* .020	* .010	* .000	* .000	* .004	* .052
FE	1.279	* 1.613	* 1.599	* 1.461	* 1.457	* 1.566	* 1.162	* 1.104
Mg	3.578	* 3.232	* 3.206	* 3.154	* 3.466	* 3.279	* 3.652	* 3.794
Mn	.057	* 4.977	* .049	* 5.097	* .068	* 5.024	* .066	* 5.143
CA	2.046	* 1.944	* 2.050	* 2.215	* 1.893	* 1.957	* 1.874	* 1.961
K	.022	* .099	* .039	* .056	* .033	* .083	* .038	* .038
NNA	.109	* 2.176	* .343	* 2.386	* .301	* 2.573	* .096	* 2.008
F	.018	* .018	* .018	* .019	* .000	* .000	* .000	* .018
CL	.000	* .000	* .000	* .000	* .000	* .000	* .000	* .000
O	23.000	* 23.000	* 23.000	* 23.000	* 23.000	* 23.000	* 23.000	* 23.000
FE	26.33	* 33.29	* 33.28	* 31.65	* 29.60	* 32.31	* 24.14	* 22.53
Mg	73.67	* 66.71	* 66.72	* 68.35	* 70.40	* 67.69	* 75.86	* 77.47
F/M	.373	* .514	* .520	* .477	* .430	* .498	* .327	* .306
F/FM	.272	* .340	* .342	* .323	* .300	* .332	* .246	* .234

41 SPOT 3
 42 RANDOM 1
 43 CENTRAL, RANDOM 1
 44 SPOT 6 05-03-4196
 45 LOZENGE IN CPX - PIC 1631,3
 46 ANAR 1B - ACT MARGIN - PIC 1631
 47 ANAR 1B - AMP ON MARGIN - PIC 1631
 48 ***SAMPLE PERE 12 SPOT 10 ENCL AMPH, 05-04-4202

STO2	57	58	59	60	61	62	63	64
54.32	50.33	49.32	52.71	54.37	54.87	47.79	49.12	
TIO2	.08	.82	.74	.42	.01	.00	1.19	.88
A2O3	2.00	6.77	6.79	4.49	1.49	1.87	7.46	6.55
C2O3	.36	.02	.08	.01	.22	.07	.05	.05
FE0	8.32	10.99	10.98	9.91	10.73	9.49	10.78	11.49
MGO	19.92	15.26	16.30	16.70	17.42	18.64	16.70	15.51
MNO	.37	.31	.34	.29	.38	.34	.38	.40
CAO	12.52	11.96	12.07	12.10	12.55	12.55	11.51	11.86
K2O	.07	.63	.60	.36	.09	.08	.66	.58
NA2O	.36	.99	.91	.50	.15	.17	1.00	.79
F	.04	.00	.00	.00	.00	.00	.00	.00
CL	.00	.00	.00	.00	.00	.00	.00	.00
SUM	98.36	98.08	98.13	97.49	97.41	98.08	97.52	97.23
-O= F+CL	.02	.00	.00	.00	.00	.00	.00	.00
SUM	98.34	98.08	98.13	97.49	97.41	98.08	97.52	97.23
SI	7.639	*	7.223	7.098	7.525	7.788	7.752	7.145
AL	.331	7.970	.777	8.000	.475	8.000	.248	8.000
AL	.000	*	.368	.249	.280	.040	.063	.268
TI	.008	*	.088	.080	.045	.001	.000	.130
CR	.040	*	.002	.009	.001	.025	.008	.006
FE	.978	*	1.319	1.321	1.183	1.285	1.121	1.308
MG	4.175	*	3.264	3.496	3.554	3.719	3.925	3.363
MN	.044	5.246	.038	5.080	.035	5.098	.041	5.158
CA	1.886	*	1.839	1.861	1.851	.046	1.900	.047
K	.013	*	.115	.110	.066	.016	.014	.122
NNA	.098	1.997	.275	2.230	.138	2.055	.042	1.984
F	.018	*	.000	.000	.000	.000	.000	.000
CL	.000	*	.000	.000	.000	.000	.000	.000
O	23.000	*	23.000	23.000	23.000	23.000	23.000	23.000
FE	18.99	*	28.78	27.43	24.98	25.68	22.22	26.59
MG	81.01	*	71.22	72.57	75.02	74.32	77.78	73.41
F/M	.245		.416	.390	.343	.358	.296	.375
F/FM	.197		.294	.280	.255	.264	.228	.273

57 C-1 SKUDZZY
 58 ****SAMPLE ARN003-053 - AMP
 59 ARN003-053 - AMP
 60 ****SAMPLE C3 - DARK AMP ZONE
 61 DARK AMP ZONE
 62 DARK AMP ZONE
 63 BRIGHT AMP ZONE
 64 ****PERE 10B - AMP - PIC 1629

STO2	55.49	65	49.40	66
TIO2	.16		.73	
A2O3	2.38		7.69	
C2O3	.08		.07	
FE0	9.19		11.10	
MGO	17.56		15.47	
MNO	.49		.34	
CAO	12.01		11.34	
K2O	.17		.60	
NA2O	.29		.81	
F	.00		.00	
CL	.00		.00	
SUM	97.82		97.55	
-O= F+CL	.00		.00	
SUM	97.82		97.55	
SI	7.827	*	7.122	*
AL	.173	8.000	.878	8.000
AL	.223	*	.429	*
TI	.017	*	.079	*
CR	.009	*	.008	*
FE	1.084	*	1.338	*
MG	3.692	*	3.324	*
MN	.059	5.083	.042	5.220
CA	1.815	*	1.752	*
K	.031	*	.110	*
NNA	.079	1.925	.226	2.089
F	.000	*	.000	*
CL	.000	*	.000	*
O	23.000	*	23.000	*
FE	22.70		28.70	
MG	77.30		71.30	
F/M	.309		.415	
F/FM	.236		.293	

65 AMP LINEAR DOMAIN - PIC 1630

66 AMP MARGIN TO CPX- PIC 1630

Table 3: Mineral Chemical Analyses of Muscovite & Biotite

Table 3: MICA, KURUPUNG BATHOLITH, Jim Renaud (Phd Thesis), September 2009-2013

	1	2	3	4	5	6	7	8
ST02	37.54	37.62	37.07	37.42	46.42	38.44	37.26	36.52
T102	2.29	.38	3.03	2.79	.02	.45	2.61	2.94
A203	14.99	19.07	16.51	16.60	34.52	14.38	15.20	15.63
C203	.05	.00	.01	.03	.00	.01	.13	.22
FEO	14.93	12.32	14.44	14.75	2.19	11.90	16.14	17.02
MGO	15.40	15.63	15.00	14.77	1.53	18.88	14.50	13.21
MNO	.32	.35	.28	.48	.02	.20	.30	.35
BAO	.03	.09	.26	.22	.21	.16	.01	.03
CAO	.00	.03	.06	.04	.02	.00	9.36	.51
K20	9.68	9.08	8.55	8.33	10.65	10.45	.05	9.71
NA20	.07	.04	.09	.09	.18	.06	.04	.08
F	1.45	1.43	1.29	1.40	.21	1.74	.00	.00
CL	.02	.01	.03	.01	.01	.01	.00	.07
STM	96.77	96.05	96.62	96.93	95.98	96.68	95.60	96.29
-O= F+CL	.62	.60	.55	.59	.09	.73	.00	.02
STM	96.15	95.45	96.07	96.34	95.89	95.95	95.60	96.27
SI	5.529	* 5.459	* 5.424	* 5.454	* 6.172	* 5.608	* 5.431	* 5.485
AL	2.471	8.000	2.541	8.000	2.576	8.000	2.392	8.000
AL	.131	*	.721	*	.271	*	.041	*
TI	.254	*	.041	*	.333	*	.080	*
CR	.006	*	.000	*	.306	*	.049	*
FE	1.839	*	1.495	*	.001	*	.001	*
MG	3.381	*	3.381	*	1.767	*	1.452	*
MN	.040	5.650	.043	5.681	.059	4.105	.025	5.712
CA	.000	*	.005	*	.009	*	.000	*
BA	.002	*	.005	*	.015	*	.009	*
K	1.819	*	1.681	*	.011	*	.001	*
NA	.020	1.840	.011	1.702	1.596	*	1.944	*
F	.675	*	.656	*	.026	1.646	.017	1.971
CL	.005	*	.002	*	.597	*	.803	*
O	22.000	*	22.000	*	.002	*	.002	*
FE	35.23	30.66	35.07	35.91	22.000	26.13	22.000	41.96
MG	64.77	69.34	64.93	64.09	44.54	73.87	61.56	58.04
F/M	.556	.455	.551	.579	.811	.360	.636	.738
F/FM	.357	.313	.355	.367	.448	.265	.389	.425

1 *****SAMPLE ARN053-108.5m ALB IN EP DOMAIN
 2 MICA INCLUSION IN KFIELD ZONE, AREA 1, PIC 29-1008
 3 MICA CENTER
 4 MICA CENTER
 5 MUSC W EP IN PLAG, PT 7, PIC 1014
 6 *****SAMPLE ARN053 108.5A, POINT 9 MICA, PIC 1031
 7 *****SAMPLE ANAR-1A MAGMATIC OVERGOWTH SPOT 4 05-03-4194
 8 *****PERE 12 SPOT 3

	9	10	11	12	13	14	15
STO2	37.38	39.39	37.53	37.77	38.07	36.46	45.47
TIO2	2.77	1.90	4.35	2.85	3.47	1.10	.51
A2O3	15.88	14.63	15.18	16.08	15.45	19.25	35.50
C2O3	.11	.00	.44	.40	.79	.02	.00
FEO	16.58	11.66	7.22	11.88	9.60	13.60	3.98
MGO	13.13	19.65	21.21	18.14	19.17	14.77	.81
MNO	.34	.17	.00	.20	.16	.24	.03
BAO	.01	.08	.35	.20	.32	.18	.08
CAO	.27	.00	.01	.00	.01	.00	.00
K2O	9.32	9.78	9.74	8.53	9.02	10.08	9.86
NA2O	.06	.06	.06	.02	.05	.12	.25
F	.00	.00	.00	.00	.00	.00	.00
CL	.00	.00	.00	.00	.00	.00	.00
SUM	95.85	97.32	96.09	96.07	96.11	95.82	96.49
-O=	.00	.00	.00	.00	.00	.00	.00
F+CL	.00	.00	.00	.00	.00	.00	.00
SUM	95.85	97.32	96.09	96.07	96.11	95.82	96.49
SI	5.588	5.663	5.395	5.488	5.500	5.389	6.041
AL	2.412	8.000	2.337	2.512	2.500	2.611	1.959
AL	.386	*	.142	.241	.130	.742	3.598
TI	.311	*	.205	.311	.377	.122	.051
CR	.013	*	.000	.046	.090	.002	.000
FE	2.073	*	1.402	1.444	1.160	1.681	.442
MG	2.926	*	4.211	3.928	4.128	3.254	.160
MN	.043	5.752	.021	.025	.020	.030	.003
CA	.043	*	.000	.000	.002	.000	.000
BA	.001	*	.005	.011	.018	.010	.004
K	1.777	*	1.793	1.581	1.662	1.900	1.671
NA	.017	1.838	.017	.006	.014	.034	.064
F	.000	*	.000	.000	.000	.000	.000
CL	.000	*	.000	.000	.000	.000	.000
O	22.000	*	22.000	22.000	22.000	22.000	22.000
FE	41.47	24.98	16.04	26.87	21.93	34.06	73.38
MG	58.53	75.02	83.96	73.13	78.07	65.94	26.62
F/M	.723	.338	.191	.374	.286	.526	2.778
F/EM	.420	.253	.160	.272	.222	.345	.735

9 PERE 12 SPOT 4 05-04-4199
 10 ****ARN053-89.3m BRIGHT BIOTITTE
 11 DARK BIOTITTE DOMAIN
 12 BRIGHT BIOTITTE
 13 DARK BIOTITTE
 14 BIOTITTE
 15 PHENGITTE

Table 4: Mineral Chemical Analyses of Chlorite

Table 4: CHLORITE, KURUPUNG BATHOLITH, Jim Renaud (PhD Thesis), September 2009-2013

	1	2	3	4	5	6	7	8
STO2	28.66	29.46	29.36	29.70	29.60	28.29	29.61	29.16
TIO2	.00	.00	.00	.04	.03	.06	.04	.08
A2O3	17.06	21.26	21.27	21.45	23.18	24.08	19.42	20.62
C2O3	.01	.06	.06	.00	.00	.03	.03	9.03
FEO	18.25	17.20	17.86	17.98	10.29	13.08	15.34	15.43
WGO	22.18	18.96	19.48	18.78	25.37	21.50	24.22	22.83
MNO	.32	.22	.40	.44	.43	.50	.36	.39
CAO	.02	.03	.01	.01	.55	.32	.04	.23
K2O	.01	.08	.02	.00	.02	.00	.12	.15
NA2O	.04	.00	.02	.00	.02	.01	.02	.01
STM	86.55	87.27	88.48	88.40	89.49	87.87	89.20	97.93
SI	5.894	*	5.913	*	5.841	*	5.906	*
AL	2.106	8.000	2.087	8.000	2.159	8.000	2.094	8.000
AL	2.028	*	2.942	*	2.827	*	2.933	*
TI	.000	*	.000	*	.000	*	.006	*
CR	.002	*	.010	*	.009	*	.000	*
FE	3.139	*	2.887	*	2.971	*	2.990	*
MG	6.799	*	5.672	*	5.776	*	5.567	*
MN	.056	12.022	.037	11.548	.067	11.651	.074	11.570
CA	.004	*	.006	*	.002	*	.002	*
K	.003	*	.020	*	.005	*	.000	*
NA	.016	.023	.000	.027	.008	.015	.000	.002
O	28.000	*	28.000	*	28.000	*	28.000	*
FE	31.58	33.73	33.97	34.95	18.54	25.45	26.22	27.49
MG	68.42	66.27	66.03	65.05	81.46	74.55	73.78	72.51
F/M	.470	.516	.526	.550	.237	.355	.364	.389
F/FM	.320	.340	.345	.355	.192	.262	.267	.280

1 ****SAMPLE ARN053-108.5m MARGINAL CHL
 2 CHL(1)
 3 CHL(1)
 4 CHL(1)
 5 ****SAMPLE ANCO00-120 - CHL ON BT
 6 CHL - PIC 1627
 7 ****SAMPLE ARN003-053 - CHL ON AMP
 8 CHL ON AMP

	9	10	11	12	13	14	15	16
STO2	27.99	30.46	29.65	29.57	28.32	29.28	28.53	29.68
TIO2	.07	.00	.00	.00	.00	.00	.00	.13
A2O3	21.80	20.60	20.86	20.86	21.31	21.16	22.49	19.30
C2O3	.00	.05	.02	.04	.00	.01	.07	.00
FEO	19.07	13.98	14.61	14.05	14.79	15.57	16.18	14.76
MGO	20.33	23.91	23.29	23.47	23.59	22.49	22.01	24.83
MNO	.50	.13	.27	.23	.29	.30	.42	.29
CAO	.00	.06	.08	.03	.01	.04	.09	.03
K2O	.07	.18	.11	.17	.00	.31	.15	.16
NA2O	.00	.00	.01	.01	.00	.00	.00	.01
STM	89.83	89.37	88.90	88.43	88.31	89.16	89.94	89.19
SI	5.545	5.881	5.784	5.784	5.580	5.732	5.555	5.794
AL	2.455	2.119	2.216	2.216	2.420	2.268	2.445	2.206
AL	2.633	2.568	2.579	2.592	2.528	2.614	2.716	2.234
TI	.010	.000	.000	.000	.000	.000	.000	.019
CR	.000	.008	.003	.006	.000	.002	.011	.000
FE	3.159	2.257	2.383	2.298	2.437	2.549	2.635	2.410
MG	6.003	6.881	6.772	6.843	6.928	6.563	6.388	7.225
MN	.084	11.889	.021	11.735	.038	11.941	.050	11.819
CA	.000	*	.012	*	.006	*	.019	*
K	.018	*	.044	*	.042	*	.037	*
NA	.000	.018	.000	.057	.004	.002	.000	.056
O	28.000	*	28.000	*	28.000	*	28.000	*
FE	34.48	24.70	26.03	25.14	26.02	27.98	29.20	25.01
MG	65.52	75.30	73.97	74.86	73.98	72.02	70.80	74.99
F/M	.540	.331	.359	.341	.359	.396	.423	.340
F/FM	.351	.249	.264	.255	.264	.284	.297	.254

9 *****SAMPLE C3 - CHL
 10 *****SAMPLE ARN085-100.43 - BLUE CHLORITE (2)
 11 BLUE CHLORITE (2)
 12 BLUE CHLORITE (2)
 13 BLUE CHLORITE (2)
 14 BLUE CHLORITE (2) BRIGHT ZONE
 15 BLUE CHLORITE (2) DK ZONE
 16 BLUE CHLORITE (2)

	17	18	19
STO2	27.85	27.26	28.11
TIO2	.00	.10	.06
A2O3	21.96	21.58	18.61
C2O3	.07	.09	.01
FE0	15.41	15.42	13.66
MG0	22.61	22.91	26.29
MNO	.25	.08	.17
CAO	.03	.02	.24
K2O	.06	.04	.22
NA2O	.00	.00	.02
STM	88.24	87.50	87.39
SI	5.512	5.448	5.606
AL	2.488	2.552	2.394
AL	2.633	2.531	1.980
TI	.000	.015	.009
CR	.011	.014	.002
FE	2.550	2.577	2.278
MG	6.669	6.825	7.815
MN	.042	.014	.029
CA	.006	.004	.051
K	.015	.010	.056
NA	.000	.022	.008
O	28.000	.000	.014
FE	27.66	27.41	22.57
MG	72.34	72.59	77.43
F/M	.389	.380	.295
F/FM	.280	.275	.228

17 ARN085-100.43 - BLUE CHLORITE (2)
 18 ***ARN053-89.3m
 19 ANOTHER CHLORITE

Table 5: Mineral Chemical Analyses of Plagioclase & Feldspar

Table 5: FIELDSPARKS, KURUPUNG BATHOLITH, Jim Renaud (PhD Thesis), September 2009-2013

	1	2	3	4	5	6	7	8
STO2	65.75	64.45	63.72	64.77	68.86	69.44	69.97	64.74
A2O3	22.93	22.54	22.87	21.87	19.18	19.37	19.59	18.45
CAO	1.87	4.07	3.99	3.22	.07	.06	.15	.01
NA2O	7.74	8.04	9.11	10.09	11.46	11.36	9.50	.34
K2O	1.30	.20	.26	.06	.04	.04	.06	16.62
BAO	.00	.00	.00	.00	.00	.00	.00	.28
FEO	.03	.06	.15	.00	.03	.06	.04	.13
SiM	99.62	99.36	100.10	100.01	99.64	100.33	99.31	100.57
SI	11.535	11.389	11.248	11.421	12.050	12.058	12.125	12.003
AL	4.465	4.611	4.752	4.544	3.950	3.942	3.875	3.969
AL	.275	.083	.006	.000	.005	.022	.184	.000
CA	.351	.771	.755	.608	.013	.011	.028	.002
NA	2.633	2.755	3.118	3.449	3.888	3.825	3.238	.120
K	.291	.045	.059	.013	.009	.009	.013	3.870
BA	.000	.000	.000	.000	.000	.000	.000	.020
FE	.004	.009	.022	.000	.004	.009	.006	.020
O	32.000	32.000	32.000	32.000	32.000	32.000	32.000	32.000
AlBI	80.39	77.15	79.31	84.73	99.44	99.48	98.73	3.01
ORTH	8.88	1.26	1.49	.33	.23	.23	.41	96.94
ANOR	10.73	21.58	19.20	14.94	.34	.29	.86	.05

1 ****SAMPLE ARN063-128.8m - ALB IN EP DOMAIN
 2 IN C Q QTZ
 3 IN C Q QTZ
 4 IN EPIDOTE DOMAIN - C2
 5 IN C-3
 6 POINT 1
 7 POINT 2
 8 POINT 3 KSPAR

FIELDSPARKS, KURUPUNG BATHOLITH, Jim Renaud (PhD Thesis), September 2009-2013

STO2	25	64.75	26	64.99	27	64.76	28	64.62	29	64.95	30	64.65	31	65.05	32	64.97
A203	18.74	18.43	18.46	18.10	18.52	18.52	18.52	18.52	18.52	18.52	18.52	18.52	18.52	18.52	18.83	
CAO	.00	.01	.00	.00	.01	.01	.01	.01	.01	.01	.01	.01	.01	.01	.02	
NA20	.89	.53	.44	.93	1.15	1.15	1.15	1.15	1.15	1.15	1.15	1.15	1.15	1.15	.70	
K20	15.43	16.16	16.51	15.69	15.15	15.15	15.15	15.15	15.15	15.15	15.15	15.15	15.15	15.20	15.20	
BAO	.42	.26	.16	1.01	.66	.66	.66	.66	.66	.66	.66	.66	.66	.63	.33	
FEO	.19	.14	.11	.09	.24	.24	.24	.24	.24	.24	.24	.24	.24	.11	.07	
SUM	100.42	100.52	100.44	100.44	100.68	100.57	100.57	100.57	100.22	100.22	100.12	100.12	100.22	100.22	100.12	
SI	11.931	11.978	12.006	11.978	11.978	11.978	11.978	11.978	11.952	11.937	11.937	12.002	12.002	11.961	*	
AL	4.069	4.003	3.971	3.954	4.016	4.030	4.030	4.030	4.016	4.030	4.030	3.998	3.998	4.039	16.000	
AL	.000	.000	.000	.000	.000	.000	.000	.000	.000	.000	.000	.024	.024	.046	*	
CA	.000	.002	.000	.000	.002	.014	.014	.014	.002	.014	.014	.002	.002	.004	*	
NA	.318	.189	.156	.334	.410	.326	.326	.326	.410	.326	.326	.132	.132	.250	*	
K	3.626	3.799	3.845	3.710	3.556	3.662	3.662	3.662	3.556	3.662	3.662	3.659	3.659	3.569	*	
BA	.030	.019	.011	.073	.048	.056	.056	.056	.048	.056	.056	.046	.046	.024	*	
FE	.029	.022	.017	.014	.037	.014	.014	.014	.037	.014	.014	.017	.017	.011	3.903	
O	32.000	32.000	32.000	32.000	32.000	32.000	32.000	32.000	32.000	32.000	32.000	32.000	32.000	32.000	*	
ALBI	8.06	4.75	3.89	8.27	10.34	8.14	8.14	8.14	10.34	8.14	8.14	3.49	3.49	6.54	*	
ORTH	91.94	95.20	96.11	91.73	89.61	91.51	91.51	91.51	89.61	91.51	91.51	96.46	96.46	93.36	*	
ANOR	.00	.05	.00	.00	.05	.35	.35	.35	.05	.35	.35	.05	.05	.10	*	

- 25 NEXT ZONE OUT
- 26 NEXT ZONE OUT
- 27 OUTERMOST ZONE
- 28 ZONE -1
- 29 ZONE -2
- 30 ZONE -3
- 31 ZONE -4
- 32 OUTER MOST MARGIN OF KSPAR

STO2	33	65.21	34	65.30	35	64.96	36	65.48	37	64.38	38	64.83	39	65.23	40	65.13
A2O3		18.31		18.41		18.70		18.55		18.57		18.20		18.18		18.15
CAO		.08		.02		.03		.07		.09		.03		.01		.01
NA2O		1.14		.69		.93		1.55		1.34		1.57		.46		.72
K2O		15.18		16.18		15.45		16.18		15.07		16.08		16.18		16.08
BAO		.68		.20		.22		.66		.63		.59		.35		.58
FEO		.17		.16		.15		.27		.12		.18		.11		.03
SiM		100.77		100.96		100.44		100.69		100.20		100.48		100.52		100.70
SI	11.987	*	11.983	*	11.947	*	11.985	*	11.985	*	11.912	*	11.987	*	12.023	*
AL	3.966	15.953	3.981	15.964	4.053	16.000	4.001	15.986	4.049	15.960	3.965	15.952	3.949	15.971	3.943	15.950
AL	.000	*	.000	*	.000	*	.000	*	.000	*	.000	*	.000	*	.000	*
CA	.016	*	.004	*	.006	*	.014	*	.018	*	.006	*	.002	*	.002	*
NA	.406	*	.245	*	.332	*	.550	*	.481	*	.204	*	.164	*	.257	*
K	3.559	*	3.787	*	3.624	*	3.294	*	3.556	*	3.792	*	3.804	*	3.781	*
BA	.049	*	.014	*	.016	*	.047	*	.046	*	.043	*	.025	*	.042	*
FE	.026	4.056	.025	4.075	.023	4.001	.041	3.947	.019	4.119	.028	4.073	.017	4.012	.005	4.087
O	32.000	*	32.000	*	32.000	*	32.000	*	32.000	*	32.000	*	32.000	*	32.000	*
AlBI	10.21		6.08		8.37		14.26		11.85		5.11		4.14		6.37	
ORTH	89.40		93.82		91.48		85.39		87.71		94.75		95.81		93.58	
ANOR	.40		.10		.15		.36		.44		.15		.05		.05	

33 ****ARN005 42.7-42.85m - PEGMATITE DIKE, KSPAR CORE
 34 MARGINAL ZONE
 35 OUTER ZONE
 36 OUTER ZONE
 37 CORE
 38 ANOTHER CENTRAL
 39 ****SAMPLE ANGC011-120m POINT 1- PIC 1014 AREA 1
 40 POINT 2

FELDSPARKS, KURUPUNG BATHOLITH, Jim Renaud (PhD Thesis), September 2009-2013

STO2	57	64.87	58	65.20	59	67.94	60	65.62	61	65.11	62	68.34	63	67.81	64	68.61
A2O3		18.51		18.41		20.01		18.52		18.65		19.44		19.80		19.99
CAO		.02		.04		.63		.13		.06		.29		.32		.35
NA2O		.30		.40		11.24		.18		.69		11.10		11.91		11.90
K2O		16.26		16.44		.13		15.60		15.41		.69		.10		.03
BAO		.34		.24		.00		.22		.76		.08		.04		.00
FEO		.23		.12		.13		.07		.17		.02		.00		.00
SUM		100.53		100.85		100.08		100.34		100.85		99.96		99.98		100.88
SI	11.966	*	11.986	*	11.879	*	12.040	*	11.960	*	11.976	*	11.884	*	11.900	*
AL	4.023	15.989	3.988	15.974	4.121	16.000	3.960	16.000	4.037	15.997	4.014	15.990	4.089	15.973	4.086	15.986
AL	.000	*	.000	*	.001	*	.045	*	.000	*	.000	*	.000	*	.000	*
CA	.004	*	.008	*	.118	*	.026	*	.012	*	.054	*	.060	*	.065	*
NA	.107	*	.143	*	3.810	*	.064	*	.246	*	3.771	*	4.047	*	4.002	*
K	3.825	*	3.855	*	.029	*	3.651	*	3.611	*	1.54	*	.022	*	.007	*
BA	.025	*	.017	*	.000	*	.016	*	.055	*	.005	*	.003	*	.000	*
FE	.035	3.997	.018	4.041	.019	3.978	.011	3.812	.026	3.949	.003	3.988	.000	4.132	.000	4.073
O	32.000	*	32.000	*	32.000	*	32.000	*	32.000	*	32.000	*	32.000	*	32.000	*
ALBI		2.73		3.56		96.29		1.71		6.35		94.76		98.00		98.24
ORTH		97.17		96.24		.73		97.60		93.34		3.88		.54		.16
ANOR		.10		.20		2.98		.68		.31		1.37		1.46		1.60

- 57 IMMED ADJ CENTRAL PLAG NOW ALBITE
- 58 POINT 4
- 59 POINT 5 DARK GROWTH ZONES
- 60 IN TRIANG DOMAIN W MICRO TWINNING AT MARGIN
- 61 AT MARGIN ZONED GRAIN
- 62 POINT 6 PLAG INCL BA-ZONED KSPAR
- 63 POINT 7
- 64 POINT 8

FIELDSPARS, KURUPUNG BATHOLITH, Jim Renaud (PhD Thesis), September 2009-2013

STO2	65	64.34	*	11.957	*	11.973	*	11.956	*	11.975	*	11.983	*	11.920	*	12.029	*
A203	66	18.56	*	18.56	*	18.44	*	18.52	*	18.52	*	18.51	*	19.81	*	18.31	*
CAO	67	.03	*	.08	*	.12	*	.01	*	.06	*	.09	*	.35	*	.01	*
NA20	68	.47	*	.61	*	.40	*	.27	*	.74	*	1.04	*	11.40	*	.15	*
K20	69	15.46	*	15.15	*	15.77	*	16.50	*	15.37	*	15.31	*	1.19	*	16.13	*
BAO	70	.67	*	.58	*	.44	*	.43	*	.50	*	.35	*	.00	*	.32	*
FEO	71	.08	*	.11	*	.14	*	.16	*	.15	*	.19	*	.04	*	.10	*
SUM	72	99.61	*	99.38	*	99.95	*	100.72	*	100.29	*	100.97	*	99.88	*	100.20	*
SI	65	11.958	*	11.957	*	11.973	*	11.956	*	11.975	*	11.983	*	11.920	*	12.029	*
AL	66	4.042	*	4.043	*	4.025	*	4.025	*	4.024	*	3.992	*	4.080	*	3.971	*
AL	67	.022	*	.024	*	.000	*	.000	*	.000	*	.000	*	.007	*	.011	*
CA	68	.006	*	.016	*	.024	*	.002	*	.012	*	.018	*	.066	*	.002	*
NA	69	.169	*	.230	*	.144	*	.097	*	.265	*	.369	*	3.869	*	.054	*
K	70	3.665	*	3.594	*	3.726	*	3.881	*	3.615	*	3.574	*	.042	*	3.797	*
BA	71	.049	*	.042	*	.032	*	.031	*	.036	*	.025	*	.000	*	.023	*
FE	72	.012	*	.017	*	.022	*	.025	*	.023	*	.029	*	.006	*	.015	*
O		32.000	*	32.000	*	32.000	*	32.000	*	32.000	*	32.000	*	32.000	*	32.000	*
ALBI		4.41	*	5.74	*	3.69	*	2.43	*	6.80	*	9.32	*	97.28	*	1.39	*
ORTH		95.43	*	93.84	*	95.70	*	97.52	*	92.90	*	90.24	*	1.07	*	98.56	*
ANOR		.16	*	.42	*	.61	*	.05	*	.30	*	.45	*	1.65	*	.05	*
65 DOME 1A - BRIGHT ZONE CONCENTRIC KSPAR, C1, PIC 1017																	
66 SPOT 2																	
67 SPOT 3																	
68 SPOT 4 REL BRIGHT																	
69 SPOT 5																	
70 SPOT 6																	
71 SPOT 7 DARK ALBITE ZONE																	
72 SPOT 8																	

FIELDSPARKS, KURUPUNG BATHOLITH, Jim Renaud (PhD Thesis), September 2009-2013

	73	74	75	76	77	78	79	80
STO2	64.73	65.04	69.68	68.64	64.28	64.94	64.23	64.31
A2O3	18.50	18.25	19.38	19.25	18.98	18.53	18.90	18.56
CAO	.01	.21	.10	.35	.08	.04	.12	.00
NA2O	.27	.17	11.59	10.86	1.88	.34	.68	.19
K2O	16.63	16.37	.16	.13	14.05	15.92	15.04	16.84
BAO	.52	.29	.00	.01	.92	.78	1.05	.70
FE0	.11	.11	.00	.15	.10	.12	.06	.06
SUM	100.77	100.44	100.91	99.39	100.29	100.67	100.08	100.66
SI	11.949	12.003	12.048	11.810	11.860	11.972	11.900	11.917
AL	4.024	3.969	3.949	4.190	4.127	4.025	4.100	4.053
AL	.000	.000	.000	.020	.000	.000	.026	.000
CA	.097	.061	.019	.070	.016	.008	.024	.000
NA	3.915	3.853	3.885	3.908	.673	.122	.244	.068
K	.038	.021	.000	.031	3.306	3.743	3.554	3.980
BA	.017	.017	.000	.001	.067	.056	.076	.051
FE	32.000	32.000	32.000	32.000	32.000	32.000	32.000	32.000
O	2.41	1.54	98.63	97.50	16.84	3.14	6.39	1.69
ALBI	97.54	97.41	.90	.77	82.77	96.66	92.99	98.31
ORTH	.05	1.05	.47	1.74	.40	.20	.62	.00
ANOR								

- 73 SPOT 9
- 74 OUTER EXTREME ZONE
- 75 SPOT 10 ALBITE ZONE
- 76 *****DOME 1A POINT 1 PLAG, CENTRAL W EPID, C2, PIC 1019
- 77 POINT 2 BRIGHT ZONE
- 78 POINT 3
- 79 POINT 4
- 80 POINT 5

FIELDSPARKS, KURUPUNG BATHOLITH, Jim Renaud (PhD Thesis), September 2009-2013

STO2	89	64.31	90	64.83	91	63.55	92	64.23	93	64.52	94	64.08	95	64.60	96	63.85
A2O3	18.55	18.32	18.37	18.71	18.71	18.60	18.60	18.60	18.33	18.33	18.33	18.83	18.83	18.83	18.83	18.83
CAO	.02	.04	.21	.21	.21	.26	.22	.22	.00	.00	.07	.07	.02	.02	.04	.04
NA2O	.22	.21	.21	.22	.26	.22	.22	.22	.27	.27	.71	.71	.44	.44	.65	.65
K2O	16.15	16.24	16.24	16.15	15.94	16.15	16.15	16.15	16.15	16.15	15.32	15.32	15.91	15.91	15.28	15.28
BAO	.81	.37	.89	.26	.78	.91	.91	.78	.91	.91	.18	.18	.69	.69	1.32	1.32
FEO	.14	.13	.19	.06	.07	.07	.06	.06	.07	.07	.18	.18	.11	.11	.10	.10
SUM	100.20	100.14	99.41	99.48	100.50	99.87	100.10	100.10	100.10	100.10	100.10	100.07	100.07	100.07	100.07	100.07
SI	11.937	11.997	11.911	11.954	11.931	11.867	11.979	11.878	11.979	11.878	11.979	11.878	11.979	11.878	11.979	11.878
AL	4.057	3.995	4.057	4.046	4.069	4.123	4.005	4.122	4.005	4.122	4.005	4.122	4.005	4.122	4.005	4.122
AL	.000	.000	.000	.020	.007	.000	.000	.005	.000	.000	.000	.005	.000	.000	.005	.000
CA	.004	.008	.042	.004	.000	.014	.004	.008	.000	.004	.014	.004	.000	.004	.008	.008
NA	.079	.075	.094	.079	.097	.259	.158	.234	.079	.158	.259	.158	.234	.079	.158	.234
K	3.824	3.833	3.810	3.834	3.809	3.676	3.763	3.625	3.809	3.763	3.676	3.625	3.763	3.625	3.625	3.625
BA	.059	.037	.065	.019	.057	.067	.050	.096	.057	.050	.067	.096	.050	.050	.096	.096
FE	.022	.020	.030	.009	.011	.028	.017	.016	.011	.017	.028	.016	.017	.016	.028	.028
O	32.000	32.000	32.000	32.000	32.000	32.000	32.000	32.000	32.000	32.000	32.000	32.000	32.000	32.000	32.000	32.000
ALBI	2.03	1.92	2.39	2.03	2.48	6.56	4.03	6.06	2.48	6.56	4.03	6.06	4.03	6.06	4.03	6.06
ORTH	97.87	97.87	96.54	97.87	97.52	93.09	95.87	93.73	97.52	93.09	95.87	93.73	95.87	93.73	93.73	93.73
ANOR	.10	.20	1.07	.10	.00	.36	.10	.21	.00	.36	.10	.21	.10	.21	.10	.21

89 POINT 14
 90 ADJ MICROCLINE, SPOT 1, PIC 1023
 91 SPOT 2
 92 SPOT 3
 93 ****DOME 1A - POINT 1 PIC 1025
 94 POINT 2
 95 POINT 3
 96 POINT 4

FIELDSPARKS, KURUPUNG BATHOLITH, Jim Renaud (PhD Thesis), September 2009-2013

	113	114	115	116	117	118	119	120
STO2	64.95	64.20	63.28	64.28	63.86	63.15	62.25	62.80
A2O3	18.46	18.41	18.83	18.27	18.34	18.96	19.30	19.11
CAO	.04	.02	.00	.01	.00	.02	.00	.01
NA2O	.39	.34	.24	.25	.27	.24	.30	.27
K2O	15.71	15.93	15.29	16.39	15.74	15.23	14.56	14.78
BAO	.48	1.01	1.85	.55	1.17	2.83	3.49	3.88
FE0	.09	.05	.04	.19	.17	.20	.09	.00
SUM	100.12	99.96	99.53	99.94	99.55	100.63	99.99	100.85
SI	11.966	11.951	11.820	11.962	11.947	11.812	11.742	11.779
AL	4.004	4.038	4.180	4.006	4.043	4.179	4.258	4.221
AL	.014	.000	.032	.000	.000	.000	.031	.002
CA	.008	.004	.000	.002	.000	.004	.000	.002
NA	.140	.123	.088	.090	.098	.087	.110	.098
K	3.701	3.782	3.701	3.890	3.756	3.634	3.503	3.536
BA	.035	.074	.138	.040	.086	.207	.258	.285
FE	.014	3.912	.008	3.990	.027	.031	.014	3.916
O	32.000	32.000	32.000	32.000	32.000	32.000	32.000	32.000
ALBI	3.63	3.14	2.33	2.26	2.54	2.34	3.04	2.70
ORTH	96.17	96.76	97.67	97.69	97.46	97.56	96.96	97.24
ANOR	.21	.10	.00	.05	.00	.11	.00	.06

113 ****ARN-053 108.5B, MICROCLINE POINT 1

114 POINT 2

115 POINT 3 BRIGHT ZONE IN VEINLEFT

116 PIC 1031 POINT 1

117 POINT 2

118 POINT 3

119 POINT 4

120 POINT 5

Table 6: Mineral Chemical Analyses of Oxides

Table 6: OXIDES, KURUPUNG BATHOLITH, Jim Renaud (PhD Thesis), September 2009-2013

	1	2	3	4	5	6	7	8
STO2	.39	.48	.52	.50	.52	.44	.44	.50
TIO2	.27	.21	.23	.22	.71	.30	.22	.20
A2O3	.28	.24	.30	.31	.25	.25	.28	.30
C2O3	1.56	1.07	.52	2.14	1.37	1.52	.43	.39
FeO	96.15	96.09	97.90	93.83	95.11	95.50	97.15	97.71
MNO	.09	.11	.15	.13	.14	.10	.09	.15
MGO	.33	.28	.27	.24	.24	.17	.29	.32
ZNO	.08	.39	.12	.40	.28	.25	.28	.26
NiO	.09	.06	.09	.09	.04	.11	.19	.27
SUM	99.24	98.93	100.10	97.86	98.66	98.64	99.37	100.10
SI	.147	.182	.196	.191	.197	.168	.167	.188
TI	.077	.060	.065	.063	.202	.086	.063	.057
AL	.125	.108	.133	.140	.112	.112	.125	.133
CR	.466	.322	.155	.647	.411	.458	.129	.116
FE	30.400	*	30.788	29.992	30.147	30.406	30.830	30.755
MN	.029	*	.035	.048	.045	.032	.029	.048
MG	.186	*	.159	.137	.136	.096	.164	.180
ZN	.022	*	.109	.113	.078	.070	.078	.072
Ni	.027	31.480	.018	31.543	.028	31.352	.034	31.462
O	32.000	*	32.000	32.000	32.000	32.000	32.000	32.000
F/M	163.632	192.772	203.757	219.665	222.681	315.526	188.137	171.587
F/FM	.994	.995	.995	.995	.996	.997	.995	.994
1 *****SAMPLE ANAR-1A SPOT 5 05-03-4194								
2 SAMPLE ANAR-1A SPOT 6								
3 *****SAMPLE ANAR-1B INCL IN AMPH, SPOT 2, 05-03-4196								
4 *****SAMPLE PERE 12 SPOT 9, 05-04-4202								
5 SAMPLE PERE 12 SPOT 7, 05-04-4203								
6 SAMPLE PERE 12 SPOT 8, 05-04-4203								
7 SPOT 8								
8 SPOT 2								

	9	10	11	12	13
STO2	.53	.48	.55	.04	.00
TIO2	.23	.22	.21	.11	.00
A2O3	.26	.28	.33	.06	.04
C2O3	.40	2.83	.99	4.23	.30
FeO	96.09	94.10	98.57	89.06	94.43
MNO	.14	.13	.15	.24	.05
MGO	.44	.33	.25	.00	.00
ZNO	.35	.33	.13	.43	.00
NTO	.19	.23	.25	.08	.01
SUM	98.63	98.93	101.43	94.25	94.83
SI	.202	.181	.204	.016	.000
TI	.066	.062	.058	.033	.000
AL	.117	.124	.144	.028	.019
CR	.121	.844	.290	1.331	.096
FE	30.655	29.672	30.530	29.631	31.808
MN	.045	.042	.047	.081	.017
MG	.250	.185	.138	.000	.000
ZN	.099	.092	.036	.126	.000
NI	.058	31.613	.074	.026	.003
O	32.000	32.000	32.000	32.000	32.000
F/M	122.712	160.215	221.562	219.665	222.681
F/FM	.992	.994	.996	.995	.996

9 SPOT 2
 10 SPOT 4
 11 SPOT 11
 12 ***ARN053-108.5m - CR-MT
 13 ***ANCO00-120 - MT - PIC 1627

Table 7: Mineral Chemical Analyses of Epidote

Table 7: EPIDOTE, KURUPUNG BATHOLITH, Jim Renaud (PhD Thesis), September 2009-2013

	1	2	3	4	5	6	7
STO2	38.03	38.20	37.89	37.82	38.13	37.70	37.51
TIO2	.04	.01	.05	.00	.13	.00	.00
A2O3	27.28	25.27	24.48	26.07	23.24	28.44	27.81
C2O3	.00	.10	2.12	2.38	.10	.04	.00
FeO	11.07	14.60	11.40	9.14	13.82	8.73	10.51
MgO	.02	.05	.03	.09	.07	.01	.01
MnO	.10	.00	.00	.33	.36	1.05	.27
K2O	.02	.03	.04	.02	.10	.04	.06
CaO	22.68	20.38	22.66	22.22	22.08	22.50	22.76
Na2O	.00	.02	.04	.01	.00	.00	.01
NiO	.00	.00	.00	.00	.00	.00	.00
SUM	99.24	98.66	98.71	98.08	98.03	98.51	98.94
SI	.963	.983	.974	.967	.995	.954	.952
AL	.814	1.776	.742	1.752	.714	1.802	.831
AL	.000	.000	.000	.000	.000	.000	.000
TI	.001	.000	.001	.000	.003	.000	.000
CR	.000	.002	.043	.048	.002	.001	.000
FE	.234	.314	.245	.195	.301	.185	.223
MN	.002	.000	.000	.007	.008	.023	.006
MG	.001	.002	.001	.003	.003	.000	.000
CA	.615	.562	.624	.609	.617	.610	.619
K	.001	.001	.001	.001	.003	.001	.002
NA	.000	.001	.002	.000	.000	.000	.000
NI	.000	.883	.918	.864	.000	.000	.850
O	4.000	4.000	4.000	4.000	4.000	4.000	4.000
FO	.32	.61	.47	1.72	.89	.20	.17
FA	99.68	99.39	99.53	98.28	99.11	99.80	99.83
F/M	313.396	163.834	213.209	59.064	113.695	549.486	605.033
F/FM	.997	.994	.995	.983	.991	.998	.998

1 ****ARN053-108.5m - PIC 1624 - DARK EPIDOTE ZONE
 2 PIC 1624 - BRIGHT EPIDOTE ZONE
 3 CR-EPIDOTE
 4 CR-EPIDOTE
 5 ****ARN053-89.3m
 6 DARK EPIDOTE
 7 BRIGHT EPIDOTE

Table 8: Mineral Chemical Analyses of Zircon and Uranium-bearing Phases

Table 8: Zircon and Uranium Analyses, KURUPUNG BATHOLITH, Jim Renaud (PhD Thesis), September 2009-2013

SAMPLE	SPECIES	SiO2 Wt%	TiO2 Wt%	Al2O3 Wt%	Cr2O3 Wt%	FeO Wt%	MgO Wt%	MnO Wt%	K2O Wt%	CaO Wt%	Na2O Wt%	UO2 Wt%	ThO2 Wt%	CuO Wt%	PbO Wt%
ARN-063 113.4	Coffinite	34.17	4.73	1.02	0.18	2.65	0.45	0.01	0.00	2.02	0.00	37.26	0.00	0.02	0.45
ARN-063 113.4	Coffinite	18.08	0.07	0.63	0.00	0.12	0.18	0.01	0.00	6.30	0.11	58.65	0.00	0.00	0.27
ARN-063 113.4	Brannerite	6.05	30.63	0.07	0.00	1.01	0.01	0.00	0.01	2.76	0.06	35.48	1.11	0.00	5.27
ARN-063 113.4	Brannerite	3.34	28.35	0.01	0.00	0.62	0.00	0.12	0.00	3.31	0.02	40.01	1.41	0.00	6.79
ARN-063 113.4	Coffinite	12.64	0.15	1.08	0.04	0.16	0.34	0.02	5.27	0.62	0.00	65.50	0.00	0.00	3.63
ARN-063 113.4	Thortite/Ekenite	19.28	0.06	0.07	0.00	0.48	0.00	0.59	0.00	2.05	0.00	7.51	55.31	0.18	0.67
ARN-063 113.4	Thortite/Ekenite	20.65	0.11	0.66	0.00	1.22	0.08	0.04	0.02	1.99	0.00	17.41	45.66	0.14	3.92
ARN-063 113.4	Brannerite	1.35	51.05	0.23	1.00	13.18	0.13	1.49	0.00	0.24	0.06	2.90	0.00	0.00	10.09
ARN-063 113.4	Brannerite	2.56	45.27	0.52	1.36	10.67	0.21	0.06	0.02	0.37	0.10	4.27	0.00	0.00	19.16
ARN-063 113.4	Coffinite	22.90	0.15	1.82	0.02	0.06	0.06	0.00	0.00	2.61	0.30	55.18	0.15	0.00	0.52
ARN-063 113.4	Zircon	33.42	0.05	0.54	0.05	0.29	0.22	0.10	0.00	0.66	0.01	0.79	0.00	0.00	0.12
ARN-063 113.4	Uranian Zircon	15.58	0.26	2.01	0.00	0.32	0.19	0.35	0.00	4.98	0.19	41.31	0.00	0.15	2.89
ARN-063 113.4	U-Pb-silicate	12.73	0.18	1.01	0.05	0.02	0.00	0.00	0.00	0.50	0.22	31.42	0.01	0.00	52.90
ARN-063 113.4	Brannerite	5.62	40.92	0.72	0.23	1.70	0.12	0.30	0.01	2.01	0.20	22.35	0.00	0.06	18.38
ARN-031 98.5	Coffinite	11.70	0.23	1.90	0.04	0.20	0.00	0.13	0.00	5.88	0.27	69.02	0.00	0.00	4.28
ARN-031 98.5	Brannerite	2.56	33.80	0.12	0.21	7.62	0.25	0.91	0.00	2.08	0.02	26.92	0.00	0.06	8.12
ARN-031 98.5	Brannerite	3.95	31.86	0.12	0.00	2.16	0.03	0.28	0.00	6.34	0.07	38.60	0.00	0.02	5.02
ARN-031 98.5	Brannerite	0.00	35.86	0.00	0.01	3.61	0.02	0.57	0.04	4.65	0.00	36.19	0.83	0.00	4.12
ARN-031 98.5	Thortite/Ekenite	25.69	0.06	0.00	0.00	1.35	0.02	0.00	0.19	1.10	0.07	3.47	54.52	0.00	0.20
ARN-031 98.5	Brannerite	7.63	27.65	0.77	0.14	1.95	0.02	0.27	0.00	1.65	0.02	32.76	0.31	0.00	12.58
ARN-031 98.5	Brannerite	6.29	37.70	0.75	0.03	6.04	0.00	0.44	0.00	1.83	0.00	20.80	0.00	0.00	8.61
ARN-031 98.5	U-silicate	9.98	0.00	1.66	0.00	0.08	0.08	0.57	0.00	3.43	0.33	69.84	0.00	0.02	2.28
ARN-031 98.5	Coffinite	25.92	4.03	0.52	0.00	2.16	0.00	0.21	0.05	0.54	0.00	64.26	0.00	0.00	3.24
ARN-031 98.5	Coffinite	19.65	0.01	0.00	0.00	3.25	0.00	0.00	0.00	0.00	0.00	70.26	0.01	0.00	7.01
ARN-031 98.5	Coffinite	39.82	0.00	0.03	0.00	5.06	0.00	0.07	0.10	0.00	0.05	56.21	0.00	0.00	0.00
ARN-031 98.5	Coffinite	48.05	0.00	0.00	0.00	6.16	0.01	0.00	0.00	0.00	0.00	47.09	0.00	0.01	0.00
ARN-031 98.5	Coffinite	58.05	0.00	8.10	0.00	5.01	0.15	0.06	0.20	4.05	0.00	20.05	0.15	0.00	0.00
ARN-094 107.1	Brannerite	3.10	38.36	0.00	0.00	5.01	0.15	0.06	0.20	4.05	0.00	45.05	0.00	0.11	4.09
ARN-094 107.1	Brannerite	20.62	31.64	0.00	0.00	3.15	0.00	0.00	0.00	4.25	0.02	40.72	0.00	0.00	0.00
ARN-094 107.1	Brannerite	13.21	42.91	0.00	0.00	5.16	0.00	0.00	0.00	7.26	0.01	18.61	0.20	0.00	13.11
ARN-094 107.1	Brannerite	15.25	47.15	0.00	0.00	3.01	0.00	0.00	0.25	9.11	0.00	15.21	0.00	0.00	10.08
ARN-094 107.1	Coffinite	19.14	0.00	0.00	0.00	2.98	0.00	0.00	0.00	0.00	0.00	71.12	0.00	0.10	8.05
ARN-094 107.1	Coffinite	39.01	0.00	0.00	0.00	5.64	0.29	0.00	0.00	0.00	0.06	55.58	0.00	0.00	0.00
ARN-030 175.8	Brannerite	10.24	39.65	0.00	0.00	2.87	0.00	0.00	0.19	7.58	0.00	31.24	0.00	0.00	9.61
ARN-030 175.8	Brannerite	2.14	38.15	0.00	0.00	5.87	0.00	0.00	0.00	3.14	0.00	44.87	0.00	0.00	6.20
ARN-030 175.9	Zircon granule	31.07	0.00	0.11	0.00	2.04	0.07	0.26	0.02	1.38	0.09	0.26	0.00	0.00	0.13
MOD ALT ZIRC	Zircon granule	30.08	0.16	0.20	0.00	2.20	0.08	0.20	0.00	1.49	0.02	0.36	0.00	0.00	0.55
MOD ALT ZIRC	Pitted Zircon Margin	36.28	0.13	0.00	0.00	0.18	0.00	0.00	0.00	0.00	0.00	0.00	0.00	0.20	0.00
ARN-063 113.4	Pitted Zircon Margin	30.36	0.03	1.29	0.03	2.76	0.39	0.27	0.00	1.49	0.07	0.64	0.00	0.01	0.59
ARN-063 113.4	Moderately altered Zircon granule	36.14	0.13	0.00	0.00	0.18	0.00	0.00	0.00	0.00	0.00	0.10	0.00	0.20	0.00
ARN-063 113.4	Uranian Zircon	39.00	4.31	0.15	0.02	9.18	0.19	0.34	0.09	5.00	0.12	6.01	0.06	0.02	0.46
ARN-003-98.5	Hydrothermal Zircon	30.66	0.05	1.03	0.05	2.31	0.97	0.20	0.00	1.78	0.10	0.79	0.00	0.02	0.72
ARN-003-98.6	Hydrothermal Zircon	30.71	0.05	1.00	0.00	1.70	0.06	0.17	0.03	1.02	0.10	2.01	0.18	0.00	0.78
ARN-003-98.7	Hydrothermal Zircon	29.13	0.09	0.14	0.00	1.25	0.06	0.07	0.01	1.09	0.04	5.83	0.59	0.01	1.42
ARS-043-146	Hydrothermal Zircon	29.08	0.00	0.78	0.08	3.39	0.21	0.12	0.02	1.89	0.18	3.48	0.22	0.03	0.06
ARS-043-147	Hydrothermal Zircon	30.93	0.05	0.34	0.04	1.64	0.40	0.26	0.00	1.18	0.61	4.18	0.39	0.09	0.00
ARS-043-148	Hydrothermal Zircon	60.00	0.61	0.62	0.00	2.02	0.36	0.12	0.00	3.20	0.11	2.00	0.21	0.12	0.51
ARN053-89.3m	U-Pb-silicate (KASOLITE)	11.66	0.05	1.72	0.02	0.42	0.05	0.00	0.00	1.56	0.04	32.82	0.00	0.00	43.16

Appendix B

Geochronology

Geochronology of Titanite

Geochronology and Isotopic Geochemistry

Work Order No.: **A11-14102**

Date: **March 8, 2012**

Customer: **Renaud Geological Consulting Ltd**

Number of samples: **1**

Sample type: **rock**

Analytical works: **U-Pb dating, TIMS**

Mineral separation: **Sphene**

Contact person: **Jim Renaud**

This report may be reproduced without our consent. If no instructions were given at time of sample submittal regarding excess material, it will be discarded within 90 days of this report. Our liability is limited solely to the analytical cost of these analyses. Test results are representative only of material submitted for analysis.

CERTIFIED BY:

Dr. Yakov Kapusta

Dr. Yakov Kapusta

**Geochronology and Isotopic Geochemistry
General Manager**

Sample ARNO22 141.9m-142.1m (Actlabs ID YK-YK-408) was submitted for sphene separation and U-Pb dating by TIMS.

Analytical technique. Chemical decomposition and separation of U and Pb was done by using modified T.Krogh technique (Krogh, 1973) with further purification of U following to Horwitz et al. (1992). ^{202}Pb - ^{235}U spike was added to the samples prior to dissolution. Analytical blanks are at 15 pg of Pb and 1 pg of U. The Pb and U isotope ratios were measured on the Finnigan MAT 261 mass spectrometer. For data calculation the PbDat and Isoplot programs of K.Ludwig were used (Ludwig, 1991, 1999).

Studied sphene forms brown irregular transparent or semitransparent grains enriched by opaque inclusions. Two handpicked aliquots consisting of 12 and 14 clean sphene grains have been analyzed (table 1). One aliquot (N1) yielded a concordant age of 2094 ± 5 Ma (MSWD=0.64) and another is slightly discordant and yielded similar age of 2095 ± 1 Ma. ($^{207}\text{Pb}/^{206}\text{Pb}$). Concordia age calculation for both samples is **2094.3 \pm 4.9 Ma** (MSWD=1.8).

REFERENCES:

Horwitz E.Ph., Dietz M.L., Chiarizia R., Diamond H., Essling A.M., Graczyk D.
Separation and preconcentration of uranium from acidic media by extraction chromatography .

Analytica Chimica Acta. 1992.V.266, p.25-37.

Krogh T.E. A low-contamination method for hydrothermal decomposition of zircon and extraction of U and Pb for isotopic age determination // Geochim. et cosmochim. acta. 1973.V.37. P.485-494.

Ludwig K.R. PbDat for MS-DOS, version 1.21 // U.S. Geol. Survey Open-File Rept. 88-542. 1991. 35p.

Ludwig K.R. ISOPLOT/Ex.Version 2.06. A geochronological toolkit for Microsoft Excel.

Berkley Geochronology Center Sp.Publ. 1999. № 1a. 49 pp.

Stacey J.S., Kramers I.D. Approximation of terrestrial lead isotope evolution by a two-stage model.

Earth Planet. Sci. Lett. 1975. V. 26. N.2. P. 207-221.

Table 1. Results of U-Pb isotopic studies (sample YK-408)

N	Ident	Weight, mg	Concentration, ppm		Isotopic ratios					Rho	Age, Ma		
			Pb	U	$^{206}\text{Pb}/^{204}\text{Pb}$	$^{207}\text{Pb}/^{206}\text{Pb}$	$^{208}\text{Pb}/^{206}\text{Pb}$	$^{207}\text{Pb}/^{235}\text{U}$	$^{206}\text{Pb}/^{238}\text{U}$		$^{207}\text{Pb}/^{235}\text{U}$	$^{206}\text{Pb}/^{238}\text{U}$	$^{207}\text{Pb}/^{206}\text{Pb}$
1	50 mkm, 12	0.15	139.6	282.6	1768	0.1298±1	0.3337±1	6.8604±137	0.3832±8	0.98	2094±4	2091±4	2096±1
2	50 mkm, 14	0.17	163.5	334.1	1826	0.1298±1	0.3033±1	6.9430±139	0.3880±8	0.95	2104±5	2114±6	2095±1

Note: a – isotopic ratios corrected for blank and common Pb (Stacey and Kramers, 1975). Errors (2σ) are given in last decimal places.

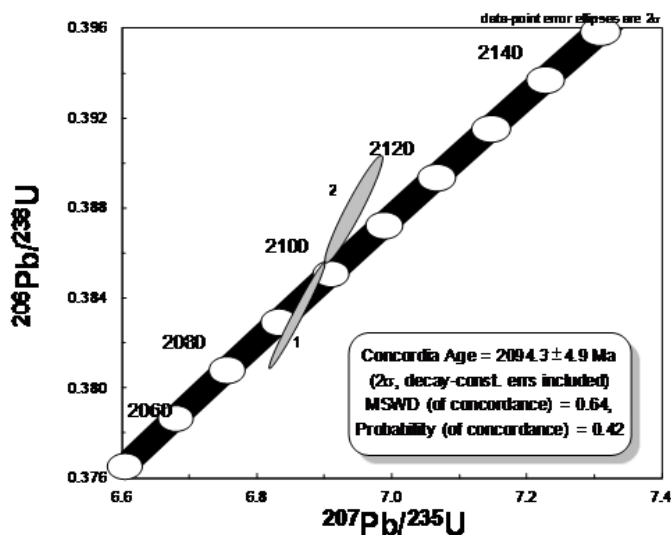


Figure 1: Results of U/Pb isotopic studies on titanite.

Geochronology of Pegmatite Dikes & Ba-Kfeldspar

Geochronology and Isotopic Geochemistry

Work Order No.: **A11-14102**Date: **March 22, 2012**

Customer: **Renaud Geological Consulting Ltd**
Number of samples: **1**
Sample type: **Rock**
Analytical works: **U-Pb analysis by SHRIMP (zircons)**
Contact person: **Jim Renaud**

This report may be reproduced without our consent. If only selected portions of the report are reproduced, permission must be obtained. If no instructions were given at time of sample submittal regarding excess material, it will be discarded within 90 days of this report. Our liability is limited solely to the analytical cost of these analyses. Test results are representative only of material submitted for analysis.

CERTIFIED BY:

_____ **Dr. Yakov Kapusta** _____

Dr. Yakov Kapusta

Geochronology and Isotopic Geochemistry
General Manager

2

One samples were submitted for U-Pb zircon grains analysis by SHRIMP:

ARN005 42.7m-42.85m

Actlabs ID YK-407

Zircons were separated from above listed sample.

Zircon grains were mounted in epoxy together with chips of the TEMORA (Middledale Gabbroic Diorite, New South Wales, Australia) and 91500 (Geostandard zircon, Wiedenbeck, 1995) reference zircons. The grains were sectioned approximately in half and polished. Images were prepared for all zircons. The U-Pb analyses of the zircons were made using SHRIMP-II. The data were reduced in a manner similar to that described by Williams (1998, and references therein). SQUID Excel Macro of Ludwig (2000) was used. Uncertainties given for individual analyses (ratios and ages) are at the one sigma level, however the uncertainties in calculated concordia ages are reported as two sigma levels. The Ahrens-Wetherill (1956) concordia plots, probability density plots and discordia age calculations have been prepared using ISOPLOT/EX (Ludwig, 1999).

REFERENCES

Ludwig, K.R., 1999. User 's manual for Isoplot/Ex, Version 2.10, A geochronological toolkit for Microsoft Excel. Berkeley Geochronology Center Special Publication No.1a, 2455 Ridge Road, Berkeley CA 94709, USA.

Ludwig, K.R., 2000. SQUID 1.00, A User's Manual; Berkeley Geochronology Center Special Publication. No.2, 2455 Ridge Road, Berkeley, CA 94709, USA.

Black, L.P., Kamo, S.L. etc., 2003, TEMORA 1: a new zircon standard for U-Pb geochronology. *Chemical Geology*, 200, 155-170

Wiedenbeck M., Alle P., Corfu F., Griffin W.L., Meier M., Oberli F., von Quadt A., Roddick J.C. and Spiegel W. (1995) Three natural zircon standards for U-Th-Pb, Lu-Hf, trace element and REE analyses. *Geostandards Newsletter*, 19, 1-23.

Wetherill, G.W., 1956. Discordant uranium-lead ages., *Trans. Amer. Geophys. Union*, 37, 320-326.

Spot	% $^{206}\text{Pb}_c$	ppm U	ppm Th	$^{232}\text{Th}/^{238}\text{U}$	ppm $^{206}\text{Pb}^*$	(1) $^{206}\text{Pb}/^{238}\text{U}$ Age	(1) $^{207}\text{Pb}/^{206}\text{Pb}$ Age	% Discordant	(1) $^{206}\text{Pb}^*/^{238}\text{U}$ $\pm\%$	(1) $^{207}\text{Pb}^*/^{206}\text{Pb}^*$ $\pm\%$	(1) $^{207}\text{Pb}^*/^{235}\text{U}$ $\pm\%$	(1) $^{206}\text{Pb}^*/^{238}\text{U}$ $\pm\%$	err corr
YK-407_1.1	0.11	130	208	1.66	42.8	2094 \pm 23	2091 \pm 16	0	2.605 1.3	0.1295 0.89	6.85 1.6	0.3838 1.3	.819
YK-407_2.1	0.11	141	169	1.23	46.6	2094 \pm 23	2110 \pm 16	1	2.605 1.3	0.1309 0.89	6.92 1.6	0.3837 1.3	.819
YK-407_3.1	0.15	212	355	1.73	68.5	2055 \pm 21	2089 \pm 13	2	2.662 1.2	0.12931 0.74	6.695 1.4	0.3755 1.2	.855
YK-407_4.1	0.15	119	141	1.23	39	2076 \pm 23	2080 \pm 19	0	2.631 1.3	0.1287 1.1	6.74 1.7	0.3799 1.3	.778
YK-407_5.1	0.16	282	521	1.91	91.3	2060 \pm 21	2095 \pm 12	2	2.655 1.2	0.12979 0.67	6.738 1.4	0.3765 1.2	.870
YK-407_6.1	0.09	240	392	1.69	77.1	2049 \pm 22	2105 \pm 16	3	2.672 1.3	0.1305 0.93	6.73 1.6	0.3742 1.3	.807
YK-407_7.1	0.08	252	462	1.90	79.8	2021 \pm 21	2096 \pm 12	4	2.715 1.2	0.12984 0.69	6.594 1.4	0.3683 1.2	.866
YK-407_8.1	0.36	86	94	1.13	28	2064 \pm 25	2098 \pm 22	2	2.647 1.4	0.13 1.3	6.76 1.9	0.3774 1.4	.738
YK-407_9.1	0.08	82	109	1.36	26.9	2073 \pm 25	2113 \pm 20	2	2.636 1.4	0.1311 1.1	6.86 1.8	0.3793 1.4	.779
YK-407_10.1	0.09	251	336	1.38	81.1	2055 \pm 21	2097 \pm 12	2	2.663 1.2	0.12993 0.71	6.726 1.4	0.3754 1.2	.861

Errors are 1-sigma; Pb_c and Pb* indicate the common and radiogenic portions, respectively.
Error in Standard calibration was 0.46%
(1) Common Pb corrected using measured ^{204}Pb .

Table 1: U-Pb age date determinations for zircons in the pegmatite dike.

YK-407

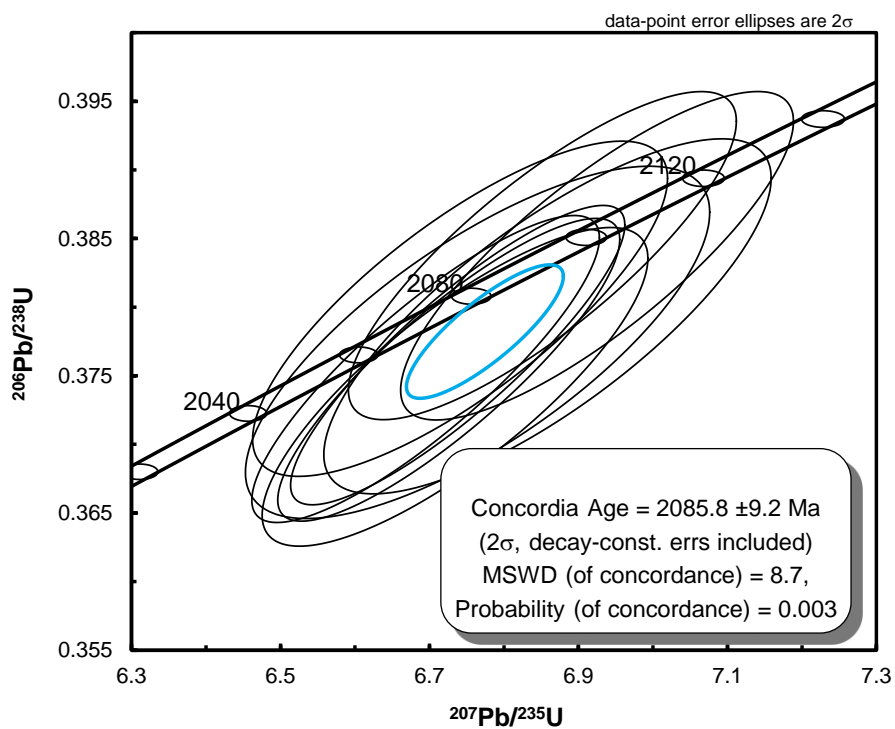


Figure 2: Concordia age diagram for zircons in pegmatite dike.

Geochronology and Isotopic Geochemistry

Work Order No.: **A11-14102**

Date: **May 24, 2012**

Number of samples: **1**

Sample type: **rock**

Analytical works: **Ar-Ar dating**

Mineral separation: **needed**

Contact person: **Jim Renaud**

This report may be reproduced without our consent. If no instructions were given at time of sample submittal regarding excess material, it will be discarded within 90 days of this report. Our liability is limited solely to the analytical cost of these analyses. Test results are representative only of material submitted for analysis.

CERTIFIED BY:

_____ **Dr. Yakov Kapusta** _____

Dr. Yakov Kapusta

**Geochronology and Isotopic Geochemistry
General Manager**

I. Overview

One sample was submitted for mineral separation and Ar-Ar dating:

ACCO-N-B 34.75m-35.18m k-feldspar

Actlabs ID YK-409

YK-409, separate consists of 100% k-feldspar (SEM confirmed)

Summary Table of $^{40}\text{Ar}/^{39}\text{Ar}$ results

<u>Sample</u>	<u>IIA (Ma)</u> <u>$\pm 1\sigma$</u>	<u>TFA</u> <u>$\pm 1\sigma$</u>	<u>WMPA</u> <u>(Ma)$\pm 1\sigma$</u>	<u>Ca/K</u>	<u>Comments</u>
2. YK-409 K-feldspar	—	2534 \pm 14	2071.0 \pm 13	0.45-6.94	Three steps plateau

Explanation:

$\pm 1\sigma$ = Estimated uncertainty (1 sigma);

IIA = Inverse Isochrone age

TFA = Total fusion age;

WMPA = Weighted mean plateau age;

Ca/K = Apparent Ca / K ratios;
Intermediate Plateau age

WMIPA = Weighted mean

II. Flux Monitoring and Isotope measurements

The sample wrapped in Al foil was loaded in evacuated and sealed quartz vial with K and Ca salts and packets of LP-6 biotite interspersed with the samples to be used as a flux monitor. The sample was irradiated in the nuclear reactor for 48 hours. The flux monitors were placed between every two samples, thereby allowing precise determination of the flux gradients within the tube. After the flux monitors were run, J values were then calculated for each sample, using the measured flux gradient. LP-6 biotite has an assumed

age of 128.1 Ma. The neutron gradient did not exceed 0.5% on sample size. The Ar isotope composition was measured in a Micromass 5400 static mass spectrometer. $^{1200^\circ\text{C}}$ blank of ^{40}Ar did not exceed $n \cdot 10^{-10}$ cc STP

III Results

YK-409 K-feldspar

The sample yielded saddle shaped age spectrum with three steps plateau characterized by 71 % of ^{39}Ar , Age value of 2071 ± 13 Ma.

On the Inverse Isochrone Plot points don't form any linear regression.

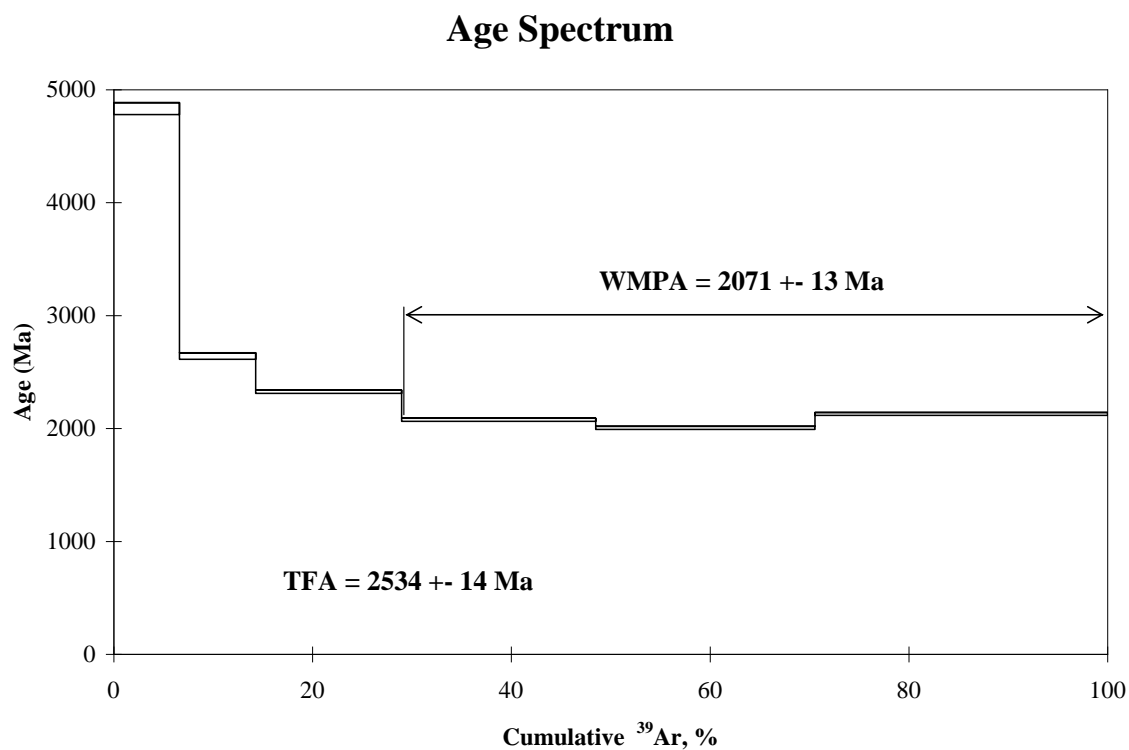


Figure 3: Age spectrum graph for Ba-Kfeldspar megacrysts.

Ca/K Spectrum

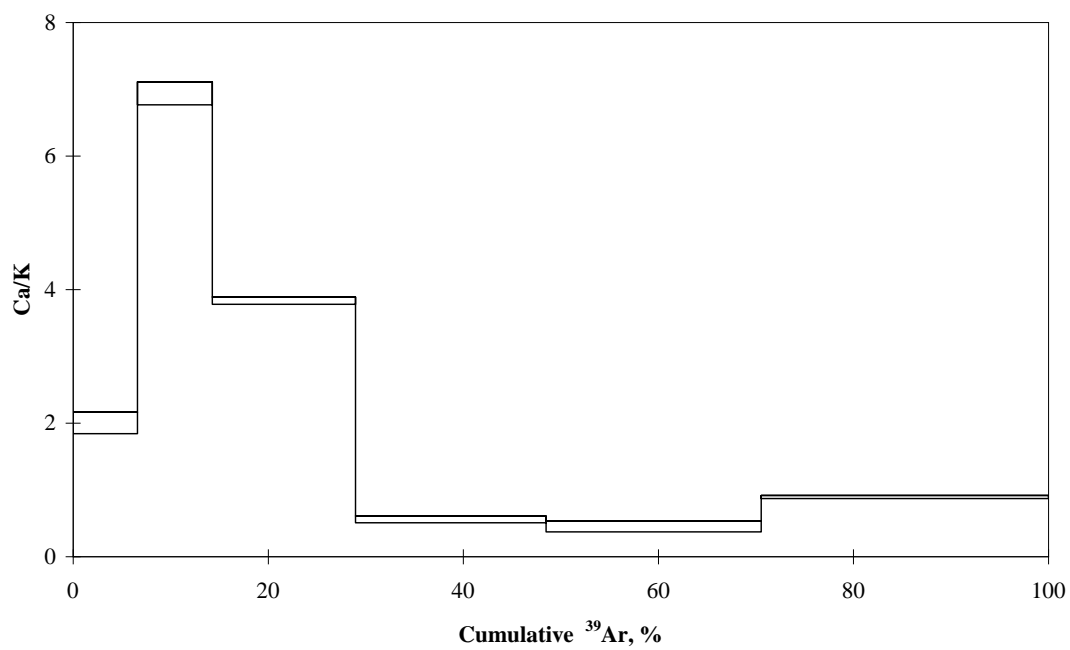


Figure 4: Graph of K/Ca ratio of each individual heating step. The graph is used to help establish when fluid inclusions are degassing from a feldspar.

Geochronology of the Lamprophyre Dike

Geochronology and Isotopic Geochemistry

Work Order No.: **A12-05956**

Date: **November 2, 2012**

Number of samples: **1**

Sample type: **rock**

Analytical works: **Ar-Ar dating**

Mineral separation: **needed**

Contact person: **Jim Renaud**

This report may be reproduced without our consent. If no instructions were given at time of sample submittal regarding excess material, it will be discarded within 90 days of this report. Our liability is limited solely to the analytical cost of these analyses. Test results are representative only of material submitted for analysis.

CERTIFIED BY:

_____ **Dr. Yakov Kapusta** _____

Dr. Yakov Kapusta

**Geochronology and Isotopic Geochemistry
General Manager**

I. Overview

One sample was submitted for mineral separation and Ar-Ar dating:

ARN053 89.3 biotite Actlabs ID YK-281

YK-281, biotite (SEM confirmed)

Summary table of $^{40}\text{Ar}/^{39}\text{Ar}$ results

<u>Sample</u>	<u>IIA (Ma)</u> $\pm 1 \sigma$	<u>TFA</u> $\pm 1 \sigma$	<u>WMPA</u> <u>(Ma)</u> $\pm 1 \sigma$	<u>Ca/K</u>	<u>Comments</u>
1. YK-281 biotite	—	1871.3 \pm 10.5	2011.2 \pm 11.0	0.047-1.045	Three steps plateau

Explanation:

$\pm 1 \sigma$ = Estimated uncertainty (1 sigma);

IIA = Inverse Isochrone age

TFA = Total fusion age;

WMPA = Weighted mean plateau age;

Ca/K = Apparent Ca / K ratios;
Intermediate Plateau age

WMIPA = Weighted mean

II. Flux Monitoring and Isotope measurements

The samples wrapped in Al foil was loaded in evacuated and sealed quartz vial with K and Ca salts and packets of LP-6 biotite interspersed with the samples to be used as a flux monitor. The sample was irradiated in the nuclear reactor for 48 hours. The flux monitors were placed between every two samples, thereby allowing precise determination of the flux gradients within the tube. After the flux monitors were run, J values were then calculated for each sample, using the measured flux gradient. LP-6 biotite has an assumed age of 128.1 Ma. The neutron gradient deed not exceeded 0.5% on sample size. The Ar isotope composition was measured in a Micromass 5400 static mass spectrometer. 1200°C blank of ^{40}Ar deed not exceed $n \cdot 10^{-10}$ cc STP

III Results

YK-281 biotite

The sample yielded discordant age spectrum with stair case rising up followed by three steps plateau characterized by 39.3 % of ^{39}Ar , Age value of 2011.2 ± 11.0 Ma.

On the Inverse Isochrone Plot points don't form any significant linear regression.

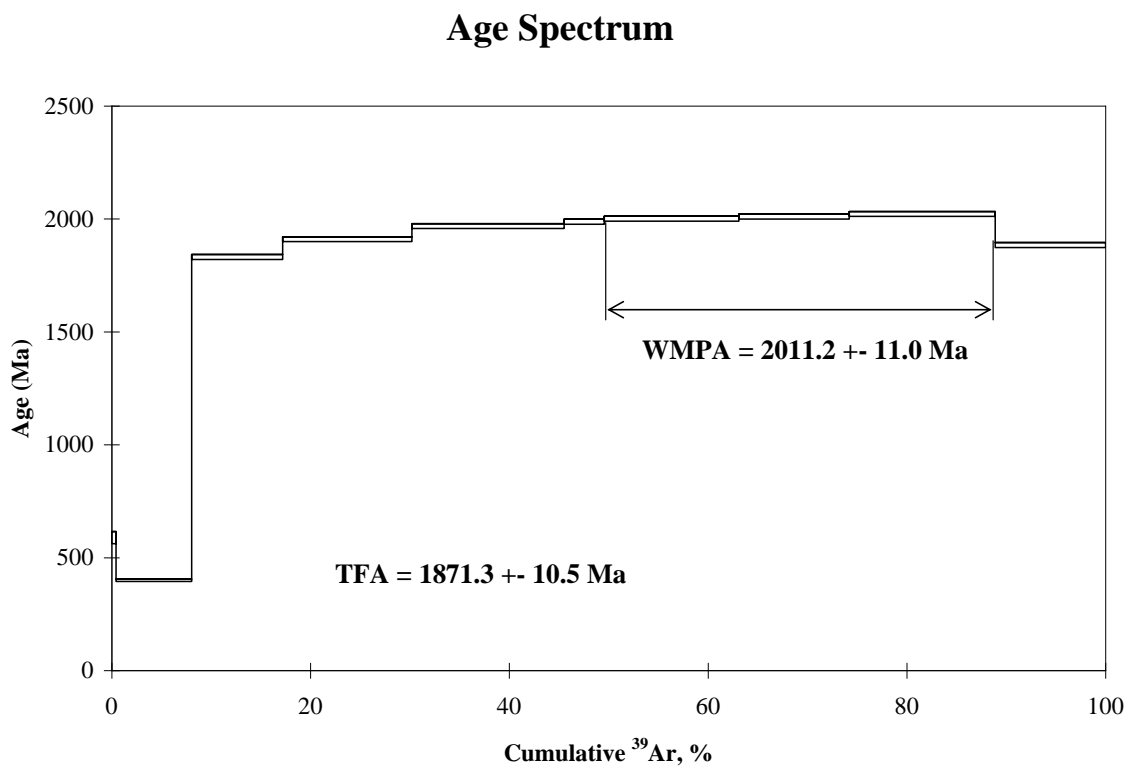


Figure 5: Age spectrum graph for Ba-Kfeldspar megacrysts.

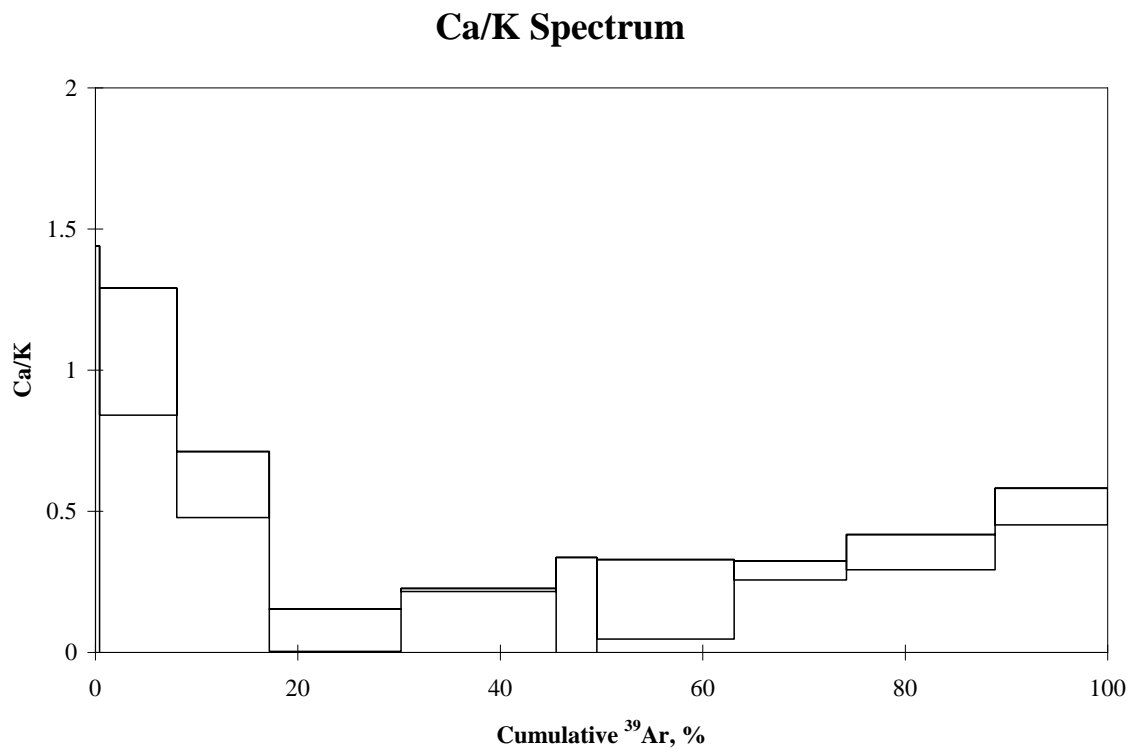


Figure 6: Graph of K/Ca ratio of each individual heating step. The graph is used to help establish when fluid inclusions are degassing from a biotite.

Isochron diagram

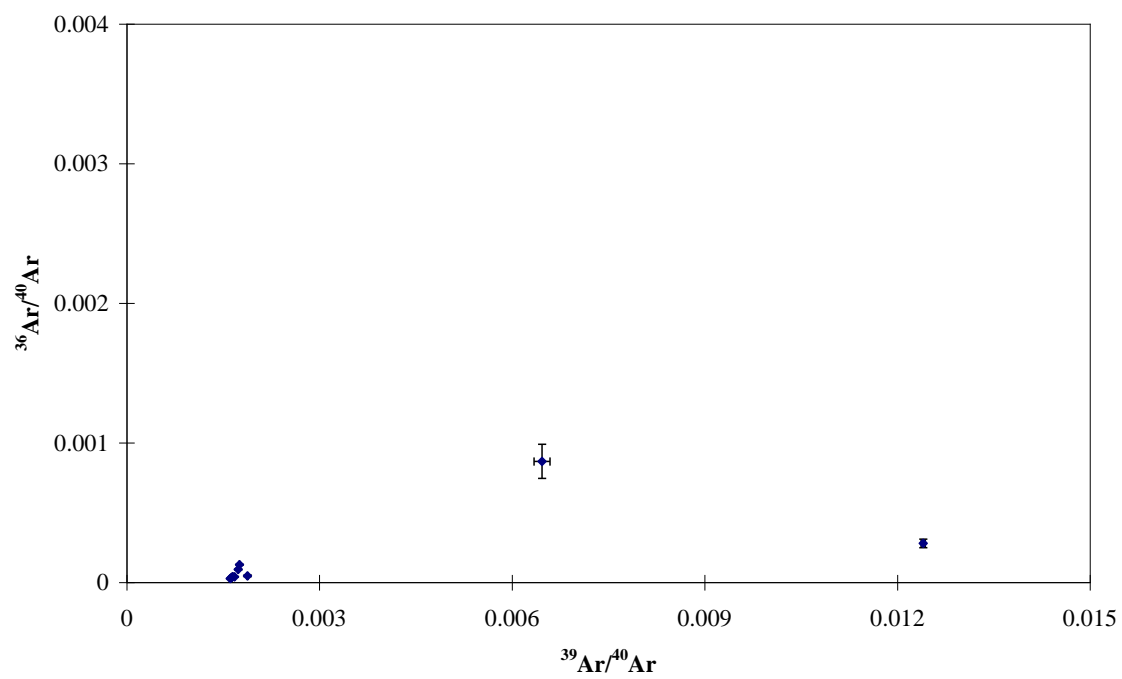


Figure 7: Isochron diagram

Tabulated data

Sample: YK-281 biotite **J=0.003355 ± 0.000030**

T°C	$^{40}\text{Arcc(STP)}$	$^{40}\text{Ar}/^{39}\text{Ar}$	$\pm 1\sigma$	$^{38}\text{Ar}/^{39}\text{Ar}$	$\pm 1\sigma$	$^{37}\text{Ar}/^{39}\text{Ar}$	$\pm 1\sigma$	$^{36}\text{Ar}/^{39}\text{Ar}$	$\pm 1\sigma$	Ca/K	$\Sigma^{39}\text{Ar}$ (%)	Age (Ma)	$\pm 1\sigma$
500	6.8^*e^{-9}	154.70	2.97	0.0280	0.0228	0.0781	0.3217	0.1343	0.0190	0.281	0.4	588.7	26.6
600	63.5^*e^{-9}	80.65	0.21	0.0204	0.0014	0.2960	0.0626	0.0226	0.0025	1.066	8.0	399.9	4.9
700	504.3^*e^{-9}	532.18	1.91	0.0151	0.0023	0.1651	0.0325	0.0256	0.0034	0.594	17.2	1831.6	11.3
750	777.0^*e^{-9}	577.26	1.17	0.0229	0.0016	0.0218	0.0208	0.0543	0.0020	0.078	30.2	1910.2	10.9
800	945.3^*e^{-9}	596.61	0.82	0.0177	0.0005	0.0614	0.0016	0.0246	0.0014	0.221	45.5	1968.3	10.9
850	252.6^*e^{-9}	606.77	1.73	0.0196	0.0039	0.0131	0.0804	0.0257	0.0028	0.047	49.5	1988.2	11.4
950	858.7^*e^{-9}	612.22	1.24	0.0191	0.0024	0.0522	0.0392	0.0224	0.0020	0.188	63.1	2001.0	11.1
1000	707.0^*e^{-9}	616.18	0.89	0.0188	0.0012	0.0806	0.0092	0.0200	0.0014	0.290	74.2	2010.3	11.0
1065	943.8^*e^{-9}	621.38	0.65	0.0138	0.0013	0.0986	0.0173	0.0176	0.0010	0.355	88.9	2022.0	11.0
1130	656.1^*e^{-9}	570.56	1.18	0.0294	0.0016	0.1435	0.0180	0.0730	0.0021	0.517	100.0	1884.3	10.8

Table 2: Ar/Ar age date determinations for biotite in the lamprophyre dike.

Appendix C

Table 1: Whole Rock and Trace Element Geochemistry of a Representative Sample Suite of the Unaltered, K-Na Metasomatized, and Mineralized Kurupung Batholith

(the sample suite was used as a reference suite for comparison to the >22000 analyses in the U3O8 Corp. database)



Date Submitted: 12-Jul-11
Invoice No.: A11-6612
Invoice Date: 11-Aug-11
Your Reference:

ATTN: Jim Renaud

CERTIFICATE OF ANALYSIS

21 Rock samples were submitted for analysis.

The following analytical package was requested: Code 4E-Res (11+) INAA(INAAGEO)/Major Elements Fusion ICP(WRA)/Total Digestion ICP (TOTAL)

REPORT **A11-6612**

This report may be reproduced without our consent. If only selected portions of the report are reproduced, permission must be obtained. If no instructions were given at time of sample submittal regarding excess material, it will be discarded within 90 days of this report. Our liability is limited solely to the analytical cost of these analyses. Test results are representative only of material submitted for analysis.

Notes:

Total includes all elements in % oxide to the left of total. Values above the upper limit should be assayed for most accurate values.

CERTIFIED BY :

Emmanuel Esemé , Ph.D.
Quality Control

ACTIVATION LABORATORIES LTD.



Analyte Symbol	SI02	AI2O3	Fe2O3(T)	MNO	MgO	CaO	Na2O	K2O	TiO2	P2O5	LOI	Total	Au	Ag	As	Ba	Be	Bi	Br	Cd	Co	Cr	Cs	Cu	
Unit Symbol	%	%	%	%	%	%	%	%	%	%	%	%	ppb	ppm	ppm	ppm	ppm	ppm	ppm	ppm	ppm	ppm	ppm	ppm	ppm
Detection Limit	0.01	0.01	0.01	0.001	0.01	0.01	0.01	0.01	0.001	0.01		0.01	1	0.5	1	1	1	2	0.5	0.5	0.5	0.1	0.5	0.2	1
Analysis Method	FUS-ICP	FUS-ICP	FUS-ICP	FUS-ICP	FUS-ICP	FUS-ICP	FUS-ICP	FUS-ICP	FUS-ICP	FUS-ICP	FUS-ICP	FUS-ICP	INAA	MULTI- INAA/TD- ICP	INAA	FUS-ICP	FUS-ICP	TD-ICP	INAA	TD-ICP	INAA	INAA	INAA	INAA	TD-ICP
PERE 12	59.91	15.86	6.01	0.094	4.10	4.44	3.79	3.70	0.691	0.46	1.65	100.7	< 1	< 0.5	6	982	2	< 2	< 0.5	< 0.5	23.5	203	0.7	165	
ARN 019 40.55-40.78m	59.69	14.41	6.04	0.092	4.00	4.80	4.04	4.19	0.725	0.60	1.42	100.0	< 1	< 0.5	5	1260	3	< 2	< 0.5	< 0.5	20.0	149	1.4	73	
ARN021 117.70-117.90m	59.00	14.65	5.70	0.084	3.41	4.59	3.83	4.43	0.676	0.50	1.10	97.97	4	< 0.5	6	1219	3	< 2	< 0.5	< 0.5	18.3	143	1.8	90	
ARN022 141.90-142.0m	58.42	14.76	6.07	0.092	3.96	5.21	4.05	3.90	0.766	0.58	1.08	98.88	< 1	< 0.5	4	1250	3	< 2	< 0.5	< 0.5	20.2	160	1.8	66	
ARN 053 108.5m	63.73	14.47	4.21	0.064	2.65	3.05	4.78	3.80	0.547	0.38	1.52	99.19	2	< 0.5	6	1249	4	< 2	< 0.5	< 0.5	13.6	109	3.2	70	
ARN 100 164.5m	56.95	14.00	6.18	0.093	3.99	5.50	3.91	4.07	0.775	0.66	2.96	99.08	< 1	< 0.5	< 1	1195	3	< 2	< 0.5	< 0.5	22.4	156	2.7	76	
ARN 085 96.5m	57.22	14.75	5.80	0.095	3.49	4.75	4.52	3.44	0.757	0.56	3.65	99.02	< 1	< 0.5	6	1383	3	< 2	< 0.5	< 0.5	20.0	148	2.6	101	
ARN 063 128.8m	60.70	14.14	4.96	0.077	3.12	4.10	3.87	4.72	0.681	0.50	1.14	98.02	< 1	< 0.5	8	1216	3	< 2	< 0.5	< 0.5	17.2	125	2.1	116	
ARN 094 102.3m	64.68	14.69	3.63	0.059	2.15	3.11	4.15	4.54	0.488	0.32	0.91	98.73	< 1	< 0.5	6	1268	3	< 2	< 0.5	< 0.5	11.8	79.1	2.9	80	
ARW 030 208.8m	62.37	15.11	4.08	0.061	2.34	2.71	4.26	4.31	0.551	0.33	1.97	98.09	< 1	< 0.5	3	1508	3	< 2	< 0.5	< 0.5	13.0	84.7	1.5	41	
ARN 048 85.5m	61.22	14.71	4.54	0.070	2.68	3.45	4.24	4.35	0.602	0.43	1.83	98.12	< 1	< 0.5	6	1278	3	< 2	< 0.5	< 0.5	14.6	100	2.5	55	
ARS 029 83.5m	61.92	15.50	4.41	0.071	2.54	3.50	4.41	3.94	0.557	0.36	1.58	98.80	< 1	< 0.5	< 1	1343	3	< 2	< 0.5	< 0.5	15.4	93.4	2.9	53	
ARS 094 151.80m	62.67	14.49	3.87	0.072	2.52	3.93	4.28	3.88	0.480	0.28	3.91	100.6	< 1	< 0.5	2	1170	2	< 2	< 0.5	< 0.5	12.9	84.5	4.1	31	
ARS 090 230.5m	3.73	0.51	0.18	0.696	0.27	51.66	0.19	0.02	0.018	0.01	41.37	98.66	< 1	< 0.5	< 1	20	< 1	< 2	< 0.5	0.7	1.4	4.7	< 0.2	31	
ARS 090 209.25m	57.13	16.80	4.12	0.074	2.45	3.90	8.05	0.46	0.553	0.34	4.34	98.22	7	< 0.5	< 1	938	10	< 2	< 0.5	< 0.5	15.1	93.2	1.9	111	
ARS 043 154.0m	56.70	15.70	4.32	0.079	1.84	4.50	8.49	0.30	0.480	0.35	5.66	98.43	< 1	0.7	< 1	929	3	< 2	< 0.5	< 0.5	14.2	118	2.3	96	
ACCOR1 NORTHCO11 123.0m	54.28	17.97	3.48	0.095	2.29	6.16	7.89	1.07	0.570	0.21	5.01	99.02	12	0.6	< 1	1343	12	< 2	< 0.5	< 0.5	17.5	113	3.5	77	
ARW008 106.8m	58.99	16.53	3.89	0.050	2.75	3.17	8.30	0.14	0.631	1.14	2.71	98.32	< 1	< 0.5	< 1	169	5	< 2	< 0.5	< 0.5	14.6	89.3	2.3	34	
C2	56.71	16.52	4.53	0.057	2.79	4.34	8.18	0.55	0.537	0.37	5.86	100.5	< 1	0.6	< 1	777	3	< 2	< 0.5	< 0.5	15.1	116	2.5	50	
C5	48.94	12.06	5.51	0.148	1.56	4.69	6.07	0.07	0.526	0.38	6.68	86.64	27	7.8	21	120	38	< 2	< 0.5	< 0.5	10.0	123	< 0.2	19	
ARN053 89.3m	47.88	12.00	7.73	0.094	12.45	4.20	1.96	2.87	2.019	2.08	5.20	98.28	< 1	1.0	2	589	7	< 2	< 0.5	< 0.5	59.0	341	34.9	104	

Analyte Symbol	Unit Symbol	Detection Limit	Analysis Method	Hf	Hg	Ir	Mo	Ni	Pb	Rb	Sb	S	Sc	Se	Sr	Ta	Th	U	V	W	Y	Zn	Zr	La	Ce	Nd	Sm
				ppm	ppm	ppb	ppm	ppm	ppm	ppm	ppm	%	ppm	ppm	ppm	ppm	ppm	ppm	ppm	ppm	ppm	ppm	ppm	ppm	ppm	ppm	ppm
PERE 12				6.0	< 1	< 1	< 2	113	10	90	0.7	0.005	12.3	< 0.5	734	1.9	12.6	3.9	122	< 1	22	61	242	77.7	145	92	11.1
ARN 019 40.55-40.78m				6.7	< 1	< 1	< 2	74	14	110	0.8	0.007	11.2	< 0.5	1131	< 0.3	20.7	4.8	109	< 1	23	64	280	100	182	99	14.7
ARN021 117.70-117.90m				6.8	< 1	< 1	3	68	12	150	0.6	0.008	10.2	< 0.5	1158	1.8	20.1	7.1	101	2	23	59	287	88.2	172	89	13.9
ARN022 141.90-142.0m				6.2	< 1	< 1	< 2	75	16	110	0.6	0.006	11.5	< 0.5	1282	1.3	18.8	6.2	115	< 1	24	62	295	98.0	189	102	14.6
ARN 053 108.5m				5.9	< 1	< 1	< 2	60	20	110	0.8	0.009	7.70	< 0.5	916	1.6	22.0	11.5	78	< 1	17	56	228	98.6	172	98	11.5
ARN 100 164.5m				6.1	< 1	< 1	< 2	75	14	110	0.6	0.009	12.4	< 0.5	1122	2.3	19.8	5.2	121	< 1	27	70	251	98.4	193	106	15.1
ARN 085 96.5m				7.9	< 1	< 1	2	79	15	80	0.8	0.017	10.5	< 0.5	1088	< 0.3	20.9	5.4	106	< 1	24	72	316	98.0	188	98	13.8
ARN 063 128.8m				7.1	< 1	< 1	2	66	17	140	1.3	0.009	9.17	< 0.5	1196	1.3	21.5	9.1	96	4	22	63	284	90.3	172	113	12.9
ARN 094 102.3m				5.6	< 1	< 1	< 2	47	19	140	1.0	0.003	6.25	< 0.5	1032	1.4	22.0	5.6	66	< 1	17	47	209	79.8	143	80	9.80
ARW 030 208.8m				5.7	< 1	< 1	< 2	52	18	110	0.6	0.006	7.21	< 0.5	1069	< 0.3	17.4	5.7	72	< 1	17	52	193	98.6	168	76	10.5
ARN 048 85.5m				5.7	< 1	< 1	< 2	61	17	130	1.1	0.006	7.63	< 0.5	1019	1.5	23.8	6.8	83	< 1	19	55	262	122	205	99	13.1
ARS 029 83.5m				7.2	< 1	< 1	< 2	54	15	100	0.7	0.067	8.40	< 0.5	2820	2.0	16.3	5.4	80	< 1	18	54	222	72.6	132	83	10.7
ARS 094 151.80m				6.1	< 1	< 1	< 2	46	13	110	0.4	0.005	7.12	< 0.5	745	< 0.3	10.6	5.2	73	< 1	17	48	220	62.9	114	66	9.10
ARS 090 230.5m				0.4	< 1	< 1	< 2	2	22	< 10	< 0.1	0.003	2.04	< 0.5	2206	1.1	0.6	7.3	< 5	< 1	9	2	40	22.4	36	20	2.39
ARS 090 209.25m				8.0	< 1	< 1	< 2	52	140	< 10	0.8	0.027	8.40	< 0.5	701	2.4	18.9	375	69	< 1	12	52	275	103	167	129	16.8
ARS 043 154.0m				9.8	< 1	< 1	< 2	50	263	< 10	1.5	0.032	10.5	< 0.5	979	2.4	16.3	588	84	< 1	22	53	375	98.0	151	113	18.5
ACCOR1 NORTHCO11 123.0m				12.5	< 1	< 1	3	58	281	60	1.1	0.021	9.52	< 0.5	1053	2.8	21.1	606	55	< 1	28	47	619	106	179	136	22.2
ARW008 106.8m				12.3	< 1	< 1	< 2	50	173	30	0.8	0.003	8.09	< 0.5	558	1.8	13.3	229	96	< 1	30	61	422	65.4	111	82	14.0
C2				11.0	< 1	< 1	< 2	53	321	< 10	0.8	0.035	9.00	< 0.5	1063	3.3	12.9	719	84	< 1	24	60	451	105	169	144	24.0
C5				980	< 1	< 1	< 2	33	1070	< 10	4.2	0.003	19.7	< 0.5	837	2.1	138	2050	85	< 1	52	45	83820	187	270	316	44.5
ARN53 89.3m				31.0	< 1	< 1	< 2	339	54	220	2.0	0.002	25.6	< 0.5	578	3.8	11.6	35.9	300	15	51	117	135	285	212	29.9	

Analyte Symbol	Eu	Tb	Yb	Lu	Mass
Unit Symbol	ppm	ppm	ppm	ppm	g
Detection Limit	0.05	0.1	0.05	0.01	
Analysis Method	INAA	INAA	INAA	INAA	INAA
PERE 12	3.31	0.7	1.75	0.27	1.152
ARN 019 40.55-40.78m	3.86	1.0	1.78	0.26	1.371
ARN021 117.70-117.90m	3.95	0.9	1.82	0.26	1.366
ARN 022 141.90-142.0m	3.91	1.0	1.86	0.29	1.344
ARN 053 108.5m	3.00	0.8	1.20	0.21	1.337
ARN 100 164.5m	4.19	1.0	2.16	0.30	1.274
ARN 085 96.5m	3.86	0.8	1.78	0.26	1.128
ARN 063 128.8m	3.85	0.8	1.64	0.27	1.189
ARN 094 102.3m	2.89	< 0.1	1.37	0.20	1.370
ARW 030 208.8m	2.99	0.6	1.44	0.22	1.319
ARN 048 65.5m	3.05	0.8	1.67	0.20	1.288
ARS 029 83.5m	3.19	< 0.1	1.41	0.13	1.235
ARS 094 151.80m	2.89	0.9	1.26	0.10	1.409
ARS 090 230.5m	0.71	0.3	0.25	< 0.01	1.334
ARS 090 209.25m	3.30	< 0.1	0.81	< 0.01	1.189
ARS 043 154.0m	2.97	< 0.1	1.53	< 0.01	1.183
ACCOR1 NORTHCO11 123.0m	3.74	< 0.1	2.14	< 0.01	1.206
ARW 008 106.8m	3.67	1.1	1.92	< 0.01	1.162
C2	3.54	< 0.1	1.96	< 0.01	1.156
C5	< 0.05	< 0.1	4.54	< 0.01	1.305
ARN053 89.3m	7.94	3.3	3.62	0.31	1.109

Factor Analysis

&

Mass Balance

Methods

Pearson Factor Analysis:

Factor analysis collects experimental variables into "factors", which appear to behave similarly. The method was used here to identify elements with a strong positive correlation with uranium. These factors, although hypothetical, are presumed to exist. During factor analysis, factors are constructed as linear combinations of groups of variables. Although in a geochemical sense, "factors" usually represent the combined or integrated effects of several geochemical factors or processes (e.g. background values, weathering and secondary dispersion, mineralization, adsorption, etc.), it may be possible, under favorable circumstances, to recognize a specific factor as a meaningful geochemical process (or association). Thus factor analysis can expose geochemical associations caused by the above mentioned geochemical processes.

The data was imported into a factor analysis program derived to establish a Pearson correlation coefficient. A correlation coefficient is a numerical index that indicates the strength and direction of a relationship between two variables. There are a number of different correlation coefficients, but the most common and most useful is the Pearson correlation coefficient that assumes a straight line relationship between two variables. A correlation coefficient is a numerical or index of the amount of association between two sets of scores. It ranges in size from +1 through 0 to -1. The positive sign indicates a positive correlation, i.e. the scores on one variable increase as the scores on the other variable increase. The negative sign indicates a negative correlation, i.e. the score of one variable increases, the score on the other variable decreases. A correlation

of 1 indicates a perfect correlation between two variables. In other words, a straight line relationship exists between both variables. A value of 0 indicates that the points are scattered randomly around a straight line drawn through the data. A correlation coefficient of -1 would indicate a strong negative relationship between the two variables.

Mass Balance:

Simple comparison of the bulk chemical analysis of granitic rocks and alteration products is not sufficiently satisfactory for deducing chemical changes resulting from hydrothermal alteration. During the alteration of rocks, the abundance of a chemical component may change by real gain or loss, dilution with addition of other components, concentration with leaching of soluble components or, change in rock volume. The mass balance equation of Gresens (1967) calculates real gains and losses, taking into account possible changes in rock volume and specific gravity during metasomatic processes. The main premise behind Gresens' equation is that some components of the host rock were potentially immobile during metasomatism, and that if these can be identified, they can be utilized to determine volume change which has occurred. Gains and losses of elements can then be established assuming the volume change is a factor common to the behaviour of all components (i.e. that the alteration is pervasive and not site specific or localized).

The first thing is to establish net gains and losses of elements relative to an unaltered host. This was accomplished using a Microsoft Excel spreadsheet program called EASYGRESGRANT. The spreadsheet is used to quantify volume changes and to perform mass balance modelling in metasomatic systems. The program has a data-entry

section consisting of two sheets allowing you to input geochemical data of unaltered and altered samples. The user can then choose the sample numbers to be modelled and select reference frames for mass balance calculations (i.e constant mass, constant volume, or immobile elements). The immobile element selection was used for dealing with the Kurupung database. This method involves first selecting “clusters of slopes” method which consists of estimating the slopes for all elements considered. Clusters of elements with close slope values are selected as immobile elements. As a check, an isocon diagram can be generated. On this diagram, the concentrations of the selected altered and unaltered samples are plotted such that elements defining straight lines through the origin will have a similar geochemical behaviour (i.e. the immobile elements). This line connecting immobile elements is called an *isocon* line. The slope of the isocon line defines the mass change in the alteration whereas a deviation of a data point from this line represents the concentration change for that component. From here, the mass-balance numerical results are generated. The program can compile results from either the “clusters of slopes” method or the isocon method. The output is an Excel table which displays a column with the elements/oxides modelled; two columns with the composition of the unaltered and altered samples; and two columns with the mass-balance results in relation to the original element mass and to the original rock mass. Additionally, the sheet displays the volume and mass changes, and the value of the slope of the isocon line used in the calculations.

Drill Logs
&
Photographed Drill Core for Sample ARN-031

HOLE#		ARN-031		1		CORE DIAMETER		NQ (Ø = 8.76 m) NQ (8.76 - 134.20 mts)							
AREA:		Arroyo Verde				DATE STARTED:		08/05/2008							
COORDINATES:		204230 E / 692252 N				COMPLETED:		08/05/2008							
AZIMUTH:		140				LOGGED BY:		F. Solano							
DEPTH:		134.20 mts													
Box #	From	To	% Rcv	LITHOLOGY	STRUCT	OTHERS	ALTERATION	MINERALIZATION	CPS	Sample	Standard	Blank	AMS	Duplicate	
0	0	1	45	Grd. Phanicritic Medium Orange					160						
1	1	2	55	Grd. Phanicritic Medium Light Green					160	50048					
1	2	3	65	Grd. Phanicritic Medium Light Green					160						
1	3	4	80	Grd. Phanicritic Medium Light Green					160	50050					
1	4	5	85	Grd. Phanicritic Medium Light Green	4	1	2	2	1	160					
2	5	6	90	Grd. Phanicritic Medium Dark Green	3	2	2	2	1	160					
2	6	7	98	Grd. Phanicritic Medium Dark Green	3	2	2	2	1	160	50051				
2	7	8	80	Grd. Phanicritic Medium Dark Green	5	2	2	2	1	160	50052				
2	8	9	95	Grd. Phanicritic Medium Dark Green	6	1	2	2	1	160					
3	9	10	95	Grd. Phanicritic Medium Dark Green	5	1	2	2	1	160	50053				
3	10	11	88	Grd. Phanicritic Medium Dark Green	4	2	2	2	1	160					
3	11	12	98	Grd. Phanicritic Medium Dark Green	3	1	2	2	1	160					
3	12	13	98	Grd. Phanicritic Medium Dark Green	5	1	2	2	1	160	50054				
3	13	14	88	Grd. Phanicritic Medium Dark Green	4	2	2	2	1	160	50055				
4	14	15	98	Grd. Phanicritic Medium Dark Green	6	1	2	2	1	160					
4	15	16	98	Grd. Phanicritic Medium Dark Green	5	1	2	2	2	160	50056				
4	16	17	88	Grd. Phanicritic Medium Dark Green	5	1	2	2	1	160					
4	17	18	98	Grd. Phanicritic Medium Dark Green	3	1	2	2	1	160					
4	18	19	98	Grd. Phanicritic Medium Dark Green	2	2	2	2	1	160	50057				
5	19	20	88	Grd. Phanicritic Medium Dark Green	3	1	2	2	1	160	50058				
5	20	21	88	Grd. Phanicritic Medium Dark Green	3	1	2	2	1	160					
5	21	22	98	Grd. Phanicritic Medium Dark Green	1	2	2	2	1	160	50059	5000			
5	22	23	88	Grd. Phanicritic Medium Dark Green	5	1	2	2	2	160					
6	23	24	88	Grd. Phanicritic Medium Dark Green	3	2	2	2	2	160					
6	24	25	98	Grd. Phanicritic Medium Dark Green	8	1	2	2	2	160	50061				
6	25	26	88	Grd. Phanicritic Medium Dark Green	5	1	2	2	2	160	50062				
6	26	27	88	Grd. Phanicritic Medium Dark Green	9	1	2	2	2	160					
6	27	28	98	Grd. Phanicritic Medium Dark Green	4	1	2	2	1	160	50063				
7	28	29	88	Grd. Phanicritic Medium Dark Green	4	1	2	2	1	160					
7	29	30	88	Grd. Phanicritic Medium Dark Green	5	1	2	2	1	160	50064				
7	30	31	98	Grd. Phanicritic Medium Dark Green	3	1	2	2	1	160					
7	31	32	88	Grd. Phanicritic Medium Dark Green	2	1	2	2	1	160	50065				
7	32	33	88	Grd. Phanicritic Medium Dark Green	3	1	2	2	1	160					
8	33	34	98	Grd. Phanicritic Medium Dark Green	2	2	2	2	1	160	24229	24230			
8	34	35	88	Grd. Phanicritic Medium Dark Green	6	1	2	2	2	200	24231	24232			
8	35	36	88	Grd. Phanicritic Medium Dark Green	9	1	3	2	1	160	24233	24234			
8	36	37	98	Grd. Obiterrate Medium Gray	8	1	1	3	2	1	160	24235	24236		
8	37	38	88	Grd. Obiterrate Medium Gray	7	1	1	3	2	1	160	24237	24238		
9	38	39	88	Grd. Phanicritic Medium Dark Green	4	1	2	2	2	160	24239	24240	24241		
9	39	40	98	Grd. Phanicritic Medium Dark Green	3	1	2	2	1	160					
9	40	41	98	Grd. Phanicritic Medium Gray	2	1	2	2	2	160	50066				
9	41	42	88	Grd. Phanicritic Medium Gray	10	1	2	2	2	160					
10	42	43	98	Grd. Phanicritic Medium Dark Green	6	1	2	2	2	160	50067				
10	43	44	98	Grd. Phanicritic Medium Dark Green	8	2	2	2	2	160					
10	44	45	98	Grd. Phanicritic Medium Dark Green	6	2	2	2	2	160	50068				
10	45	46	98	Grd. Phanicritic Medium Dark Green	6	2	2	2	2	160					
10	46	47	98	Grd. Phanicritic Medium Dark Green	5	2	2	2	2	160	50070				
11	47	48	98	Grd. Phanicritic Medium Dark Green	2	2	2	2	2	160					
11	48	49	98	Grd. Phanicritic Medium Dark Green	4	2	2	2	2	160	50071				
11	49	50	98	Grd. Phanicritic Medium Dark Green	2	2	2	2	2	160	50072				
11	50	51	88	Grd. Phanicritic Medium Dark Green	2	2	2	2	2	160					
11	51	52	88	Grd. Phanicritic Medium Dark Green	4	1	2	2	2	160	50073				
12	52	53	98	Grd. Phanicritic Medium Dark Green	2	2	2	2	1	160					
12	53	54	88	Grd. Phanicritic Medium Dark Green	6	1	2	2	1	160					
12	54	55	98	Grd. Phanicritic Medium Reddish Gray	7	1	1	3	2	2	280	50074			
12	55	56	98	Grd. Phanicritic Medium Dark Green	8	2	2	2	2	160	50075				
12	56	57	88	Grd. Phanicritic Medium Dark Green	6	2	2	2	2	160					
13	57	58	98	Grd. Phanicritic Medium Dark Green	12	2	2	2	2	160					
13	58	59	98	Grd. Phanicritic Medium Dark Green	9	1	2	2	2	160	50076				
13	59	60	88	Grd. Phanicritic Medium Green Gray	11	1	2	2	2	160	24242	24243			
14	60	61	88	Grd. Obiterrate Medium Reddish Gray	14	1	2	2	3	1	150	24244	24245		
14	61	62	98	Mv. Banded Fine Reddish Gray	7	1	3	2	1	350	24246	24247			
14	62	63	98	Grd. Phanicritic Medium Reddish Gray	3	2	2	2	3	4	350	24248	24249		
14	63	64	98	Grd. Phanicritic Medium Dark Green	2	2	2	2	2	160	24250	24251			
14	64	65	98	Grd. Phanicritic Medium Reddish Gray	4	2	2	2	3	2	410	24252	24253		
14	65	66	98	Grd. Phanicritic Medium Reddish Gray	2	1	2	2	3	2	410	24254	24255	24255	
14	66	67	98	Grd. Phanicritic Medium Reddish Gray	2	1	2	2	3	2	410	24256	24257		
15	67	68	98	Grd. Phanicritic Medium Reddish Gray	2	1	2	2	2	2	410	24258	24259		
15	68	69	88	Grd. Phanicritic Medium Reddish Gray	3	2	2	2	2	2	410	24260	24261		
15	69	70	98	Grd. Phanicritic Medium Dark Green	4	2	2	2	1	160	24262	24263			
15	70	71	98	Grd. Phanicritic Medium Dark Green	3	2	2	2	2	160	24264	24265			
15	71	72	88	Grd. Phanicritic Medium Dark Green	4	2	2	2	1	160	50078				
16	72	73	88	Grd. Phanicritic Medium Dark Green	3	1	2	2	2	160					
16	73	74	98	Grd. Phanicritic Medium Dark Green	3	1	2	2	2	200	50079				
16	74	75	88	Grd. Phanicritic Medium Dark Green	2	2	2	2	2	160	50080				
16	75	76	98	Grd. Phanicritic Medium Dark Green	3	2	2	2	2	160					
16	76	77	98	Grd. Phanicritic Medium Dark Green	4	1	2	2	1	160	50081				
17	77	78	88	Grd. Phanicritic Medium Dark Green	5	1	2	2	2	160					
17	78	79	98	Grd. Phanicritic Medium Dark Green	2	2	2	2	1	150					
17	79	80	98	Grd. Phanicritic Medium Dark Green	4	2	2	2	1	150	50083				
18	80	81	85	Grd. Phanicritic Medium Dark Green	3	2	2	2	2	160	50085				
18	81	82	98	Grd. Phanicritic Medium Dark Green	2	2	2	2	2	160					
18	82	83	98	Grd. Phanicritic Medium Dark Green	4	1	2	2	2	160	50086				
18	83	84	88	Grd. Phanicritic Medium Reddish Gray	6	1	1	2	2	170					
19	84	85	98	Grd. Phanicritic Medium Dark Green	7	1	2	2	2	160	50087				
19	85	86	98	Grd. Phanicritic Medium Dark Green	4	1	2	2	2	160	24267	24268	24268		
19	87	88	98	Grd. Obiterrate Medium Reddish Gray	3	1	2	2	2	270	24270	24271			
19	88	89	98	Grd. Obiterrate Medium Reddish Gray	5	1	2	2	3	3	400	24272	24273		
19	89	90	98	Grd. Obiterrate Medium Reddish Gray	4	2	1	3	3	2	420	24274	24275		
20	90	91	98	Grd. Obiterrate Medium Reddish Gray	5	2	2	2	3	2	420	24276	24277		
20	91	92	98	Grd. Obiterrate Medium Reddish Gray	3	1	2	1	3	2	420	24278	24279		
20	92	93	98	Grd. Obiterrate Medium Reddish Gray	8	1	2	1	3	2	420	24280	24281		
20	93	94	98	Grd. Obiterrate Medium Reddish Gray	3	1	2	2	3	2	420	24282	24283	24282	
21	94	95	98	Grd. Obiterrate Medium Reddish Gray	8	2	1	3	3	3	420	24284	24285		
21	95	96	98	Mv. Banded Fine Reddish	5	3	2	1	3	3	420	24286	24287		



Sample ARN-031 Boxes 1,2,3



Sample ARN-031 Boxes 4,5,6



Sample ARN-031 Boxes 7,8,9



Sample ARN-031 Boxes 10,11,12



Sample ARN-031 Boxes 13,14,15



Sample ARN-031 Boxes 16,17,18



Sample ARN-031 Boxes 19,20,21



Sample ARN-031 Boxes 22,23,24



Sample ARN-031 Boxes 25,26,27



Sample ARN-031 Boxes 28,29

**Table 2: Rock Density Calculations and
Trace element Analysis of Drill Hole ARN-031
(for mass balance calculations)**

DEPTH (m)	LENTGH (cm)	DIAMETER (cm)	RADIO (cm)	DRY WEITGH (gr)	DRY WEITGH (kg)	VOLUME DISPLACED (ml)	DENSITY BY VOLUME
4.71	7.103		0	225	0.225	80	2.8125
10.1	6.416		0	133	0.133	40	3.325
27.3	6.849		0	146	0.146	50	2.92
36.81	6.731		0	145	0.145	40	3.625
49.4	6.862		0	163	0.163	50	3.26
60.8	6.969		0	145	0.145	50	2.9
67.15	7.084		0	138	0.138	40	3.45
83.3	6.156		0	143	0.143	50	2.86
92.6	6.78		0	151	0.151	50	3.02
95.5	6.683		0	158	0.158	50	3.16
109.6	6.804		0	155	0.155	50	3.1
123.6	6.704		0	123	0.123	40	3.075
131.46	6.951		0	161	0.161	50	3.22
25.06	7.462	6.203	3.1015	587	0.587	210	2.7952381
34.76	6.924		0	129	0.129	50	2.58
59.6	6.865		0	163	0.163	60	2.71666667
73.93	7.194		0	148	0.148	60	2.46666667
86.7	7.07		0	157	0.157	60	2.61666667
95.3	7.098		0	164	0.164	60	2.733333333
105.6	6.896		0	154	0.154	60	2.56666667
120.3	6.805		0	137	0.137	50	2.74
135.8	7.253		0	158	0.158	60	2.633333333
149.85	7.141		0	148	0.148	50	2.96
159.24	7.004		0	154	0.154	50	3.08
170.08	7.138	4.755	2.3775	340	0.34	130	2.61538462

Drill core density measurements completed by U3O8 Corp. The “Density by Volume” values were utilized in the mass balance calculations.

Geochemical Analyses for Mass Balance Calculations

Received: April 20, 2012
 Report Date: May 03, 2012
 Page: 1 of 3

CERTIFICATE OF ANALYSIS

GTG12000214.1

CLIENT JOB INFORMATION

Project: ARN-031
 Shipment ID: NONE GIVEN
 P. O. Number: 48
 Number of Samples: 48

SAMPLE DISPOSAL

STOR-PLP Store After 90 days Invoice for Storage
 STOR-RJT Store After 90 days Invoice for Storage

Acme does not accept responsibility for samples left at the laboratory after 90 days without prior written instructions for sample storage or return.

SAMPLE PREPARATION AND ANALYTICAL PROCEDURES

Method Code	Number of Samples	Code Description	Test Wgt (g)	Report Status	Lab
R200-250	44	Crush, split and pulverize 250 g rock to 200 mesh			GTG
VAN Split Pulp	48	Analysis sample split/package			VAN
1EX	48	4 acid digestion - ICP-MS analysis - U package	0.25	Completed	VAN
MIXP	48	Mix pulps on arrival			VAN
STD	48	Insertion of a Acme Supplied CRM			VAN

ADDITIONAL COMMENTS

Blank material consists of locally sourced granite. Slightly elevated levels of Mn and Cu should be expected.

Invoice To:

CC: Mariano Castro
 Gabriel Bastias

This report supersedes all previous preliminary and final reports with this file number dated prior to the date on this certificate. Signature indicates final approval; preliminary reports are unsigned and should be used for reference only. All results are considered the confidential property of the client. Acme assumes the liabilities for actual cost of analysis only. Results apply to samples as submitted. * asterisk indicates that an analytical result could not be provided due to unusually high levels of interference from other elements.



Acme Labs

Acme Analytical Laboratories (Vancouver) Ltd.

Project: ARN-031
Report Date: May 03, 2012

Page: 2 of 3

Part: 2 of 3

CERTIFICATE OF ANALYSIS

GTG12000214.1

Method Analyte Unit MDL	P		La		Cr		Mg		Ba		Ti		Al		Na		K		W		Zr		Ce		Sn		Y		Nb		Ta		Be		Sc		Li		S	
	1EX %	1EX ppm	1EX %	1EX ppm	1EX %	1EX ppm	1EX %	1EX ppm	1EX %	1EX ppm	1EX %	1EX ppm	1EX %	1EX ppm	1EX %	1EX ppm	1EX %	1EX ppm	1EX %	1EX ppm	1EX %	1EX ppm	1EX %	1EX ppm	1EX %	1EX ppm	1EX %	1EX ppm	1EX %	1EX ppm	1EX %	1EX ppm	1EX %	1EX ppm	1EX %	1EX ppm	1EX %	1EX ppm	1EX %	1EX ppm
50049	Drill Core	0.225	64.0	109	2.16	1239	0.457	7.58	1.698	3.93	1.4	94.3	154	1.2	23.2	17.7	0.9	3	10	29.6	<0.1																			
50050	Drill Core	0.220	64.9	101	2.09	1286	0.428	7.50	2.097	4.04	1.1	91.6	154	0.9	20.9	16.9	0.9	3	9	26.8	<0.1																			
50051	Drill Core	0.229	66.8	90	1.98	1175	0.421	7.39	3.048	3.69	1.1	92.1	156	0.9	22.8	17.1	0.9	4	8	23.9	<0.1																			
50052	Drill Core	0.232	66.2	85	1.90	947	0.383	7.21	3.593	2.89	1.3	122.0	155	0.9	20.7	16.3	1.0	4	8	41.6	<0.1																			
50053	Drill Core	0.209	69.5	81	1.88	1133	0.398	7.25	3.119	3.59	1.5	84.6	164	0.9	21.8	16.7	1.0	3	8	26.2	<0.1																			
50054	Drill Core	0.221	60.7	95	1.92	1141	0.412	7.07	3.113	3.58	1.5	91.1	145	0.7	20.8	15.9	0.9	4	8	23.0	<0.1																			
50055	Drill Core	0.237	68.8	99	2.08	1115	0.413	7.08	3.100	3.49	1.4	91.3	162	0.8	22.9	16.2	0.9	3	8	22.2	<0.1																			
50056	Drill Core	0.225	70.1	98	2.00	1126	0.405	7.40	3.173	3.66	1.0	77.4	162	1.0	22.7	16.2	1.0	3	8	20.9	<0.1																			
50057	Drill Core	0.227	68.8	93	2.00	1163	0.420	7.38	3.111	3.67	1.0	84.1	166	0.9	23.2	17.0	1.0	4	8	22.3	<0.1																			
50058	Drill Core	0.229	74.8	96	2.02	1149	0.419	7.38	3.132	3.47	1.3	79.3	177	0.9	24.2	17.4	1.0	3	9	22.4	<0.1																			
50059	Drill Core	0.206	71.7	88	1.91	1139	0.403	7.39	3.161	3.77	1.6	82.6	166	0.9	22.1	17.0	1.0	3	8	21.2	<0.1																			
50060	Drill Core	0.001	0.7	6	0.02	12	0.005	0.15	0.045	0.04	<0.1	1.5	2	<0.1	0.2	0.1	<0.1	<1	<1	0.7	<0.1																			
50061	Drill Core	0.211	64.1	92	1.88	1056	0.388	7.16	3.469	3.13	1.4	85.7	154	0.9	21.2	15.1	1.0	4	8	23.5	<0.1																			
50062	Drill Core	0.227	74.1	94	1.97	1207	0.417	7.39	3.224	3.53	1.5	84.7	169	0.9	22.7	17.1	1.0	4	8	22.3	<0.1																			
50063	Drill Core	0.179	62.6	74	1.64	967	0.350	6.14	2.628	3.17	1.5	76.2	144	0.8	19.7	15.2	0.9	2	7	18.2	<0.1																			
50064	Drill Core	0.214	65.5	93	1.89	1115	0.410	7.21	3.122	3.45	2.0	96.2	151	0.9	22.4	17.8	1.1	4	8	20.7	<0.1																			
50065	Drill Core	0.204	70.8	87	1.89	1099	0.377	7.27	3.400	3.53	1.8	95.2	163	0.9	22.2	15.3	0.9	4	8	26.0	<0.1																			
50066	Drill Core	0.225	67.0	98	1.96	938	0.339	7.09	4.808	1.66	1.2	94.4	159	0.8	18.2	13.5	0.7	4	8	58.7	<0.1																			
50067	Drill Core	0.190	62.7	76	1.70	1116	0.340	6.88	3.159	3.55	5.5	86.1	150	0.8	20.5	15.6	1.1	4	7	35.7	<0.1																			
50068	Drill Core	0.198	62.9	82	1.78	1045	0.354	6.81	3.046	3.59	1.8	86.7	151	0.8	20.6	15.9	1.1	3	8	32.9	<0.1																			
50069	Core Pulp	0.114	27.2	73	1.28	243	0.303	5.84	3.543	0.38	1.6	186.4	62	3.4	24.2	7.7	0.8	55	11	16.5	0.2																			
50070	Drill Core	0.209	67.5	89	1.86	1096	0.396	6.94	3.070	3.70	1.6	75.2	159	0.9	21.3	16.8	1.0	3	8	15.8	<0.1																			
50071	Drill Core	0.203	63.8	85	1.81	1060	0.396	6.88	2.980	3.37	1.9	86.7	152	0.9	21.0	17.0	1.0	4	8	15.2	<0.1																			
50072	Drill Core	0.200	69.0	84	1.79	1051	0.387	7.02	3.043	3.59	1.5	79.5	157	1.0	20.5	16.2	0.9	3	8	12.3	<0.1																			
50073	Drill Core	0.192	62.3	83	1.77	1059	0.394	6.90	3.033	3.86	1.7	85.3	146	0.7	19.5	15.4	0.9	3	8	13.6	<0.1																			
50074	Drill Core	0.264	54.4	89	1.83	875	0.356	6.88	4.116	2.47	2.3	272.6	135	0.8	21.1	14.6	0.9	5	7	28.9	<0.1																			
50075	Drill Core	0.209	67.8	88	1.87	1283	0.400	6.94	3.008	3.91	2.0	81.6	155	0.9	20.6	15.8	1.0	4	8	17.7	<0.1																			
50076	Drill Core	0.256	65.1	94	1.91	727	0.315	6.66	4.764	0.94	1.3	148.4	156	0.8	20.0	11.5	0.7	7	8	52.4	<0.1																			
50077	Core Pulp	0.038	14.7	92	0.64	291	0.162	4.37	1.189	1.95	3.0	61.8	30	2.1	9.9	5.6	0.6	2	4	39.8	<0.1																			
50078	Drill Core	0.188	63.5	82	1.78	1194	0.401	6.82	3.035	3.86	1.5	78.0	150	0.9	19.0	16.4	1.0	3	8	18.8	<0.1																			

This report supersedes all previous preliminary and final reports with this file number dated prior to the date on this certificate. Signature indicates final approval; preliminary reports are unsigned and should be used for reference only.



Acme Labs

Acme Analytical Laboratories (Vancouver) Ltd.

Project: ARN-031

Report Date: May 03, 2012

Page: 2 of 3

Part: 3 of 3

CERTIFICATE OF ANALYSIS

GTG12000214.1

Method	Analyte	1EX	1EX
		Rb	Hf
Unit		ppm	ppm
MDL		0.1	0.1
50049	Drill Core	97.5	3.0
50050	Drill Core	109.6	3.0
50051	Drill Core	102.1	3.0
50052	Drill Core	107.1	2.9
50053	Drill Core	121.7	2.8
50054	Drill Core	104.6	2.8
50055	Drill Core	107.5	2.8
50056	Drill Core	122.9	2.6
50057	Drill Core	121.2	2.4
50058	Drill Core	123.0	2.5
50059	Drill Core	122.4	2.5
50060	Drill Core	2.3	<0.1
50061	Drill Core	106.3	2.7
50062	Drill Core	123.1	2.6
50063	Drill Core	116.5	2.3
50064	Drill Core	111.0	2.9
50065	Drill Core	123.2	3.0
50066	Drill Core	85.1	2.8
50067	Drill Core	124.7	2.8
50068	Drill Core	125.0	2.9
50069	Core Pulp	17.0	4.0
50070	Drill Core	132.4	2.4
50071	Drill Core	108.2	2.5
50072	Drill Core	124.1	2.5
50073	Drill Core	127.0	2.6
50074	Drill Core	79.0	3.3
50075	Drill Core	134.0	2.6
50076	Drill Core	46.8	2.8
50077	Core Pulp	91.8	1.4
50078	Drill Core	113.2	2.5

This report supersedes all previous preliminary and final reports with this file number dated prior to the date on this certificate. Signature indicates final approval; preliminary reports are unsigned and should be used for reference only.



Acme Labs

Acme Analytical Laboratories (Vancouver) Ltd.

Project: ARN-031
Report Date: May 03, 2012

Page: 3 of 3

Part: 3 of 3

CERTIFICATE OF ANALYSIS

GTG12000214.1

Method	Analyte	Unit	1EX	1EX
			Rb	Hf
MDL			ppm	ppm
STD BL-4A	Core Pulp		16.9	3.8
50079	Drill Core		93.8	2.9
50080	Drill Core		93.7	2.4
50081	Drill Core		76.3	2.7
50082	Drill Core		102.6	2.8
50083	Drill Core		100.6	2.7
50084	Drill Core		2.6	<0.1
50085	Drill Core		109.6	2.9
50086	Drill Core		109.7	2.7
50087	Drill Core		125.3	2.9
50088	Drill Core		85.7	2.5
50089	Drill Core		129.9	2.9
50090	Drill Core		119.0	3.0
50091	Drill Core		106.1	2.5
50092	Drill Core		118.6	2.9
50093	Drill Core		118.7	2.6
50094	Drill Core		108.9	2.6
50095	Drill Core		103.3	2.9

QUALITY CONTROL REPORT

GTG12000214.1

Method Analyte Unit MDL	WGHT Wgt kg	1EX	1EX	1EX	1EX	1EX	1EX	1EX	1EX	1EX	1EX	1EX	1EX	1EX	1EX	1EX	1EX	1EX	1EX	1EX	1EX	1EX	1EX
		Mo ppm	Cu ppm	Pb ppm	Zn ppm	Ag ppm	Ni ppm	Co ppm	Mn ppm	Fe %	As ppm	U ppm	Au ppm	Tl ppm	Sr ppm	Cd ppm	Sb ppm	Bi ppm	V ppm	Ca ppm			
Pulp Duplicates																							
50050	Drill Core	2.98	1.7	86.8	23.4	71	<0.1	76.4	20.0	684	3.69	6	4.9	<0.1	19.2	969	0.2	1.0	0.5	97	2.28		
REP 50050	QC		1.7	88.1	24.7	72	<0.1	76.5	20.7	675	3.73	6	4.9	<0.1	19.1	1001	<0.1	1.1	0.4	98	2.26		
50086	Drill Core	1.74	1.4	81.3	20.4	61	0.2	58.2	16.1	608	3.03	3	4.9	<0.1	19.2	1860	0.2	0.6	0.4	81	2.80		
REP 50086	QC		1.3	86.5	19.5	63	<0.1	61.2	16.1	609	3.01	3	4.3	<0.1	17.9	1770	<0.1	0.6	0.4	80	2.78		
Core Reject Duplicates																							
50057	Drill Core	2.08	2.3	103.3	23.1	63	<0.1	67.4	18.3	642	3.31	6	5.7	<0.1	20.6	1155	0.1	0.9	0.4	93	3.08		
DUP 50057	QC		2.1	100.1	23.2	64	0.1	63.9	18.3	623	3.31	7	5.6	<0.1	18.7	1151	0.2	0.8	0.3	95	3.08		
50091	Drill Core	1.66	1.6	78.8	20.9	61	0.1	61.7	17.2	566	2.93	7	3.7	<0.1	16.2	1171	<0.1	0.9	0.4	77	2.72		
DUP 50091	QC		1.7	79.5	21.7	63	0.1	63.7	16.9	574	2.98	6	3.7	<0.1	15.6	1131	0.1	0.7	0.4	79	2.74		
Reference Materials																							
STD OREAS124	Standard		6.9	4.1	11.3	13	<0.1	9.2	4.0	649	1.52	4	1817	<0.1	5.5	175	<0.1	0.1	<0.1	25	0.09		
STD OREAS124	Standard		7.9	5.7	18.3	15	<0.1	11.0	4.2	678	1.49	4	1798	<0.1	5.9	198	<0.1	<0.1	<0.1	24	0.11		
STD OREAS45C	Standard		2.2	604.2	24.6	79	0.4	319.8	102.0	1097	18.36	13	2.4	<0.1	11.1	32	0.2	0.9	<0.1	267	0.49		
STD OREAS45C	Standard		2.2	615.6	25.6	82	0.4	327.7	101.0	1100	17.91	12	2.2	<0.1	10.7	38	0.2	0.9	0.2	267	0.49		
STD OREAS45C Expected			2.26	620	24	83	0.28	333	104	1160	18.33	10.1	2.4	0.045	10.2	36.4	0.15	0.79	0.21	270	0.482		
STD OREAS124 Expected			7.2	4.5	17.2	14		9.3	4.2	675	1.5325	3	1779		5.9	180				21	0.089		
BLK	Blank		<0.1	0.3	0.2	<1	<0.1	0.1	<0.2	2	<0.01	2	0.1	<0.1	<0.1	<1	<0.1	<0.1	<0.1	<1	<0.01		
BLK	Blank		<0.1	0.4	0.2	<1	<0.1	0.2	<0.2	<1	<0.01	<1	<0.1	<0.1	<0.1	1	<0.1	<0.1	<0.1	<1	<0.01		
Prep Wash																							
G1-GTG	Prep Blank		0.5	21.7	20.5	51	<0.1	27.1	10.2	433	2.37	1	5.0	<0.1	9.6	280	0.1	<0.1	0.2	59	1.74		
G1-GTG	Prep Blank		0.8	22.8	20.4	50	<0.1	27.1	9.4	431	2.33	<1	6.1	<0.1	10.4	273	0.2	<0.1	0.2	60	1.74		



Acme Labs

Acme Analytical Laboratories (Vancouver) Ltd.

Project: ARN-031

Report Date: May 03, 2012

Page: 1 of 1

Part: 3 of 3

QUALITY CONTROL REPORT

GTG12000214.1

Method	Analyte	Unit	1EX	1EX
			Rb	Hf
			ppm	ppm
		MDL	0.1	0.1
Pulp Duplicates				
50050	Drill Core		109.6	3.0
REP 50050	QC		109.8	2.8
50086	Drill Core		109.7	2.7
REP 50086	QC		103.2	2.5
Core Reject Duplicates				
50057	Drill Core		121.2	2.4
DUP 50057	QC		110.4	2.8
50091	Drill Core		106.1	2.5
DUP 50091	QC		100.7	2.8
Reference Materials				
STD OREAS124	Standard		83.8	1.2
STD OREAS124	Standard		87.3	1.5
STD OREAS45C	Standard		24.7	4.3
STD OREAS45C	Standard		23.3	4.4
STD OREAS45C Expected			24	4.27
STD OREAS124 Expected			87.2	1.3
BLK	Blank		0.4	<0.1
BLK	Blank		0.2	<0.1
Prep Wash				
G1-GTG	Prep Blank		132.2	2.6
G1-GTG	Prep Blank		136.2	2.7

Sample Interval (m)	Density	Sample Number	Ti	Al	Fe	Mn	Mg	Ca	Na	K	P	s	As	Rb	Ba	Sr	Pb	Cr	Ni	V	Sc	Zn
			%	%	%	%	%	%	%	%	%	ppm	PPM	PPM	PPM	PPM	PPM	PPM	PPM	PPM	PPM	PPM
1 to 3	2.8125	50049	0.457	7.58	3.91	0.0698	2.16	2.19	1.698	3.93	0.225	500	5	97.5	1239	944	23.1	109	79.5	102	10	78
3 to 5	2.8125	50050	0.428	7.5	3.69	0.0684	2.09	2.28	2.007	4.04	0.22	500	6	109.6	1286	969	23.4	101	76.4	97	9	71
5 to 7	2.8125	50051	0.421	7.39	3.44	0.0635	1.98	2.9	3.048	3.69	0.229	500	6	102.1	1175	1169	23.2	90	68.8	96	8	68
7 to 9	2.8125	50052	0.383	7.21	3.31	0.0603	1.9	2.18	3.593	2.89	0.232	500	6	107.1	947	868	20.4	85	65.4	91	8	64
9 to 11	3.312	50053	0.398	7.25	3.21	0.0575	1.88	2.76	3.119	3.59	0.209	500	5	121.7	1133	1048	23.1	81	63.1	92	8	63
11 to 13	3.312	50054	0.412	7.07	3.38	0.0633	1.92	2.88	3.113	3.58	0.221	500	7	104.6	1141	1090	21.7	95	66.3	96	8	66
13 to 15	3.312	50055	0.413	7.08	3.43	0.0671	2.08	3.16	3.1	3.49	0.237	500	6	107.5	1115	1064	21.1	99	69.6	96	8	64
15 to 17	3.312	50056	0.405	7.4	3.27	0.065	2	3.11	3.173	3.66	0.225	500	6	122.9	1126	1129	21.8	98	68.9	93	8	65
17 to 19	3.312	50057	0.42	7.38	3.31	0.0642	2	3.08	3.111	3.67	0.227	500	6	121.2	1163	1155	23.1	93	67.4	93	8	63
19 to 21	3.312	50058	0.419	7.38	3.42	0.0659	2.02	3.14	3.132	3.47	0.229	500	6	123	1149	1165	22.8	96	68.6	94	9	65
21 to 23	3.312	50059	0.403	7.39	3.21	0.0628	1.91	2.99	3.161	3.77	0.206	500	6	122.4	1139	1138	23.3	88	62.5	90	8	63
23 to 25	3.312	50061	0.388	7.16	3.21	0.0607	1.88	2.85	3.469	3.13	0.211	500	6	106.3	1056	1052	21	92	64.6	91	8	61
25 to 27	3.312	50062	0.417	7.39	3.33	0.0635	1.97	2.98	3.224	3.53	0.227	500	8	123.1	1207	1110	22.9	94	65.2	94	8	63
27 to 29	2.92	50063	0.35	6.14	2.84	0.0541	1.64	2.57	2.628	3.17	0.179	500	6	116.5	967	939	19.9	74	53.5	80	7	55
29 to 31	2.92	50064	0.41	7.21	3.32	0.0638	1.89	3.04	3.122	3.45	0.214	500	6	111	1115	1104	23.6	93	64.5	92	8	64
31 to 33	2.92	50065	0.377	7.27	3.28	0.0615	1.89	2.91	3.4	3.53	0.204	500	6	123.2	1099	1014	23.2	87	60.2	91	8	62
33 to 35	2.92	24229	0.377	7.67	3.74	0.0684	2.07	3.36	3.457	3.03	0.231	500	6	127.8	1110	1106	25.3	93	69.2	94	9	70
35 to 37	2.92	24230	0.384	7.93	3.93	0.0697	2.17	3.3	3.906	2.79	0.257	500	4	113.1	1280	1077	24.7	96	71.9	96	8	73
37 to 39	2.92	24231	0.388	7.73	3.75	0.0662	2.1	3.15	3.51	3	0.228	500	5	125.5	1048	1130	23.9	90	67.2	92	8	72
39 to 41	2.92	24232	0.341	7.23	3.29	0.0591	1.53	3.56	4.414	0.46	0.329	500	6	25.7	1496	768	84.4	75	54.1	94	6	53
41 to 43	2.92	24233	0.348	7.64	2.87	0.0458	1.62	2.7	4.679	0.22	0.353	500	5	14.5	1668	743	131.1	71	54	90	6	53
43 to 45	2.92	24234	0.39	7.8	3.54	0.0603	1.68	3.42	5.618	0.23	0.279	500	5	15.2	1730	802	264.8	83	58.4	110	8	57
45 to 47	2.92	24235	0.401	8.22	3.63	0.0791	1.67	4.71	5.669	0.32	0.26	500	4	30.6	1241	1069	365.2	89	64.2	112	8	55
47 to 49	3.625	24236	0.437	7.39	3.61	0.0663	1.9	3.41	5.029	0.3	0.252	500	5	24.4	2483	879	737.6	87	63.9	105	9	62
49 to 51	3.625	24237	0.423	7.76	3.86	0.0681	2.23	3.69	5.623	0.78	0.275	500	4	52.4	1654	855	129.1	96	71	107	9	72
51 to 53	3.625	24238	0.376	7.44	3.53	0.0562	2.08	2.81	4.907	1	0.237	500	3	56.6	866	809	14.5	83	63.2	91	7	70
53 to 55	3.625	24239	0.37	7.87	3.78	0.0676	2.09	3.56	4.947	1.07	0.244	500	3	63.8	896	864	60.2	99	67.7	96	8	68
55 to 57	3.625	24240	0.411	8.05	3.96	0.0699	2.09	3.34	3.361	3.38	0.269	500	5	141.8	1123	1095	71.9	91	67.2	99	9	70
57 to 59	3.625	50066	0.339	7.09	3.29	0.0639	1.95	3.14	4.808	1.66	0.225	500	5	95.1	938	861	14.5	98	64.8	85	8	64
59 to 61	3.625	50067	0.34	6.88	2.94	0.057	1.7	2.9	3.159	3.55	0.19	500	5	124.7	1116	916	23.1	76	55.3	82	7	56
61 to 63	3.625	50068	0.354	6.81	2.96	0.0573	1.78	2.77	3.046	3.59	0.198	500	6	125	1045	904	22	82	56.5	84	8	57
63 to 65	3.625	50070	0.396	6.94	3.25	0.0614	1.86	2.8	3.07	3.7	0.209	500	6	132.4	1096	1092	22.4	89	62.7	90	8	61
65 to 67	3.625	50071	0.396	6.88	3.17	0.0612	1.81	2.86	2.98	3.37	0.203	500	8	108.2	1060	1059	22	85	60.5	91	8	61
67 to 69	3.26	50072	0.387	7.02	3.04	0.0589	1.79	2.75	3.043	3.59	0.2	500	6	124.1	1051	1072	23	84	57.5	85	8	57
69 to 71	3.26	50073	0.394	6.9	3.14	0.0594	1.77	2.73	3.033	3.86	0.192	500	7	127	1059	1090	23.2	83	59.4	87	8	59
71 to 73	3.26	50074	0.356	6.88	3.23	0.0616	1.83	3.09	4.116	2.47	0.264	500	7	79	875	970	40.5	89	60.1	84	7	60
73 to 75	3.26	50075	0.4	6.94	3.19	0.0608	1.87	2.77	3.008	3.91	0.209	500	7	134	1283	1068	23	88	59.9	90	8	59
75 to 77	3.26	50076	0.315	6.66	3.31	0.0633	1.91	3.01	4.764	0.94	0.256	500	5	46.8	727	894	41.8	94	65.2	86	8	62
77 to 79	3.26	24242	0.374	7.47	3.48	0.0604	1.9	2.9	2.947	3.76	0.212	500	5	147.2	1213	1313	24	87	63.2	84	8	63
79 to 81	3.26	24243	0.349	7.46	3.35	0.0635	1.95	3.01	2.992	3.77	0.226	500	6	139.6	1210	1163	26.8	97	67.2	94	8	67
81 to 83	3.26	24244	0.346	7.41	3.44	0.0657	2.06	3.07	3.194	3.39	0.233	500	5	132.7	1212	1238	22.7	98	67.4	96	9	65
83 to 85	3.26	24245	0.39	7.55	3.8	0.078	2.35	3.66	3.53	2.32	0.261	500	5	124.4	1464	1785	18	101	78.3	101	10	75
85 to 87	3.26	24246	0.28	7.57	3.48	0.0656	2.06	3.57	4.9	1.02	0.291	500	4	65.6	1098	988	94.8	100	65.6	90	9	70
87 to 89	2.9	24247	0.318	8.1	4.26	0.0732	2.49	3.86	5.064	0.35	0.378	500	5	25.4	224	870	258.4	119	80.8	97	10	78
89 to 91	2.9	24248	0.294	7.73	3.48	0.0783	2.21	3.67	5.108	0.32	0.268	500	5	22.5	186	800	151.8	96	70.4	83	9	66
91 to 93	2.9	24249	0.238	7.27	3.19	0.0659	1.99	3.05	5.41	0.58	0.256	500	4	26.9	272	689	108.6	97	66.6	81	8	60
93 to 95	2.9	24250	0.249	7.28	3	0.0331	1.35	6.82	5.155	0.37	0.542	500	4	32	271	2108	252.2	77	50.4	73	8	59
95 to 97	2.9	24251	0.302	6.85	3.32	0.0544	1.87	2.76	4.469	1.39	0.233	500	4	77.4	884	1096	14.7	91	63.9	84	7	63
97 to 99	2.9	24252	0.358	7.42	3.26	0.0616	1.92	2.76	3.455	3.41	0.221	500	5	137.4	1243	1339	22.7	87	63.6	90	8	63
99 to 101	2.9	24253	0.325	7.36	3.25	0.0616	1.92	2.81	3.403	3.2	0.213	500	5	133.7	1123	1544	21.5	87	63.9	86	7	61
101 to 103	2.9	24254	0.257	7.41	3.27	0.0534	1.95	2.8	4.355	1.57	0.222	500	3	73.3	891	989	73.6	91	62.6	87	7	66
103 to 105	2.9	24256	0.233	7.96	3.15	0.078	1.53	4.88	5.88	0.33	0.247	500	3	22	636	1146	201	85	59.2	8		

Sample Interval (m)	Density	Sample Number	Ti	Al	Fe	Mn	Mg	Ca	Na	K	P	s	As	Rb	Ba	Sr	Pb	Cr	Ni	V	Sc	Zn
84 to 86	2.86	50087	0.34	6.55	3.15	0.0573	1.8	2.83	2.915	3.53	0.198	500	4	125.3	1610	1535	22.1	83	61.3	83	7	61
86 to 88.5	2.86	24267	0.28	5.87	2.96	0.0616	1.68	2.82	2.914	2.78	0.175	500	3	99.7	1806	921	22.9	77	56.7	81	6	61
88.5 to 89	2.86	24269	0.256	5.71	2.82	0.0543	1.88	2.33	3.697	1.57	0.175	500	2	46.3	774	631	17	76	57.3	79	5	64
87 to 87.5	2.86	24270	0.284	5.66	2.78	0.0504	1.87	2.15	4.769	0.24	0.187	500	2	8.1	660	598	12.8	78	56.1	81	5	60
87.5 to 88	2.86	24271	0.261	5.81	2.94	0.066	1.71	3.3	4.819	0.2	0.209	500	2	8.2	827	706	71.3	72	54.2	101	5	64
88 to 88.5	2.86	24272	0.234	5.75	2.73	0.0582	1.45	3.5	4.476	0.2	0.273	500	3	10.7	806	858	81.8	71	51.1	94	5	56
88.5 to 89	2.86	24273	0.233	5.75	2.89	0.0567	1.61	3.41	4.643	0.23	0.266	500	4	11.1	725	832	159.6	73	56	107	5	62
89 to 89.5	2.86	24274	0.276	5.58	2.79	0.0542	1.43	3.34	5.148	0.27	0.211	500	4	10.1	776	771	190.9	84	64.1	112	5	67
89.5 to 90	2.86	24275	0.257	6.07	3.2	0.0585	1.84	3.11	5.067	0.27	0.212	500	4	9.9	695	721	184.9	76	60	107	5	67
90 to 90.5	2.86	24276	0.264	6.84	3.74	0.0762	2.54	3.75	4.232	0.2	0.204	500	3	17.1	1773	1006	148.1	65	58.2	104	7	95
90.5 to 91	2.86	24277	0.245	5.83	2.61	0.0562	1.25	4.38	5.537	0.17	0.193	500	2	5.7	1002	921	203	70	50.3	91	4	54
91 to 91.5	2.86	24278	0.258	5.83	3.1	0.0503	1.6	3.21	4.956	0.3	0.197	500	2	9.8	905	849	945.7	81	61.2	98	5	65
91.5 to 92	2.86	24279	0.311	7.76	3.38	0.0665	1.47	4.36	5.171	0.22	0.243	500	3	16.1	1071	899	404.2	83	63.4	88	8	58
92 to 92.5	2.86	24280	0.278	8.01	3.19	0.0742	2.03	4.26	4.726	0.29	0.241	500	3	19.3	1621	862	144	76	61.3	94	9	68
92.5 to 93	3.02	24281	0.33	8.12	3.35	0.0793	1.56	4.86	5.228	0.25	0.24	500	3	21.6	1021	916	540.2	73	60.2	89	8	53
93 to 93.5	3.02	24283	0.348	8.2	3.17	0.0648	2.14	3.82	4.962	0.29	0.241	500	4	24.7	1025	878	409.8	79	66.4	107	9	67
93.5 to 94	3.02	24284	0.362	8.08	3.34	0.0729	2.17	3.99	5.086	0.19	0.22	500	3	19.3	1080	955	1139.3	81	70.8	88	8	54
94 to 94.5	3.02	24285	0.34	8.02	3.44	0.0586	2.32	3.21	5.019	0.22	0.214	500	3	20.4	1309	888	686.6	79	71.2	103	9	68
94.5 to 95	3.02	24286	0.324	8.04	2.57	0.0533	2.56	2.92	5.011	0.24	0.231	500	3	19.4	1863	812	197.5	73	63.1	95	8	64
95 to 95.5	3.16	24287	0.496	6.04	4.31	0.0866	3.42	5.29	6.79	0.34	0.651	500	5	38.8	2589	1221	1313.1	104	123.3	173	12	88
95.5 to 96	3.16	24288	0.758	4.43	6.7	0.087	4.32	7.82	0.988	0.43	1.93	500	9	72.3	1057	1796	1764.2	202	218.7	384	17	163
96 to 96.5	3.16	24289	0.552	6.4	4.21	0.0483	2.38	3.79	3.757	0.21	1	500	5	30	734	1058	2461.9	124	98.5	252	9	92
96.5 to 97	3.16	24290	0.351	6.51	2.83	0.0493	1.53	3.12	4.585	0.17	0.316	500	2	22.8	1542	800	1208.8	79	71.3	172	7	68
97 to 97.5	3.16	24291	0.313	7.2	3.13	0.0483	1.72	2.79	4.913	0.19	0.299	3000	2	24.5	9311	1486	1106.6	95	89.1	206	8	84
97.5 to 98	3.16	24292	0.318	7.25	3.03	0.0491	1.24	3.26	5.052	0.16	0.301	1000	3	19.8	4863	1259	1608.5	86	73.4	225	9	64
98 to 98.5	3.16	24293	0.473	6.84	3.08	0.0809	1.67	5.06	4.437	0.23	0.49	500	5	32.6	2822	1612	2872.6	81	58.9	162	9	52
98.5 to 99	3.16	24294	0.29	7.49	3.29	0.0727	1.52	4.57	5.192	0.21	0.263	500	3	26	1788	1210	630.1	92	55.4	153	8	51
99 to 99.5	3.16	24295	0.433	6.86	3.38	0.0808	1.76	4.79	4.419	0.33	0.242	500	4	43.3	2486	1361	1887.9	97	66.6	154	7	64
99.5 to 100	3.16	24297	0.248	6.81	3.2	0.0613	2.11	3.01	4.04	0.78	0.227	500	2	57.2	897	786	172.7	91	57.2	89	7	60
100 to 100.5	3.16	24298	0.257	6.69	3.31	0.0638	1.96	2.98	3.95	1.06	0.219	500	3	59.2	934	865	69.5	91	59.9	84	7	63
100.5 to 101	3.16	24299	0.281	6.42	3.21	0.0585	1.85	2.7	4.346	0.65	0.204	500	3	29	640	633	13.3	94	60.9	81	7	60
101 to 101.5	3.16	24300	0.359	7.15	3.43	0.0595	1.94	1.93	4.052	1.22	0.207	500	3	53.2	1032	661	13	94	61.6	84	7	65
101.5 to 102	3.16	24301	0.334	6.31	3.09	0.0445	1.82	0.77	3.486	1.81	0.197	500	3	88.4	1234	493	12.7	86	58.3	75	7	59
102 to 102.5	3.16	24302	0.316	6.62	3.19	0.0513	1.91	0.84	3.584	1.66	0.198	500	3	65.3	1091	513	13.6	83	60.2	78	7	63
102.5 to 103	3.16	24303	0.348	6.57	3.26	0.0537	1.94	0.95	3.438	1.77	0.21	500	3	71.9	1057	558	13.7	94	60.2	79	7	61
103 to 103.5	3.16	24304	0.352	6.46	3.44	0.0563	1.97	1.04	2.946	2.35	0.208	500	4	93.5	1364	537	15.3	93	61.5	83	7	67
103.5 to 104	3.16	24305	0.327	6.66	3.15	0.064	1.69	2.09	2.487	2.53	0.189	500	4	105.1	1960	706	18.9	93	57	80	7	59
104 to 104.5	3.16	24306	0.295	6.61	3.24	0.0663	1.72	2.49	3.228	2.44	0.193	500	4	94.6	1258	842	18	91	57.4	80	7	61
104.5 to 105	3.16	24307	0.29	6.42	3.09	0.0618	1.67	2.9	3.611	1.66	0.185	500	4	72.4	897	818	16.9	88	56.9	74	7	56
105 to 105.5	3.16	24308	0.25	6.71	3.15	0.0722	1.66	3.4	4.302	0.68	0.191	500	4	32.4	637	876	13.6	90	57.5	74	7	56
105.5 to 106	3.16	24310	0.3	6.45	3.06	0.0638	1.92	2.87	4.086	0.75	0.207	500	5	31.7	928	728	13.1	95	58.2	76	7	61
106 to 106.5	3.16	24311	0.246	6.12	2.92	0.0709	1.65	3.17	4.359	0.44	0.173	500	3	14.5	489	805	13.4	81	51.6	69	6	55
106.5 to 107	3.16	24312	0.229	6.94	3.35	0.0668	1.76	2.74	4.911	0.33	0.207	500	4	14	361	639	120.1	83	55.7	71	7	58
107 to 107.5	3.16	24313	0.308	6.81	3.09	0.0582	1.89	2.25	3.121	2.48	0.205	500	2	96	1900	762	17.8	91	58	82	7	60
107.5 to 108	3.16	24314	0.329	6.78	3.2	0.0674	1.81	3	3.257	2.13	0.191	500	3	90.1	1746	870	17.2	91	57	81	7	63
108 to 108.5	3.16	24315	0.306	7.65	3.19	0.0486	1.8	2.25	3.506	1.87	0.204	500	3	84.7	1633	935	19.1	85	58	71	8	59
108.5 to 109	3.16	24316	0.348	6.8	3.24	0.0569	1.78	2.52	2.507	2.64	0.195	500	4	105	1715	946	20.3	93	57.6	80	7	59
109 to 109.5	3.16	24317	0.372	6.64	3.29	0.0564	1.72	2.77	2.679	2.9	0.195	500	4	96.4	1608	943	21.2	92	59.8	81	6	63
109.5 to 110	3.1	24318	0.339	6.4	3.25	0.0612	1.68	2.7	2.727	3.08	0.193	500	5	89	1471	1426	22.4	91	58.7	81	6	60
110 to 110.5	3.1	24319	0.357	6.56	3.38	0.0574	1.85	2.49	2.416	2.98	0.205	500	4	111.8	2177	973	22.5	101	63.4	85	7	66
110.5 to 111	3.1	24320	0.354	6.94	3.43	0.0636	2.12	2.62	2.998	2.7	0.22	500	5	94.4	1826	928	21.4	113	65.2	87	7	68
111 to 111.5	3.1	24321	0.301	6.91	3.46	0.066	1.65	3.31	4.84	0.6	0.211	500	4	22.9	558	845	168.7	89	56.5	85	7	59
111.5																						

Sample Interval (m)	Density	Sample Number	Bi		U		Zr		Hf		Y		Nb		Ta		Th		La		Ce		Mo		Cu		Ag		Co		Au		Cd		Sb		W		Sn		Be		Li					
			PPM	PPM	PPM	PPM	PPM	PPM	PPM	PPM	PPM	PPM	PPM	PPM	PPM	PPM	PPM	PPM	PPM	PPM	PPM	PPM	PPM	PPM	PPM	PPM	PPM	PPM	PPM	PPM	PPM	PPM	PPM	PPM	PPM	PPM	PPM	PPM	PPM	PPM	PPM	PPM	PPM	PPM				
1 to 3	2.8125	50089	0.4	3.3	94.3	3	23.2	17.7	0.9	17.1	64	154	1.7	92.5	<0.1	22.5	<0.1	<0.1	0.7	1.4	1.2	3	29.6																									
3 to 5	2.8125	50090	0.5	4.9	91.6	3	20.9	16.9	0.9	19.2	64.9	154	1.7	86.8	<0.1	20	<0.1	0.2	1	1.1	20	3	26.8																									
5 to 7	2.8125	50091	0.3	4.3	92.1	3	22.8	17.1	0.9	18.6	65.8	156	2.2	86.4	0.1	19.3	<0.1	<0.1	0.8	1.1	0.9	4	23.9																									
7 to 9	2.8125	50092	0.4	23.5	122	2.9	20.7	16.3	1	20.8	65.2	155	1.7	102.4	0.1	18.4	<0.1	0.1	0.7	1.3	0.9	4	41.6																									
9 to 11	3.312	50093	0.4	6.8	84.6	2.8	21.8	16.7	1	21.5	69.5	164	1.9	102.3	0.1	16.9	<0.1	<0.1	0.7	1.5	0.9	3	26.2																									
11 to 13	3.312	50094	0.6	5.4	91.1	2.8	20.8	15.9	0.9	16.7	60.7	145	2.3	85	0.1	18.7	<0.1	0.1	0.8	1.5	0.7	4	23																									
13 to 15	3.312	50095	0.4	6	91.3	2.8	22.9	16.2	0.9	18.2	68.8	162	2	95.3	0.1	19.7	<0.1	<0.2	0.8	1.4	0.8	3	22.2																									
15 to 17	3.312	50096	0.4	5.5	77.4	2.6	22.7	16.2	1	21.3	70.1	162	2.2	81.4	<0.1	18.2	<0.1	<0.1	1.1	1	1	3	20.9																									
17 to 19	3.312	50097	0.4	5.7	84.1	2.4	23.2	17	1	20.6	68.8	166	2.3	103.3	<0.1	18.3	<0.1	0.1	0.9	1	0.9	4	22.3																									
19 to 21	3.312	50098	0.3	6.3	79.3	2.5	24.2	17.4	1	21.2	74.8	177	2.1	104.4	0.1	19.6	<0.1	<0.1	0.9	1.3	0.9	3	22.4																									
21 to 23	3.312	50099	0.2	7.5	82.6	2.5	22.1	17	1	21.2	71.7	166	2	85.9	<0.1	17.5	<0.1	0.2	0.9	1.6	0.9	3	21.2																									
23 to 25	3.312	50061	0.3	13.3	85.7	2.7	21.2	15.1	1	18.7	64.1	154	2.1	88.8	0.1	17.7	<0.1	<0.1	1	1.4	0.9	4	23.5																									
25 to 27	3.312	50062	0.3	7	84.7	2.6	22.7	17.1	1	23.1	74.1	169	2.3	105	0.1	18	<0.1	<0.1	1.1	1.5	0.9	4	22.3																									
27 to 29	2.92	50063	0.2	5.8	76.2	2.3	19.7	15.2	0.9	19.1	62.6	144	2	85.3	<0.1	15.2	<0.1	<0.1	0.9	1.5	0.8	2	18.2																									
29 to 31	2.92	50064	0.3	6.4	96.2	2.9	22.4	17.8	1.1	21.3	65.5	151	2.4	95.5	<0.1	18	<0.1	0.2	1	2	0.9	4	20.7																									
31 to 33	2.92	50065	0.4	11.3	95.2	3	22.2	15.3	0.9	21.7	70.8	163	2	97.6	0.1	17.6	<0.1	0.1	0.9	1.8	0.9	4	26																									
33 to 35	2.92	24289	0.8	6.7	100	3.5	22.7	17.5	0.7	28.5	91.6	197	1.9	124.3	0.05	19.8	0.05	0.2	0.9	1.7	1.1	4	28.1																									
33.5 to 34	2.92	24290	0.5	19.6	92.1	3	21.3	17.1	0.6	24.2	86.4	194	2.2	128.7	0.05	19.9	0.05	0.2	0.7	1.3	1.1	4	37.5																									
34 to 34.5	2.92	24291	0.7	7	85.1	3	22	18.8	0.7	22.1	83	179	2.2	114.8	0.05	19.5	0.05	0.1	1	1.3	0.8	4	35.7																									
34.5 to 35	2.92	24292	0.8	107	383.4	4	14.2	17.5	0.9	19.6	54.4	124	0.3	81.5	0.1	15.4	0.05	0.5	0.3	1.9	0.8	5	45.6																									
35 to 35.5	2.92	24293	0.7	273.7	647	3.8	14.8	14.4	0.7	18.9	57.4	131	0.4	100.2	0.2	15.3	0.05	0.7	0.3	2.4	1.1	6	39.4																									
35.5 to 36	2.92	24294	0.8	433.4	1577.2	5.5	21.2	15.9	0.7	18.4	65.3	151	1.4	122.2	0.4	16.5	0.05	2.2	0.4	2.1	0.9	10	47.3																									
36 to 36.5	2.92	24295	0.7	868.6	438.5	3.6	23.8	16.4	0.7	23.3	89	190	0.8	94.1	0.2	16.3	0.05	0.6	0.4	2.5	1.2	7	44.1																									
36.5 to 37	3.625	24296	1.2	1647.8	1308	5.3	22.8	19.5	0.9	24.1	68.6	171	0.4	117	0.5	18.3	0.05	1.7	0.5	2	1.2	14	46.3																									
37 to 37.5	3.625	24297	0.6	206.9	260.2	3.6	18.3	17.1	0.7	21.5	75.5	176	1.1	92.1	0.05	20.1	0.05	0.3	0.2	1.8	0.8	10	65.2																									
37.5 to 38	3.625	24298	0.8	45.3	99.3	3	19	16.1	0.7	19.3	64	151	1.3	113.8	0.05	18.3	0.05	0.3	0.4	1.1	0.9	5	60																									
38 to 38.5	3.625	24299	0.7	71	105.2	2.8	20.2	14.4	0.6	21	70.8	163	0.8	120.8	0.05	20.2	0.05	0.3	0.4	1.6	1.1	5	64.1																									
38.5 to 39	3.625	24300	0.8	105.5	207.8	3.6	25.8	18.9	0.9	24.5	87.6	195	2.6	120.6	0.1	18.8	0.05	0.2	0.9	1.4	1	4	22.4																									
39 to 41	3.625	50066	0.3	16.7	94.4	2.8	18.2	13.5	0.7	21.4	67	159	0.9	112.5	0.1	18.1	<0.1	0.2	0.4	1.2	0.8	4	58.7																									
41 to 43	3.625	50067	0.4	8.8	86.1	2.8	20.5	15.6	1.1	21.7	62.7	150	2.5	83.5	<0.1	15.8	<0.1	<0.1	0.7	5.5	0.8	4	35.7																									
43 to 45	3.625	50068	0.4	7.6	86.7	2.9	20.6	15.9	1.1	22.2	62.9	151	1.9	73.1	<0.1	16.3	<0.1	<0.1	1	1.8	0.8	3	32.9																									
45 to 47	3.625	50070	0.4	6.7	75.2	2.4	21.3	16.8	1	21.3	67.5	159	2.5	82.1	0.1	17.2	<0.1	0.1	1.1	1.6	0.9	3	15.8																									
47 to 49	3.625	50071	0.4	7.1	86.7	2.5	21	17	1	19.2	63.8	152	2.7	72.3	0.1	17	<0.1	0.1	1	1.9	0.9	4	15.2																									

Sample Interval (m)	Density	Sample Number	Bi	U	Zr	Hf	Y	Nb	Ta	Th	La	Ce	Mo	Cu	Ag	Co	Au	Cd	Sb	W	Sn	Be	Li
84 to 86	2.86	50087	0.6	5.7	86.7	2.9	17.6	13.5	0.9	17.7	60.7	146	1.7	134.9	0.2	36.9	<0.1	<0.1	0.9	1.9	0.8	3	51.2
86 to 86.5	2.86	24267	0.4	4.5	60.5	2.5	12.8	12.5	0.6	13.4	44	107	1.4	89.2	0.05	16.5	0.05	0.1	0.6	1.8	0.8	3	45.4
86.5 to 87	2.86	24269	0.3	6.1	74.5	2.8	12.5	10.5	0.5	10.5	37.9	91	0.4	90.7	0.05	17.2	0.05	0.1	0.2	1.7	0.6	4	39.6
87 to 87.5	2.86	24270	0.3	53.5	81.5	2.9	11.1	10.9	0.5	9.2	36.8	86	0.3	77.7	0.05	16.9	0.05	0.1	0.3	2	0.5	5	42.1
87.5 to 88	2.86	24271	0.4	63.2	97.2	2.8	11.3	10	0.5	11.1	37.2	87	0.4	118.6	0.1	36.6	0.05	0.2	0.3	2	0.7	5	39.9
88 to 88.5	2.86	24272	0.3	107.8	97.1	2.6	11.9	8.8	0.4	12.7	44.1	92	0.4	70.4	0.05	15.6	0.05	0.2	0.2	1.9	0.5	5	35.4
88.5 to 89	2.86	24273	0.4	218.2	147.1	2.9	12.9	9.4	0.4	11.2	43.7	99	0.3	84.3	0.05	17.2	0.05	0.4	0.3	1.5	0.7	8	40.9
89 to 89.5	2.86	24274	0.4	203.1	119.1	2.9	10.3	10.2	0.4	9.8	37.7	85	0.3	99.8	0.05	17.8	0.05	0.2	0.3	1.6	0.7	18	40.4
89.5 to 90	2.86	24275	0.4	259.7	92	2.8	9.7	10.3	0.5	11.1	41.7	94	0.3	61.7	0.05	18.9	0.05	0.2	0.3	1.3	0.6	8	47.9
90 to 90.5	2.86	24276	0.5	912	131.4	3.1	16.3	12.1	0.6	20.1	66.8	152	0.4	64.8	0.05	19.1	0.05	0.2	0.4	1.9	0.8	6	60.4
90.5 to 91	2.86	24277	0.4	170.3	198.8	3.1	10.1	9.4	0.5	10.8	39.9	87	0.5	137.6	0.2	15.2	0.05	0.3	0.3	1.6	0.5	9	33.4
91 to 91.5	2.86	24278	0.3	144.6	100	2.7	10.3	9.9	0.5	10.8	45.8	100	0.3	98.8	0.05	19	0.05	0.2	0.2	1.1	0.4	5	41.4
91.5 to 92	2.86	24279	0.5	897.6	142.6	3	20.9	13.7	0.6	18.6	76.1	163	0.7	101.8	0.05	16	0.05	0.3	0.4	2	0.5	5	40.5
92 to 92.5	2.86	24280	0.3	172.5	88.5	3.1	19.7	11.4	0.7	20.3	91.1	183	0.7	126.7	0.05	18.3	0.05	0.1	0.2	1.5	0.8	4	56.9
92.5 to 93	3.02	24281	0.5	1267.7	211.9	3.1	20.8	13	0.5	16.9	80	165	9.4	75.5	0.05	16	0.05	0.3	0.4	4.4	0.7	5	41.8
93 to 93.5	3.02	24283	0.4	938.8	148.1	3.3	18	12.9	0.7	20.6	86.8	175	8.3	101	0.05	17.6	0.05	0.3	0.3	1.8	0.5	7	64.9
93.5 to 94	3.02	24284	0.7	2998.7	200.5	3	19.6	16.1	0.7	20.9	85.5	176	32.3	136.4	0.1	17.6	0.05	0.5	0.5	2.3	0.4	3	68.3
94 to 94.5	3.02	24285	0.4	1576.4	97	3.4	20.1	13.8	0.6	22.1	78.2	170	1.2	95.6	0.05	19.4	0.05	0.1	0.5	2.2	0.8	3	73.2
94.5 to 95	3.02	24286	0.2	190.6	81	3.4	20	11.9	0.5	19.7	84.2	170	3.3	63.9	0.05	17.4	0.05	0.2	0.3	2.8	0.8	5	70.8
95 to 95.5	3.16	24287	1	3631.1	983.1	8.3	31.9	19.3	0.6	12.9	76.4	170	10.4	121.1	0.3	25.9	0.05	1.1	0.8	4.8	1.1	10	98.1
95.5 to 96	3.16	24288	2.8	4564	2000	13.5	20.8	26.7	0.8	17.3	127.1	281	65.7	522	1.2	46.3	0.05	3.5	1	7	1.9	11	148.3
96 to 96.5	3.16	24289	2.2	7570	2000	7.6	45.4	24.8	0.7	20.8	86.3	183	5.6	136.4	0.9	25.3	0.05	3.3	1.1	3.9	1.5	9	68.2
96.5 to 97	3.16	24290	1	3175.7	1039.2	4.5	20.3	17.4	0.5	15.2	60.9	126	1.6	70.4	0.4	19.8	0.05	1.7	0.6	1.7	1.2	4	45.1
97 to 97.5	3.16	24291	1.2	2545.1	1399.6	6.8	20.5	14.9	0.5	16.2	62.2	128	1	116.3	0.8	22.5	0.05	3.6	0.6	1.4	1	10	50.5
97.5 to 98	3.16	24292	1.6	3862.5	2000	15	31	17	0.5	17.8	66.3	147	1.1	115.2	2.9	18.2	0.05	11.9	0.7	1.1	1	9	41.2
98 to 98.5	3.16	24293	2.3	7976	2000	13.1	47.2	29.6	0.6	18.4	85.1	178	1.7	95.5	3	15.7	0.05	12.7	1.3	3.8	0.9	29	66.2
98.5 to 99	3.16	24294	0.8	1542	2000	7.1	21.7	13.3	0.5	16.7	76.4	156	0.6	72.7	1	15.9	0.05	4.2	0.5	2.1	1.1	25	51.9
99 to 99.5	3.16	24295	1.8	4744	1864.6	5.7	19.8	22	0.5	21.8	70.9	144	6	86.1	0.8	18.9	0.05	3.4	0.9	3.7	1	6	56.7
99.5 to 100	3.16	24296	0.4	289.6	661.8	2.8	17.4	9.4	0.5	17.8	65.5	143	0.5	68.7	0.05	17.5	0.05	1.2	0.2	1.2	0.8	6	35.6
100 to 100.5	3.16	24298	0.4	18.5	98.9	2.7	17.1	9.9	0.5	17.8	56.8	131	0.8	76.6	0.05	17.6	0.05	0.1	0.3	0.9	0.8	3	46.5
100.5 to 101	3.16	24299	0.3	13.6	87.7	2.4	15	9.7	0.5	13.5	50	115	0.7	60.2	0.05	17.7	0.05	0.2	0.3	1.5	0.7	3	42.9
101 to 101.5	3.16	24300	0.7	7.4	81.3	2.5	17.6	15.7	0.7	15.9	58.8	133	1.8	142.8	0.05	17.4	0.05	0.1	0.6	0.8	0.7	3	42.4
101.5 to 102	3.16	24301	0.4	6.7	73.3	2.3	16	13.3	0.6	15.8	63.6	134	1.4	91	0.05	16.6	0.05	0.1	0.6	0.6	1	2	54.4
102 to 102.5	3.16	24302	0.4	5.9	79	2.5	17.3	13.3	0.5	16.2	62.6	136	1.4	93.8	0.05	17	0.05	0.1	0.6	0.8	0.8	2	40.8
102.5 to 103	3.16	24303	0.5	6.1	77.7	2.3	18.6	14.1	0.7	16.2	68.4	144	1.6	84.2	0.05	17.4	0.05	0.1	0.6	0.7	0.9	3	43.2
103 to 103.5	3.16	24304	0.5	7.6	86.9	2.7	18.7	14.8	0.6	18.3	70.3	151	1.6	71.2	0.05	17.6	0.05	0.1	0.7	0.8	0.8	3	46.1
103.5 to 104	3.16	24305	0.6	5.3	82.9	2.4	17.2	13.8	0.6	16.2	61.2	135	1.6	105.7	0.1	16.4	0.05	0.1	0.7	0.8	0.7	2	38.1
104 to 104.5	3.16	24306	0.5	6.2	82.9	2.4	17	12.6	0.6	16.3	60.9	133	1.5	92	0.05	16.9	0.05	0.2	0.7	0.7	0.9	3	43.8
104.5 to 105	3.16	24307	0.6	7.7	84.1	2.6	16.2	11	0.5	16.2	54.7	123	1.2	79.6	0.05	16.3	0.05	0.2	0.6	1	0.6	3	50.8
105 to 105.5	3.16	24308	0.7	8.3	76.2	2.4	14.5	8.5	0.3	15.8	59.3	136	0.5	105.6	0.05	16.6	0.05	0.2	0.5	0.6	0.7	4	36.5
105.5 to 106	3.16	24310	0.9	17.1	82.7	2.6	15.9	10.8	0.5	14.7	54.2	138	0.9	130.6	0.1	17.7	0.05	0.2	0.7	0.7	0.9	5	41.2
106 to 106.5	3.16	24311	0.6	14.3	75.8	2.3	12.4	9.1	0.4	12.8	44.3	102	0.6	47.3	0.05	15	0.05	0.2	0.5	0.5	0.5	4	35.6
106.5 to 107	3.16	24312	0.9	302.2	89.1	2.9	13.1	9.4	0.4	15.6	57.2	125	0.2	155.3	0.1	16.7	0.05	0.2	0.3	0.6	0.8	5	38.8
107 to 107.5	3.16	24313	0.4	30.9	94.2	2.7	17.2	12.7	0.5	17	59.5	131	1.1	106.8	0.05	17.5	0.05	0.3	0.3	0.7	0.7	4	40.6
107.5 to 108	3.16	24314	0.5	16	98.4	2.8	17.7	15.6	0.8	16.8	58.9	136	1.7	159.8	0.1	16.8	0.05	0.2	0.5	0.7	0.8	3	37.6
108 to 108.5	3.16	24315	0.6	37.3	75.8	2.5	20	15.2	0.8	19.7	85.6	166	1.3	168.2	0.05	17.9	0.05	0.1	0.5	0.8	0.9	3	39.7
108.5 to 109	3.16	24316	0.4	5.1	84.6	2.6	16.8	16.4	0.8	16	58.2	129	1.8	105.9	0.05	17.3	0.05	0.1	0.6	0.9	0.7	3	30.1
109 to 109.5	3.16	24317	0.3	4.7	89.9	2.7	15.9	13.4	0.4	14.9	54.6	122	1.8	51.9	0.05	17.2	0.05	0.2	0.8	1	0.8	3	34.5
109.5 to 110	3.1	24318	0.4	6.9	87	2.6	15.4	16.5	1	15.1	52.5	119	2.5	52.1	0.05	16.9	0.05	0.2	0.9	1.4	0.6	4	21.6
110 to 110.5	3.1	24319	0.5	6.5	78.2	2.4	17.1	15.6	0.7	16.7	52.8	123	1.9	67.7	0.05	18.6	0.05	0.1	0.8	0.7	0.9	4	36.3
110.5 to 111	3.1	24320	0.5	6.7	101.3	3.1	17.8	15.7	0.8	15.7	52.9	122	1.8	97.3	0.1								

Appendix D

Drill Core and Outcrop Sample Lists

with

Location Maps

ARICHENG NORTH		SAMPLE DESCRIPTION
SAMPLE	METERS	
ARN003	42.5	INTENSE ZIRCON VEINING
	43	PEGMATITE CUTTING MYLONITE BRECCIA
	43.4	CHLORITE MYLONITE
	46.5	MORE PINKIFIED CHLORITE MYLONITE
ARN021	53	BACKGROUND FOLIATED GRANITOID - MAGNETIC
ARN022	117.7	BACKGROUND FOLIATED GRANITOID - MAGNETIC
ARN031	141.9	BACKGROUND FOLIATED GRANITOID - MAGNETIC
	86	BACKGROUND FOLIATED GRANITOID
	91	BLOCKY SECONDARY K-SPAR GRANITOID
	95.8	CHLORITE MYLONITE WITH TAN SERICITE ALTERATION
	98.5	HIGH GRADE ORE - OXIDIZED CATACLASITE MICROBRECCIA + ZIRCON VEINING
	99.6	BACKGROUND FOLIATED GRANITOID
ARN048	65.5	BLOCKY SECONDARY K-SPAR GRANITOID
	69.5	BLOCKY SECONDARY K-SPAR GRANITOID WITH NO HEMATITE (HANGINGWALL)
	75.5	BLOCKY RETICULATE WITH SUBTLE HEMATIZATION (700CPS)
ARN053	73.5	RETICULATE CHLORITE+MT GRANITOID - 800CPS
	77.46	CHLORITE MICROBRECCIA WITH PINK ALTERATION
	80.46	MORE K-SPAR OVER CHLORITE - 1600CPS
	87	MICROBRECCIA WITH POTENTIAL PITCHBLEND FILLED MICROFRACTURES; ZIRCON VEINS
	89.3	BIOTITE LAMPORPHYRE DIKE
	108.5	BACKGROUND FOLIATED GRANITOID - MAGNETIC
ARN063	111.10	CHLORITIZED GRANITOID
	112.00	BLOCKY SECONDARY K-SPAR GRANITOID
	113.40	HIGH GRADE ORE - OXIDIZED CATACLASITE MICROBRECCIA
	116.20	CHLORITE MYLONITE
	116.80	FOLIATED CHLORITE MYLONITE GRANITOID
	128.80	POORLY FOLIATED ACTINOLITE-MT GRANITOID
ARN085	96.50	BACKGROUND FOLIATED GRANITOID - MAGNETIC
	100.43	CHLORITE MYLONITE
	102.10	QTZ-K-SPAR PEGMATITE
	106.50	QUARTZ VEIN
ARN094	102.30	K-METASOMATIZED GRANITOID; WEAKLY FOLIATED; LOOKS LIKE CPX AT CORES OF AMPHIBOLE
	107.20	ALBITIZATION+ZR-VEINING (1900 CPS)
ARN100	29.00	METASEDIMENTS WITH ALTERNATING BEDS OF WACKE AND SANDSTONE
	44.50	LENS OF INTRUSIVE IN METASEDIMENTS WITH MEGACRYSTIC KSPAR
	68.70	MYLONITIC DIORITE GENERALLY WELL FOLIATED WITH PORPHYROCLASTS OF PLAG
	113.50	MYLONITIC DIORITE OVERGROWN BY LATE SECONDARY KSPAR
	114.60	ALBITIZED ULTRAMYLONITE WITH ZR VEINS
	157.00	ULTRAMYLONITE WITH PINK FELDSPAR; ALBITIZED WITH HEMATITE-ZR VEINS
	164.50	BACKGROUND FOLIATED KURUPUNG
	197.50	SILICIFIED MYLONITIZED METSEDIMENTS
ARN094	102.30	K-METASOMATIZED GRANITOID; WEAKLY FOLIATED; LOOKS LIKE CPX AT CORES OF AMPHIBOLE
	107.20	ALBITIZATION+ZR-VEINING (1900 CPS)

Table 1: List of drill core samples collected from Aricheng North.

ARICHENG SOUTH	
SAMPLE	METERS
ARS027	100.15
	MYLONITE CHLORITE GRANITOID; ACTINOLITE GONE TO CHLORITE; WEAK SECONDARY K-SPAR
	RETICULATE TEXTURED CATACLASITE; MORE CHLORITE; NOT MAGNETIC; PALE WHITE ALBITE?
	RETICULATE TEXTURED CATACLASITE; CHLORITE; NOT MAGNETIC; PALE WHITE ALBITE?
ARS029	123.80
	UNOXIDIZED CATACLASITE WITH MICROBRECCIA
	BLOCKY SECONDARY K-SPAR OVER CHLORITIZED GRANITOID - 200CPS - MAG 46
	HYDROTHERMAL CATACLASTIC DISAGGREGATION - 250CPS - MAG 28.1
ARS043	86.50
	WEAKLY HEMATIZED CHLORITE MICROBRECCIA - 270 TO 290CPS - MAG 2.67
	ZIRCON VEINED MICROBRECCIA; BRECCIA CLASTS ARE POTASSIC
	K-SPAR CATACLASITE WITH INSPIENT ALBITE ALTERATION
	ZIRCON IN QUARTZ VEIN
	154.00
	CATACLASITE WITH RINDING OF K-SPAR BY ALBITE+HEMATITE
ARS076	151.90
	DISSAGGREGATED CATACLASITE; POTASSIC AND SODIC ALTERATION; WEAK OXIDATION
	MAFIC XENOLITH WITH SECONDARY K-FELDSPAR HOSTED IN BLOCKY K-SPAR OVERGROWING CHLORITE GRANITOID
	163.20
	NON-POTASSIC MYLONITE GRANITOID
ARS090	165.40
	BLOCKY CATACLASITE WITH ZIRCON MICROBRECCIA - 1200CPS
	BLOCKY SECONDARY K-SPAR OVER CHLORITIZED GRANITOID
ARS094	230.50
	UNDEFORMED PEGMATITE DIKE; FEATHERY TEXTURE SALONG COUNTRY ROCK CONTACT
	151.80
	K-SPAR MEGACRYSTIS
	153.50
	ALBITE RIND ON KSPAR
	154.00
	OSCILLATORY ZONED SECONDARY K-FELDSPAR
	155.00
	OSCILLATORY ZONED SECONDARY K-FELDSPAR
	156.00
	MAFIC XENOLITH WITH SECONDARY K-FELD INCLUSION (SUGGESTS LATE KSPAR)
	156.80
	REDDENING OF ALBITE COINCIDENT WITH PINK CALCITE AND XENOLITHS
ARICHENG WEST	
SAMPLE	METERS
ARW005	45.5
	ZR VEINS+HEMATITE
	46.6
	BLACK CHLORITE HOSTING BRANNERITE?; HIGH GRADE ZONE WITH NO ZR - GRADE CARRIED BY BLACK CHLORITE
ARW008	62
	MAFIC XENOLITHS (ORIGIN?)SPECTULAR HEMATITE INTERIOR TO GLAST AND ZR ON OUTER MARGIN OF GLAST
	106.8
	RETICULATE TEXTURED CATACLASITE
	119.6
	HEMATITE OXIDIZED ZIRCON MICROBRECCIA
	125.5
	HEMATITE CHLORITE MICROBRECCIA
ARW009	127.5
	CATACLASIZED SECONDARY K-SPAR OVER MAGNETIC GRANITOID
	57.40
	CATACLASIZED SECONDARY K-SPAR OVER MAGNETIC GRANITOID
ARW030	54.50
	RETICULATE TEXTURED CATACLASITE
	175.80
	VERY LITTLE ZIRCON; ABUNDANT BLACK CHLORITE (700 CPS)
	181.00
	BLACK CHLORITE SEAMS
	185.00
	EXAMPLE OF DISSEMINATED ZR (NO VEINS)
	199.80
	STRINGERS OF BLACK CHLORITE INTERGROWN WITH ZR (1800 CPS)
	208.8
	FRESH KURUPUNG; MAGNETIC; A FEW SECONDARY KSPAR

Table 2: List of drill core samples collected from Aricheng South and West.

ACCORI NORTH		
SAMPLE	METERS	SAMPLE DESCRIPTION
ACCORIB	34.75	MEGACRYSTIC K-FELDSPAR
ACC011	120.00	BACKGROUND FOLIATED GRANITOID: WEAK SECONDARY K-SPAR
	123.00	CHLORITE CATACLASITE WITH INSPIENT ALBITE ALTERATION - WEAKLY OXIDIZED
	126.80	HEMATITE MILLED BRECCIA (ON ITS WAY TO OXIDIZED MICROBRECCIA)
	144.40	MILLED CATACLASITE WITH MINOR MICROBRECCIA
ACC013	191.85	BLOCKY SECONDARY K-SPAR GRANITOID
	192.50	BLACK CHLORITE MICROBRECCIA ON MARGIN OF MILLED BRECCIA
	208.40	MILLED CATACLASITE WITH LATE CALCITE VEINLETS
	216.80	ENHANCED OXIDATION WITH FINE GRAINED HYDROTHERMAL ALBITE
	235.70	BIG LAMPROPHYRE DIKE FOOTWALLED TO OXIDIZED MILL BRECCIA
	249.80	FOLIATED LAMPROPHYRE
MEAMU		
SAMPLE	METERS	SAMPLE DESCRIPTION
MEAMU002	21.5	WEAKLY CHLORITIZED: 30% KSPAR MEGACRYSTS; COARSE AMPHIBOLE CRYSTALS
	39	HORNBLENDE DIORITE OVGROWN BY 30% SECONDARY KSPAR
	96.5	BIOTITE LAMPROPHYRE DIKE WITH INCLUSIONS OF HORNBLENDE DIORITE
ILLIWA		
SAMPLE	METERS	SAMPLE DESCRIPTION
ILLIWA 001	44.4	VERY LITTLE MEGACRYSTIC KSPAR (5%) IN HORNBLENDE GRANITOID; MAFIC XENOLITH PRESENT IN SAMPLE
ANOMALY A		
SAMPLE	METERS	SAMPLE DESCRIPTION
ANOMA 004	39.2	URANOPHANE/ALUTINITE? IN ZR VEINS WITH ASSOCIATED PINK CALCITE
	80	BACKGROUND KURUPUNG; MODERATELY MAGNETIC; 1% KFELDSPAR; WEAKLY CHLORITIZED
ANOMA 006	90	MAFIC ENGLAVE (GPX BEARING?)
	93	ZR MICROBRECCIA WITH RETICULATE TEXTURED CATACLASITE
	112.75	MAFIC FRAGMENT WITH BIOTITE+AMPHIBOLE+GREEN MICA?
WCC		
SAMPLE	METERS	SAMPLE DESCRIPTION
WCC001	136.4	WHITE PLAGIOCLASE ASSOCIATED WITH GROWTH OF SECONDARY KSPAR

Table 3: List of drill core samples collected from Accori North, Meamu, Illiwa, Anomaly A, and WCC.

ACCORI SOUTH/NORTH/LA/RCHENG NORTH/SW/SE P7/HIMABAKA SE/CMENTS (JUNE 4 2009)		
SAMPLE	COORDINATES	SAMPLE DESCRIPTION
1	800543/687550	ACCORI SOUTH-SECONDARY K-FELD GRANITOID 140/22- NON-MAGNETIC
2,3,4	798250/689500	ACCORI NORTH-A, GROWTH OF SECONDARY K-SPAR MEGACRYSTIS OVER FOLIATION WEAKLY MAGNETIC. MAGNETITE GONE TO HEIMATITE, 265/62, 2000CPS
5		MEDIUM GRAINED FB GRANITOID, BACKGROUND GRANITE, UMINERALIZED, 300CPS
6	804804/692009	HIGH GRADE - HEIMATIZED K-SPAR GRANITOID BIR COAL, 9990CPS
7	807002/689595	DIABASE DIKE WITH FINE GRANNEO CHILL- MAGNE TIC, CPY-PPRR
NO SAMPLE	807800/694012	SAPROLITIC HORNFEISED MICA, SCHIST, RELECT TURBIDITE BEDS, BEDDING PARALLEL, FOLIATION AT 140 DEGREES, SECOND FOLIATION AT 300 DEGREES, ALSO DOLEIRITE SEDIMENT CONTACT
ANARABSI CAMP (JUNE 8 2009)		
SAMPLE	COORDINATES	SAMPLE DESCRIPTION
1	798507/703370	FOULATED ACTINOLITE-MAGNETITE GRANITOID, MAGNETIC
2	798427/702309	DOLEIRITE DIABASE, COARSE PRR, 1000CPS, WEAKLY SHEARSING INTO RIVER AT 50 DEGREES
3		DOLEIRITE DIABASE, COARSE PRR, 1000CPS, WEAKLY SHEARSING INTO RIVER AT 50 DEGREES
4		AMPHIBOLE-PHLOGOPHANE-MAGNETITE KURUPANS GRANITE DIABASE
5A	794445/703891	SHEETED DIKES WITH CHILL MARGINS, SHEETED DIKES FEEDING THE KORAMAX, MULTIPLE CHILLS ON MULTIPLE 1/2 METER DIKES, WITH COLUMNAR COOLING JOINTS
5B	794445/703892	CHILL MARGIN FROM 5A
6	794445/706647	FINE GRANNEO DIABASE DIKE
7	798831/706653	HIMABAKA MAROON SLATE, GRADED BEDS, BALL AND FLAME STRUCTURES, TOPS TO THE WEST, BEDDING 020/70
8	794345/706864	HIMABAKA SEDIMENTS INTERLAYERED WITH BASALTS, 120/70 FOLIATION
ROCK POINT/LARCHENG SOUTH/RCHENG WEST/WILD COW LANDING (JUNE 10 2009)		
SAMPLE	COORDINATES	SAMPLE DESCRIPTION
1	805043/689501	CHLORITIZED FOLIATED GRANITOID
2	805152/689505	FINE GRANNEO DIABASE DIKE, MAGNETIC, FINE GRANNEO DISSEMINATED METALLICS, STRIKING 45 DEGREES
3	805152/689514	WEAKLY FOLIATED GRANITOID WITH FOLIO SECONDARY K-FELD
4	805152/689514	WEAKLY FOLIATED GRANITOID WITH FOLIO SECONDARY K-FELD
5	805445/689542	COARSE GRAINED DIABASE, STRIKING 10/90
6	805445/689542	CHLORITE-MAGNETITE GRANITOID ON MARGINS OF SAMPLE 5
7	805445/689546	ALONG BASE OF RIDGE IS QUARTZ-FELDSPAR PEGMATITE DIKE, STRIKING 140 DEGREES
8	805256/689532	DARK CHLORITE-HEMATITE CATACLASTIC WITH ONDRE MICROBRECCIA, NON-MAGNETIC, 1100CPS
9	806311/689564	DIABASE DIKE CUTTING ROAD, MAGNETIC, PPRR
10	806776/689513	NON-MAGNETIC DIABASE DIKE
NO SAMPLE	805445/689500	RADIOMETRIC ANOMALY ON ALLUVIAL WHITE SANDS (ARCHENG WEST)
11	806765/689264	SLIGHTLY MAGNETIC SECONDARY K-FELDSPAR GRANITOID, QTZ, VENE PARALLEL FOLIATION, LATE CHLORITE VENE CUTTING ALL, 140 DEGREE FOLIATION, 190CPS, WILD COW LANDING
12	806226/687697	COARSE INTERIOR TO MAGNETIC DIABASE, COARSE INTERIOR - LOW MAGNETISM, APHANITIC MARGIN - HIGH MAGNETISM, PYROXENE-PLAG MODERATELY MAGNETIC, COARSE INTERIOR TO DIKE
PERENONS/EPING RIVER (JUNE 11 2009)		
SAMPLE	COORDINATES	SAMPLE DESCRIPTION
1	822152/67529	PORPHYRITIC DIKE, FEEDER TO KORAMAX, COOLING JOINTS, COOLING JOINTS, MODERATE MAGNETISM
2	822152/67562	WEATHERED STRIPED DIABASE, NON-MAGNETIC
NO SAMPLE	822027/676592	CONTACT BETWEEN FOLIATED HIMABAKA MAFES AND HIMABAKA MAFES, FOLIATION N/SCHIST, 10/69, FOLIATION N/MAFES 10/75
3	822027/676592	MAGNETIC DIABASE
4	822716/677624	NON-MAGNETIC DIABASE, DIKES INTRUDING ALONG FAULTS AND CRYSTALLING AT 1000 DEGREES, DURING COOLING AT 300 DEGREES FORM CHL WITH NEUM OF 100 AND DERIVATING DIKE, PERHAPS INTERSECTION OF WYLOWITE FAULT ZONE WITH DIKES-MINERALIZATION
5A	822002/677454	COARSE GRAINED MAGNETIC DIABASE
5B	822002/677454	DIKE WITHIN A DIKE, APHANITIC
6	822203/677090	FAMILY FOLIATED CHLORITE-ACTINOLITE GRANITOID, WEAKLY MAGNETIC
7	821598/676787	UNFOLIATED NON-MAGNETIC ACTINOLITE-CHLORITE GRANITOID
8	820167/6770219	UNFOLIATED NON-MAGNETIC ACTINOLITE-CHLORITE GRANITOID, NO SECONDARY K
9	818326/677265	WEAKLY MAGNETIC ACTINOLITE-CHLORITE GRANITOID, A LITTLE MORE PINK
10	818798/6767679	UNFOLIATED, SECONDARY K GRANITOID
11	818042/677672	SECONDARY K GROWING ON FRACTURE PLANES, WEAKLY MAGNETIC
12	815326/677655	BACKGROUND GRANITE, NO FOLIATION, NO SECONDARY K, WEAKLY MAGNETIC, GOOD GECHEM SAMPLE
13A	815353/676254	IMPURE SAPROLITE FOLIATED BASALT
13B	815353/676254	NON-MAGNETIC SAPROLITIC DIABASE
DOMIE HOUNTAN (JUNE 12 2009)		
SAMPLE	COORDINATES	SAMPLE DESCRIPTION
1	798000/697235	PINK SECONDARY K-SPAR OBLITERATES FOLIATION, START OF DISSAGGREGATION DUE TO CHLORITE GROWTH, STARTING GROWTH OF ALBITE
2	799108/697841	MORE SECONDARY K AND MORE ALBITE, WEAKLY MAGNETIC GRANITOID
3A	799867/694909	ANORTHOSTIC GABBRO SILL, FEEDER TO THE KORAMAX
3B		FINE GRANNEO MARGIN
3C	801026/6943370	MEGACRYSTIC SECONDARY K, ALSO EUPHERAL WHITE ALBITE, DISSAGGREGATED
4		ORE - HEIMATIZED FINE GRANNEO SLICED GRANITOID, YELLOW AND BLACK UNMINERALS, 6000-9990CPS, MANY SAMPLES TAKEN TO ESTABLISH SUITE OF UNMINERALS

Table 4: Outcrop sample list.

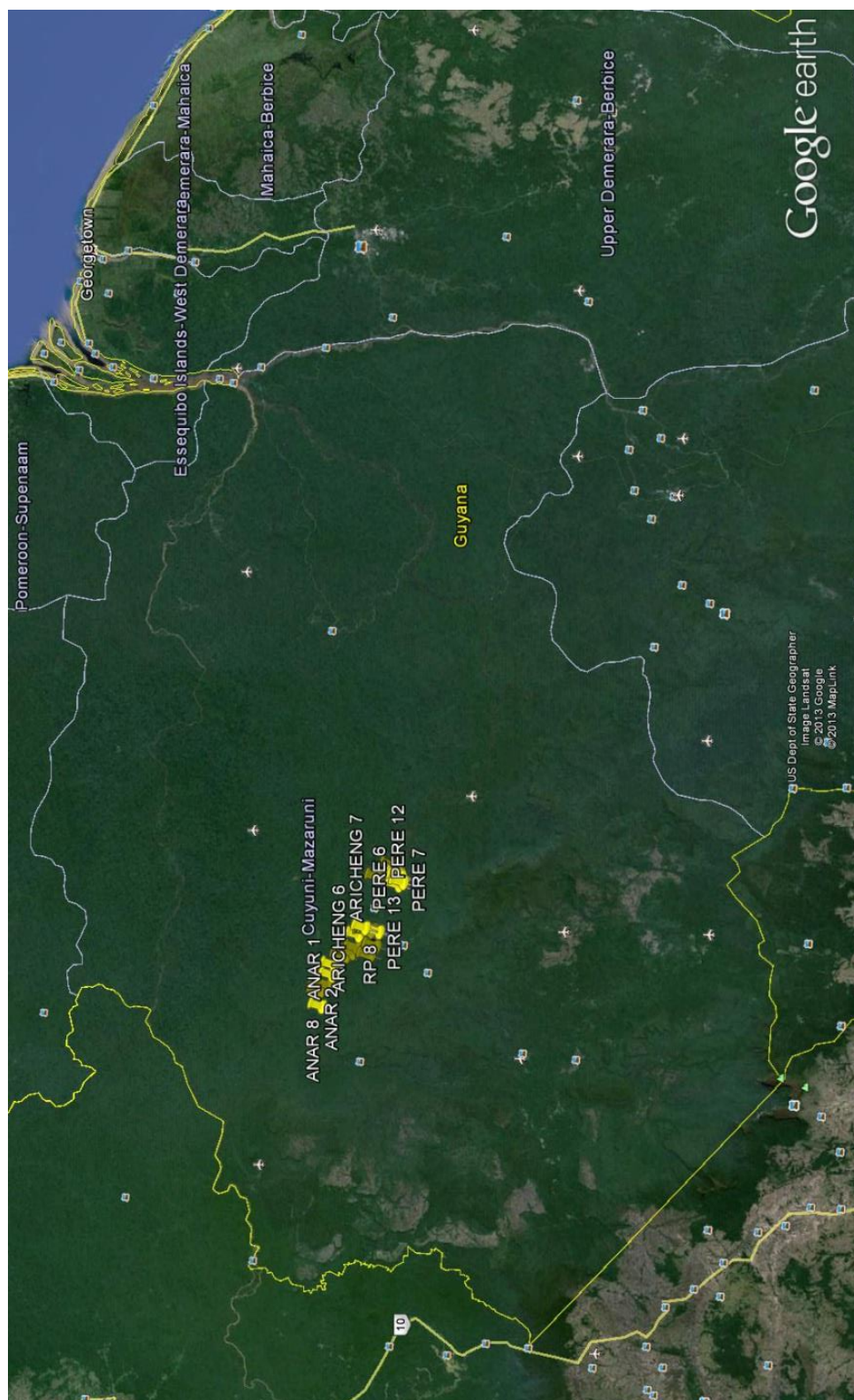


Figure 2: Google Earth image giving a regional perspective of the study area with sample locations labelled.

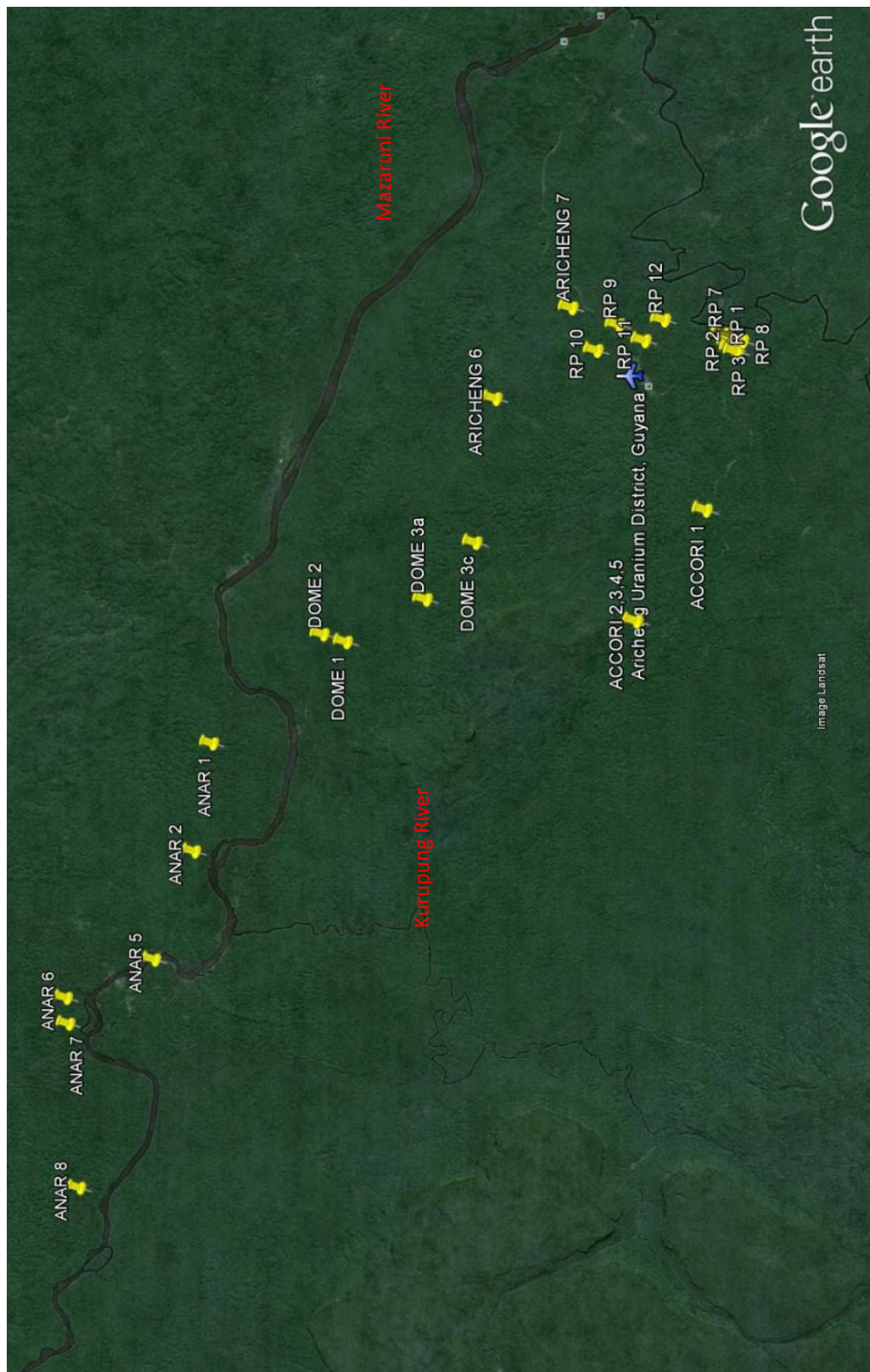


Figure 4: Google Earth image illustrating hand sample locations.

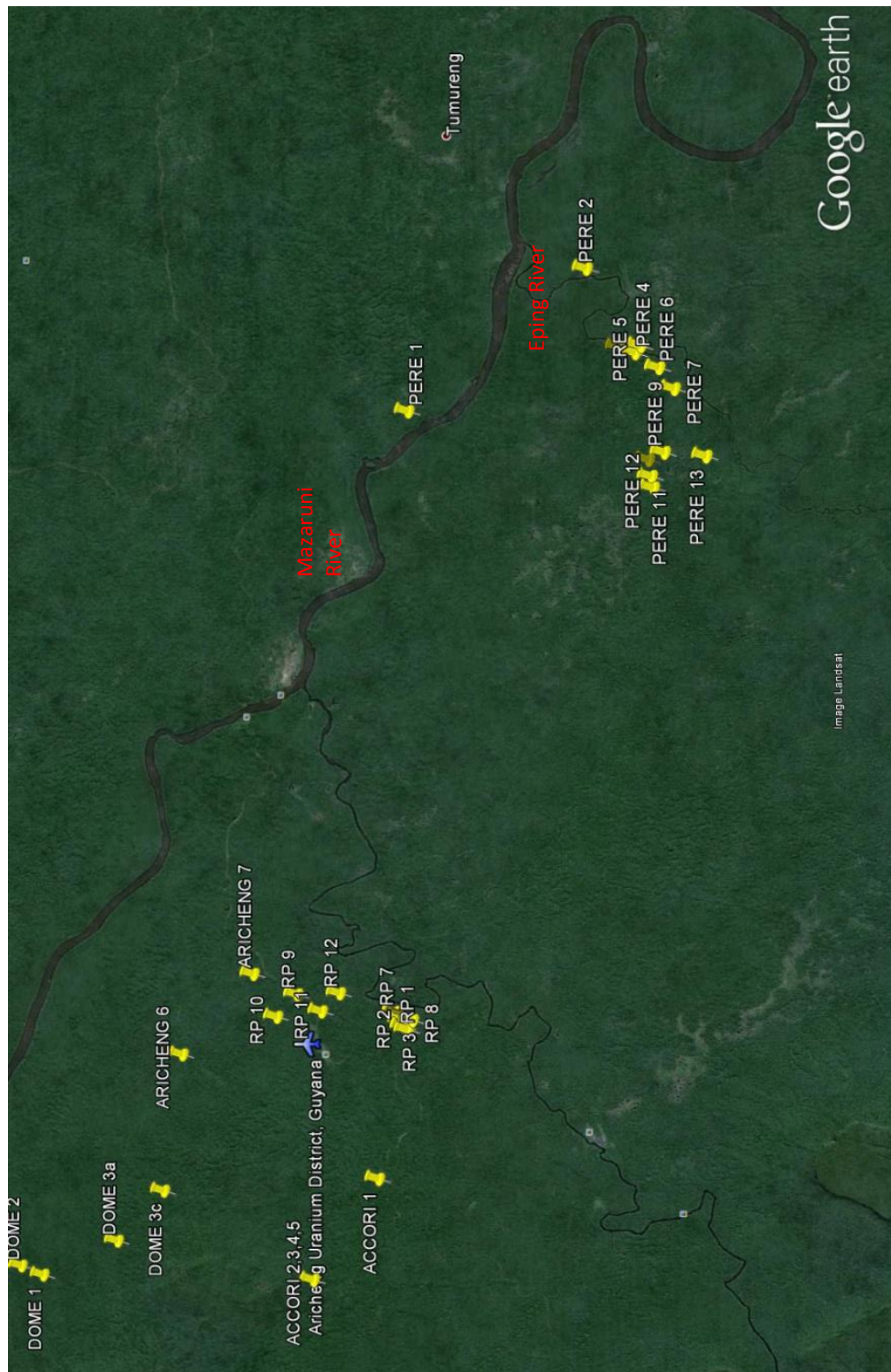


Figure 6: Google Earth images illustrating hand sample locations. Note the blue airplane symbol represents the Aricheng base camp and airstrip.

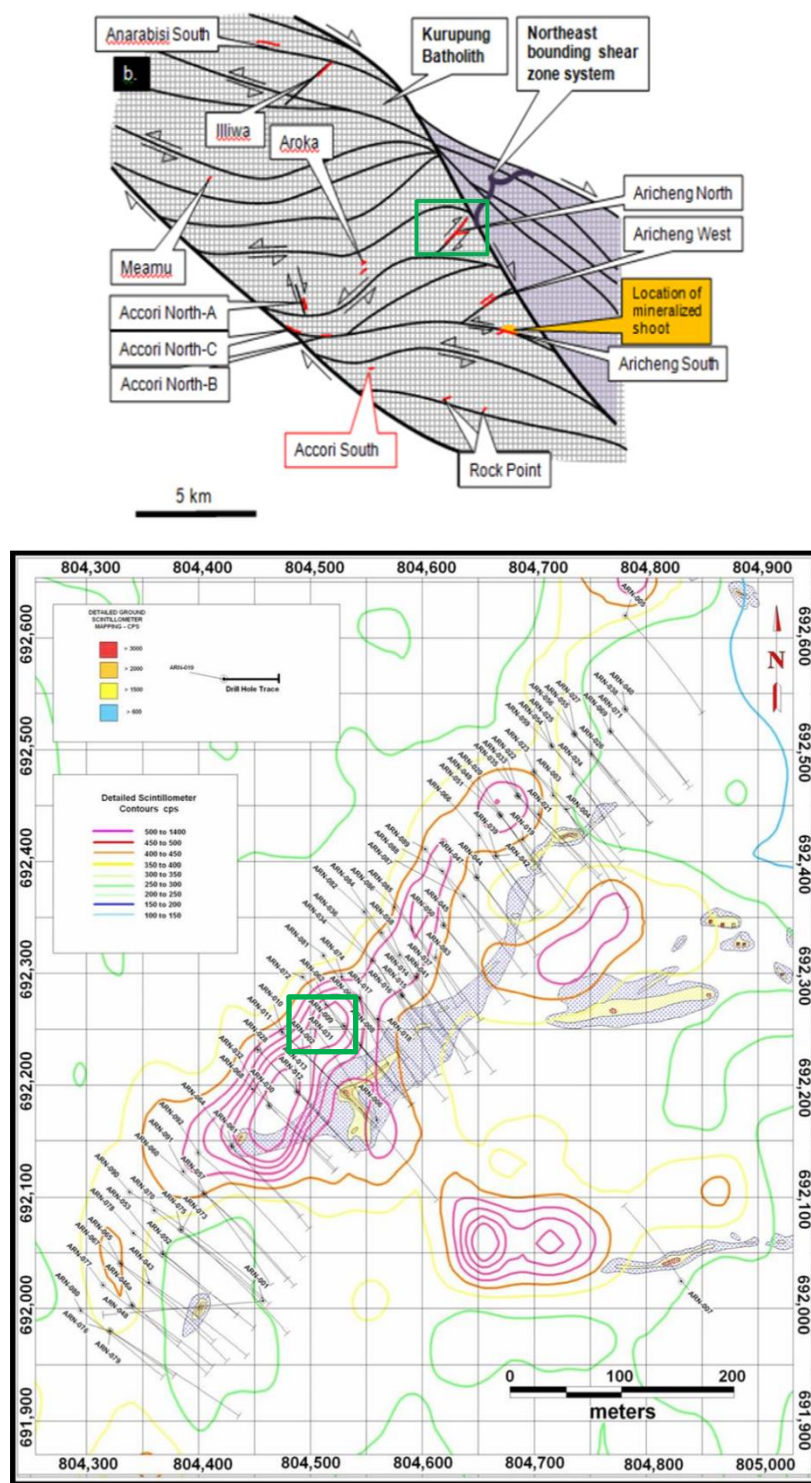


Figure 7: These figures are used here to demarcate the location of drill hole ARN-031 used for mass balance calculations. The upper image illustrates the location of the Aricheng North prospect (enclosed within green box). The lower image is a drill hole location map illustrating the drill hole location of ARN-031.

Appendix E

**Report by Donald W. Davis:
Geochronology of magmatic and hydrothermal zircon from an altered
granite in Guyana**

Geochronology of magmatic and hydrothermal zircon from an altered granite in Guyana

Donald W. Davis

November 16, 2006

1. INTRODUCTION

The sample, designated U308-06-1, consisted of two small ca. 2 inch fragments of split drill core from an extensively veined granitoid rock.

2. METHODS

The sample was ground in an alumina mortar and the fine fraction removed by stirring and decanting in water. This was followed by paramagnetic separations with the Frantz isodynamic separator and density separations using bromoform and methylene iodide. Final sample selection was by hand picking under a microscope, choosing the least altered, uncracked grains.

The sample contained both magmatic (Optical Images 1 to 4) and hydrothermal zircon (Optical Images 5 to 6). Exterior surfaces of selected magmatic zircon grains were removed by air abrasion (Krogh, 1982). Hydrothermal zircon is abundant in the heavy mineral separates and consists of clusters of white micron-sized crystals intergrown with other minerals such as quartz and feldspar, as revealed by backscattered electron (BSE) imaging and energy dispersive analysis (EDS) in the scanning electron microscope. Hydrothermal zircon was imaged both as whole grains (BSE Images 2 to 7) and in polished section (BSE Images 8 to 16). This zircon appears white opaque or turbid, which is normally an indication of alteration and associated secondary Pb loss (Krogh and Davis, 1974). In order to remove intergrown minerals, which would contribute common Pb, without further disturbance to the zircon, the clusters were annealed at 1000°C for 3 days and then leached in nitric acid and HF at 110°C for several hours. The annealing process repairs most of the radiation damage accumulated by the decay of U and renders the zircon crystal inert to dissolution and leaching at moderate temperature (Mattinson, 2005). The residue after HF treatment consists of micro-crystallites of white zircon (Optical Image 6).

Weights of mineral fractions were estimated from micro-photographs (Matthews and Davis, 1999). Estimated weights should be accurate to about $\pm 20\%$ for the large magmatic grains but are much more uncertain for the hydrothermal grains, whose size

made them difficult to handle and to image. This affects only U and Pb concentrations, which should be considered order-of-magnitude estimates for the hydrothermal fractions. Uncertainty in weight does not affect age information, which depends only on isotope ratio measurements.

Zircon grains were washed in HNO₃ prior to dissolution, except for some of the hydrothermal samples, which were pipetted directly into the dissolution capsule in acetone or alcohol. ²⁰⁵Pb-²³⁵U spike was added to the dissolution capsules during sample loading. Zircon was dissolved using concentrated HF in teflon bombs at 200°C (Krogh, 1973). Samples were redissolved in 3N HCl to ensure equilibration with the spike. U and Pb were separated from zircon samples weighing more than 5 micrograms using 50 microliter anion exchange columns. Pb and U solutions were loaded onto Re filaments using silica gel and analyzed using either a VG354 or a MM354 mass spectrometer in single collector or multi-collector mode, respectively. Single collector measurements were made using a Daly detector in pulse counting mode. The mass discrimination correction for this detector is constant at 0.07%/AMU. Thermal mass discrimination corrections are 0.10% /AMU. Dead time of the counting system was about 20 nsec. Daly dead time and Faraday cup calibrations were monitored using the SRM982 Pb standard.

3. RESULTS and INTERPRETATIONS

Results of U-Pb isotopic analyses are given in Table 1. U-Pb data are plotted on concordia diagrams in Figs 1 to 3 (2 sigma error ellipses on all figures). Analyses are numbered on the diagrams according to Table 1. Average age errors are given at 95% confidence levels. Data reduction and regressions were carried out using programs of Davis (1982) and Ludwig (2003). Probabilities of fit would be expected to be 50% on average for random data with correctly chosen analytical errors. All age errors in this report are quoted at 2 sigma. The two populations of zircon showed very different U-Pb systematics (Fig. 1).

4.1 Magmatic zircon

A small mount of clear euhedral zircon was found in the heavy mineral separate (Optical Image 1). Some grains show evidence for cores and overgrowths. A fraction of uncracked grains with no visible evidence of cores was picked (Optical Image 2) and abraded. Three of these grains were analyzed (Optical Image 3). Two gave overlapping ²⁰⁷Pb/²⁰⁶Pb ages of about 2100 Ma, although one datum is above concordia. The third analysis is concordant but distinctly younger at 2074 ± 4 Ma (Fig. 2). In order to search for an unaltered hydrothermal component, a fraction of clear zircon that appeared less euhedral and more polycrystalline was also picked and abraded. Analyses on two of these grains (Optical Image 4, a third grain was lost) are above concordia and they have somewhat younger ²⁰⁷Pb/²⁰⁶Pb ages down to 2064 ± 4 Ma (Fig 2). Considering the striking difference between these grains and grains that are clearly hydrothermal (see below), they could have largely consisted of cracked magmatic grains although an argument is presented in the next section that some of the grains may have had a hydrothermal component.

Reverse discordance is rare in zircon and indicates either loss of U relative to Pb or gain of radiogenic Pb. It can be due to accidental incomplete dissolution of sample but this can be ruled out by the fact that the phenomenon was observed in two grains from the same sample dissolved during different sessions and not observed in samples from other rocks that were dissolved during these sessions. The scatter in $^{207}\text{Pb}/^{206}\text{Pb}$ ages may be due to inheritance, or it may be related to a complex history of U and Pb mobility and/or intergrowth of magmatic and hydrothermal components (see below). If the zircon is entirely magmatic and the scatter is due to inheritance combined with recent mobility, the best interpretation for the age of the rock would be about 2065 Ma, the approximate age of the two youngest grains.

4. Hydrothermal zircon

The bulk powder from the rock contains a very high proportion (ca. 10% or more) of brownish polycrystalline aggregates (Optical Image 5). BSE imaging, combined with EDS analysis, show that these consist largely of small, white, opaque zircon crystals intergrown with feldspar and Fe-oxide (BSE Images 1 to 16). There are also micron-scale high-U grains scattered through some of the aggregates (BSE Images 9C and 11B). These may represent primary hydrothermal minerals or they could have formed from alteration of U-rich zircon. There is an indication of zoning in the hydrothermal crystals that is visible in some polished sections (e.g. BSE Images 8, 10, 13 & 15). In the cases of BSE Images 8B and 13B, where EDS analyses were made of darker and lighter zones, the darker zone appears to have slightly more Si, Ca and Fe relative to Zr, compared to the lighter zone (see files 'Polished mount 3-1-2-1' and 'Polished mount 3-1-2-2' for BSE Image 8B, and 'Polished mount 3-6-2-1' and 'Polished mount 3-6-2-2' for BSE Image 13B in the 'Report:/EDS Spectra' directory on the accompanying CD-ROM). This suggests that the darker colouration represents more altered zircon.

Hydrothermal grain clusters were annealed to remove radiation damage and then treated with nitric and hydrofluoric acids to dissolve minerals besides zircon (see Methods section above). This zircon, which is in the form of very small whitish micro-crystals (Optical Image 6), proved to be extremely high in U. Analyses of two multi-grain fractions gave overlapping data that are about 87% discordant (points 2-2 and 2-3, Fig. 3). These two data agree because each fraction contained many hundreds of grains so there is a strong averaging effect. Estimates of the weights and therefore the U concentrations are very imprecise but it is likely that the average U concentration exceeds 5000 ppm. In order to obtain a data set with a range of discordance, which would allow calculation of a Pb loss line, two single micro-grains and one small cluster containing only a few grains were analyzed. Two of these yielded fairly radiogenic Pb isotopic compositions, while the cluster gave a less radiogenic and therefore less precise datum but it is still useful since this datum shows the least discordance (point 2-1, Fig. 3). A linear regression defines an upper concordia intercept age of 1995 ± 15 Ma with a lower age intercept near 0 Ma.

In the case of a single Pb loss event, the upper concordia intercept would normally be interpreted as the primary age of the zircon, and is considered to be a minimum age where there has been a multi-stage history of Pb loss. However, these data

should be interpreted with caution because of the highly unusual character of the zircon and uncertainty about the nature of the Pb loss mechanisms.

The high U content and age of the zircon indicates that it would have been highly damaged. Its opaque nature and the whitish colouration both before and after treatment with HF are indications of the presence of alteration, which is usually associated with Pb loss. Alteration is also indicated by the presence of small Ca and Fe peaks in the X-ray spectra of all analyzed spots on hydrothermal grains. No clear, unaltered zircon could be found in the annealed fraction down to the 10 micron scale. Therefore, the grains are likely to have undergone substantial secondary (low temperature) Pb loss as they accumulated radiation damage and became susceptible to alteration by ambient fluids. Given the high U concentrations, this is likely to have started after a time interval much shorter than the age of the zircon. Therefore, one might expect to see a high lower concordia intercept age from this mechanism, which is common in highly damaged zircon from other rocks, unless the altered domains continued to lose Pb until recent time, or Pb was removed from the altered domains during laboratory leaching.

A second mechanism of Pb loss that must be considered in this case is alpha recoil. Decay of an alpha-emitting radionuclide causes the daughter nucleus to recoil through the crystal lattice. This is the principal mechanism for inducing radiation damage. For zircon, recoil distances vary from about 20 nm to 30 nm but there are 8 alpha decays in the ^{238}U system and 7 in the ^{235}U system so the average total displacement for a radiogenic Pb isotope will be roughly 0.1 micron (Romer, 2003). Since the average total recoil displacement of ^{206}Pb is about 7% more than that of ^{207}Pb , the ^{206}Pb isotope will suffer greater loss than ^{207}Pb , leaving a crystal with a higher (and therefore apparently older) $^{207}\text{Pb}/^{206}\text{Pb}$ age. Thus, for very small grains whose Pb loss is dominated by alpha recoil, the $^{207}\text{Pb}/^{206}\text{Pb}$ age cannot be taken as a minimum estimate. In the present case, the radius of the hydrothermal zircon crystals is generally around 10 microns, which is 100 times larger than the recoil distance. Therefore, one might expect to see recoil loss on the order of 1%, much smaller than the ca. 90% loss recorded by the data. It may therefore be concluded that the dominant loss mechanism was chemical alteration of the zircon so the $^{207}\text{Pb}/^{206}\text{Pb}$ age, which is effectively the 1995 ± 15 Ma upper concordia intercept of the Pb loss line in this case, can be taken as a minimum age estimate on crystallization of the zircon. A maximum estimate may be given by the youngest age indicated by the magmatic zircon, 2064 ± 4 Ma.

Although alpha recoil does not appear to have played a significant role in Pb loss from the hydrothermal zircon, it may provide a mechanism for explaining the reverse discordance of the magmatic zircon. Hydrothermal zircon would probably tend to nucleate preferentially on surfaces and along cracks in earlier magmatic zircon. Since the U concentration of this component is much higher than in the magmatic zircon, radiogenic Pb implantation by alpha recoil may have had a significant influence on the Pb isotopic composition near the surfaces. Exterior surfaces are removed by abrasion but internal cracks, such as in the 'polycrystalline' grains, could contain hydrothermal zircon much of which was eventually removed by alteration, leaving an excess of implanted Pb in the host magmatic crystal. The viability of this suggestion is hard to evaluate, although micro-photos show that the three analyses with reverse discordance are from grains with cracks or large inclusions (Optical Images 3 & 4).

Another observation suggesting that the analyzed 'magmatic' zircon might have contained a hydrothermal component is the Th/U ratio, which is calculated from the age and measured radiogenic $^{208}\text{Pb}/^{206}\text{Pb}$. Most magmatic zircon from granitoid rocks has Th/U ratios that vary in the range 0.2 to 1.0. This ratio is commonly low (<0.1) in pegmatitic and metamorphic zircon and it would also be expected to be low in hydrothermal zircon because Th is relatively insoluble in aqueous fluids compared to U under oxidizing conditions. In fact, the Th/U ratios of the hydrothermal zircon are low (0.03 to 0.07, except for datum 2-1, which is less reliable because of the high common Pb correction, see Table 1). The Th/U ratio in the most reversely discordant 'polycrystalline' grain is distinctly lower than that found in the other magmatic zircon (0.1 vs 0.4-1.0, respectively) and approaches that in the hydrothermal zircon. This grain also has an usually high U concentration tending toward that of the hydrothermal grains. In fact, there is a good correlation between the U concentrations and U/Th ratios for the 'magmatic' zircon, which indicates that the average Th concentration in the grains was relatively constant compared to U. One way for this to happen would be to mix a low U magmatic zircon component with a component that has much higher U concentration but little Th. Addition of a small amount of this component would have a significant affect on the U concentration without affecting significantly the volume of the grain, which controls the Th concentration. If this low Th/U grain was dominated by a hydrothermal component, then the age of this component is probably close to 2065 Ma.

4. CONCLUSIONS

The granitoid pluton was emplaced near the end of the Trans-Amazonian magmatic event (e.g. Norcross et al. 2000), probably within the age range 2065-2100 Ma. It was subsequently altered and veined with hydrothermal zircon having a minimum age of 1995 ± 15 Ma and possibly approaching 2065 Ma. It is therefore probable that the hydrothermal event was also associated with the final stages of the Trans-Amazonian orogeny. The hydrothermal zircon has a concentration of at least several thousand ppm U. This is high relative to normal magmatic zircon and suggests that the U concentration of the fluids responsible for the alteration was also quite high.

If further work is necessary to refine the geochronology of the zircon, SHRIMP analysis on carefully imaged grains should be considered. The high-uranium character and old age of the hydrothermal zircon would theoretically allow fairly precise ages to be measured even with the smallest available spot size of the primary beam (about 5 microns). This may allow a more definitive measurement of the age of the hydrothermal component if unaltered zircon can be found at this scale.

REFERENCES

- Davis, D.W., 1982. Optimum linear regression and error estimation applied to U-Pb data. *Canadian Journal of Earth Sciences*, 19, 2141-2149.
- Jaffey, A.H., Flynn, K.F., Glendenin, L.E., Bentley, W.C. and Essling, A.M. 1971. Precision measurement of half-lives and specific activities of ²³⁵U and ²³⁸U. *Physical Review* 4: 1889-1906.
- Krogh, T.E. 1982. Improved accuracy of U-Pb ages by the creation of more concordant systems using an air abrasion technique. *Geochimica et Cosmochimica Acta* 46: 637-649.
- Krogh, T.E. 1973. A low contamination method for hydrothermal decomposition of zircon and extraction of U and Pb for isotopic age determinations. *Geochimica et Cosmochimica Acta* 37: 485-494.
- Krogh, T.E., Davis, G.L., 1974. Alteration in zircons with discordant U-Pb ages. *Carnegie Inst. Washington Yearb.* 73, 560-567.
- Ludwig, K.R. 2003. User's manual for Isoplot 3.00 a geochronological toolkit for Excel. *Berkeley Geochronological Center Special Publication* 4, 71 p.
- Matthews, W. and Davis, W.J. 1999. A practical image analysis technique for estimating the weight of abraded mineral fractions used in U-Pb dating. In *Radiogenic Age and Isotopic Studies: Report 12; Geological Survey of Canada, Current Research 1999-F*, p. 1-7.
- Mattinson, J. 2005. Zircon U-Pb chemical abrasion (CA-TIMS) method: Combined annealing and multi-step partial dissolution analysis for improved precision and accuracy of zircon ages. *Chem. Geol.* 220: 47-66.
- Norcross, C., Davis, D.W., Spooner, E.T.C. and Rust, A. 2000. U-Pb and Pb-Pb age constraints on Paleoproterozoic magmatism, deformation and gold mineralization in the Omai area, Guyana shield. *Precambrian Research*, 102: 69-86.
- Romer, R.L. 2003. Alpha recoil in U-Pb geochronology: effective sample size matters. *Contributions to Mineralogy and Petrology*, 145: 481-491.
- Stacey, J.S. and Kramers, J.D. 1975. Approximation of terrestrial lead isotope evolution by a two-stage model. *Earth Planet. Sci. Lett.*, 26: 207-221.

Table 1: U-Pb isotope analyses on zircon from an altered granite in Guyana

No.	Analysis	Fraction	Wt. mg	U ppm	Th/U	Pbtot pg	Pbcom pg	²⁰⁶ Pb/ ²⁰⁴ Pb meas.	²⁰⁷ Pb/ ²⁰⁴ Pb meas.	²⁰⁶ Pb/ ²³⁸ U Age (Ma)	2 Sig	²⁰⁷ Pb/ ²³⁵ U Age (Ma)	2 Sig	²⁰⁷ Pb/ ²⁰⁶ Pb Age (Ma)	2 Sig	Disc %	Rho Concordia	
U308-06-1 Magmatic zircon																		
1-1	dwtd5004	1 Ab euh zr, brn, incl	0.0022	127	0.51	129.6	2.3	3289	442	2268	4	2182	3	2103	3	-9.3	0.82321	
1-2	dwtd5014	1 Ab polcr, brn, crk	0.00025	925	0.11	96.5	2.8	2231	298	2255	5	2158	3	2067	5	-10.8	0.75263	
1-3	dwtd5005	1 Ab euh zr, incl	0.0009	145	1.04	64.1	12.4	272	48.58	2108	12	2104	15	2100	23	-0.5	0.65556	
1-4	dwtd5013	1 Ab polycr, crk	0.00034	303	0.43	42.6	1.2	2219	296	2093	5	2079	3	2064	4	-1.6	0.79835	
1-5	dwtd5006	1 Ab euh zr, brn	0.0008	209	0.68	72.1	1.4	2983	396	2069	7	2071	4	2074	4	0.3	0.84260	
Hydrothermal zircon																		
2-1	dwtd5087	Ann, lch, zr cluster	0.0001	572	0.16	8.9	7.3	44.72	18.880	392	12	742	74	2020	246	83.0	0.25224	
2-2	dwtd5043	Ann, lch, zr bulk	0.005	7839	0.07	1771	22.4	4596	574	286	6	576	9	1984	6	87.4	0.98600	
2-3	dwtd5044	Ann, lch, zr bulk	0.010	7960	0.07	3479	43.0	4691	586	277	4	562	6	1985	5	87.8	0.97897	
2-4	dwtd5075	1 Ann, lch zr	0.00002	6105	0.03	4.5	1.1	298	49.27	239.0	0.9	493	8	1958	32	89.4	0.81528	
2-5	dwtd5074	1 Ann, lch zr	0.00002	6560	0.04	2.5	0.3	513	75.50	122.6	0.4	281.9	3	1969	20	94.6	0.69040	

FOOTNOTES TO TABLE

Analyses are ordered from highest to lowest ²⁰⁶Pb/²³⁸U age

Ab - abraded, Ann - annealed; lch - leached, euh - euhedral; brn - pale brown; frag - fragment; polycr - polycrystalline; incl - inclusions

Pbtot - total Pb in analysis in picograms

Pbcom - common Pb assuming the isotopic composition of laboratory blank:

206/204 - 18.221; 207/204 - 15.612; 208/204 - 39.360 (errors of 2%).

Th/U calculated from radiogenic ²⁰⁸Pb/²⁰⁶Pb ratio and ²⁰⁶Pb/²³⁸U age.

Rho - Correlation coefficients of X-Y errors on the concordia plot.

Uranium decay constants are from Jaffey et al. (1971).

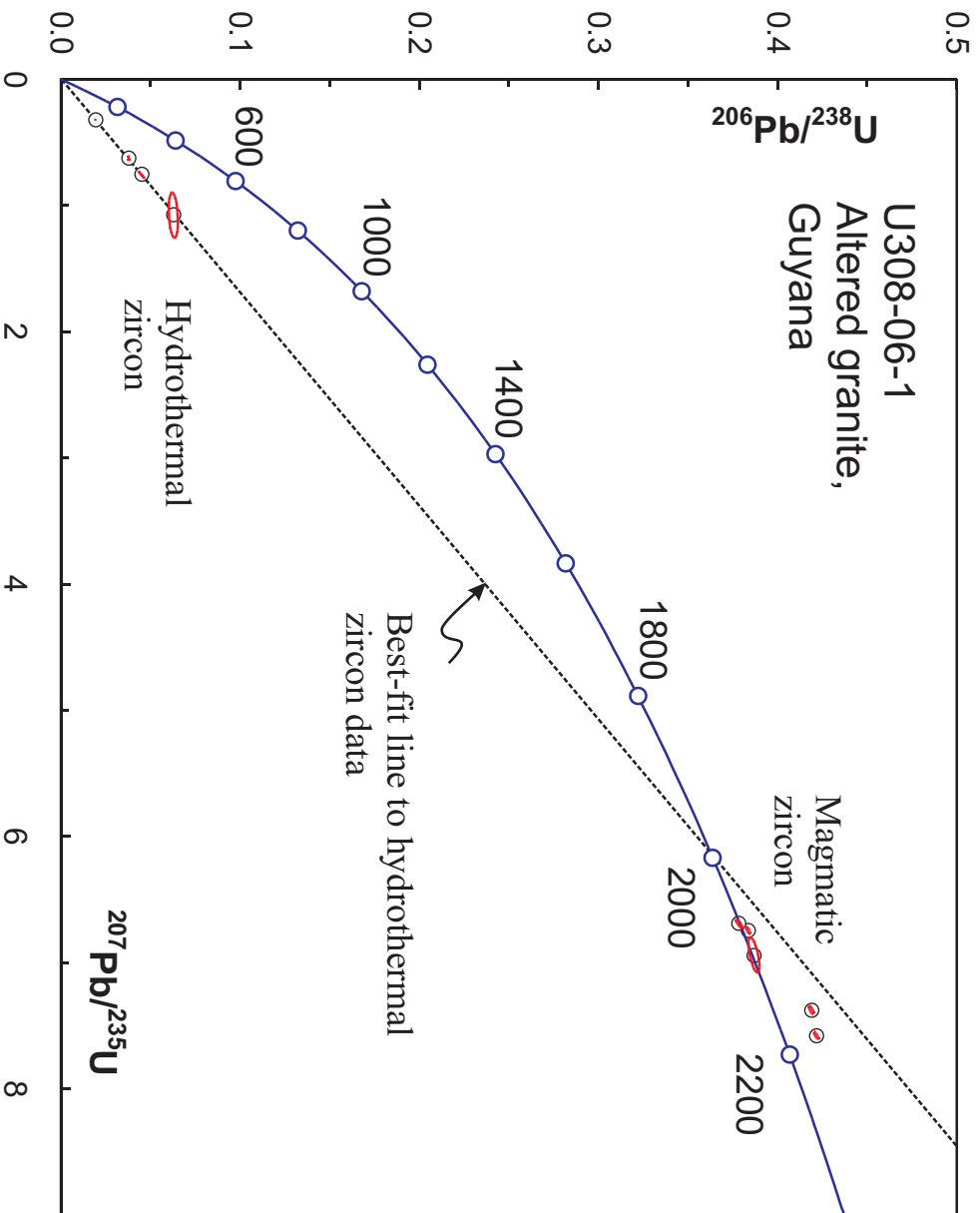


Figure 1

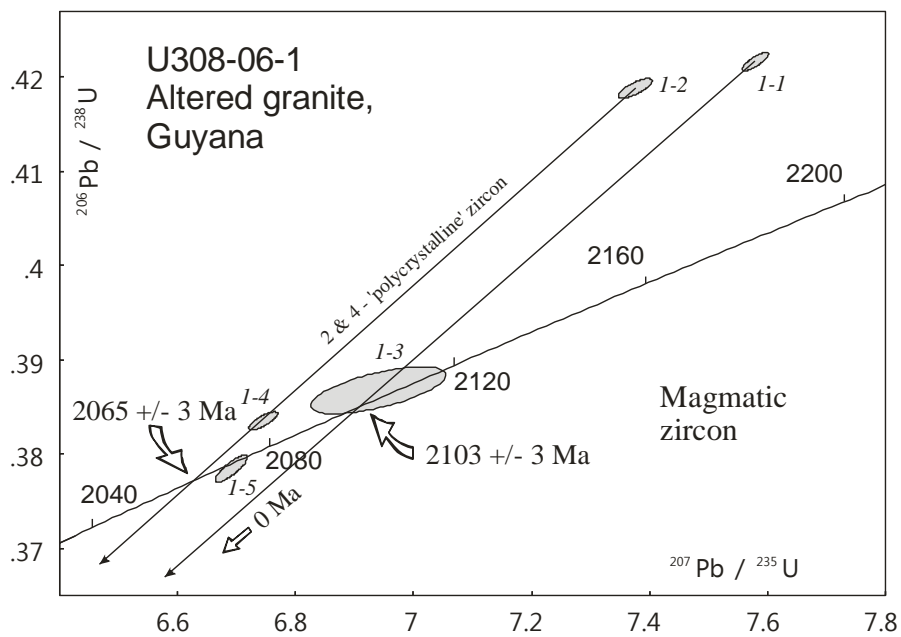


Figure 2

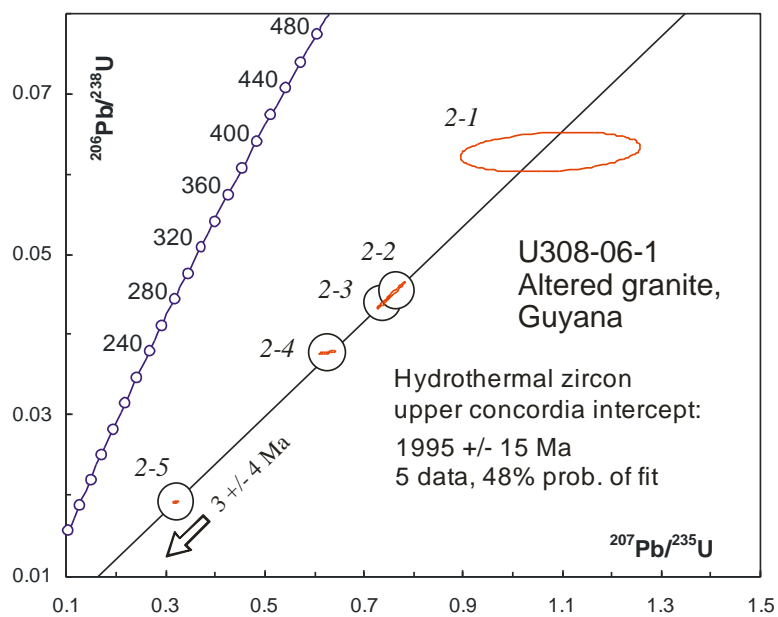
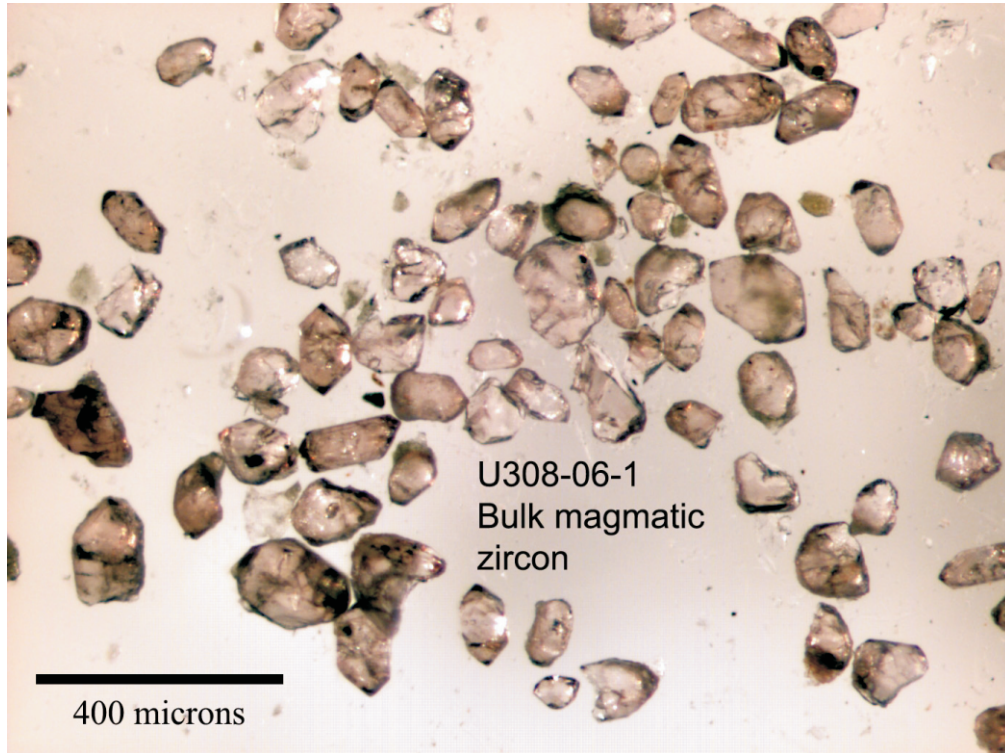


Figure 3

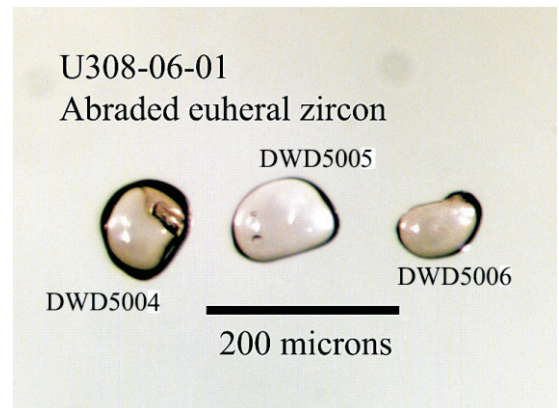
Images of magmatic zircon



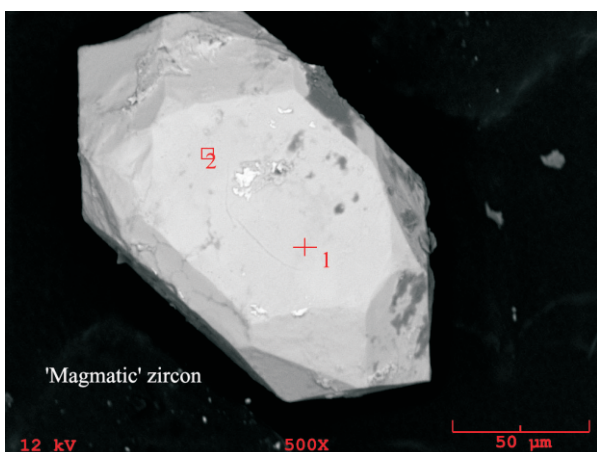
Optical image 1



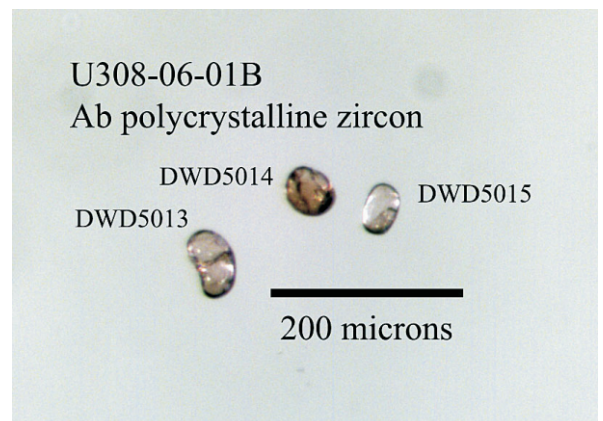
Optical image 2



Optical image 3

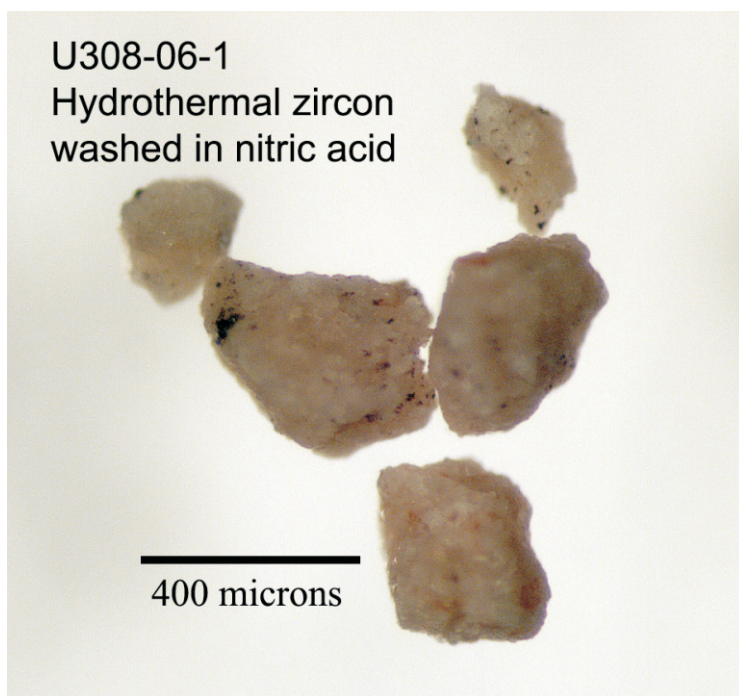


BSE Image 1

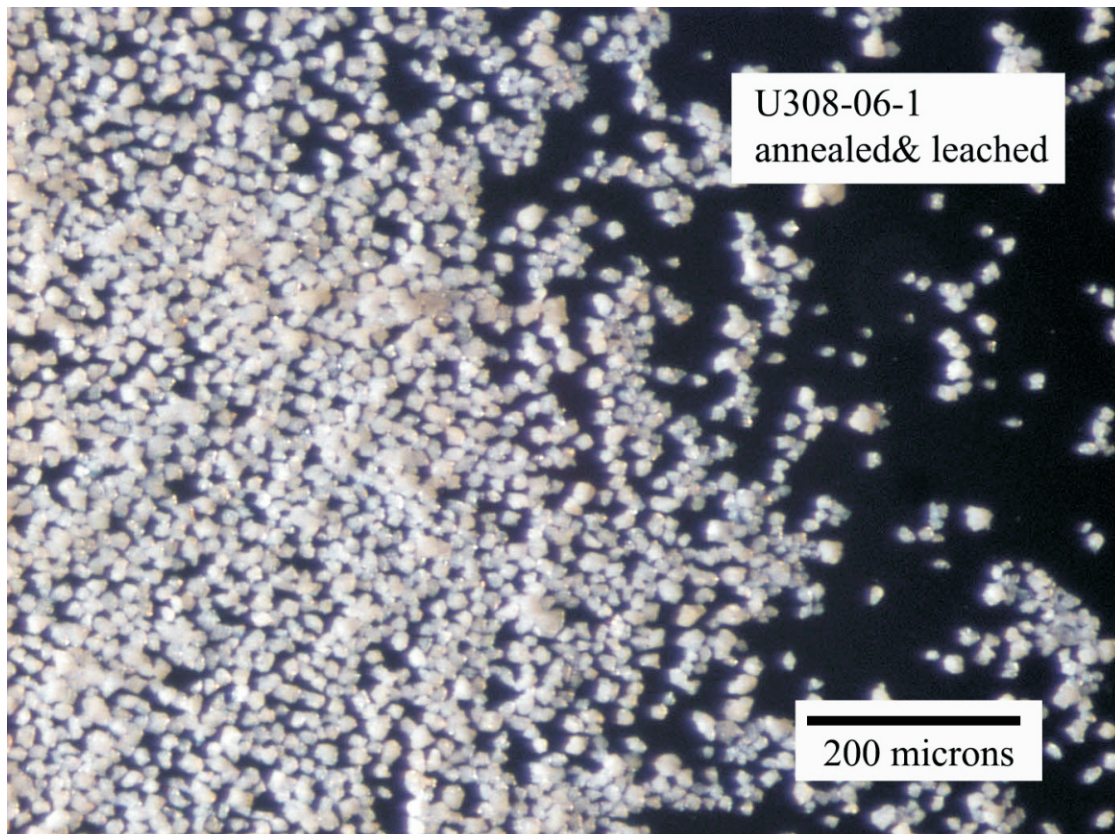


Optical image 4

Optical Images of hydrothermal zircon³¹³



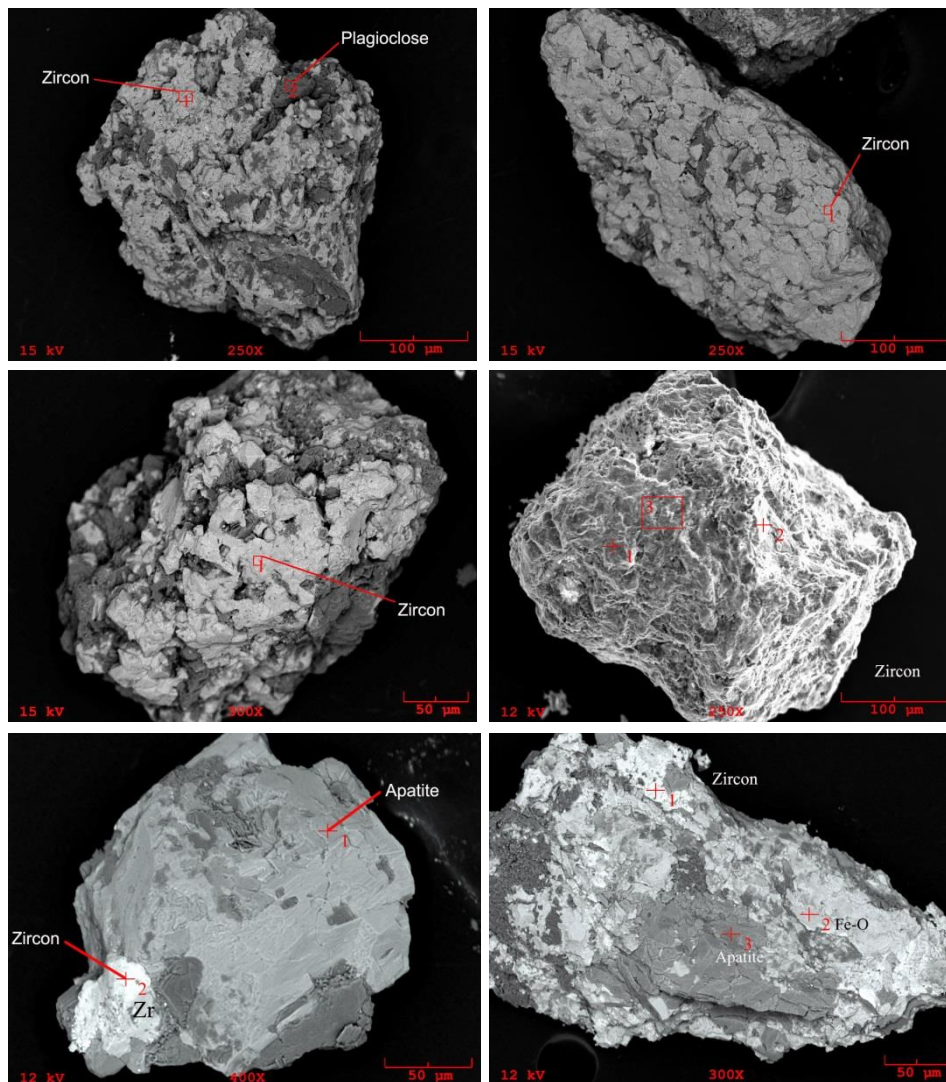
Optical image 5



Optical image 6

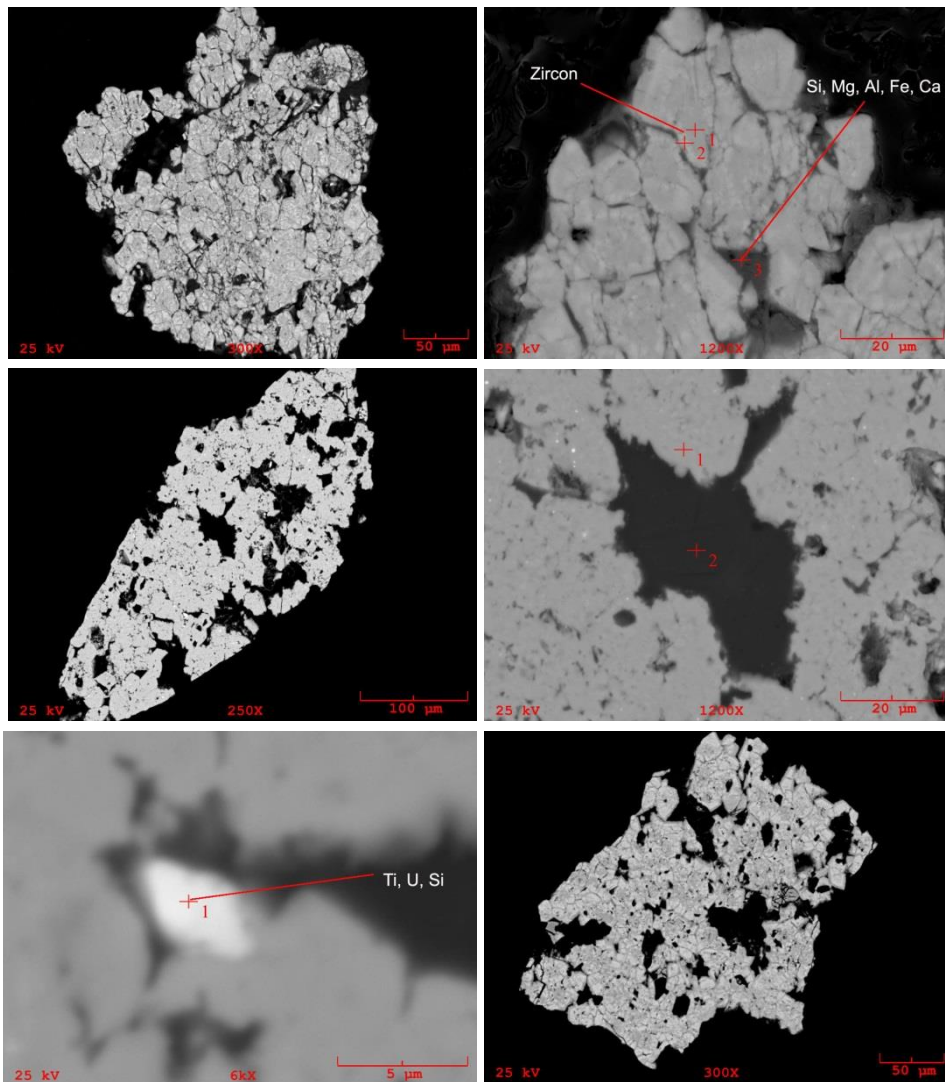
Electron Backscatter images of whole hydrothermal zircon

BSE images 3-7



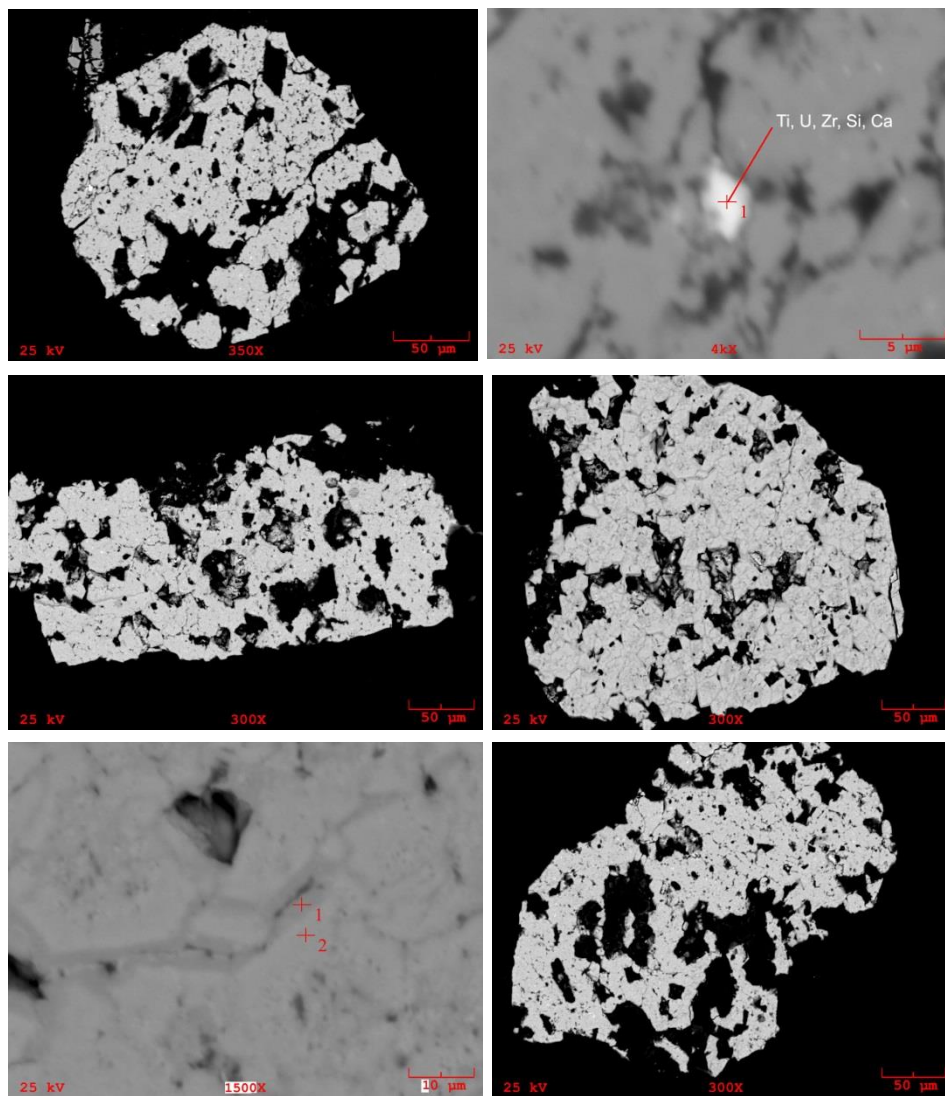
Electron Backscatter images of whole hydrothermal zircon

BSE images 8-10



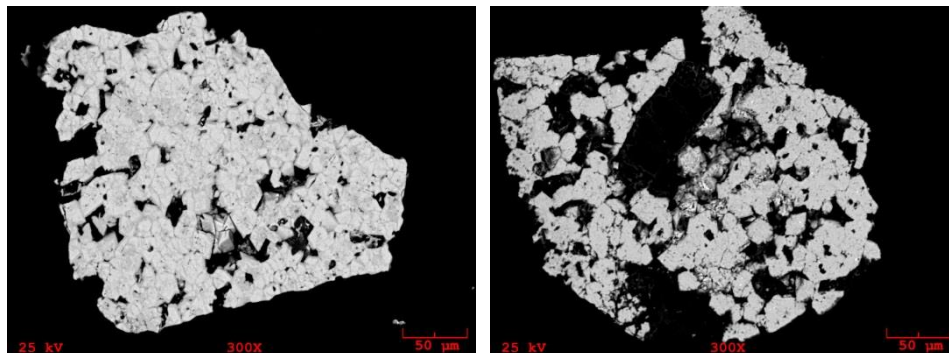
Electron Backscatter images of whole hydrothermal zircon

BSE images 11-14



Electron Backscatter images of whole hydrothermal zircon

BSE images 15-16



Curriculum Vitae: Jim Renaud, P.Geo.

Current Company: Renaud Geological Consulting Ltd.

Education: Ph.D. (Economic Geology), Western University, Canada, 2009-2014
 MSc. (Economic Geology), Western University, Canada, 2000-2003
 Honors Standing in Geology, Western University, Canada, 1999-2000
 BSc. Chemistry and Geology, Western University, Canada, 1996-1999

Honours and Awards:

NSERC-IPS2 scholarship, Western University (2010-2013)
 Robert & Ruth Lumsden award, Western University (2010-2011)
 Hugh E. McKinstry grant, Society of Economic Geologists, Western University (2010-2011)
 William Fyfe Scholarship in Environmental Sustainability, Western University (2010)

Related Work Experience: President, Renaud Geological Consulting Ltd.,

- Director of business operations and technical consultant
- Management of two JEOL 733 Electron Microprobes
- Geometallurgical troubleshooting via petrographic studies & microprobe analyses
- Technical Report Writing

Academic and Government Related Publications:

Phil J.A. McCausland, Roberta L. Flemming, Graham C. Wilson, Jim Renaud, David Dillon and David W. Holdsworth, 2013. The Wood Lake, Ontario H4 ordinary chondrite, a new Canadian meteorite. *The Canadian Journal of Earth Sciences*, V50, #1.

Renaud, J., MacLachlan, K., and Cairns, S., 2002. Stratigraphy and structure of the Aylmer Lake Volcanic Belt and surrounding metasedimentary rocks, part of NTS 75N/16, and 76C/1. *Current Research 2002*, Geological Survey of Canada.

MacLachlan, K., Relf, C, Cairns, S., Renaud, J., and Mills, A., 2002. New bedrock mapping and preliminary U/Pb geochronology in the Walmsley Lake area, southeastern Slave Province, NWT. *Current Research 2002*, Geological Survey of Canada.

- Renaud, J., and Duke, N., 2001. Stratigraphic reconstruction and geochemistry of the Aylmer Lake Volcanic Belt, southeastern Slave Province, NWT. 29th Yellowknife Geoscience Forum Program and Abstracts of Talks and Posters: p.62-63.
- MacLachlan, K., Relf, C., Cairns, S., Renaud, J., Hardy, F., and Davis, W.J., 2001. New results of the bedrock and surficial mapping components of the Walmsley Lake TGI project, southeastern Slave Province, NWT. 29th Yellowknife Geoscience Forum Program and Abstracts of Talks and Posters: p.50-51.
- Renaud, J., MacLachlan, K., Relf, C., and Duke, N., 2001. Volcanic stratigraphy and mineral potential of the Aylmer dome, southeastern Slave Province, NWT. Current Research 2001-C5; Geological Survey of Canada.
- Renaud, J., Armstrong, K., Gochnauer, K., and Duke, N., 2000. The stratigraphy and economic potential of the Aylmer dome, southeastern Slave Province, NWT. 28th Yellowknife Geoscience Forum Program and Abstracts of Talks and Posters: p. 67-68